UNIVERSITY OF SOUTHAMPTON

FACULTY OF ENGINEERING, SCIENCE & MATHEMATICS

School of Ocean and Earth Science

From continental thinning to sea-floor spreading: a geophysical study of rifted margins southwest of the UK

by

Andrew David Bullock

This dissertation is submitted for the degree of Doctor of Philosophy

August 2004

UNIVERSITY OF SOUTHAMPTON

ABSTRACT

FACULTY OF ENGINEERING, SCIENCE & MATHEMATICS
SCHOOL OF OCEAN AND EARTH SCIENCES

Doctor of Philosophy

FROM CONTINENTAL THINNING TO SEA-FLOOR SPREADING: A GEOPHYSICAL STUDY OF RIFTED MARGINS SOUTHWEST OF THE UK

by Andrew David Bullock

Geophysical methods were used to examine the crustal structure of the Goban Spur and North Biscay margins and the evolution from rifting to sea-floor spreading processes.

A 169 km wide-angle velocity model across the Goban Spur margin was produced and a 120 km wide region identified between undisputed oceanic crust and thinned continental crust, where velocities increase from 4.5 km s^{-1} to 6.8 km s^{-1} in the top 4 km beneath acoustic basement. At depth it can be divided into a region where a 1.5 km thick high velocity layer (7.2-7.6 km s^{-1}) exists and a region where this layer is absent, but velocities of $\sim$7 km s^{-1} are present. Wide-angle PmP arrivals are observed across the whole of the intermediate region, but a normal incidence reflection Moho is not present. The intermediate region is interpreted to consist of exhumed mantle where the high velocity layer is present and slow-spreading oceanic crust further seaward where this layer does not exist. The exhumed mantle region is 70 km wide, has a Poisson's ratio >0.34 at top basement and an extremely low topographic expression. The serpentinite content is estimated to decrease with depth from 100% at top basement to <25%, 5-7 km into basement. The observed magnetic anomaly is best fit by a thin, 1-1.5 km, layer of magnetisation 2-3 A m^{-1} and may be attributed to magnetite formation during a prolonged interaction of serpentinite with seawater. The region of slow-spreading oceanic crust is 50 km wide, consists of a series of basement ridges raised 400 m above the adjacent exhumed mantle and has a Poisson's ratio of $\sim$0.29 at top basement.

Reprocessing and migration of multichannel seismic profiles across the North Biscay margin show that continental crust was thinned from >24 km to $\sim$3 km over a distance of $\sim$200 km, at the expense of both upper and lower crust. Preferential thinning of the lower crust is evident in the gravity model and the disappearance of deep layered reflectivity. Seaward of this pinch-out, 60 km of upper continental crust, 3-6 km thick, directly overlies serpentinised upper mantle <3 km thick and with an average density of 3 $\times 10^3$ kg m^{-3}. The S-reflector changes significantly along the margin, shallowing westward from 12 km depth to just beneath top basement. The waveform and amplitude of S show it to mark a step increase in velocity consistent with the Moho towards the west and and intra-crustal event to the east. An upper crustal detachment isolated from S overlies the pinch-out of lower crust and may have been formed by the sudden release of stress accumulated within the upper crust during the period of maximum lower crustal strain.

Goban Spur and North Biscay sit firmly within the amagmatic classification of rifted margins, which have now been mapped from 36° to 53° N in the eastern North Atlantic, between the Azores-Gibraltar and Charlie-Gibbs fracture zones.

Graduate School of the Southampton Oceanography Centre

This PhD dissertation by

Andrew David Bullock

has been produced under the supervision of the following persons

Supervisor

Dr. Timothy Minshull

Chair of Advisory Panel

Prof. Harry Bryden

Member of Advisory Panel

Dr. Doug Masson

"We shall refrain here from citing the literature in support of our statements. The obvious needs no backing by outside opinion, and the wilfully blind cannot be helped by any means."

Alfred Wegener, 1929.

Die Entstehung der Kontinente und Ozeane, 4^{th} edition. Page 133 of the English translation (The origin of continents and oceans) by John Biram, 1966.

Acknowledgements

Many thanks to my supervisor Tim Minshull for his help and guidance during the course of my studies and for the exhaustive proof-reading of this thesis, much of it at very short notice. Special thanks must also be extended to Phil Cole and Tim Henstock for the substantial improvements they have suggested from the initial drafts. This thesis has benefited much from their advice.

This study would not have been possible without the efforts of the officers and crew of *RRS Charles Darwin* cruise 124 who had to contend with trying conditions and some impatient scientists. I would also like to extend my thanks to George Batten for acquiring swath bathymetric data during *RRS Charles Darwin* cruise 116 and David Billett for improving on our failed dredge attempt during *RRS Discovery* cruise 255.

Some of this work was completed at Amerada Hess Ltd, where I was welcomed into the North Atlantic margins group for a three-month period. I depended on the technical advice of Stuart Fairhead, Andy King and John Smallwood during this time and appreciate it greatly. My time in London would have been less energetic without the opportunity to gate-crash the 5-a-side football team, and for that I thank you all.

While working on my thesis I have been lucky enough to spend some time at other institutions. Particular thanks must go to Thomas Leythauser at GEOMAR, Kiel, and Keith Louden at Dalhousie who invited me on the cruise to the conjugate margin. I look forward to seeing the results! Too many people welcomed me to these cities to mention them all, but I look forward to returning the compliment someday.

During my time at Southampton Oceanography Centre I have received considerable support from many people as the lines between academic and social life became increasingly blurred. The Simons (Topping and Dean) and Nev have proven their abilities in all matters computing; sharing an office with Christos has provided me with ample opportunity to learn expletives in Greek; and Jenny, Jude, Chris, Sarah, Jules and Dhananjai, you have, at times, made me smile. I will miss you all. Cricket is an essential part of life and I thank Mike and Pete for making a 'decent' bowler and opening batsman out of me.

Roz has been a special friend to me for the past three years, but two bits of advice should follow: try to spend longer than a few months in the country at some point soon, and upon meeting someone for the first time, it is considered impolite to rubbish their entire work. I guess our friendship survived that episode and long may it continue.

I would like to give special thanks to Chris, who has put up with a lot in the last year to help me finish, usually accepting it with a smile, and provided the constant reminder that the end would come. Finally I would like to thank my parents for their support over the last few years. It has meant a lot to me and it is with great love that I dedicate this thesis to them.

Contents

List of Figures

List of Tables

Abbreviations and Acronyms

AGC	Automatic gain control
BIRPS	British Institutions Reflection Profiling Syndicate
CD-116	*RRS Charles Darwin* cruise 116, 1999
CD-124	*RRS Charles Darwin* cruise 124, 2000
CDP	Common depth point
CMQZ	Cretaceous magnetic quiet zone
DAS	Deconvolution after stack
DBS	Deconvolution before stack
(D)GPS	(Differential) Global positioning system
DPG	Differential pressure gauge type OBH
DSDP	Deep Sea Drilling Project
FAA	Free-air gravity anomaly
f.s.r.	Full-spreading rate
GMT	Generic Mapping Tools
MAR	Mid-Atlantic Ridge
MCS	Multichannel seismic data
Moho	Mohorovičić discontinuity
MOR	Mid-ocean ridge
NMO	Normal moveout
N-MORB	Normal mid-ocean ridge basalt
OBH	Ocean bottom hydrophone
OBS	Ocean bottom seismometer
Q_p, Q_s	Seismic P- and S-wave quality factor
RMS	Root-mean-square
SB	Sonobuoy
SEG-C	Society of Exploration Geophysicists digital recording standard C
SEG-D	Society of Exploration Geophysicists digital recording standard D
SEG-Y	Society of Exploration Geophysicists digital recording standard Y
SNR	Signal to noise ratio
SOC	Southampton Oceanography Centre
SP	Shotpoint
TWT	Two-way travel time
WAM	Western Approaches Margin MCS line
XBT	Expendable bathythermograph

Chapter 1

Introduction

1.1 Continental Rifting

1.1.1 A dynamic earth

Our understanding of the Earth's interior has changed vastly over the last century with the rapid growth of remote sampling methods (e.g., seismic, electromagnetic, gravity and magnetic); satellite altimeters can be used to infer changes in deep structure and there are plans to sample ever deeper levels with the new generation of drill ships. We no longer apply to the entire history of Earth development the concept of *catastrophism*, so strongly supported by theologians up to, and beyond, the nineteenth century, but follow the principle of *uniformitarianism*, developed from the ideas of James Hutton in 1795 that propose a continuous cycle of earth development through deformation processes operating presently and in the past (Kearey and Vine, 1990).

The Earth, in its simplest form, consists of four layers: the inner and outer core, mantle and crust. The inner core appears to be solid, consisting of pure iron and is surrounded by a fluid outer core, composed largely of iron and nickel and believed to drive the Earth's magnetic field. The mantle is the largest region of the Earth and believed to be chemically homogeneous, except for minor and trace elements, and consists of peridotite or eclogite; strong anisotropy, isostatic support and S-wave velocities suggest that the upper mantle consists largely of peridotite with abundant olivine. Two major boundaries at 410 and 660 km depth are associated with olivine-spinel and spinel-perovskite phase changes and form a transition zone separating the upper and lower mantle. Variation in the isotopic signature of melt products suggest that the mantle is not well mixed throughout; compositional heterogeneity may be caused by multiple, but geographically variable, melting

cycles and recycling of oceanic and continental material (e.g., Hofmann, 1997). Overlying the mantle is the Earth's crust. This layer is relatively thin, varying from ~5 to 60 km and exhibits the topography that we observe, from the highest peaks (Mt. Everest: 8850 m) to the deepest basins (Challenger Deep, Marianas Trench: -11,520 m). The oldest crustal material observed is ~4300 Ma (Western Australia) while crust within ocean basins is relatively young, <200 Ma, due to the constant recycling of plate tectonic processes. A comparison of crustal types is made in Chapter 2.

Plate tectonic theory describes the lithosphere, formed of the crust and the upper mantle, as consisting of solid plates that move relative to each other and decoupled from the asthenosphere beneath (Figure 1.1). The close fit of the coastlines of South America and Africa, now widely separated by the Atlantic ocean, was initially observed as early as 1756 by Professor Theodor Lilienthal (Kearey and Vine, 1990) and subsequently by many others including Alfred Wegener (Wegener, 1929). Geometrical arguments are supplemented by fossil and faunal records, Global Positioning System observations, magnetic lineations formed by sea floor spreading and earthquake events to provide evidence for the relative motion of plates. These motions mean the Earth is in a constantly active state, with new crust formed at mid-ocean ridges e.g., the Mid-Atlantic Ridge (MAR: Figure 1.1) and destroyed at subduction margins e.g., the Japan Trench (JT: Figure 1.1). Transform plate boundaries e.g., the San Andreas Fault (SAF: Figure 1.1) exist where crust is neither produced nor destroyed and plates move against each other. The extensional processes experienced prior to plate separation and leading to the formation of rifted continental margins are considered in this thesis.

1.1.2 The formation of rifted margins

Rifted margins form by the deformation of a continental block under extension. Initiation of the rift process may be encouraged by upwelling of hot asthenospheric material beneath the continent, causing thermal uplift and plate thinning (e.g., under mantle plume influence) (e.g., Sengör and Burke, 1978; Spohn and Schubert, 1982) or by far-field tensional forces set up within the plate (e.g., Sengör and Burke, 1978; Buck, 1986). In the absence of pre-rift mantle thermal anomalies or driving forces deep within the mantle (e.g., Mutter et al., 1988; Holbrook et al., 2001), it can be assumed that mantle upwelling occurs as a passive response to lithospheric extension.

Continental rifting can be described in three major phases. Initially, stress focuses within the continental block, possibly controlled by some rheological variation within the body

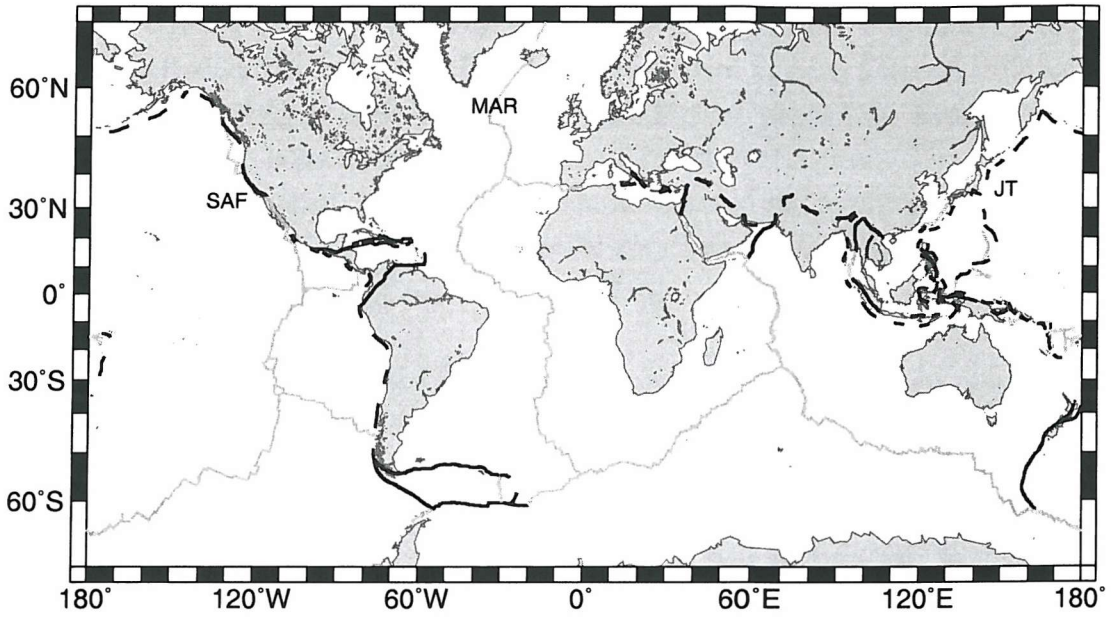

Figure 1.1: Global map showing continents and different types of plate boundaries. Grey lines indicate accretionary boundaries, dashed black lines mark convergent boundaries and solid black lines are transform boundaries. MAR is the Mid-Atlantic Ridge, SAF is the San Andreas Fault and JT is the Japan Trench. After Cole (2003).

rock, weakness due to an earlier period of tectonism or some intrusive feature e.g., magmatic underplate (Whitmarsh et al., 2001a) and allows the initiation of faulting.

During extension, the continent thins and tilted fault blocks form in the upper crust, tending to decrease in both size and spacing seawards (e.g., Winterer et al., 1988). Deeper continental crust, outside of the brittle regime, may deform by ductile flow or creep (Section 1.1.3). Many margins appear to have experienced a single rifting phase, but seismic evidence showing the relative ages of syn-rift sedimentary packages suggests that some margins may have experienced multiple phases of continental extension (e.g., Galicia Bank: Reston et al., 2003). As extension continues, the crust thins further and mantle upwelling occurs beneath the rift axis and may cross the mantle solidus, producing melt products (Section 1.1.5) and encouraging the initiation of sea-floor spreading. The transition from rifting to spreading is not an abrupt one. Continental rifting may continue during early sea-floor spreading; there is not a sudden transfer of strain to the rift axis, but it remains diffuse throughout the margin and melt volumes may increase gradually until final break-up occurs (e.g., Bonatti, 1985; Taylor et al., 1999).

The transition from continental rifting to sea-floor spreading may be complex and, depending on the margin under consideration, there may be an intermediate stage. Extensive volcanism (e.g., White et al., 1987a) or amagmatic extension (e.g., Whitmarsh et al., 2001a) have both been observed towards the end of rifting and it is these differences that lead to the classification of rifted margins as volcanic or non-volcanic (Mutter, 1993). Rifted margins are considered volcanic if a well developed underplated layer and a seaward dipping reflector sequence is present and there is evidence for both extrusive and intrusive magmatism near the time of rifting (White et al., 1987a; White and McKenzie, 1989), while non-volcanic margins exhibit little or no syn-rift volcanism. Factors influencing melt production such as lithospheric rheology and the deformation mechanism are considered in Sections 1.1.3 and 1.1.4; variation in magmatic style at North Atlantic margins are examined in Section 1.2.

1.1.3 Rheology of the lithosphere

Rheology is the study of the flow and deformation of materials under applied stresses. The way in which the material deforms depends on the magnitude of the stress and the time which it is applied for. Elastic deformation occurs if the applied stress is less than the yield stress; when the applied stress exceeds the yield stress, the material experiences permanent deformation in a brittle (e.g., Byerlee, 1978) or ductile (e.g., Goetze, 1978) manner. Brittle failure results in deformation by fracturing of the material, with displacement occurring along narrow slip planes, and is the dominant deformation mechanism within the upper 5-10 km of the lithosphere. Ductile deformation does not result in failure of the material, but a more gradual non-elastic change in shape. Ductile flow is the main deformation process operating in the asthenosphere and may be observed at various depths within the lithosphere depending on the local composition and geothermal gradient.

Yield strength curves for oceanic crust, continental crust and serpentinised peridotite are calculated using Byerlee's friction law (e.g., Byerlee, 1968; Byerlee, 1978) and experimental plastic flows (e.g., Kohlstedt et al., 1995) and shown in Figure 1.2. These curves involve extrapolation over many orders of magnitude from laboratory measurements, so there is some uncertainty in the absolute values from these calculations and the horizontal axes therefore are not labelled. Variations can be attributed largely to compositional differences between crustal types; upper continental crust was considered to be wet quartzite and lower continental crust a combination of dry quartzite and anorthosite

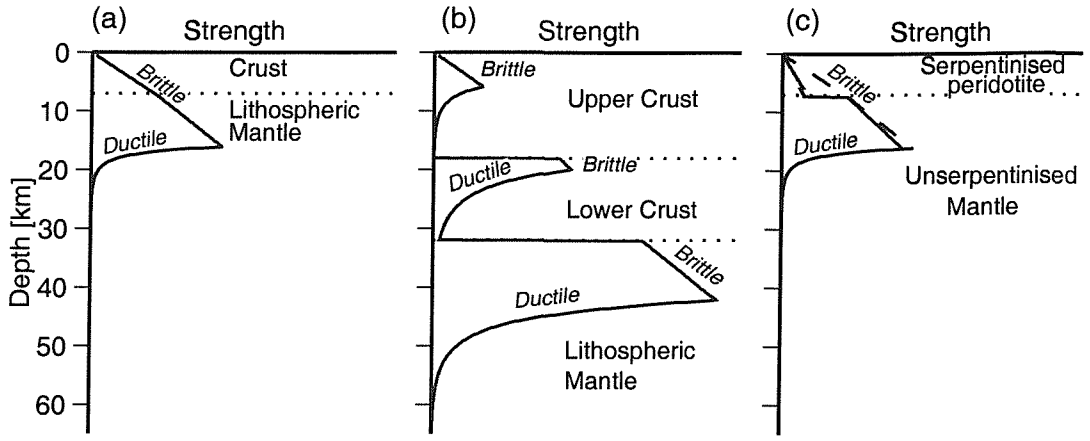

Figure 1.2: Yield strength curves for (a) oceanic lithosphere, (b) continental lithosphere and (c) serpentinised peridotite. (a) and (b) after Molnar (1988) with strain rates of 10^{-15} s^{-1} and $4{\times}10^{-15}$ s^{-1} respectively (Pérez-Gussinyé et al., 2001b). (c) calculated using the friction law for serpentinite (Escartín et al., 1997b) below 400° C and Byerlee's law (Byerlee, 1978) above 400° C. A strain rate of 10^{-15} s^{-1} is assumed. The dashed line indicates the hydrostatic-Byerlee's law limit for olivine. The horizontal axis is plotted in non-dimensional units of strength. After Cole (2003).

(Pérez-Gussinyé et al., 2001b); oceanic crust was assumed to consist of mafic igneous rocks (e.g., Escartín et al., 1997b). Serpentinite has a low coefficient of friction, ~0.3 (Escartín et al., 1997a; Escartín et al., 1997b), which reduces the strength of the lithosphere, but strength increases abruptly at the transition to unserpentinised mantle material which is modelled as olivine. If the extent of serpentinisation decreases with depth then strength may increase more gradually with depth to the top of unserpentinised mantle.

In addition to strain rate, the local geothermal gradient and crustal thickness also influence lithospheric strength (e.g., Watts, 2001a) and further rheological variations may result from the presence of water within the crust (Kusznir and Park, 1987). Strength increases with age in oceanic lithosphere (e.g., Watts et al., 1980) due to cooling away from the ridge axis and results in an increase in thickness of the brittle layer. Earthquakes are caused by brittle failure at a high strain rate and depths predicted by focal mechanism solutions show that they may be located within the crust or upper mantle for oceanic lithosphere (e.g., Huang and Solomon, 1988) (Figure 1.3). Earthquakes are concentrated within the crust of continental lithosphere (Figure 1.3); although some authors show earthquakes occurring within the upper mantle, there is some disagreement due to uncertainties in the

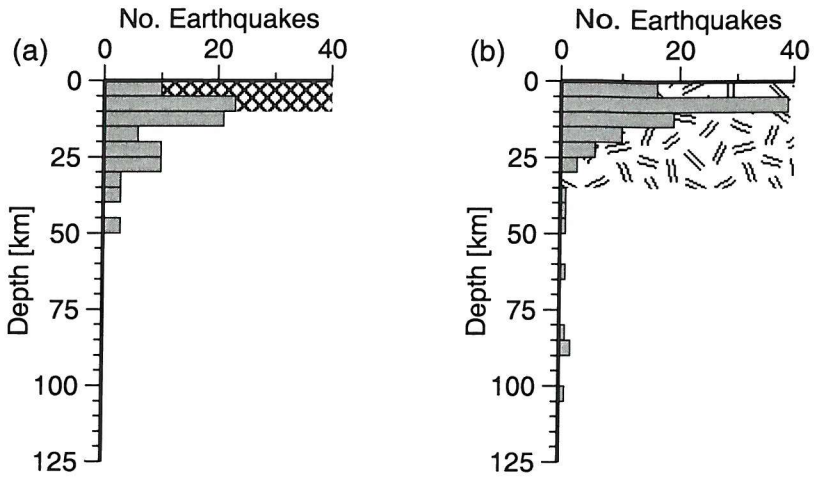

Figure 1.3: Comparison of earthquake depths for (a) oceanic and (b) continental crust. The average crustal thickness for each regime is shown by the shaded regions. Earthquakes occur throughout the crust and upper mantle in oceanic lithosphere, but occur mostly within the crust of continental lithosphere. Modified from Watts (2001a). The earthquake data are based on the compilations of Chen and Molnar (1983) and Wiens and Stein (1984).

depths of events (Chen and Molnar, 1983; Maggi et al., 2000). Changes in the geothermal gradient may cause the depth to the 400° C isotherm, taken to mark the limit of the brittle deformation field (Watts, 2001a), to vary. For continental lithosphere, an increase in the geothermal gradient reduces the thickness of the brittle layer and can put the whole of the lower crust into the ductile deformation regime, a decrease in geothermal gradient similarly increases the thickness of the brittle layer (Watts, 2001a). If there is significant mafic addition to the lower continental crust then it becomes more likely to deform in a brittle manner, due to the greater strength of mafic rocks compared to granitic rocks, and ductile deformation will be restricted to the middle crust.

1.1.4 Margin architecture and rifting models

The way in which continents deform during rifting has traditionally been considered in terms of endmember deformation mechanisms: pure and simple shear. Composite models, including an element of both of these mechanisms, have also been proposed and may help further explain many features observed within rifted margins. Results from analogue and numerical modelling are used to also consider theoretical models of continental rifting.

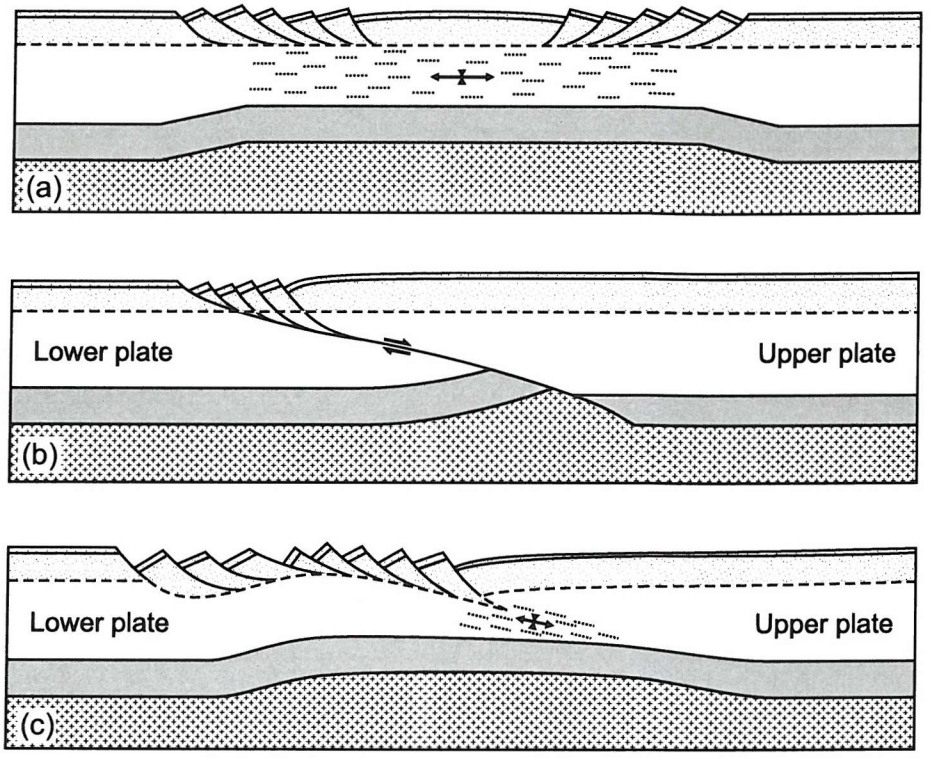

Figure 1.4: Theoretical models for continental extension. (a) Pure shear, (b) lithospheric scale simple shear and (c) composite model with simple shear restricted to the brittle crust and pure shear in the ductile lithosphere. The brittle–ductile boundary is indicated by the dashed line and dotted lines show regions experiencing pure shear deformation. Asthenospheric mantle is the deepest layer marked by crosses. From Dean (1999); modified from Lister et al. (1986) and Lister and Davis (1989).

Pure shear

The pure shear rifting model first proposed by McKenzie (1978) assumes uniform stretching throughout the lithosphere. Lithospheric extension occurs in a symmetric manner and is accommodated by normal faulting in the brittle upper crust and by ductile flow beneath the brittle–ductile transition (Figure 1.4*a*). These assumptions are unlikely to remain valid in all real world situations because, even assuming a homogeneous lithospheric composition, rheological changes with depth are expected, as discussed earlier. This rheological depth dependence is likely to be increased by heterogeneity within the lithosphere, phase changes related to the increase in pressure and temperature with depth and compositional changes as a result of magmatic or metamorphic processes (Twiss and Moores, 1992).

The lithospheric pure shear extension model provides a good fit to the observed basin geometry within the North Sea, where the strength profile of the lithosphere appears to depend on pressure and temperature only (White, 1989). Depth-dependent stretching models may provide a closer fit in situations where the degree of stretching is observed to vary greatly with depth (e.g., Davis and Kusznir, 2004). Dunbar and Sawyer (1989a) developed a simple two-layer lithospheric model to include differential stretching between the crust and mantle and illustrate the influence on melt production and break-up processes. When the mantle is weak compared to the crust, extension is focused in the mantle, encouraging early magmatism and a narrow continental margin; if the crust is weak compared to the mantle then extension is focused in the crust, forming a wide margin and impeding melt production until late in the rift development. The strength of the lower crust also influences the development of the stretching lithosphere. A weak lower crust may allow the upper crust to decouple from the mantle and the region of maximum strain to be offset from the rift axis (Hopper and Buck, 1998) with upper crustal variations supported by viscous flow of the lower crust (Buck, 1991; Hopper and Buck, 1996).

Simple Shear

Simple shear rifting models consist of a low angle shear zone or detachment fault cutting across the entire lithosphere (Figure 1.4*b*). Extension occurs asymmetrically and large relative displacements can be supported between the foot and hanging walls. This type of model was originally developed to account for the metamorphic core complexes observed in ~20 km thick crust of the Basin and Range province of the western United States (Wernicke, 1981; Wernicke, 1985) where low angle normal faults have a surface area of >10,000 km^2 with a relative displacement of at least 40 km (Lister and Davis, 1989). Core complexes and low angle detachments have also been identified in slow spreading oceanic crust west of Africa at ~25° N (Reston et al., 1996b) and on the Mid-Atlantic Ridge (e.g., Cann et al., 1997; Tucholke et al., 1998).

Detachment faults have also been proposed to play a role in rifting and break-up leading to the development of continental margins. Simple shear rifting produces an asymmetric conjugate margin pair with the upper and lower plates (Lister et al., 1986) of the extending system separated by the newly formed ocean basin. These models have been used to describe some of the asymmetry observed in the Central Atlantic (Dunbar and Sawyer, 1989b), Labrador Sea (Chian and Louden, 1994; Chian et al., 1995b) and the Northern Carnarvon Basin, north-west Australia (Driscoll and Karner, 1998).

The simple shear rifting model requires displacement along a normal fault at an angle much less than the ~45° angle predicted by Andersonian fault mechanics (Anderson, 1942). Until recently, a lack of earthquake focal mechanisms at a low angle in extensional provinces has led some authors to argue that currently active faults do not slip at low angles of dip (e.g., Jackson, 1987), potentially originating at a steep dip and rotating to be inactive at a low angle (e.g., Buck, 1988). Lavier et al. (1999) extend this idea through numerical modelling of fault growth to show that in the *rolling-hinge* model, low angle structures can be formed by rotation of the inactive part of the fault as it is offset from the active faulting.

Recent focal mechanism solutions show faulting at dips of <30° in the Gulf of Corinth (Reitbrock et al., 1996) and 25-30° in the Woodlark Basin (Abers, 1991; Abers et al., 1997; Floyd et al., 2001; Abers et al., 2002) and provides strong evidence for normal faults active, and forming (Axen, 2004), at low angles, and not rotated to these orientations after the cessation of slip. A strong intra-crustal reflection at the Galicia Bank margin has been variously interpreted, including as a lithospheric or crustal scale detachment fault within a simple shear rifting regime (e.g., Boillot et al., 1988; Whitmarsh et al., 1996a) and shown, through detailed analysis of seismic reflection data, to have been active at an angle of ~20° (Reston et al., 1996a). To explain the apparent conflict between fault mechanics and the observed low angle faults Chéry (2001) suggest that a combination of high pore pressure and rotation of the stress axes at depth encourages the formation of new faults along a low angle fault plane at depth, beneath high angle faults in the upper ~10 km of the crust. Exhumation of this low angle fault is proposed to occur by isostatic adjustment during continued extension.

Composite rifting models

Pure and simple shear deformation models can on their own explain some of the features observed at rifted continental margins, but neither can satisfactorily explain margin development in general. A composite rifting model (Figure 1.4*c*) combines pure and simple shear deformation mechanisms, including the observed low angle faults, without requiring narrow detachments or shear zones to cut the entire lithosphere. Models of this type can successfully explain differential thinning of the crust and lithospheric mantle (e.g., Ruppel, 1995), the large displacement between maximum crustal and lithospheric thinning and the focus of melt production offset from surface thinning, for example in the delamination model of Lister et al. (1986).

Pure and simple shear may act on different length scales or at different times during margin development. Sibuet (1992) suggest that at the Galicia Bank margin the entire lithosphere deforms by pure shear and simple shear is restricted to the upper crust only. Time dependent rift models have been suggested for the Iberia margin where pure shear occurs during rifting with simple shear during the late stages results in asymmetric break-up and exhumation of upper mantle (Whitmarsh et al., 2001a).

Analogue models

Analogue models at a lithospheric scale provide important information on the mechanism of deformation during extension. One common approach is to scale the thickness, viscosity, density and the strain rate to simulate an extending continental lithosphere (Davy and Cobbold, 1991). Alternating sand and silicon layers are typically chosen to represent the brittle and ductile layers of the crust and mantle (Figure 1.2*b*) (e.g., Michon and Merle, 2003). Experiments at a crustal (Michon and Merle, 2003) and a lithospheric scale (Brun and Beslier, 1996) show similar results and illustrate the strong influence of extension rate on deformation. At a low extension rate a single asymmetric graben forms within the brittle layers (Figure 1.5*a*), but at higher extension rates two grabens are formed with an asymmetric graben located towards the locus of extension (Figure 1.5*b*). Lithospheric mantle may be exhumed by bulk pure shear prior to the onset of oceanic crustal accretion, with localised simple shear and boudinage within the brittle upper mantle (Brun and Beslier, 1996). A major limitation of analogue modelling is that rheological properties are fixed and cannot be modified as extension progresses. Not including these changes may, for example, allow ductile flow within the brittle regime and not accurately model earth deformation under conditions of extreme thinning.

Numerical modelling by finite-element methods further elucidate the importance of strain rate on rift development (e.g., Bassi, 1995; Huismans and Beaumont, 2003). Slow extension rates may allow cooling and strengthening of the lithosphere which Kusznir and Park (1987) suggest will result in a wide continental rift compared to more rapid extension rates. Strain hardening (Bassi, 1995), where lithospheric rheology is modified under slow extension rates, may result in asymmetric continental break-up. In this case, strain hardening in the rift axis causes the region of maximum stress to be displaced towards a weaker, necked, region at the edge of strained crust. Following the opposite argument, a rapid extension rate produces a narrow rift and symmetrical break-up. Harry and Bowling (1999) show that 5-7 km of oceanic crust can be formed with no associated syn-rift

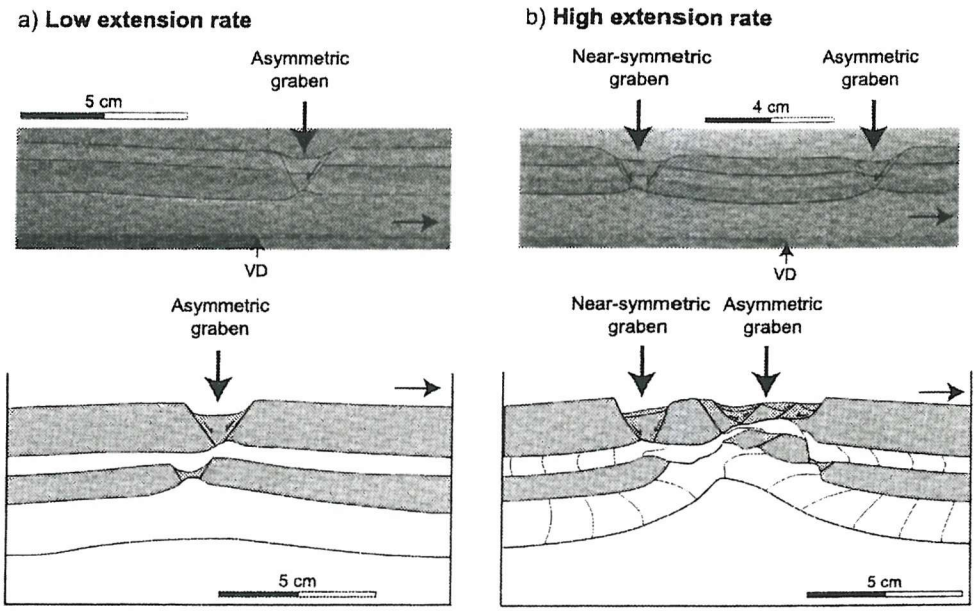

Figure 1.5: Analogue rifting models at a crustal (Michon and Merle, 2003) and lithospheric scale (Brun and Beslier, 1996). (a) Comparison at (a) low and (b) high extension rates. VD marks the velocity discontinuity introduced at the base of the crust to initiate rupture. From Michon and Merle (2003).

magmatism, without requiring large changes in mantle temperature or conductive cooling, by restricting melting to the late stages of lithospheric necking.

1.1.5 Controls on syn-rift magmatism

Partial melting of mantle material begins as it crosses the solidus, the mantle melting curve, and preferentially removes incompatible elements from the mantle (Hofmann, 1997). Two mechanisms have been proposed for melt production during rifting: passive upwelling and decompression melting beneath the thinning lithosphere as the mantle expands adiabatically, or active upwelling (e.g., Holbrook et al., 2001). Either hypothesis may apply to a rifting margin depending on the local conditions, however, following the principle of Occam's Razor, if the observations can be explained by the passive response of the asthenosphere to extension then this is preferred to a more complex active upwelling process. The observed melt volumes in the eastern North Atlantic can, with some modifications, be explained by decompression melting as response to passive upwelling (e.g., Bown and White, 1995), so this mechanism is assumed within this thesis.

Mantle potential temperature and rift duration

The mantle potential temperature is the temperature the mantle would have if raised to the surface adiabatically, without experiencing any melting. Increasing the potential temperature, under otherwise identical extension conditions, causes a mantle region to cross the adiabat sooner and a greater volume of melt to be produced (Figure 1.6). The amount of melt predicted is highly dependent on the mantle potential temperature assumed. A potential temperature of ~1300° C can form the ~6 km of magmatic crust observed at mid-ocean ridges (Bown and White, 1994) hence a potential temperature of ~1300° C is often assumed for normal upper mantle that experiences continental rifting (e.g., Bown and White, 1995; Minshull et al., 2001). Significant volumes of melt are predicted by melting models (e.g., Bown and White, 1995) where none is observed and additional factors are considered to explain this (see the following discussion on rift duration and extensional mechanisms). Melt volumes can by greatly reduced if the mantle potential temperature is lower (Figure 1.6), but these suggestions, until recently, have required the presence of anomalously cold upper mantle. Reston and Phipps Morgan (2004) documented global continental geotherms and show that, within the significant uncertainty of the measurements (±150° C: Röhm et al., 2000), the sub-lithospheric mantle may have a potential temperature as low as 1200° C. During rifting and the early stages of break-up sub-lithospheric mantle may dominate and therefore better represent mantle beneath passive continental rifts.

Assuming a finite amount of extension, rift duration controls the strain rate experienced and has a large influence on melt generation (Pedersen and Ro, 1992). A short rift duration allows less heat to be dispersed by conduction and encourages melting, while a longer rift duration has the opposite effect. Minshull et al. (2001) proposed that vertical and lateral heat conduction can explain the absence of syn-rift melt products observed at the Iberian margin (Dean et al., 2000; Russell and Whitmarsh, 2003) and that more dispersed mantle upwelling at continental break-up may increase the heat lost through conduction and further restrict melt production.

Extensional style

The mode of lithospheric deformation has a large influence on both the volume and distribution of melt products during rifting. In a simple shear extension model any melt produced during lithospheric thinning is not equally distributed between the conjugate margins, but concentrated on the upper plate margin where crustal thinning is greatest

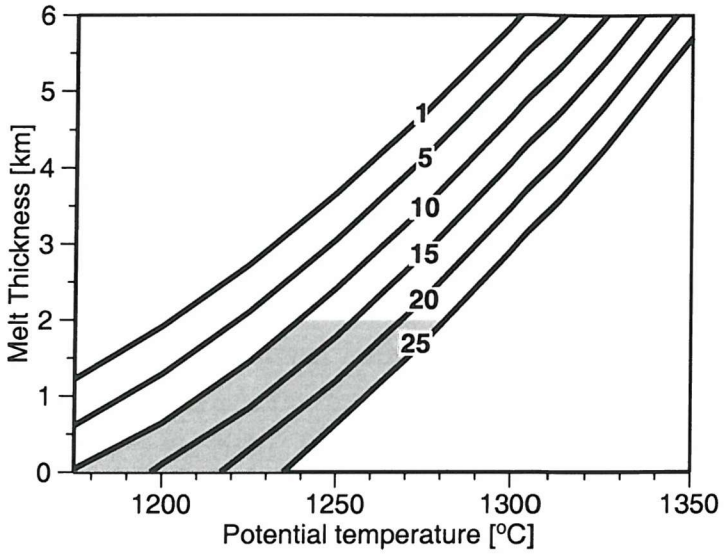

Figure 1.6: Given a finite rift duration (numbered curves in m.y.) the predicted melt thickness increases with increasing mantle potential temperature. The melting model of Bown and White (1995) and instantaneous thinning (β=50) are assumed. A melt thickness of <2 km with a rift duration of 10-25 m.y., typical for the Goban Spur margin, is shaded and suggests that low mantle temperatures may be required to inhibit melt production. After Minshull et al. (2001).

(Figure 1.4*b*). Simple shear deformation produces significantly less melting than pure shear under comparable temperature and rift duration (Figure 1.7) (Latin and White, 1990). Even with a high asthenospheric potential temperature of 1480° C little or no melting is predicted, meaning simple shear cannot be the dominant deformation mechanism at margins where large amounts of melt products are observed.

1.2 North Atlantic margins

Rifted margins bounding the North Atlantic exhibit a wide range of structural and magmatic styles (Figure 1.8). At high latitudes, north of ~55° N, volcanic margins with thick seaward dipping reflector sequences (SDRs) (e.g., Morgan et al., 1989; Barton and White, 1997) and high velocity magmatic underplate present at depth (e.g., Fowler et al., 1989) provide evidence for both intrusive and extrusive magmatism during rifting (White et al., 1987a; White and McKenzie, 1989). The SDRs have since been sampled (e.g., Roberts and Schnitker, 1984; Joron et al., 1984; Larsen et al., 1999) and shown to consist of oceanic basalts overlying crust transitional between continental and oceanic regimes

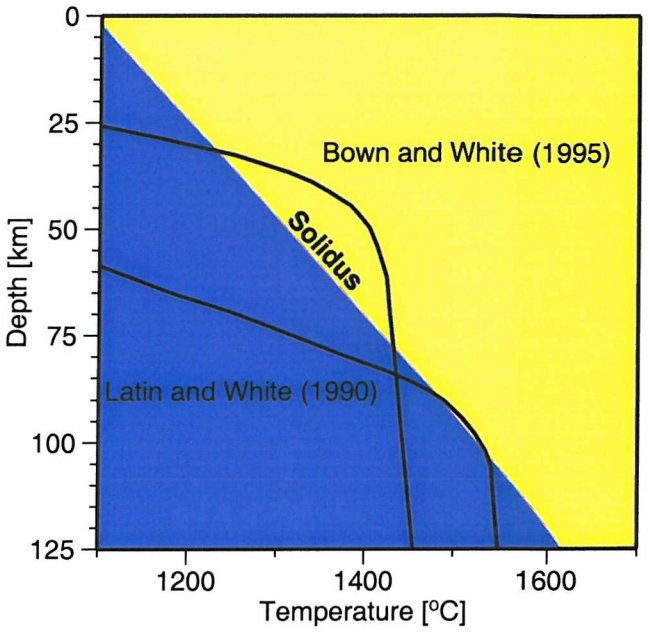

Figure 1.7: Melt production during continental rifting for continental lithosphere initially 125 km thick and stretched with a β factor of 5. Latin and White (1990) assume simple shear rifting and an asthenospheric potential temperature of 1480° C; Bown and White (1995) assume pure shear rifting over 15 m.y. and an asthenospheric potential temperature of 1400° C. The solidus is taken from McKenzie and Bickle (1988). The effects of latent heat of fusion are ignored; when included, this acts to inhibit the temperature at a given depth and reduce melting. Melting is predicted in the pure shear model, but, even with a higher mantle potential temperature, little or no melting is predicted for the simple shear model. Figure modified from Dean (1999).

(e.g., Mutter et al., 1982). These lava flows were emplaced in sub-aerial (e.g., Mutter et al., 1982; Joron et al., 1984; White et al., 1987b; Morgan and Barton, 1990) or shallow sub-marine (e.g., Viereck et al., 1988; Planke et al., 2000; Berndt et al., 2001) environments and imply a large amount of margin uplift towards the end of rifting. Excessive and sub-aerial syn-rift volcanism at North Atlantic margins can be explained by a thermal anomaly due to the influence of the Iceland mantle plume (e.g., Larsen and Saunders, 1997; Sinton and Duncan, 1997); this anomaly also results in increased melting and thicker than normal oceanic crust (White et al., 1992).

Further south there is a large decrease in the extent of syn-rift volcanism and the margins are termed non-volcanic. Non-volcanic, or magma-poor (Whitmarsh et al., 2001a), margins do not display evidence for significant syn-rift extrusive or intrusive volcanism (Mutter, 1993) and may have a broad transition continental to oceanic crust. Goban

Spur, at ~48.5° N, has a ~1.5 km thick basaltic body overlying continental crust, but little other evidence for significant volumes of syn-rift melt production. Further south, the Galicia Bank and Southern Iberia Abyssal Plain margins display an absence of syn-rift melt (e.g., Sibuet et al., 1995; Whitmarsh et al., 2001b; Russell and Whitmarsh, 2003) and a broad transition from thinned continental to oceanic crust, up to ~120 km wide, that typically exhibits velocities between 4.0 and 6.5 km s^{-1} with a high velocity gradient in the upper layer and velocities >7 km s^{-1} at its base (Whitmarsh et al., 1996a; Dean et al., 2000). Such regions have been interpreted as both thinned continental crust (e.g., Sibuet et al., 1995; Chian and Louden, 1994; Chalmers and Laursen, 1995) and slow spreading oceanic crust (e.g., Whitmarsh and Sawyer, 1996; Srivastava et al., 2000), but sampling and detailed geophysical surveys have shown this zone to consist of exhumed mantle (e.g., Whitmarsh et al., 1996b; Pickup et al., 1996; Dean et al., 2000; Whitmarsh and Wallace, 2001). Along the West Iberian margin, at the seaward edge of this transition zone, a peridotite ridge has been identified with velocities of ~6.5-7.5 km s^{-1}.

Along-margin changes in magmatic style can occur over relatively short distances and are observed at southern Greenland where non-volcanic margins are present to the west, bounding the Labrador Sea (e.g., Chian and Louden, 1994), and volcanic margins to the east (e.g., Nielsen et al., 2002). These changes are caused by the influence of the Iceland mantle plume during rifting and the presence of hotter than normal mantle (Chalmers, 1997).

1.3 The Goban Spur rifted margin

The Goban Spur margin is southwest of the UK at 48°30′ N (Figure 1.8) and was formed by the opening of the North Atlantic between Europe and Canada during the Cretaceous period. The margin extends along strike for ~150 km, bounded to the north by the Porcupine Basin and to the south by the Bay of Biscay where the margin changes orientation from 330° to 280° (Figure 1.9). The North Biscay (Section 1.4) and Amorican (Section 1.4.6) margins within the Bay of Biscay both display little volcanism prior to sea-floor spreading. To the north, the presence of extrusive volcanics within the Porcupine Basin is contested (Tate and Dobson, 1988; Reston et al., 2001) and other than possibly the Porcupine median high, this basin shows no signs of rift related volcanism. The nearest significant syn-rift volcanism is at Edoras Bank (Bull and Masson, 1996), ~500 km to the north, where rifting occurred under the influence of the Iceland mantle plume.

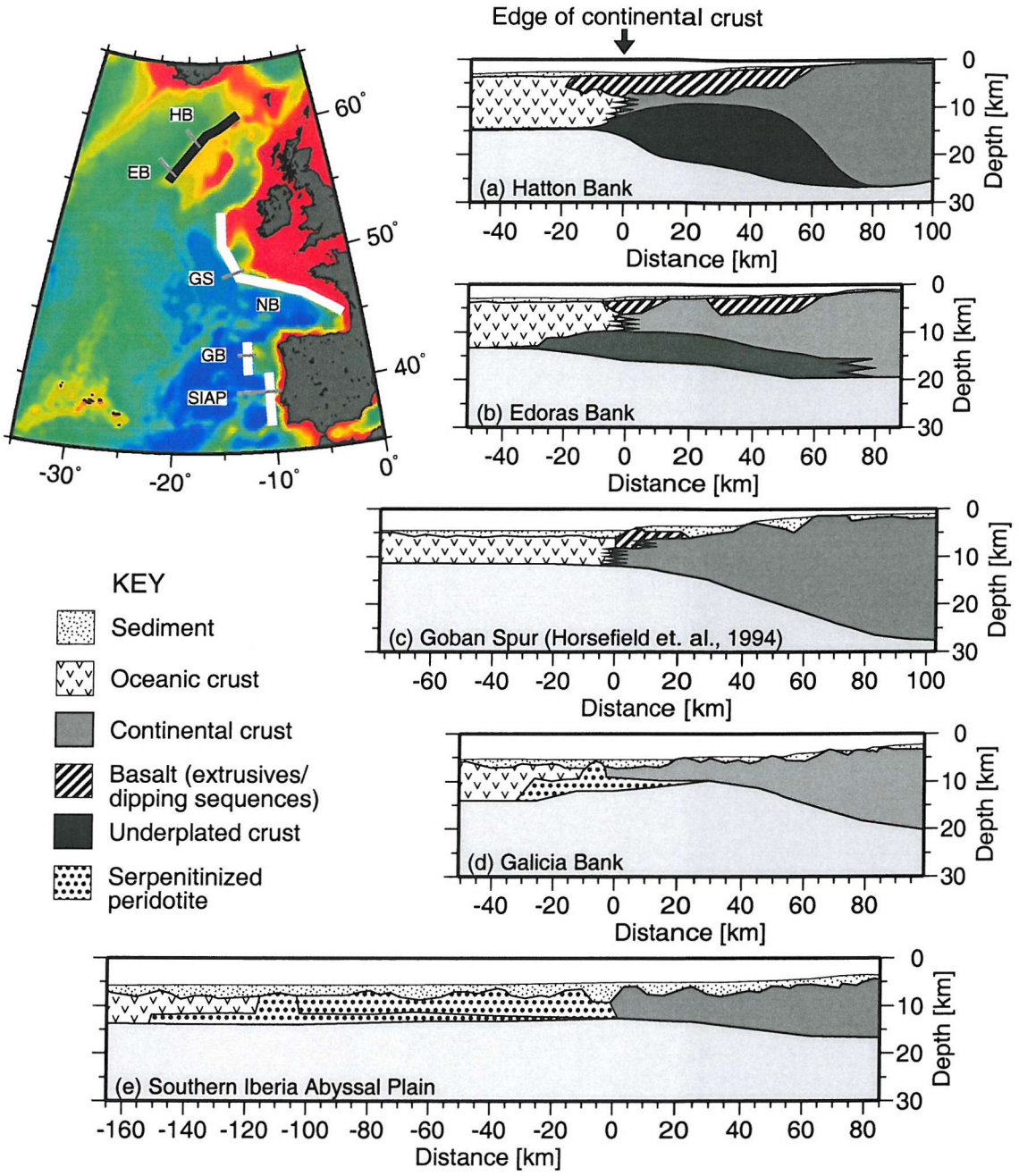

Figure 1.8: Crustal transects from wide-angle seismic surveys through the eastern North Atlantic margins of (a) Hatton Bank (HB) (Fowler et al., 1989), (b) Edoras Bank (EB) (Barton and White, 1997), (c) Goban Spur (GS) (Horsefield et al., 1994), (d) Galicia Bank (GB) (Whitmarsh et al., 1996a) and the Southern Iberia Abyssal Plain (SIAP) Dean et al. (2000). Crustal profiles are aligned along the most seaward extent of continental crust, at 0 km distance. The Goban Spur interpretation is from Horsefield et al. (1994) and is prior to the study presented in this thesis. The inset shows a colour shaded bathymetric map for the eastern North Atlantic with the margins of interest labelled and the profiles indicated by grey lines. NB indicates the North Biscay margin. Volcanic margins are indicated by solid black lines and non-volcanic margins by white lines. Figure modified from Dean (1999).

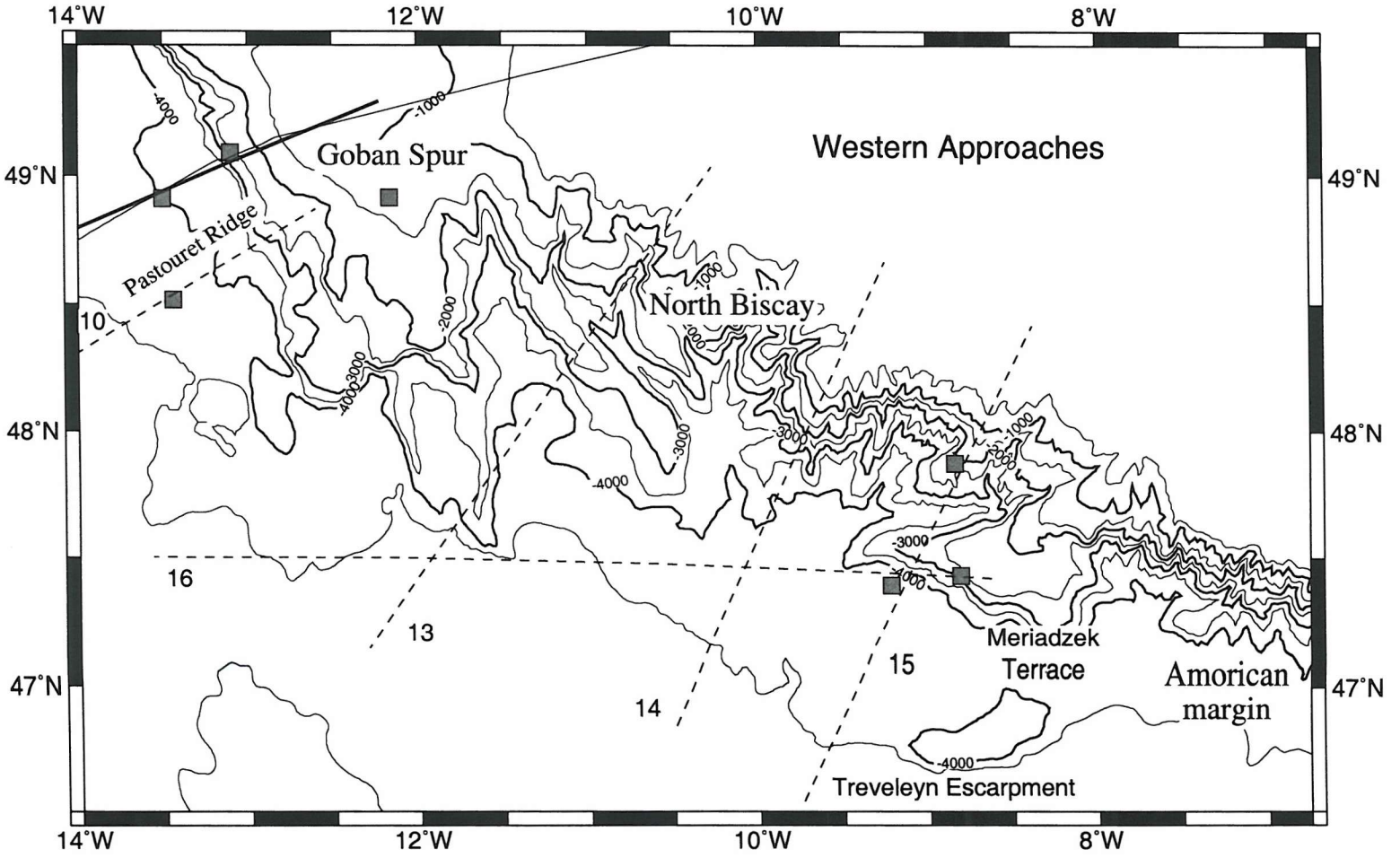

Figure 1.9: Bathymetry of the Goban Spur and Bay of Biscay margins, contoured every 500 m depth. The margin segments and important basement features are labelled. Grey squares indicate DSDP Sites from Leg 48 (North Biscay: Montadert and Roberts, 1979) and Leg 80 (Goban Spur: de Graciansky and Poag, 1985). The black line indicates reflection line WAM and the bold line is the Horsefield et al. (1994) wide-angle line. Dashed lines illustrate the CM survey profiles and are numbered correspondingly.

The Goban Spur margin has predominantly 2D features, parallel to the continental slope. Situated between multichannel seismic lines WAM and CM-10 a raised basement feature, Pastouret Ridge (Figure 1.9), is aligned with an extension of the Faraday Fracture Zone on the Mid-Atlantic Ridge (Srivastava et al., 1988a) and interpreted as an oceanic fracture zone reactivated during the Eocene (Sibuet et al., 1985). The presence of this extinct fracture zone at the Goban Spur margin means there may have been some along-strike variability in structures and deformation.

1.3.1 Previous studies

Seismic reflection

There have been several single and multichannel seismic surveys acquired in the Goban Spur region over the last 30 years (e.g., Roberts et al., 1981). The most recent survey was line WAM (Western Approaches Margin), a 645 km long profile extending from 30 km thick continental crust in the east to oceanic crust in the west (Figure 1.10) (Cheadle et al., 1986; Klemperer and Hobbs, 1991; Pinet et al., 1991).

Seismic reflection studies have largely focused on upper crustal faulting; tilted fault blocks are large (~10 km), widely separated (~20 km) and continuous for 50-100 km along strike (Masson et al., 1985). Reflective lower continental crust has been observed from full thickness to highly thinned continental crust extending for ~500 km, although imaging is poor in some regions due to increased noise levels (Peddy and Hobbs, 1987). The lower boundary of this reflectivity has been shown from gravity and wide-angle seismic modelling to coincide with the base of continental crust (Sibuet et al., 1990; Pinet et al., 1991; Grandjean et al., 2001). A number of hypotheses have been proposed to explain this reflectivity including igneous layering associated with extension at the base of the crust (Wever and Meissner, 1987) and banding or anisotropy of minerals (Wever and Meissner, 1987; Rudnick and Fountain, 1995). However, strain gradients over ductile shear zones have been shown to actually decrease reflectivity (Rey et al., 1994), and the anisotropy of granulites has been shown to be low (<5%) (Christensen and Mooney, 1995). Other hypotheses include localised pore fluid pressure variations (Wever and Meissner, 1987; Rudnick and Fountain, 1995), ductile flow in the lower crust (Reston, 1987; Reston, 1990) and molten or partially molten bodies within the lower crust (Rudnick and Fountain, 1995). The presence of widespread lower crustal layering in undeformed crust of the English Channel (Grandjean et al., 2001) and extending from the Celtic Sea to Brittany (Bois et al., 1990)

suggests that this layering pre-dates rifting and can be used to define the bounds of the lower crust. Identification of layered lower crust and upper crustal material adjacent to the continent-ocean boundary led Peddy et al. (1989) to conclude that continental rifting occurred by pure shear.

A 20 km wide body overlies thinned continental crust at the foot of the continental slope and is visible on seismic reflection line WAM between sonobuoys R3 and R8 (Figure 1.10). This body was drilled at DSDP Site 551 and is interpreted as basalt overlying, and possibly intruding, thinned continental crust (Peddy et al., 1989).

Wide-angle velocity modelling

Horsefield et al. (1994) carried out a wide-angle seismic survey coincident with WAM and produced a 200 km velocity model over the continental slope and the Goban Spur structural interpretation presented in Figure 1.8*c*. The main, margin normal, profile was based on data from three ocean bottom seismometers and, along with two crossing lines, constrained velocities within thinned continental crust and the depth to continental Moho. The velocity structure seaward of the continental slope was constrained by one instrument and was modelled as a 2.5 km thick upper layer with velocities of 4.9-5.8 km s^{-1} and a 3.5 km thick lower layer with velocities of 6.6-6.85 km s^{-1}. This region was interpreted to be normal oceanic crust, unfortunately data contributing to the model were unreversed in this region, hence the velocity structure is poorly constrained, particularly in the deep structure where there are few turning rays (Horsefield et al., 1994). The wide-angle velocity modelling presented in this thesis extends the Horsefield et al. (1994) model further seaward and utilises data from two instruments recorded in this earlier study to improve constraints over the continental slope.

Sediment and basement sampling

Many wells have been sunk on the continental shelf to sample the sediment stratigraphy in the search for hydrocarbon reservoirs (e.g., Colin et al., 1992), but are located too far east to provide detailed information about continental rifting and break-up processes. Dredge samples have been made over the continental slope and recovered limestones and sandstones (Auzende et al., 1989), limestones and metamorphic schists (Auffret et al., 1979; Sibuet et al., 1985) and, further south at ~48° N, high grade metamorphic rocks from the lower continental crust (Didier et al., 1977). As part of this project a dredge was made over anomaly 34r, recovering dolerite (Figure 1.11; Section 4.1.2).

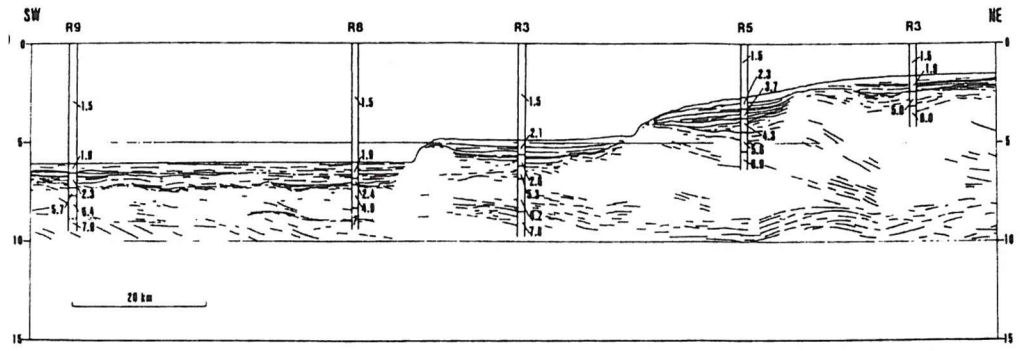

Figure 1.10: Line drawing of WAM with velocities from sonobuoy refraction studies overlain (Sibuet, 1987). The base of the deep layered reflectivity is assumed to mark the base of continental crust and coincides with the Moho from wide-angle velocity modelling (e.g., Sibuet, 1987; Horsefield et al., 1994). The vertical scale is TWT in seconds. From Pinet et al. (1991).

Basement sampling at the Goban Spur margin was carried out during Deep Sea Drilling Program (DSDP) Leg 80 (de Graciansky and Poag, 1985; de Graciansky et al., 1985). Sites 548 and 549 were located on the continental slope over two half-grabens; Site 550 was situated in the abyssal plain seaward of the continental slope, over predicted oceanic crust ~50 km south of line WAM; Site 551 was located at the foot of the continental slope over the most seaward extent of thinned continental crust (Figure 1.11). The recovered sequences are summarised in Figure 1.12. Syn-rift mudstones recovered at Site 549 were dated as Barremian (or possibly the late Hauterivian), to lower Aptian in age (de Graciansky et al., 1985). Major unconformities were observed between the Barremian and the lower Aptian and also during the Aptian which correlates with a major sea-level drop (Roberts et al., 1981) and means most Aptian strata, and potential syn-rift constraints, are missing from the sequence. A later unconformity is present between pre-Eocene and Eocene sediments, probably associated with the Pyrenean orogeny. Post-rift sediments were recovered from Sites 548, 549 and 550, the oldest of which were deposited during the lower Albian. The oldest sediments recovered seaward of the continental slope were uppermost Albian mudstones, slightly younger than suggested for the end of rifting. This age discrepancy for post-rift sedimentation is attributed to not sampling the deepest sedimentary sequence seaward of the continental slope at Site 550 (de Graciansky et al., 1985).

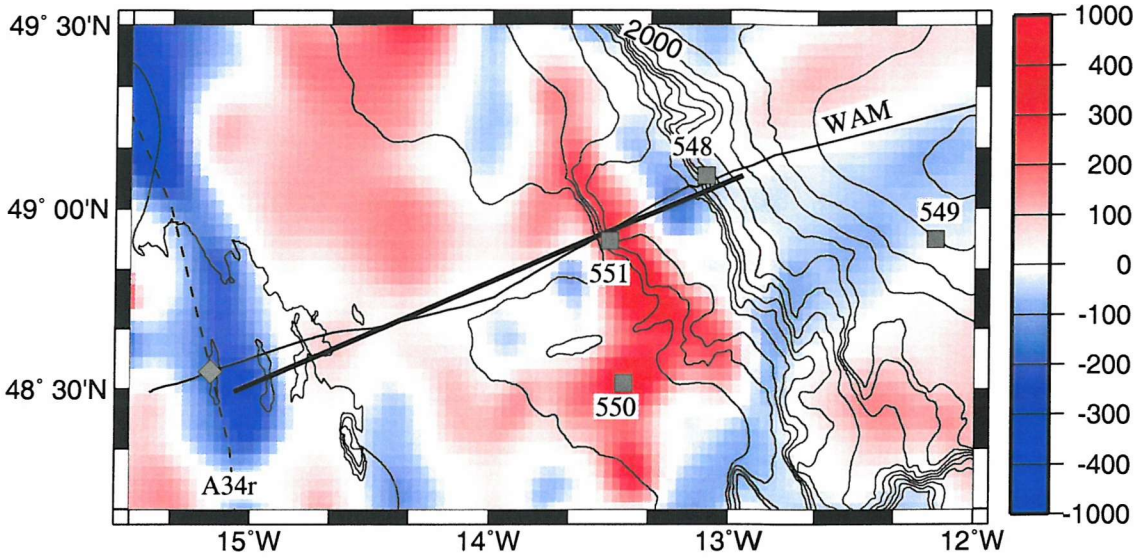

Figure 1.11: DSDP Leg 80 drill sites (grey squares) and the DY-255 dredge location (grey diamond) (Section 4.1.2) overlain onto the regional magnetic anomaly map, in nT. The deep MCS line, WAM, is shown by a black line and the wide-angle profile in this study is shown by a bold line. The first marine magnetic anomaly, 34r, is marked by a dashed line.

Continental basement comprises of Devonian metasediments at Sites 548 and 549 and were sampled to a depth of 20-30 m. At Site 550, seaward of the continental slope, ~35 m of basaltic lava flows and pillow lavas interbedded with thin limestone sediments of late Albian age were recovered (Shipboard Scientific Party, 1985a; de Graciansky et al., 1985). Basaltic lava flows and pillows at least 60 m thick were recovered at Site 551 (Shipboard Scientific Party, 1985b). These basalts have been described as oceanic thoeliites based on their geochemical signature, depleted in light rare-earth elements (Maury et al., 1985), but depending on the mechanism of late-stage margin evolution, their presence may not be a reliable indicator of the onset of full sea-floor spreading. Alteration of the Site 551 basalts has prevented accurate dating by K/Ar methods and suggests that they may have been emplaced during rifting, in shallow water depths that allowed prolonged contact with water before being buried by sediments (de Graciansky et al., 1985).

Gravity and magnetic observations and modelling

The regional gravity map (Figure 1.13*a*) shows a positive free-air anomaly (FAA) over the continental slope; a deep negative anomaly of ~30 mGal marks the foot of the slope

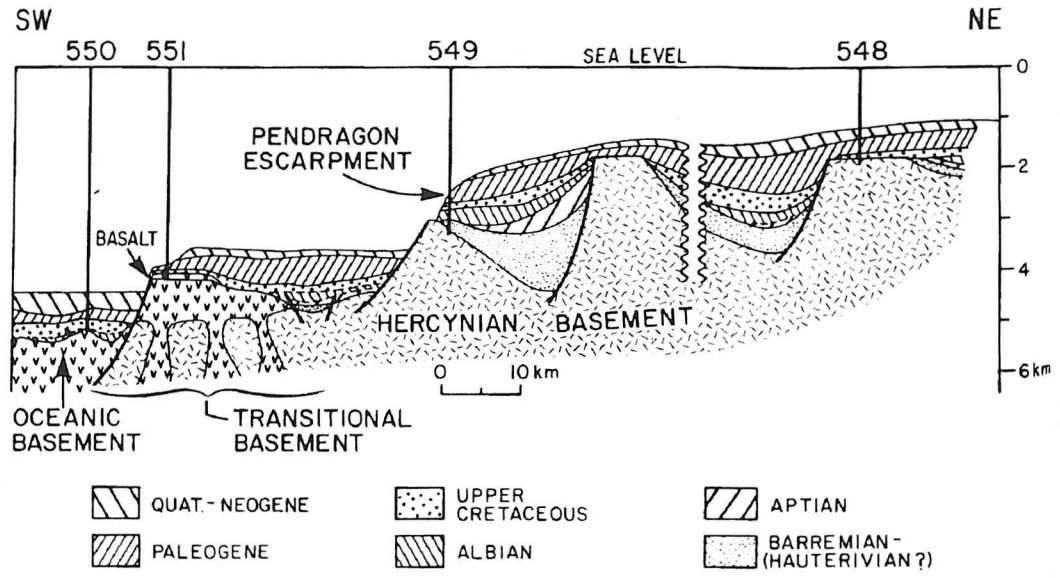

Figure 1.12: Schematic cross-section showing the results of DSDP Leg 80. Sites 548 and 550 are projected onto the line. The gap in the section between Sites 548 and 549 indicates major faults separating these two basement blocks. From de Graciansky et al. (1985).

and much weaker anomalies are present further seaward. In general the gravity anomalies parallel the margin strike and are indicators of crustal thinning within a two-dimensional structure. The slope anomaly has been attributed to an isostatic anomaly caused by the high elevation of the ridge during break-up (Rabinowitz and Labrecque, 1977; Scrutton, 1979) and, more recently, as an interference pattern at the transition between thick continental crust and thin oceanic crust, with modification by sediment loading or magmatic underplating (Watts and Marr, 1995).

The earliest sea-floor spreading magnetic anomaly is located ~120 km west of the continental slope and has been interpreted as anomaly 34r (Cande and Kristoffersen, 1977; Kristoffersen, 1978). The basalt body identified on WAM and sampled at DSDP Site 551 is associated with a positive magnetic anomaly of ~200-400 nT (Figure 1.13*b*) and limited to a narrow zone extending <100 km along margin strike. This high amplitude anomaly broadens southwards, encompassing the basalt sampled at Site 550 and appears distinct from the ~120 km wide region between the continental slope and A34r which exhibits much lower amplitudes. The zone between A34r and the continental slope has a different

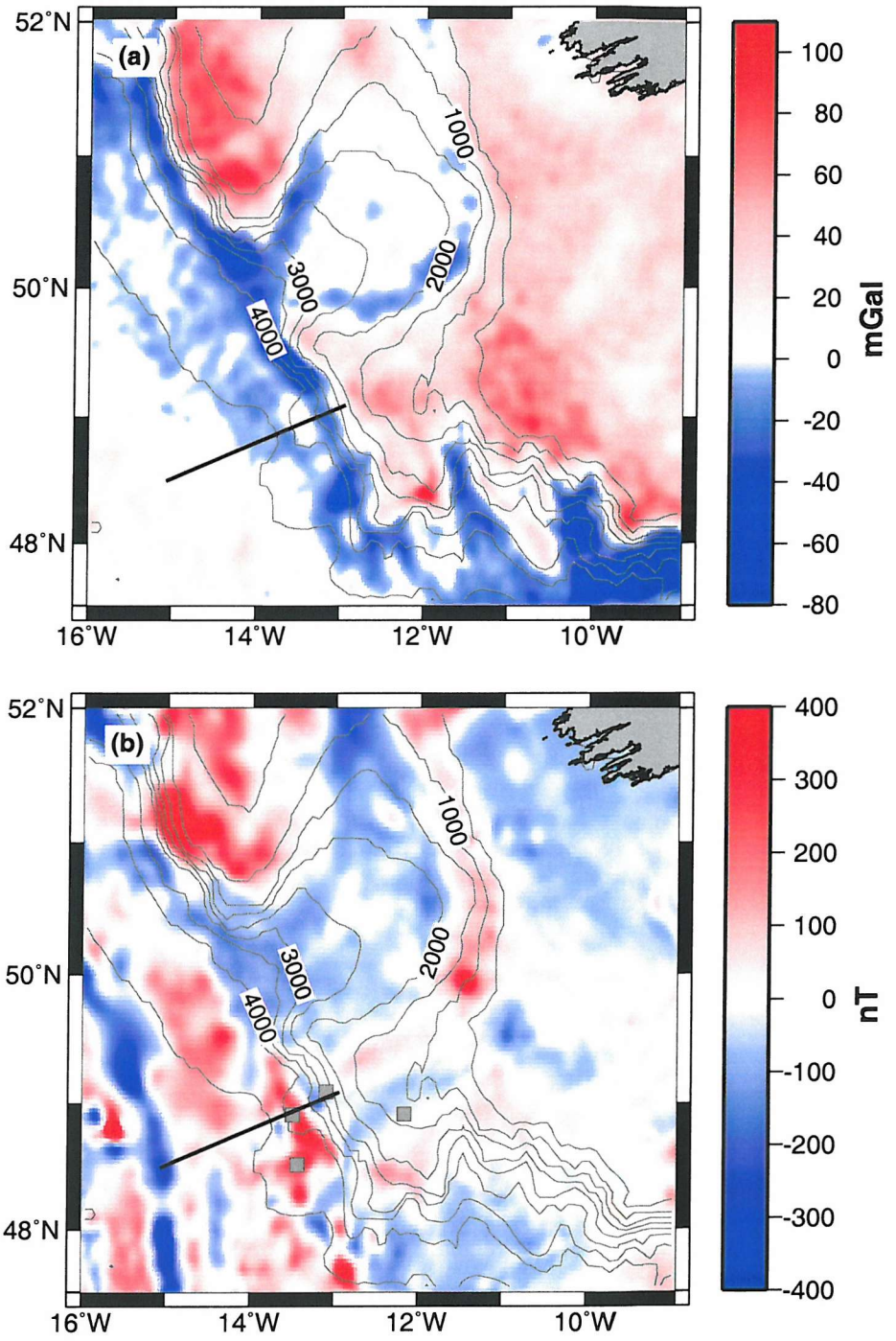

Figure 1.13: (a) The free-air gravity anomaly over Goban Spur in mGals from the satellite derived gravity grid of Sandwell and Smith (1997). (b) The Goban Spur magnetic anomaly in nT extracted from the North Atlantic magnetic anomaly grid (Verhoef et al., 1996) and reduced to the pole before plotting. The black line indicates the wide-angle seismic line in this thesis and the DSDP Leg 80 drill sites are shown by grey squares. Bathymetric contours are plotted with an interval of 500 m. The southwestern tip of Ireland is visible in the top right hand corner of the map.

magnetic character north and south of the WAM profile: northwards is a sharp, well-defined magnetic anomaly (~400 nT) whereas to the south lies a magnetically quiet zone (±100 nT), up to 200 km wide (Figure 1.13*b*). 2D magnetic modelling coincident with WAM predicts a simple structure: a magnetised body at the foot of the continental slope becoming 2 km of magnetised crust further seaward (Scrutton, 1985; Louvel et al., 1997). This structure and magnetisation (4-5.5 A m^{-1}) are compatible with a simple model of normal oceanic crust; however, it should be noted that due to the variation of magnetic anomaly along strike, north and south of the line, the anomaly these authors have fitted is substantially different to that used here (Section 5.4; Verhoef et al., 1996).

Heat flow measurements

Downhole temperature measurements made during DSDP Leg 80 estimated a heat flow of 36±15 mW m^{-2} over thinned continental crust at Site 548 and 549 with a contribution from radiogenic elements within the crust of <10 mW m^{-2} (Foucher et al., 1985). These results were incorporated in to a more detailed study by Louden et al. (1991) to show a low heat flow of 40-45 mW m^{-2} over oceanic crust increasing to 50-55 mW m^{-2} over continental crust (Figure 1.14).

These heat flow results are consistent with a pure shear model of continental rifting provided upper crustal radiogenic heating is low, 1-2 mW m^{-2} (Louden et al., 1991), an order of magnitude smaller than estimated by Foucher et al. (1985). To explain the observed low heat flow values with a upper crustal radiogenic heating of ~10 mW m^{-2}, the upper crust must thin more rapidly than the lower crust, as the lower plate within a simple shear rifting regime (e.g., Lister et al., 1986). Subsidence analysis has been used to test this suggestion and shows that if the upper/lower crust interface and depth to Moho are estimated from the WAM profile, and corrected for syn- and post-rift sediment loading, the upper and lower crust have thinned in equal proportions as predicted by the pure shear model without any depth-dependant stretching (Louvel et al., 1992). Support for this lower plate hypothesis is provided by Davis and Kusznir (2004) who show whole crust thinning to be greater than upper crust thinning by an amount that increases with the stretching factor, i.e., towards the ocean.

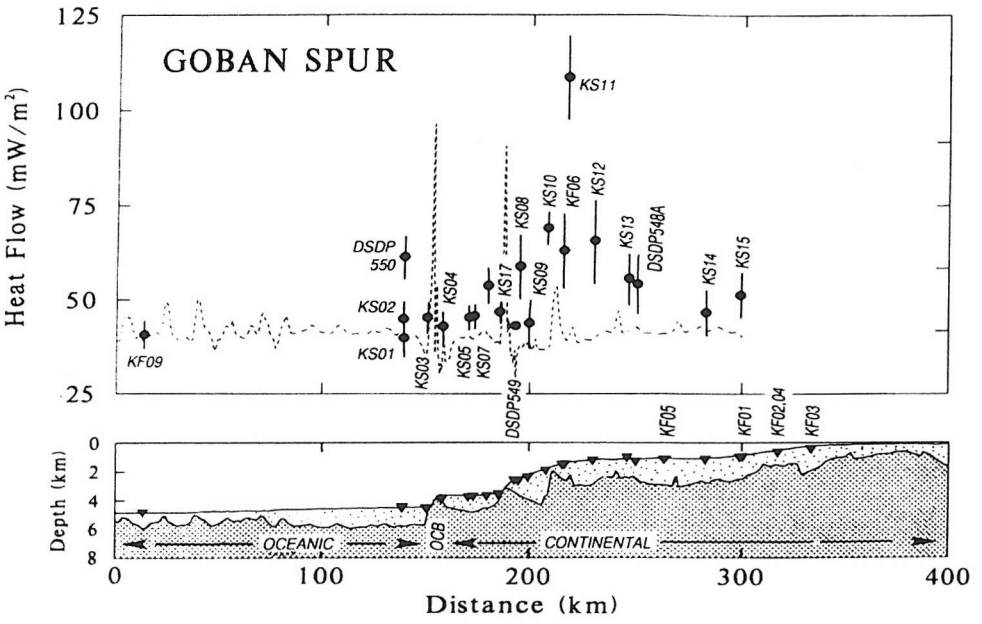

Figure 1.14: Heat flow values across the Goban Spur margin shown with $\pm 1\sigma$ uncertainties. Heat flow increases from ~40 mW m^{-2} over oceanic crust to ~55 mW m^{-2} over continental crust. From Louden et al. (1991).

1.3.2 Constraints on the rift duration and initial spreading rate

The major phases in the rift history at Goban Spur are summarised in Figure 1.15. The timing of rifting is constrained by the earliest syn-rift sediment recovered from DSDP Site 549 of late Hauterivian/early Barremian age (de Graciansky et al., 1985) and the earliest post-rift sediments present west of the continental slope: late Albian chalks and uppermost Albian mudstones overlying basalt at DSDP Site 550 (de Graciansky et al., 1985). The youngest syn-rift sediments observed were late Barremian, but the end of rifting cannot be well constrained due to an unconformity covering all of the Aptian and some of the Barremian (~12 m.y.). Stage boundaries were converted to absolute time using the timescale of Gradstein et al. (1994), placing the start of rifting at 128-126 Ma and the end at 112-106 Ma, a rift duration of 14-22 m.y. These calculations were repeated using the timescale of Harland et al. (1990), the most widely applied (e.g., Masson et al., 1985) geologic timescale prior to Gradstein et al. (1994), which gives a predicted rift duration of 18-26 m.y. (130-132 Ma to 112-106 Ma). These estimates compare to previously predicted rift durations of 16-27 m.y. (Masson et al., 1985) and 15-20 m.y. (Louden and Chian, 1999).

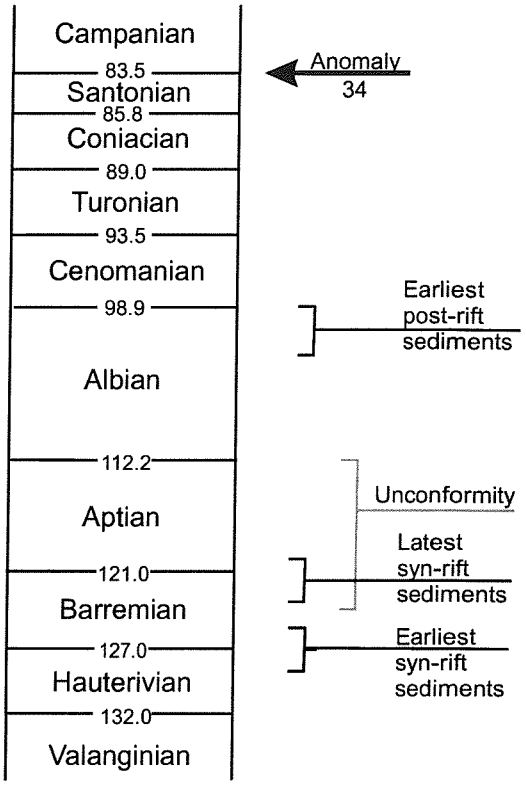

Figure 1.15: The rifting history at Goban Spur is summarised with the relative ages of sediments sampled during DSDP Leg 80 (de Graciansky and Poag, 1985) and the identification of marine magnetic anomaly 34 (e.g., Masson and Miles, 1984). The geological timescale used is that of Gradstein et al. (1994), with ages quoted in Ma.

The distance between normal oceanic crust (A34) and continental crust (DSDP Site 551) measured normal to the strike of the sea-floor spreading anomalies is 123±5 km and the time between the end of rifting and the formation of anomaly 34 at 83.5 Ma (Cande and Kent, 1992; Gradstein et al., 1994), as constrained by the latest syn-rift sediment packages and the earliest sediment to the west of the slope (de Graciansky et al., 1985), is 20.5-28.5 m.y. Using these estimates, the initial spreading rate immediately post rifting and assuming symmetrical spreading is 10±2 mm yr^{-1} (full-spreading rate). Published initial full-spreading rates range from 5 mm yr^{-1} and 9 mm yr^{-1} (Masson et al., 1985) to 15 mm yr^{-1} (Bown and White, 1995), however a repeat of the calculation performed by Bown and White (1995) using the more accurately defined timescale of Gradstein et al. (1994) results in a rate of 9-11 mm yr^{-1}, further supporting the spreading rate calculated here.

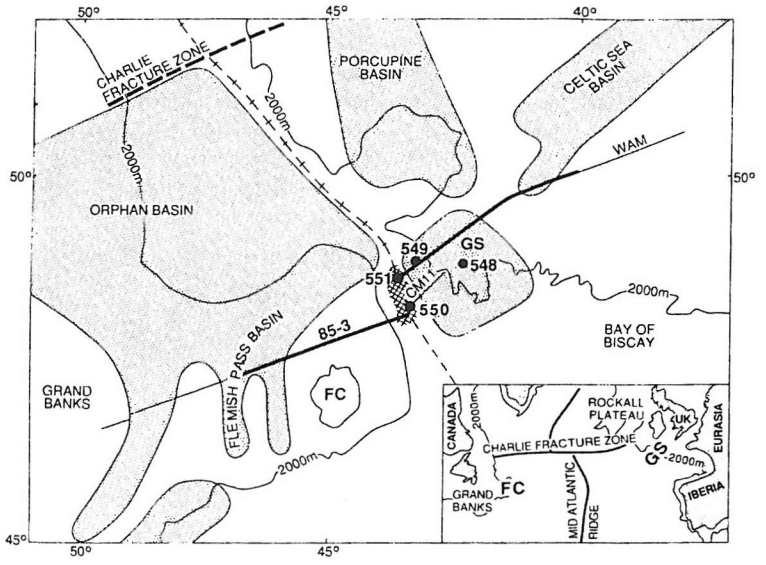

Figure 1.16: Plate reconstruction of the North Atlantic (Srivastava et al., 1988b) showing Goban Spur (GS) and northern Flemish Cap (FC) as conjugate margins. MCS lines WAM and 85-3 are approximately aligned, but have Pastouret Ridge situated between them on the European plate. Grey areas indicate sedimentary basins and zones of normal faulting. The current plate orientation is shown in the inset. From Keen et al. (1989).

1.3.3 North Atlantic reconstruction

The first marine magnetic anomaly within the North Atlantic at the latitude of Goban Spur is A34r (Cande and Kristoffersen, 1977; Verhoef et al., 1986; Srivastava et al., 1988a). This anomaly marks the end of the Cretaceous Magnetic Quiet Zone (CMQZ), a long period of a positive polarity magnetic field without magnetic reversals, and is located ~120 km seaward of the continental slope. Small magnetic anomalies present between the continental slope may be indicative of ocean crust formed within the CMQZ or crust with a low magnetisation.

A North Atlantic reconstruction to the pre-spreading arrangement was made by Srivastava et al. (1988b) based on observed sea-floor spreading anomalies within the Atlantic ocean (Figure 1.16). More recent plate reconstructions based on the observed magnetic anomalies have been attempted for the North Atlantic ocean (e.g., Coffin et al., 1992; Srivastava and Verhoef, 1992), but have only small modifications so it was chosen to use the Srivastava et al. (1988b) reconstruction for historical continuity.

1.4 The North Biscay rifted margin

The Bay of Biscay is a triangular region of oceanic crust bounded by continental margins of Europe to the north and northern Iberia to the south. The European margin consists of the North Biscay margin in the west and the Amorican margin to the east; Meriadzek Terrace and Trevelyan Escarpment are bathymetric features that act as a dividing line between these two margins, where an abrupt change in the position of the 4 km bathymetric contour illustrates a steeper continental slope towards the east (Figure 1.9).

1.4.1 Regional gravity and magnetic observations

The satellite derived free-air gravity anomaly within the Bay of Biscay region shows a small positive anomaly over thinned continental crust and a strong negative anomaly at the foot of the continental slope, with a broader extent and higher magnitude, <-150 mGal, off northern Iberia (Figure 1.17*a*). Isolated positive anomalies within the Bay of Biscay correspond to bathymetric highs and oceanic seamounts.

High amplitude linear magnetic anomalies can be identified within the Bay of Biscay (Figure 1.17*b*). Magnetic anomaly 33 extends east-west from a fossil triple junction at ~14° W, 45° N (Williams, 1975; Kristoffersen, 1978). Anomaly 34 has a strong negative peak and a weaker positive anomaly, but is present along the full width of the North Biscay margin and much weaker to the south of the relic spreading centre. A strong anomaly, parallel to the 4 km bathymetric contour of the North Biscay margin, and along the bounds of oceanic crust of the Amorican segment as defined by Thinon et al. (2003), may be anomaly M0, or potentially M3 (Sibuet et al., 2002), though overlap of the magnetic anomalies when reconstructed suggests that rifting began later slightly than M0 (Sibuet and Collette, 1991) and that this feature is a continental slope anomaly associated with the formation of initial oceanic crust during the early Cretaceous (Montadert et al., 1979).

The arrangement of magnetic anomalies within the Bay of Biscay is highly asymmetric (e.g., Williams, 1975) with the fossil ridge offset towards the south (Figure 1.17*b*). This pattern is explained by ~40 km (Roest and Srivastava, 1991) of closure between Iberia and Europe and the subduction of Bay of Biscay oceanic crust beneath the northern Iberia margin. As well as producing the asymmetric appearance of magnetic anomalies this resulted in crustal thickening (Fernández-Viejo et al., 1998), the formation of an accretionary prism (Alvarez-Marron et al., 1997) and the deep gravity low previously discussed (Figure 1.17*a*).

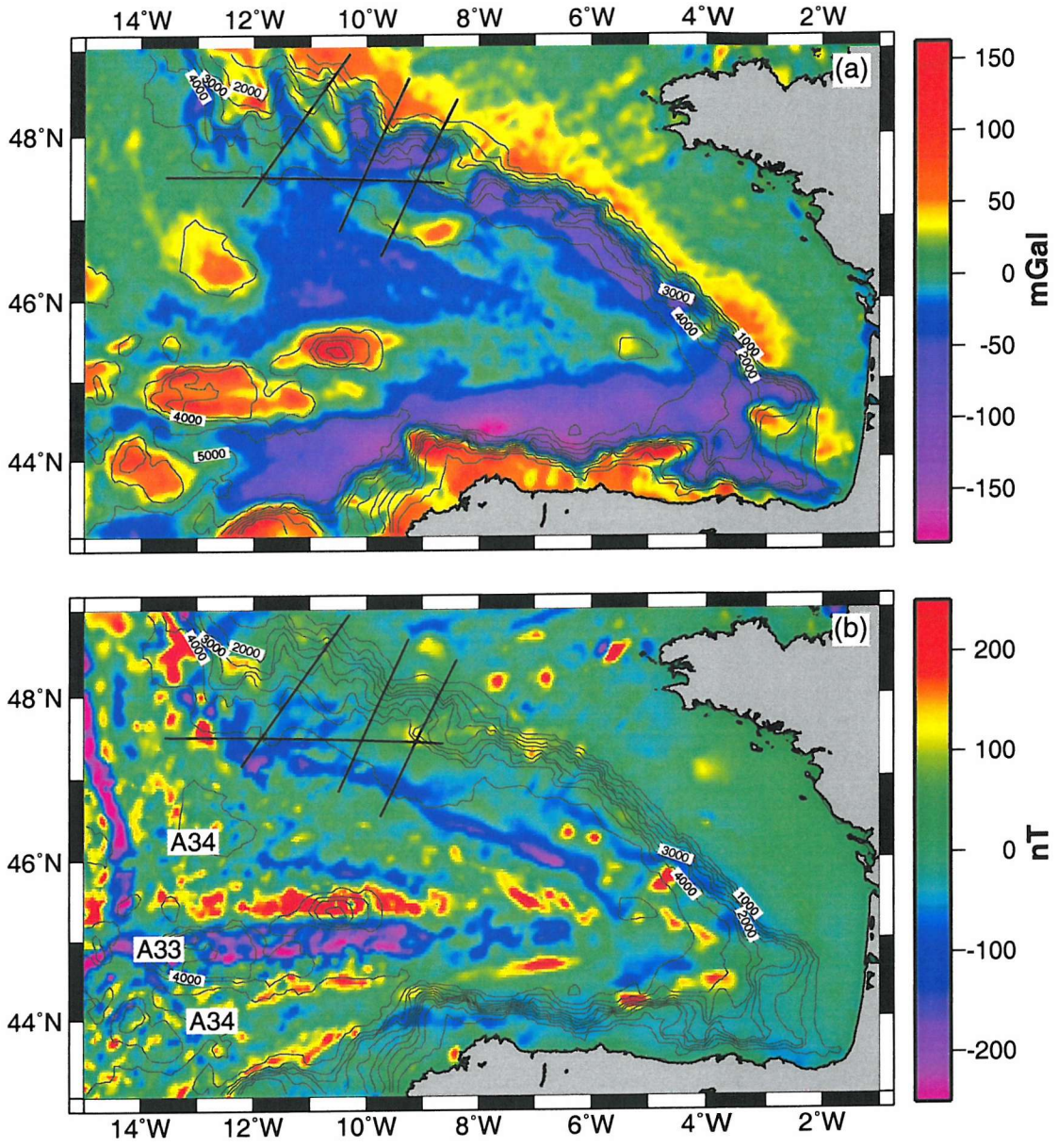

Figure 1.17: (a) Free-air gravity and (b) magnetic anomalies in the Bay of Biscay. The gravity anomaly is from the satellite derived gravity grid (Sandwell and Smith, 1997); the magnetic anomaly is extracted from the North Atlantic magnetic anomaly grid (Verhoef et al., 1996) and reduced to the pole. Scale bars are clipped at the maximum values shown. Bathymetric contours are plotted every 500 m and the position of the CM lines are overlain.

1.4.2 Reconstruction

Attempts to reconstruct the pre-drift positions of Iberia and Europe rely on observations of sea-floor spreading magnetic anomalies, sedimentation within basins of northern Spain, seismic estimates of shortening and constraints from the tectonic history of the Pyrenees. This region has experienced a complex history and an attempt to summarise with respect to proposed reconstruction methods follows.

Extension and ocean crust formation within the North Atlantic progressed from south to north occurring at the latitude of northern Iberia at ~130 Ma (Ries, 1978; Srivastava and Verhoef, 1992). At this instant, and from the late Cretaceous to the mid Eocene, Iberia moved with the African plate (Srivastava et al., 1990a; Roest and Srivastava, 1991) and independent of the European and North American plates. Four rifting phases from the Early Triassic to the Early Cretaceous have been identified in the Basque-Cantabrian basin of northern Spain (Garcia-Mondéjar, 1996); syn-rift sediments have not been recovered from the North Biscay margin, but seismic evidence suggests that extension began here during the early Cretaceous (Section 1.4.4; Montadert et al., 1979). The major rift phase occurred during the Cretaceous and resulted in an eastward rift extension between Iberia and Europe; eventual break-up led to the production of oceanic crust in the newly forming Bay of Biscay and, as extension progressed further northward on the Mid-Atlantic Ridge, the presence of a ridge-ridge-ridge triple junction at their intersection. Sea-floor spreading anomalies A33o and A34 have been identified within the Bay of Biscay and appear symmetric about the fossil ridge. A high amplitude continental slope anomaly (~100 nT) is present along the length of the margin (Figure 1.17*b*) and overlaps slightly when reconstructed to magnetic anomaly M0, which led Sibuet and Collette (1991) to conclude that spreading began later than M0. Palaeomagnetic observations suggest that Iberia underwent an anti-clockwise rotation of ~33-35° between the Jurassic and lower Cretaceous (e.g., Van der Voo, 1967; Van der Voo, 1969; Van der Voo, 1990; Juárez et al., 1998).

The triple junction was present until the late Cretaceous, at ~80 Ma, when spreading ended within the Bay of Biscay (Sibuet and Collette, 1991) before the main Pyrenean compression. Pyrenean convergence began in the middle Senonian (Cretaceous) and progressed from east to west, reaching the eastern Pyrenees in the early/middle Eocene (Boillot and Capdevila, 1977) and occurring later in the Bay of Biscay during the late Eocene from ~45-38 Ma (Srivastava et al., 1990a) and resulted in sinistral strike-slip motion along the plate boundary. Convergence between Iberia and Europe at the beginning of the Pyrenean orogeny resulted in overthrusting of the Iberian plate onto Bay of Biscay oceanic crust

(e.g., Boillot and Capdevila, 1977; Alvarez-Marron et al., 1997) and between 40 (Srivastava et al., 1990b; Roest and Srivastava, 1991) and 120 km (Le Pichon and Sibuet, 1971; Grimaud et al., 1982) of subduction beneath northern Iberia. This subduction produced the marginal troughs and gravity lows observed off northern Iberia (Figure 1.17) and accounts for the asymmetric nature of the Bay of Biscay magnetic anomalies. The absence of subduction related melts is consistent with the theoretical limit of ~150 km of convergence required to initiate melt generation (Boillot and Capdevila, 1977).

Two main hypotheses for the opening of the Bay of Biscay have been proposed: a simple rotation of Iberia (e.g., Le Pichon, 1969) or models involving rotation about a pole combined with some strike-slip motion (e.g., Sibuet, 1989; Malod and Mauffret, 1990). Various authors have suggested the first type, with poles of rotation located in the eastern Bay of Biscay (Matthews and Williams, 1968; Le Pichon, 1969), east of the Pyrenees (Williams, 1973) or within the Pyrenees (Masson and Miles, 1984). These models successfully explain the ~35° of rotation, but do not account for the pull-apart nature of Cretaceous basins in the North Pyrenean Zone (Choukroune, 1992); models with poles situated west of the Pyrenees (e.g., Le Pichon, 1969) also have difficulty in accurately fitting the magnetic anomalies within the Bay of Biscay and predict Cretaceous compression within the Pyrenees that is not observed (Ries, 1978). The second type proposed have a pole of rotation located in northern France and requires some element of sinistral strike-slip motion along the plate boundary (Sibuet, 1989). Rotation about a pole near Paris (Le Pichon and Sibuet, 1971) predicts 350-400 km of transform offset along the North Pyrenean Fault, much greater than the 100 km estimated from deep seismic profiles in the eastern Pyrenees (Choukroune and the ECORS team, 1989; Roure et al., 1989) or the 75-80 km estimated from surface structures (Teixell, 1998). An improved fit to the observed compression is predicted by the Sibuet and Collette (1991) model which has a pole of rotation located near Bordeaux and requires only ~80 km of strike-slip displacement.

Olivet (1996) suggest the reconstruction of Sibuet and Collette (1991) is inconsistent with observations in the Pyrenees, where a large basin, >200 km wide, in the eastern Pyrenees must be closed and strike-slip motion is restricted to the western Pyrenees. The models of Srivastava et al. (1990b) and Roest and Srivastava (1991) were determined by fitting of sea-floor spreading anomalies and predict four stages of development, but Olivet (1996) contend they are inconsistent with the published evolution of the Pyrenees. To improve on these models Olivet (1996) propose that there was a two stage evolution of the Bay of Biscay region between M0 and A34, with opening between 120 and 107 Ma and strike-slip

motion between 107 and 90 Ma. A fit of this reconstruction to North Atlantic magnetic anomalies is not presented for this model (Olivet, 1996). To further complicate the issue, a correlation of the principal Mesozoic continental structures on both sides of Bay of Biscay positioned the western tip of northern Iberia conjugate with the Amorican margin (Garcia-Mondéjar, 1996) in an arrangement similar to that of Srivastava et al. (1990b) and Roest and Srivastava (1991).

The Bay of Biscay reconstructions of Srivastava et al. (1990b), Sibuet and Collette (1991) and Olivet (1996) are compared in Figure 1.18. There are considerable variations in the predicted initial position of continents with either northern Galicia Bank (Figure 1.18*a*, *b*; Srivastava et al., 1990b; Sibuet and Collette, 1991) or northern Iberia (Figure 1.18*c*; Olivet, 1996) conjugate to the North Biscay margin.

1.4.3 Previous studies

DSDP Leg 48 sampling and associated measurements

Down-hole heat flow measurements made at Site 402 (36±14 mW m^{-2}) (Erickson et al., 1979) and in the vicinity of the DSDP Leg 48 Sites over the North Biscay region, give an average heat flow for the region of 45±10 mW m^{-2} (Foucher and Sibuet, 1980). This is considerably lower than the heat flow for stable continental Europe and has been attributed to a reduced contribution from radiogenic elements in the crust caused by crustal thinning (Foucher and Sibuet, 1980). The crustal thinning required to explain these heat flow observations is greater than the crustal thinning predicted by Le Pichon and Sibuet (1981) by displacement of tilted fault blocks within the upper crust.

Wide-angle seismic

Wide-angle studies over the North Biscay margin have been concentrated along MCS line CM-14 (Figure 1.9). Expanding spread surveys were made parallel to the margin, over the continental shelf, highly thinned continental crust and oceanic crust (Avedik et al., 1982). OBS were deployed at the ends of each of these expanding spread lines and the lines then repeated using an explosive source. To complete the survey a ~260 km long margin-normal line, along CM-14, was recorded using 6 OBSs (Avedik et al., 1982; Ginzburg et al., 1985). Analysis of the expanding spread surveys and initial modelling of the OBS data was presented by Avedik and Howard (1979) and Avedik et al. (1982) and further modelling was presented by Ginzburg et al. (1985) using ray tracing and amplitude fitting techniques.

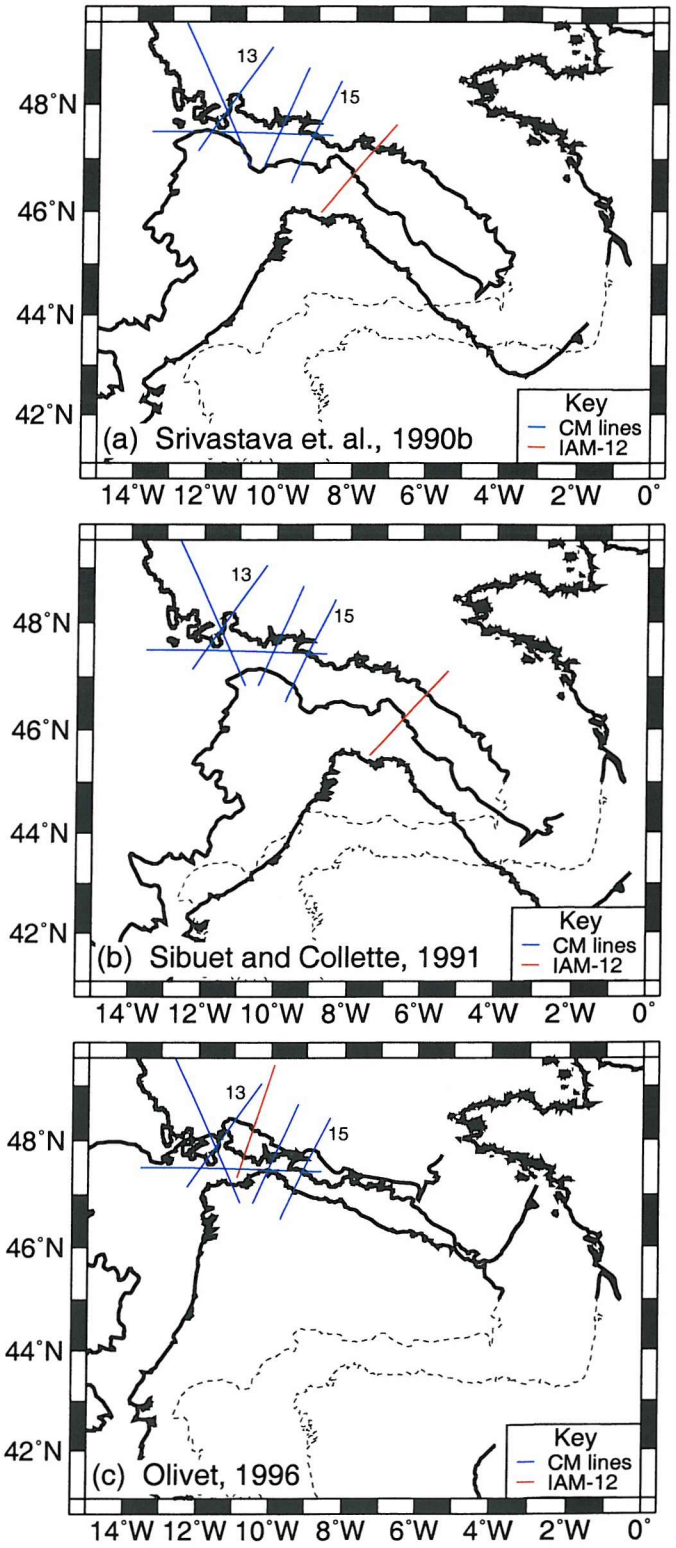

Figure 1.18: Reconstruction of Iberia to its pre-drift position, at M0, relative to Europe according to the reconstruction poles of (a) Srivastava et al. (1990b), (b) Sibuet and Collette (1991) and (c) Olivet (1996). Black lines are the reconstructed coastline and 4 km bathymetric contour; the dashed line is the present position of Iberia. MCS line IAM-12 is located over the western portion of northern Iberia (Alvarez-Marron et al., 1997).

The OBS line over thinned continental crust was re-examined using τ-p inversion techniques (Whitmarsh et al., 1986) and constrain in greater detail the velocity structure of thinned continental crust; these results were consistent with the velocity model presented by Ginzburg et al. (1985) and summarised in Figure 1.19*a*. Limond et al. (1972) carried out expanding spread surveys within the eastern Bay of Biscay and identified a crustal thickness of ~3 km and Moho reflections in probable oceanic crust.

Gravity models along this profile (Figure 1.19*b*) are consistent with these wide-angle results and support the crustal thickness and depth to Moho predictions. Approximately 2-3 km of sediment overlies the entire margin, exhibiting velocities and densities of 2.35-3.32 and 2.25-2.36 $\times 10^3$ kg m^{-3} respectively (Ginzburg et al., 1985). Continental crust thins from >16 to ~5 km thickness over a distance of 120 km; upper and lower crust appear to thin in approximately equal proportions. Velocities in continental crust form three distinct layers, ranging from 4.45 to 6.55 km s^{-1}, and becomes to a two-layer structure, with velocities of 4.45 km s^{-1} above a 6.6 km s^{-1} layer at the continent-ocean boundary. Mantle velocities of 7.9-8.05 km s^{-1} underly the entire model.

Multichannel seismic results

Although many seismic reflection surveys have been shot over the North Biscay margin only a portion have been published and frequently only a small panel is shown in support of other observations or results (e.g., Le Pichon and Barbier, 1987). Multichannel seismic lines over the margin were analysed by Montadert et al. (1979) who identified 5 main seismic layers from shallow sediments to acoustic basement. The seismic stratigraphy is detailed in Section 1.4.4.

Upper basement consists of tilted blocks of a variable size that are bounded by faults that appear listric in time and depth sections and sole out onto a bright reflector S (Section 1.4.5). By examining the displacement along these faults Le Pichon and Sibuet (1981) estimate upper crustal stretching to a maximum of β=3 and show that this is a close approximation to whole-lithosphere thinning, consistent with the pure shear model of McKenzie (1978).

A ~50 km panel of margin parallel line CM-16 was presented by Montadert et al. (1979) to illustrate the presence of the 5 seismic layers previously identified and the continuity of S along margin strike, beneath the tilted fault blocks, and its similarity to S observed at Galicia Bank. Evidence from the S-reflector is summarised in Section 1.4.5.

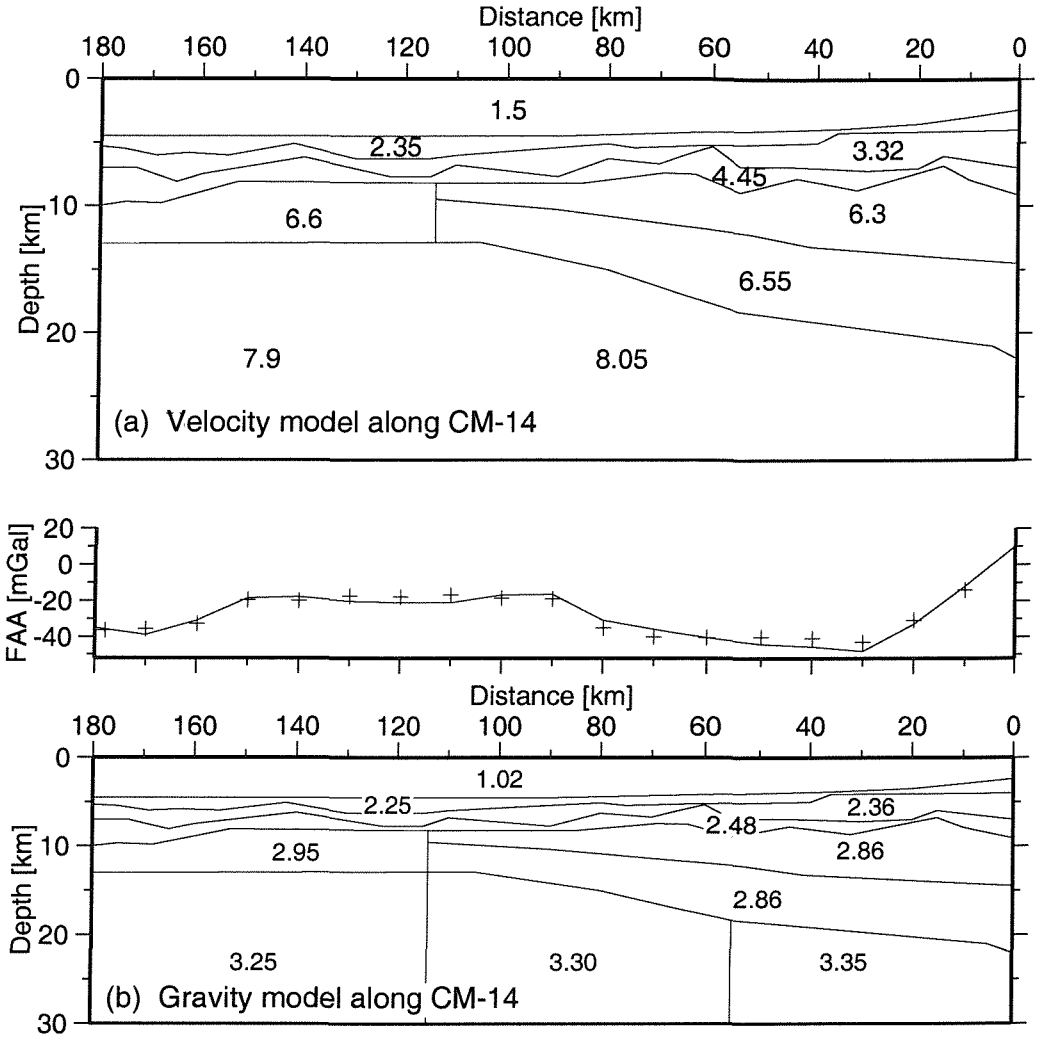

Figure 1.19: (a) Summary of wide-angle velocity models along profile CM-14 on the North Biscay margin. Velocities are given in km s^{-1} and taken from Avedik et al. (1982) and Ginzburg et al. (1985). (b) The gravity model along CM-14 based on the wide angle velocity model. Densities are given in $\times 10^3$ kg m^{-3}. The observed and predicted gravity anomalies are shown by crosses and the continuous line respectively. From Ginzburg et al. (1985).

1.4.4 Seismic stratigraphy

The observed seismic stratigraphy is constrained at DSDP Site 400A (Figure 1.20) where penetration of 777.5 m below seabed was achieved, sampling post-rift sediments from recent to Albian/Aptian (early Cretaceous) in age. The base of the Aptian sediments is considered to indicate the break-up unconformity (Montadert et al., 1979).

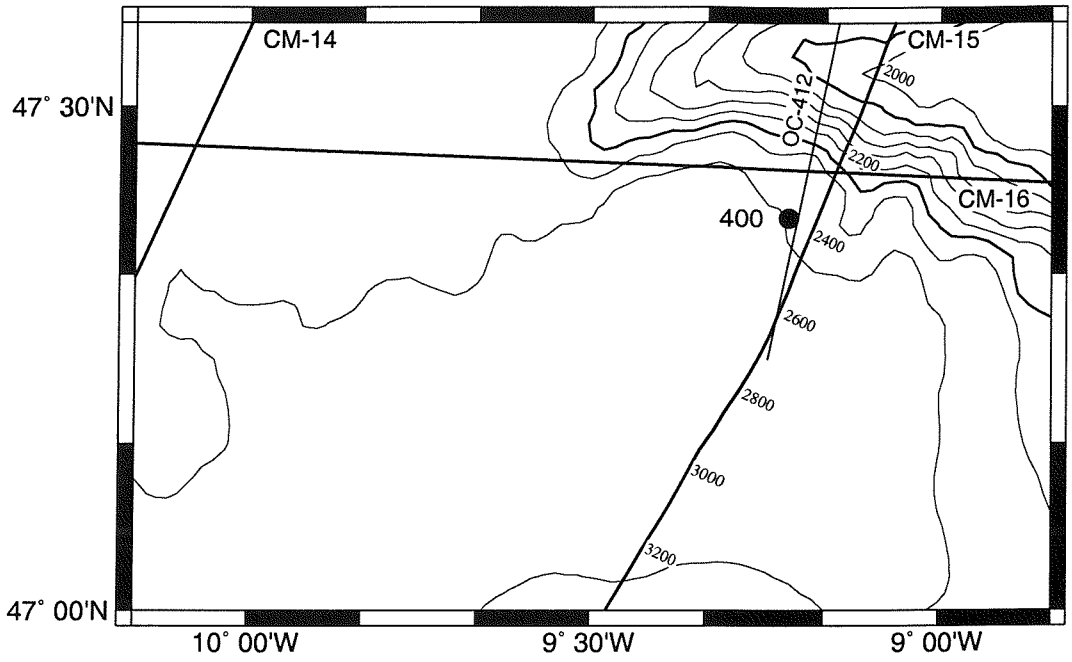

Figure 1.20: Bathymetry and seismic reflection profiles in the vicinity of DSDP Site 400. Site 400 is located close to line OC-412 and projected onto lines CM-15 at SP 2400 and CM-16 at SP 6270 where a similar reflection sequence to OC-412 is observed (Figure 1.21). Site 401 is situated further east at 8°48′ W, 47°25.65′ N and sampled similar post-rift sequences over a basement high. Seismic data are not available to project these results onto the CM lines and Site 400 results only are used here.

The 5 layers defined by Montadert et al. (1979) range from the deepest basement and sedimentary layers, unsampled at Site 400, to shallower post-rift sediments. Basement is characterised by its diffractive nature and significant topography, with dipping reflections present bounding tilted blocks; it is generally unreflective and distinctive compared to the overlying sedimentary sequences. Above basement are pre-rift sediments that parallel the top of the tilted fault blocks (e.g., B: Figure 1.21) and are themselves overlain by sediments with a divergent reflection pattern typical of syn-rotational deposition (layer 4). These syn-rift sediments are not present over all fault blocks, however the boundary between these and the sediments above corresponds to the break-up unconformity. Layer 3 has infilled the depressions between basement highs, but was deposited after basement ceased to move. It is seismically transparent, or has a slight layering, and is ~200 m thick. This layer corresponds to late Cretaceous chalks recovered from Site 400 (Figure 1.21; Montadert and Roberts, 1979). Formation 2 consists of several closely space reflectors and is identified as Eocene to Oligiocene chalks. This layer may sit unconformably beneath

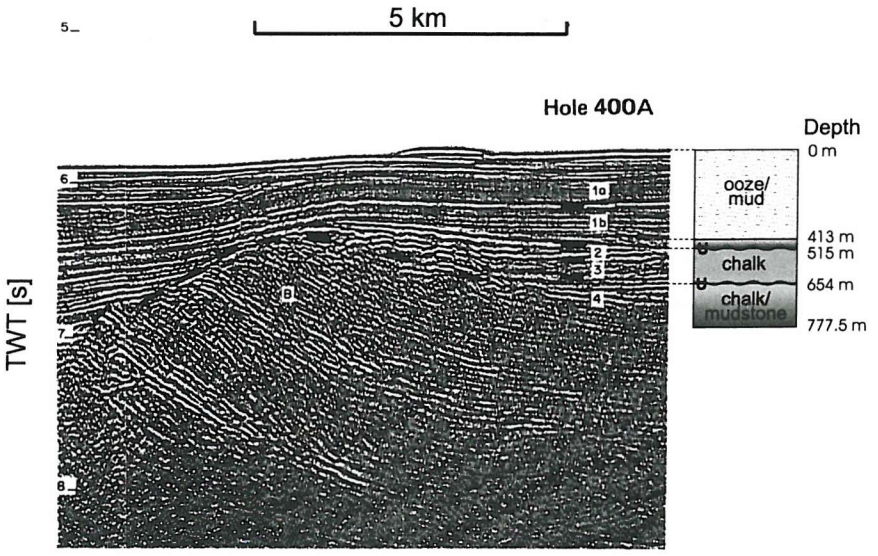

Figure 1.21: Observed stratigraphy sampled at DSDP Site 400 and extrapolated to nearby MCS line OC-412 (Figure 1.20). The seismic section is from Montadert and Roberts (1979); labels correspond to sedimentary units: 1a,1b=Post Eocene, 2=Upper Cretaceous to Eocene, 3=Albian/Aptian, 4=Syn-rift, B=Pre-rift. U marks an unconformity within the sedimentary sequence.

layer 1 which consists of Miocene to present chalks and mud and can be distinguished by its weak layering. This layer ranges from 600 m up to 1400 m thick in the abyssal plain.

1.4.5 S-reflector

S was initially identified along line CM-14 and is continuous along the North Biscay margin, from CM-13 beyond CM-15 into the Amorican margin. It is typically a strong, continuous reflector that can be identified beneath fault blocks within continental crust. Various interpretations have been suggested for the formation of the S reflector. Avedik and Howard (1979) present refraction data which suggest that S coincides with a boundary between velocities of 4.9 and 6.3 km s^{-1} and is not located within the upper crust, but is a tectonic boundary at its base. Consistent with these refraction results, S was interpreted to be a mid-crustal discontinuity marking a change in deformation style, separating the brittle upper crust from the ductile lower crust beneath (de Charpal et al., 1978; Montadert et al., 1979). Montadert et al. (1979) also suggest that, due to uncertainties in the crustal velocity model, S may mark the Moho beneath the tilted blocks. More recent wide-angle velocity modelling along CM-14 (e.g., Ginzburg et al., 1985) confirms the presence of basement velocities of ~6.3 km s^{-1} beneath S, with the Moho located deeper at ~12 km depth.

Serpentinised upper mantle beneath upper continental crust could provide the observed velocity structure and has been proposed to explain a similar low angle reflection at the Galicia Bank margin (Reston, 1996). A low angle reflection similar to S could be produced by a serpentinisation front within altered mantle (Minshull et al., 1998); serpentinite would be present above and below S, but with an impedance contrast caused by differing extents of serpentinisation. Alternative hypotheses for S may be the top of a large intrusive body, such as granite which is widespread across southwest UK and northern France (e.g., Bitri et al., 1997), or mafic underplate; or a thin intrusion that cuts across the base of the tilted fault blocks as considered for S at Galicia Bank (Reston, 1996).

The areal extent of S is mapped in Figure 1.22 based on the observations of Le Pichon and Barbier (1987) and is extended westward along the margin parallel line CM-16 to CM-13 here (see analysis in Chapter 7). S changes its position within the margin, becoming closer to the continent-ocean boundary as it extends westward. Due to crustal thinning, the position of S within basement also changes westward, being located beneath tilted blocks on CM-15 and cutting through progressively higher levels until it coincides with top basement at the seaward edge of continental crust on CM-13. Due to the wide separation of these MCS lines, detailed analysis of along-margin changes is not attempted in this study, but the interpretation of S and its margin end-member properties are considered through waveform and amplitude analysis in Section 7.5.

Restoration of MCS data from the North Biscay and Amorican margins has shown S to be located within, and cutting through, the upper continental crust and to have an original dip towards the continent (Le Pichon and Barbier, 1987). These conclusions are reached based on depth conversion of model reflectors using interval velocities defined by near normal-incidence velocity analysis, incorporating ray path bending within layers, and by assuming that upper crustal stretching factors are representative of the whole crust. A landward dip is inconsistent with the suggestion of Brun and Choukroune (1983) that S was a decollement on which fault blocks slid under gravity. The presence of lower continental crust beneath S, and thickening in the same direction as upper crust above S, is not compatible with the simple shear model of Wernicke (1985) because the lower plate is expected to thicken in the opposite direction to the upper plate. These observations can be reconciled if the lower crust acts a decoupling zone between the upper crust and upper mantle within a pure shear environment (Le Pichon and Barbier, 1987).

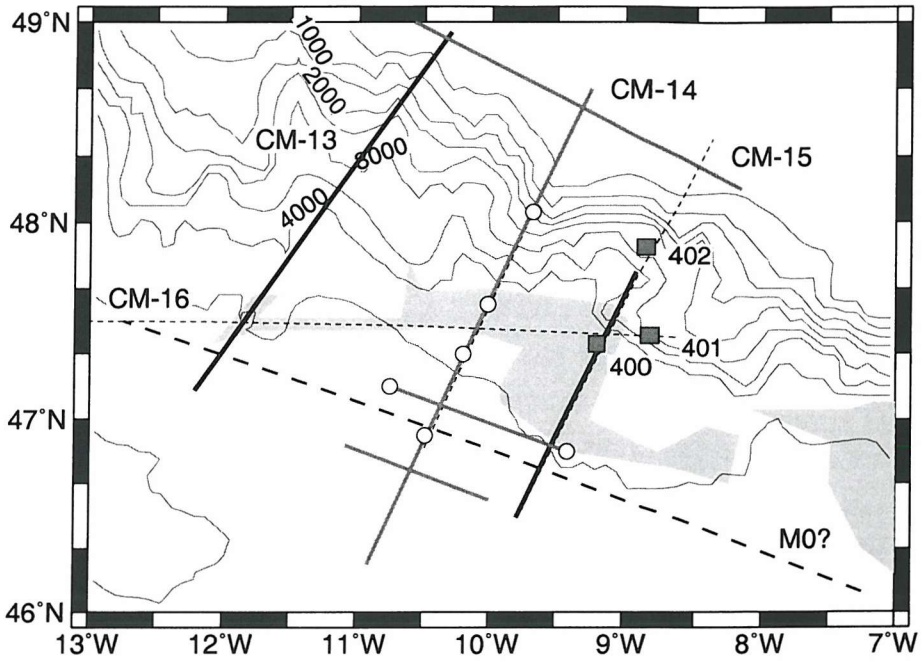

Figure 1.22: The extent of S within the continental crust as mapped by Le Pichon and Barbier (1987) and extended along CM-16 to CM-13 through the North Biscay margin. The mapped extent of S is shown by the grey region. MCS lines CM-13 to CM-16 are labelled and shown as dashed lines. Wide-angle profiles are shown as grey lines and overlay CM-14; MCS lines reprocessed in this study are shown in bold. Grey squares mark DSDP Leg 48 drill sites and white circles the OBS locations from the wide-angle experiments. The first magnetic anomaly is marked as possible M0 and bathymetric contours are plotted every 500 m.

1.4.6 Amorican margin

The multichannel seismic survey, *NORGASIS*, was carried out in 1994 over the Amorican margin between 4° and 8° W, using a high energy and low frequency source for deep crustal penetration (Avedik et al., 1996). Detailed analysis of sedimentary deformation have identified two periods of rifting during the lower Cretaceous, in the pre-Berriasian and Aptian, and separated by a tectonically quiet period (Thinon, 1999; Thinon et al., 2002). The Pyrenean convergence was shown to reach the eastern Bay of Biscay during the Eocene and was located mainly at the boundary between continental and oceanic crust (Thinon et al., 2001).

A combination of wide-angle and MCS results led Thinon et al. (2003) to identify a ~80 km wide region of high velocities (7.4-7.5 km s^{-1}) lying immediately beneath the sediments in the continent-ocean transition. Reflectivity within this transition region is high. Top

basement appears faulted and Moho reflections are present. The onset of normal oceanic crustal accretion appears to begin along the eastward continuation of the continental slope magnetic anomaly of the North Biscay margin (Figure 1.17*b*) and the broad transition region situated between this magnetic anomaly and the continental slope. A comparison between the Amorican and North Biscay margins is made in Section 7.6.4.

1.5 Thesis outline

This thesis examines geophysical data from two continental margins within the North Atlantic and the Bay of Biscay between 47° and 50° N. New seismic data were acquired at the Goban Spur margin and, along with pre-existing datasets, used to reach a new interpretation for the structure of that margin. Normal incidence seismic data from the North Biscay margin were reprocessed and used to examine the structure and style of crustal deformation during rifting. Together these margins provide an insight into Cretaceous rifting at the UK bounding continental margins.

The physical properties of continental crust, oceanic crust and serpentinite are important for interpreting geophysical observations at rifted margins and are examined in Chapter 2. This is followed in Chapter 3 by a summary of ray tracing theory, as applied to the wide-angle dataset in this thesis and modelled using *RAYINVR* (Zelt and Smith, 1992).

Chapter 4 details the acquisition and processing of the wide-angle data from *RRS Charles Darwin* cruise 124 (Minshull, 2000) at the Goban Spur margin. Modelling strategies and results are presented in Chapter 5 for all geophysical data here, including wide-angle seismic, gravity and magnetic modelling and migration of the multichannel seismic data. A discussion of these results follows in Chapter 6 and incorporates the conjugate margin and proposed rifting models derived from these results.

Chapter 7 examines the North Biscay margin by reprocessing of MCS data and further time and depth migrations. Amplitude and waveform analysis of deep reflection events, including the S-reflector, is used to produce models along lines CM-13 and CM-15 and examine along-margin changes in structure and deformation history.

The results presented here are brought together in Chapter 8 for comparison and a broader look at the regional (North Atlantic) and global implications. The final conclusions are reached and a few suggestions for further work made.

Chapter 2

Physical properties of crustal types

One of the greatest difficulties with the study of rifted continental margins is the interpretation of structures and lithologies on the basis of remotely sensed properties that are not unique. In order to distinguish between different crustal types using geophysical data it is necessary to understand their physical properties and how they vary. The general structure and physical properties of continental crust, oceanic crust and serpentinised mantle are considered in this chapter.

2.1 Continental crust

Continental crust averages ~40 km in thickness, ranging from <24 to 72 km (Figure 2.1), and generally increasing towards stable continental interiors. Continental crust typically consists of two or three seismic layers: an upper, middle and lower crust with velocities of 5.6-6.3, 6.4-6.7 and 6.8-7.2 km s^{-1} respectively (Mooney et al., 2002). The velocity-depth structure can vary widely between locations: from continental shields where tectonically stable crust forms the core of continents; orogens where crust has been deformed and thickened during mountain building, either with the addition of melt products (e.g., the Andes, South America) or continental collision and uplift (e.g., the Himalayas, Asia); or extended crust which has been thinned by regional extension (Figure 2.2). Rifted crust has experienced focused strain, forming "an elongate tectonic depression associated with which the entire lithosphere has been modified in extension" (Olsen and Morgan, 1995) and generally has a crustal thickness >30 km (e.g., East African Rift: Braile et al., 1995); continued extension produces passive margin crust which has undergone extreme thinning, to as little as 3-4 km. Section 2.1.2 considers the seismic structure of passive margin crust

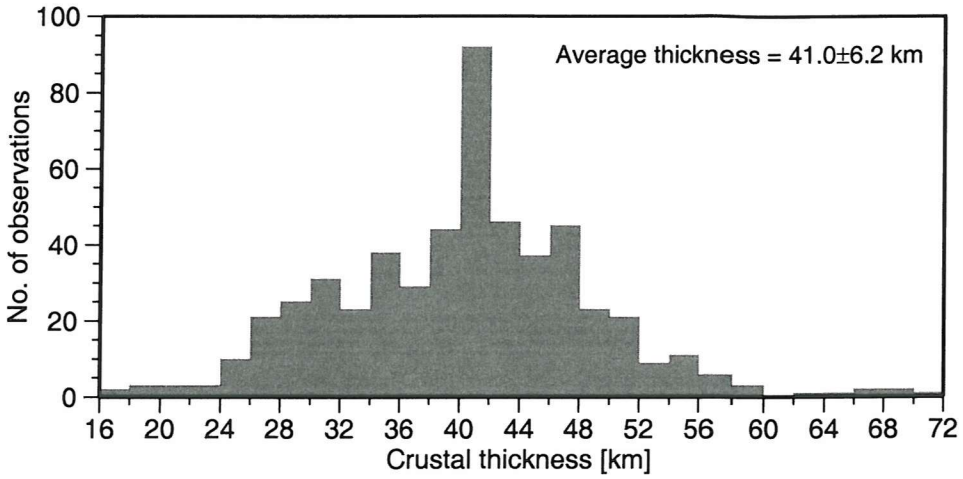

Figure 2.1: Crustal thickness observations for continental crust worldwide. The mean crustal thickness based on these observations is given; the weighted average crustal thickness, accounting for the estimated global proportion of different tectonic provinces, is 41.0±6.2 km. After Christensen and Mooney (1995).

and shows that during extreme thinning the velocity structure appears to be maintained, but over a reduced crustal thickness. The majority of western Europe and the North Atlantic margins of North America consist of extended continental crust, so I am concerned here with the physical properties of this type of crust.

2.1.1 Extended continental crust

The average thickness of extended continental crust is 30.5±5.3 km (Mooney et al., 2002) (Figure 2.2). Upper continental crust has a granitic or silicic-to-intermediate composition and velocity estimates vary from <6.2 (Rudnick and Fountain, 1995), 6.1 (Mooney et al., 2002) to 5.7-6.4 km s^{-1} (Christensen and Mooney, 1995). Middle continental crust is differentiated from the upper crust by velocities in the range 6.3-6.7 km s^{-1} . This velocity increase is believed to be caused by an increase in metamorphic grade from amphibolite to granulite facies (Christensen and Mooney, 1995). Lower continental crust consists of mafic (e.g., Rudnick and Fountain, 1995) or intermediate (Smithson et al., 1981) igneous rocks and granulite facies metamorphic rocks (Mooney et al., 2002). Velocities >6.9 km s^{-1} are commonly observed in the lower crust. This layer often exhibits extensive subhorizontal layering which may cover the entire lower crust or be restricted to the top and base of

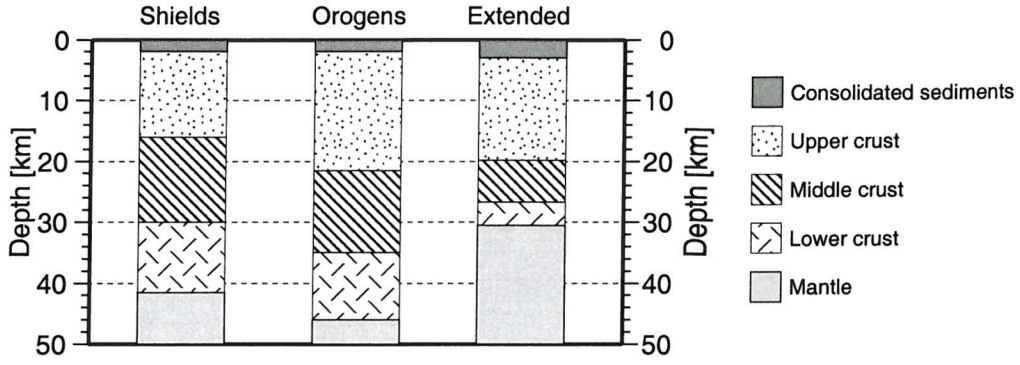

Figure 2.2: The average crustal structure is shown for three tectonic provinces: shields, orogens and extended crust. Layers are divided in to upper, middle and lower continental crust and correspond to average velocities of 5.7-6.4, 6.4-6.8 and 6.8-7.8 km s^{-1} respectively. After Christensen and Mooney (1995), Rudnick and Fountain (1995) and Mooney et al. (2002)

this layer (Rudnick and Fountain, 1995). Lower crustal layering is observed around the UK continental margins (e.g., Peddy and Hobbs, 1987) and possible compositions are discussed in Section 1.3.1.

Thin two-layer continental crust is observed at several locations globally including western Europe. It differs from stable crust in thickness and also has a lower mean crustal velocity (6.16 compared to 6.49 km s^{-1}: Mooney et al., 2002). This lower velocity is attributed to the absence of a >7 km s^{-1} layer in the lower crust, a conclusion supported for parts of western Europe by the velocity models of Horsefield et al. (1994) and Grandjean et al. (2001).

Poisson's ratio (σ) relates V_p and V_s according to Equation 2.1 and, where the S-wave velocity is known, can be used to discriminate between different lithologies with similar P-wave velocities.

$$\sigma = \frac{v_p^2 - 2v_s^2}{2(v_p^2 - v_s^2)} \quad . \tag{2.1}$$

Few Poisson's ratio studies have been published for continental crust. Braile (1977) calculate values of 0.24-0.25 for upper crust increasing to 0.29-0.31 within the lower crust; these upper crustal values are significantly lower than typically observed in oceanic crust or serpentinite.

Heat producing (radiogenic) elements within the continental crust (K, Th, U) tend to decrease with depth due to their depletion in rocks that become increasingly metamorphosed with depth, and an increase in the volume of mafic rocks within the crust (Rudnick and Fountain, 1995). Continental heat flow ranges from 30-100 mW m^{-2} and decreases towards the stable continental interiors to a steady state of ~46 mW m^{-2} (Sclater et al., 1981). Heat flow across western continental Europe is typically 60-90 mW m^{-2} (See Figure 1 of Louden et al., 1991).

2.1.2 Thinned continental crust

The formation of rifted margins involves extreme thinning of continental crust which may modify its physical properties, but few studies have concentrated on thinned crust. Holbrook et al. (1992) modelled 34 km thick crust at the U.S. East Coast continental margin, consisting of four layers with velocities of 5.9, 6.3, 6.4 and 6.85 km s^{-1}; further seaward this crust is thinned to 10 km with little change in the velocity structure except for an increase in velocity gradients due to the thinner crust and the addition of a lower 7.2 km s^{-1} layer, probably related to mafic underplating (Lase Study Group, 1986).

A wide-angle seismic study of thinned crust (~8 km thick) at the North Biscay margin (Whitmarsh et al., 1986) identified a simple two-layer velocity structure with velocities from 5.9 to 7.4 km s^{-1} divided into an upper high velocity gradient layer (0.8 s^{-1}) overlying a low gradient (0.4 s^{-1}) layer. In a comparison with other refraction models over crust <10 km thick Whitmarsh et al. (1986) report this two-layer structure to be consistent with global observations, but suggest variations in lower crust velocity gradients can be attributed to differing amounts of thinning.

2.2 Oceanic crust

Oceanic crust is formed at mid-ocean ridges where diverging plates allow mantle to upwell at the ridge axis and melt, producing a mafic crust. Normal oceanic crust is formed away from the effects of transform offsets and thermal or chemical perturbations within the mantle, over mantle with a normal asthenospheric temperature of 1300° C (White et al., 1992; Bown and White, 1994). Variations in oceanic crustal structure depends on mantle temperature and composition, proximity to transform offsets, the age of the crust and with the spreading rate.

2.2.1 Normal oceanic crust

Seismic constraints

Layering of oceanic crust was noted by Hill (1957) and Raitt (1963) who divided the earth beneath ocean basins into five layers with an average thickness and seismic velocity (Table 2.1). Advances in traveltime and amplitude modelling have allowed velocity gradients to be constrained within each layer to substantially improve the model fit compared to constant velocity layers. White (1992) produced a global compilation of oceanic crustal velocities from seismic data available at the time and maintaining the layer classification with little modification. Sediments thicken with distance from the ridge axis and can display velocities up to ~4.5 km s^{-1} which increase with depth due to compaction and a resultant porosity decrease; layer 2 is 2-3 km thick, has velocities of 2.5-6.5 km s^{-1} and exhibits high amplitude arrivals associated with a large velocity gradient, typically 0.5-1 s^{-1}; layer 3 ranges from 3-5 km thick has velocities of 6.5-7.2 km s^{-1} with a lower velocity gradient (0.1-0.2 s^{-1}) (Minshull, 2002a). Oceanic upper mantle velocities normally range from 7.9 to 8.1 km s^{-1} at the base of the crust, with a low velocity gradient. A sub-division of layer 2, layer 2A (Talwani et al., 1971), is defined for crust close to the ridge axis and corresponds to the uppermost igneous crust with velocities <4.5 km s^{-1} and a low velocity gradient.

Attenuation is described by the quality factor for both P- and S-waves, Q_p and Q_s, which accounts for energy absorption and scattering within the rock. Attenuation is high within layer 2A, Q=20-50 (Jacobson and Lewis, 1990), thought to be caused by a high layer porosity and near-axis fluid flow. Hydrothermal circulation through layer 2A results in mineral precipitation within the upper crustal pore space, reducing the porosity and increasing the seismic velocity. Layer 2A disappears with age and is not expected to be present in 100 Ma crust. White (1992) illustrate how seismic velocities of crust change with age away from the ridge axis and show that velocity scatter within the upper crust decreases with age (Figure 2.3). North Atlantic rifting occurred at ~100 Ma, so for comparisons with predicted oceanic crustal velocity structure the bounds of 0-143 Ma crust are used within this thesis.

Spudich and Orcutt (1980) and Collier and Singh (1998) estimate Poisson's ratio values of 0.32-0.48 for the upper 200 m of young oceanic crust however these high values are likely due to intense fracturing within the upper crust. Poisson's ratio values of 0.24-0.27 were estimated 0.8-1.5 km into oceanic basement, possibly related to a change in

Table 2.1: Raitt-Hill layering of normal oceanic crust

Layer	Thickness [km]	Seismic velocity [km s^{-1}]
Sea water	4.5	1.5
Layer 1 (sediment)	~0.5	~2
Layer 2 (extrusive volcanics)	1.71±0.75	5.07±0.63
Layer 3 (lower crust)	4.86±1.42	6.69±0.26
Layer 4 (upper mantle)		8.13±0.24

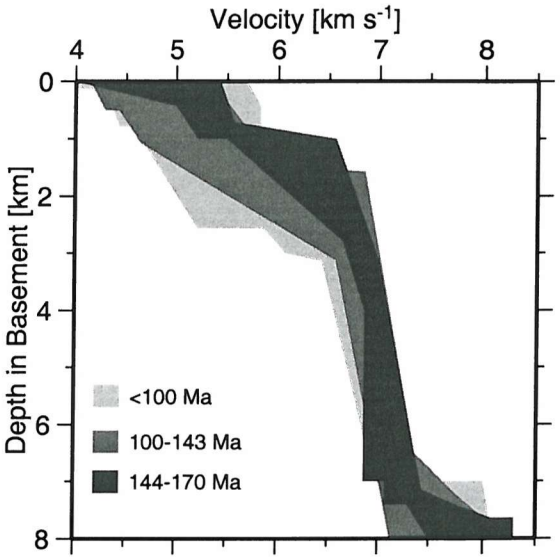

Figure 2.3: Variation of oceanic crustal velocities with age. Oceanic crust aged <100, 100-143 and 144-170 Ma shown from light to dark grey. Most variation occurs within the upper layer; velocities become less scattered in older crust with a higher velocity gradient in the upper crust and a thicker low gradient layer beneath. Velocity-depth profiles are taken from White (1992).

lithology or fluid saturation (Spudich and Orcutt, 1980) and most likely indicating the top of layer 2B, the top of oceanic crust observed off-axis. For unconstrained regions of oceanic crust a Poisson's ratio of 0.25 is often assumed (Minshull, 2002b), this compares well with laboratory estimates made from ophiolite samples (Figure 2.5; Salisbury and Christensen, 1978; Christensen and Smewing, 1981).

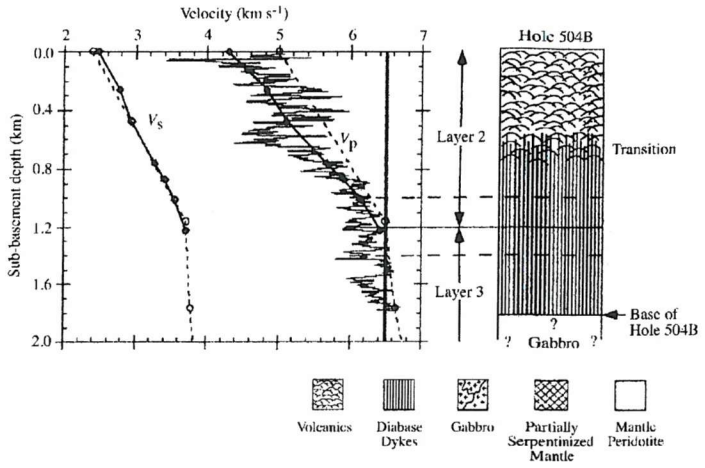

Figure 2.4: Seismic velocities correlated with the geological cross-section at ODP Hole 504b on the East Pacific Rise at ~1° N. Hole 504b penetrated 2.8 km into 6.2 Ma oceanic crust. The layer 2/3 boundary is located within the sheeted dike section and not at the transition from dikes to gabbro. From Minshull (2002b); after Detrick et al. (1994).

Geological interpretation

Geological interpretation of these seismic layers remains controversial as exposures of ocean crust generally occur in anomalous tectonic situations e.g., fracture zones, where we cannot be sure of sampling normal oceanic crust. Ocean drilling is usually restricted to the upper volcanic layer, the deepest penetration to date is 2.8 km at ODP Site 504b on the East Pacific Rise, a hole deepened by seven successive DSDP (69, 70, 83 and 92) and ODP (111, 140, 148) drilling Legs (e.g., Cann et al., 1983; Alt et al., 1993). Seismic layer 3 was sampled and the layer 2/layer 3 boundary located within the dike section (Figure 2.4).

As we have yet to drill an entire in-situ section from sediment to mantle, a large constraint on the composition of oceanic crust has come from ophiolites. Ophiolites are sections of oceanic crust now situated on land; because of the tectonic environment required to exhume them, they tend to have formed in an abnormal spreading setting such as back-arc or marginal ocean basins. The Macquarie Island ophiolite was formed in a normal ridge environment at ~20 mm yr^{-1} (full-spreading rate) and exhumed within the ocean basin in which it formed by a change in spreading orientation and rate. Unfortunately, it is incomplete in the lower sequences and not heavily studied to date (e.g., Williamson, 1988). Figure 2.5 shows compilation sections for the Bay of Islands and Oman ophiolites, illus-

trating variations in V_p, V_s and σ with lithology. Based on correlation with these ophiolite sequences, layer 2 is interpreted as extrusive volcanics and dikes, while layer 3 corresponds to gabbro (e.g., Salisbury and Christensen, 1978).

The layer 2A/2B boundary is generally interpreted as marking the transition from extrusives to sheeted dikes (Christeson et al., 1996) or a porosity boundary (e.g., Harding et al., 1989; Rohr, 1994). There is some uncertainty as to the geological significance of the layer 2/3 boundary: it is situated at the base of the dike section in the Oman ophiolite, but within the dikes at the Bay of Islands ophiolite, where it coincides with the transition from brecciated to non-brecciated dikes; a conclusion that is supported by the presence of this boundary within the dikes at Hole 504b (Figure 2.4).

Some authors have proposed that layer 3 consists entirely (Hess, 1962) or partly (e.g., Cannat, 1993; Minshull et al., 1998) of serpentinised peridotite (Figure 2.6). Serpentinised peridotite has been sampled at some mid-ocean ridge sites (e.g., Tucholke et al., 1998), but its presence appears strongly dependent on the spreading rate and is therefore discussed in Section 2.2.2. The layer 3/4 boundary is the seismic Moho and for normal oceanic crust marks the boundary between a mafic crust and ultramafic rocks beneath. In the Bay of Islands ophiolite sequence, Karson et al. (1984) identify variations in the thickness of the transition from mafic to ultramafic rocks from a few hundred meters to ~3 km, over lateral distances of ~20 km. A transitional Moho of km's depth will not be observable in seismic reflection data because there is not sufficient impedance contrast to produce observable reflections, although thicker zones may allow energy to be refracted within it at long offsets.

2.2.2 Variation with spreading rate

Crustal structure

Seismic crustal thickness is estimated from the depth to the layer 3/4 boundary and typically measures the thickness of crust at velocities <7.6 km s^{-1}. An alternative method of estimating the crustal thickness is by geochemical methods. The degree of melting defines the magmatic crustal thickness, but is also measurable by the composition of the resultant melts; hence an indirect relationship can be drawn between melt composition and melt thickness. The thickness of oceanic crust estimated from seismic and geochemical methods agrees well (Figures 2.7, 2.8), predicting a thickness of ~6.5 km for slow, intermediate and fast spreading rates; variations in crustal thickness are primarily at the expense of layer

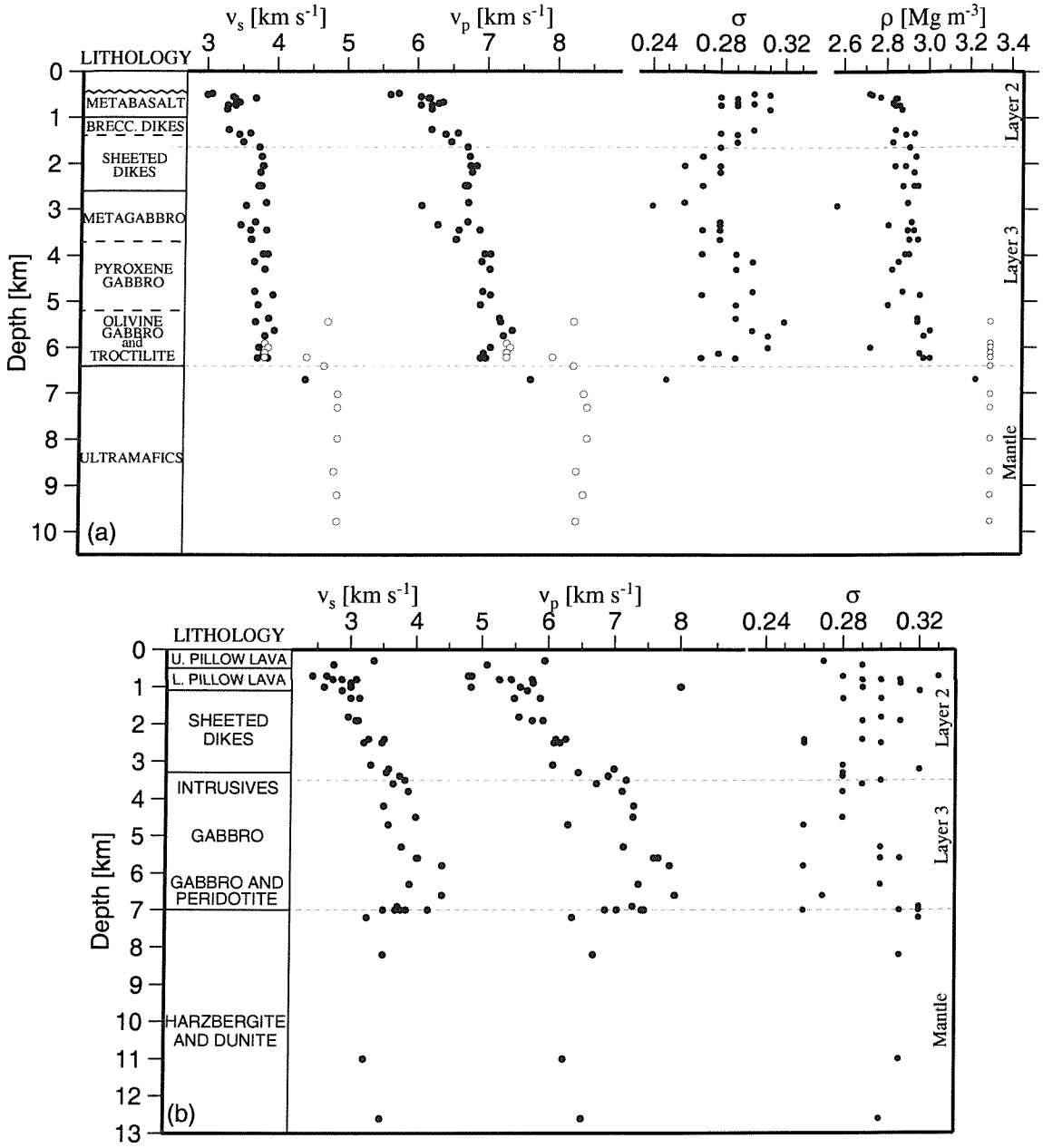

Figure 2.5: (a) Crustal section through the Bay of Islands ophiolite, western Newfoundland. V_p and V_s, Poisson's ratio (σ) and density (ρ) are shown with closed circles indicating direct measurements taken and open circles denoting those samples for which velocities were estimated through modal composition analysis. The division of seismic layers is also shown. V_p and V_s increase rapidly through layer 2 and have a much lower velocity gradient through layer 3. Poisson's ratio values decrease from 0.28-0.31 (for V_p >5.5 km s^{-1}) in layer 2 to ~0.26 at the base of the sheeted dikes before increasing again in layer 3. Values of 0.25 are predicted for the mantle. After Salisbury and Christensen (1978). (b) Crustal section through the Oman ophiolite with physical properties as for (a). After Christensen and Smewing (1981).

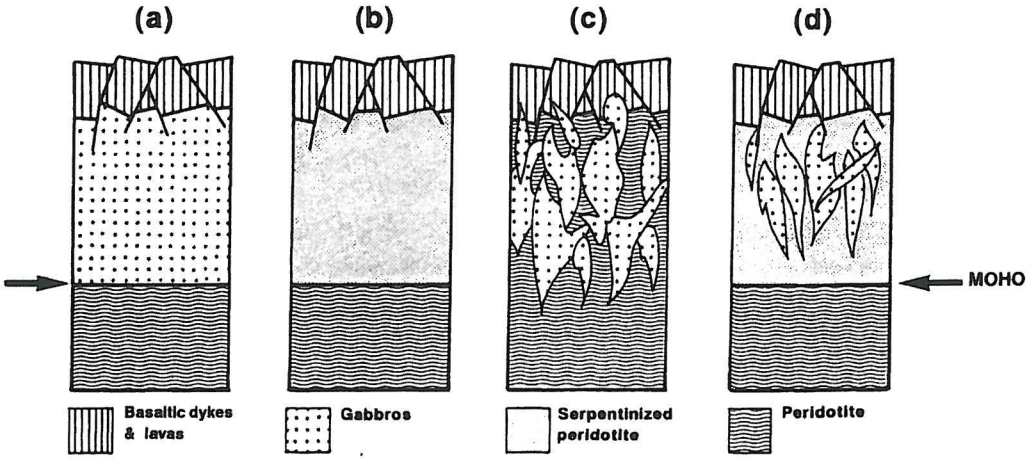

Figure 2.6: Alternative models for oceanic crust composition. (a) Layer 3 consists entirely of gabbro; (b) layer 3 consists entirely of partially serpentinised peridotite (Hess, 1962); (c) layer 3 consists of gabbroic intrusions within mantle peridotite which may have experienced some serpentinisation (Cannat, 1993); (d) layer 3 consists of gabbro intrusions within partially serpentinised peridotite; unserpentinised peridotite lies beneath the Moho. From Minshull et al. (1998).

3 with layer 2 becoming a smaller proportion of the whole crust with increasing thickness (Mutter and Mutter, 1993). At full-spreading rates <20 mm yr^{-1}, considered ultra-slow by Dick et al. (2003), crustal thickness drops rapidly to as little as ~3 km (Figure 2.8). This decrease in crustal thickness is thought to indicate a reduction in the amount of melting beneath the ridge due to heat loss by conduction at slow extension rates (Minshull et al., 2001; White et al., 2001). The close agreement of the seismically and geochemically defined crustal thicknesses implies that the seismic crust consists almost entirely of melt products and that serpentinite does not form a substantial portion of the crust (White et al., 2001). Models for oceanic crust that include large amounts of serpentinised peridotite within layer 3 (Figure 2.6*b* – *d*) are opposed by these results. However, serpentinised peridotites have been observed to outcrop on- and off-axis at slow spreading ridges (e.g., Cannat, 1993; Durand et al., 1996) and oceanic core complexes have been identified as low angle detachments that expose serpentinite under extreme extension (e.g., Cann et al., 1997; Karson and Lawrence, 1997; Tucholke et al., 1998; MacLeod et al., 2002): it is clear that in some cases serpentinite does contribute to the crust at the surface, and probably at greater depths too, but the exact volumes are not well defined. If the seismic crustal thickness underestimates the true crustal thickness then this apparent misfit can be resolved. The base of the crust is taken as a transition to velocities >7.6 km s^{-1} (White

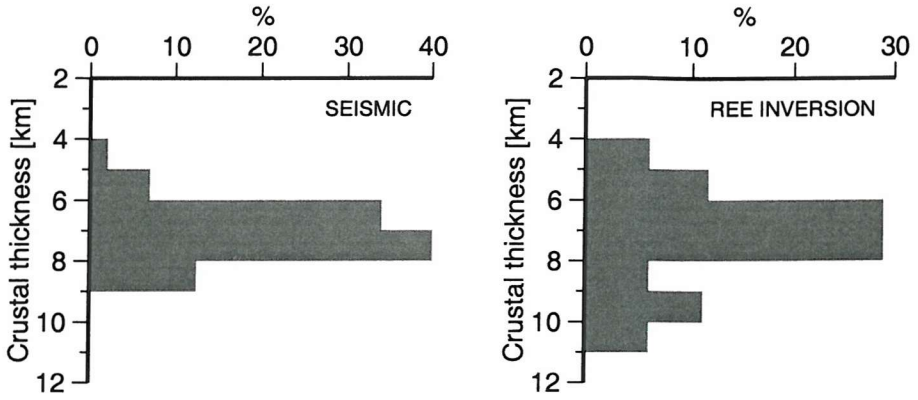

Figure 2.7: Oceanic crustal thickness away from hotspots and fracture zones, estimated by seismic (synthetic seismogram) methods and rare-earth element inversion. There is a close agreement between the two methods for normal oceanic crust. After Minshull et al. (1998).

et al., 1992; White et al., 2001), but up to 25% of oceanic gabbros may be present beneath the Moho while remaining consistent with the observed mantle velocities (Cannat, 1996); layer 3 may then contain ~25% of serpentinised ultramafic material and up to 20% of the whole crustal thickness could be composed of serpentinite. Crustal variability within ridge segments may also be important at slow spreading rates. Melt supply may vary within these segments (e.g., Muller et al., 1999), channelling towards segment centres (Dick, 1989), reducing the crustal thickness towards segment tips and allowing relatively small faults to emplace ultramafic rocks at the surface (Durand et al., 1996). Carlson (2001) estimated whole-crustal abundance of serpentinite at <13% for Atlantic normal ocean crust but if, as it appears, spreading occurs over magmatic and amagmatic cycles (e.g., Edwards et al., 2001) then serpentinite may contribute to a greater proportion of the crust during amagmatic extension periods.

Basement relief

At spreading rates >20 mm yr^{-1} crustal thickness and bulk composition are relatively uniform (Bown and White, 1994) and the greatest observable change is in basement topography. Slow spreading ridges away from hotspot influence have deep rift valleys with variable relief from ~400 m to ~2500 m (Small, 1998), distinct from fast spreading ridges which have small axial highs (~400 m) with shallow linear depressions at their crests (e.g., Heezen, 1960; Fornari et al., 1998) (Figure 2.9). These changes are caused by a reduced melt supply at slow extension rates and the increased influence of tectonic over magmatic processes (e.g., Phipps Morgan and Chen, 1993; Cannat et al., 1999).

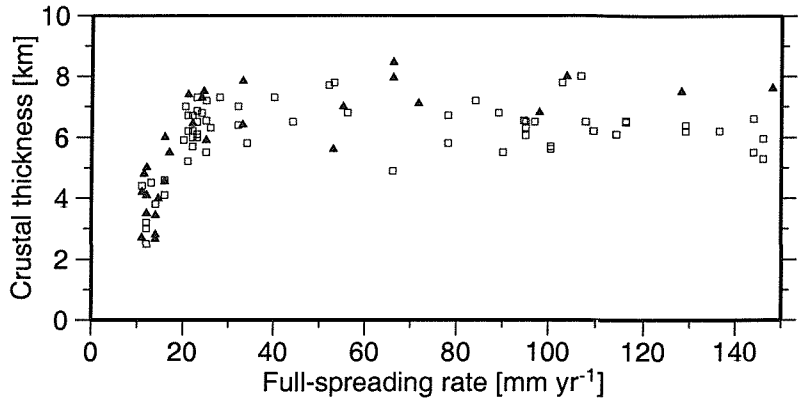

Figure 2.8: Seismic crustal thickness (squares) (data from Bown and White (1994) and White et al. (2001)) compared with geochemical estimates of crustal thickness from REE inversion (triangles) (data from White et al. (1992) and White et al. (2001)). There is good agreement at all spreading rates; crustal thickness is fairly uniform between 30-150 mm yr^{-1} and decreases rapidly at slow rates <20 mm yr^{-1}. Figure modified from White et al. (2001).

A decrease in basement relief with increasing spreading rate has been observed away from the ridge axis (Figure 7: Small, 1994), possibly due to the episodic nature of magmatic input at slow spreading ridges and extension being accommodated by tectonic deformation. Empirical relationships between spreading rate and basement relief have been constructed by several authors (e.g., Goff, 1991; Malinverno, 1991; Goff, 1992; Small, 1994) (Figure 2.10). The roughness of oceanic crust can be described by the RMS misfit between the observed topography and a best fit line through these data which accounts for thermal subsidence away from the spreading centre (e.g., Malinverno, 1991; Minshull, 1999). This analysis allows spreading rate bounds to be estimated from depth migrated seismic sections and compared to spreading rates derived from magnetic anomalies; this method assumes uniform growth of ridge segments and does not take account of variability in magmatic accretion within these segments.

2.3 Exhumed mantle

The presence of serpentinised peridotite at or near top basement of rifted margins has been well documented (e.g., Pickup et al., 1996; Whitmarsh and Sawyer, 1996; Whitmarsh and Wallace, 2001; Dean et al., 2000; Russell and Whitmarsh, 2003) so it is important to understand the range of physical properties that may be observed in these regions.

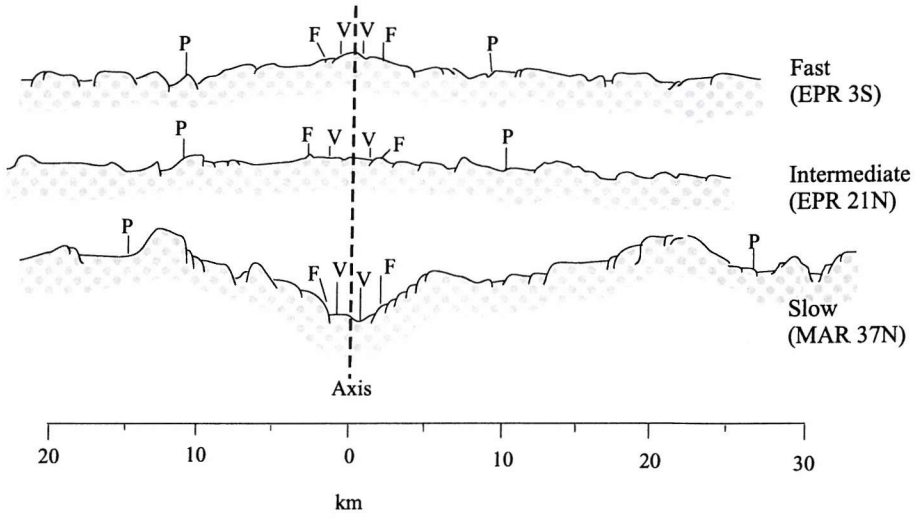

Figure 2.9: Mid-ocean ridge topography increases at decreasing spreading rates with the formation of an axial valley and broadening of the zone of faulting (P). V marks the region of extrusive volcanism and F the region experiencing intrusive accretion at fissures. 4x vertical exaggeration. After (MacDonald, 1982).

2.3.1 Introduction to serpentinite

Serpentinites form by the chemical alteration of peridotite, pyroxene and gabbro and the hydration of magnesium rich silicates and carbonates (e.g., olivine and talc) (O'Hanley, 1996). Serpentinite can itself undergo alteration and replaced by other serpentine minerals. Serpentine minerals are, in general, stable below 550° C which equates to a stability zone ~4 km beneath top basement if a thermal gradient of 130° C km^{-1}, approximately the thermal gradient in young oceanic crust (Fowler, 1990), is assumed. The stability field can vary widely for different serpentine minerals, so the range of conditions at which serpentinite can exist is broader than described here. Assuming a lithostatic pressure of 60 MPa, talc is shown to be stable at temperatures up to ~700° C (Figure 5-6: O'Hanley, 1996) which may allow serpentinite to be present 6-7 km into basement. At the MARK area on the Mid-Atlantic Ridge, the last phase of serpentinisation appears to have occurred at a temperature of ~350° C (Lawrence et al., 2002), as the serpentinite cooled past the Curie temperature for magnetite and the magnetisation was fixed within the rocks.

Serpentinisation is an exothermic reaction and should be self-limiting. The addition of water causes expansion and a reduction in permeability of the rock, cutting off the water supply and acting to slow the rate of continued serpentinisation. Once the serpentinite

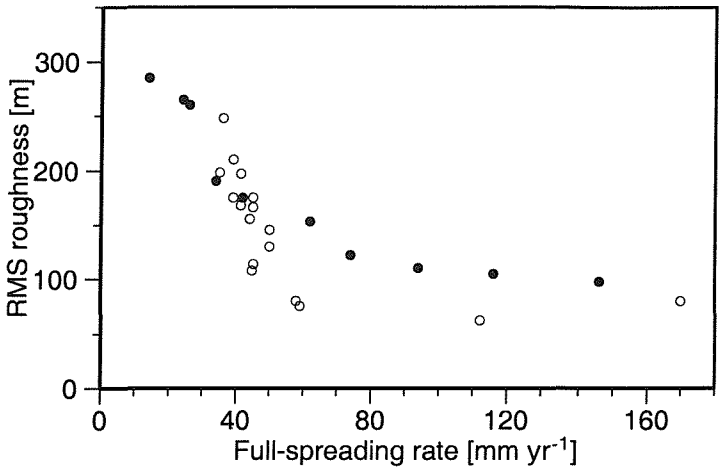

Figure 2.10: Correlation of spreading rate and basement roughness on the ridge flanks from Malinverno (1991) (black circles), Goff (1991) and Goff (1992) (open circles). Basement relief increases rapidly at spreading rates <40 mm yr^{-1}.

becomes fully hydrated, the rock must fracture to accommodate this continued expansion (O'Hanley, 1996), however, because serpentinisation is a localised process occurring at mineral boundaries, it is unlikely that sufficient stress could build up within serpentinised peridotite to produce deeply penetrating faults or large basement topography (Escartín et al., 2001).

Depending on the temperature at which hydration occurs, the alteration of peridotite will produce different mineral assemblages. At successively lower temperatures the following serpentinite sequences could be expected for decreasing pressures (O'Hanley, 1996):
olivine → anthophyllite → talc → antigorite → lizardite
olivine → talc → antigorite → lizardite
olivine → antigorite → lizardite
olivine → lizardite

Different serpentinite compositions are expected to exhibit different physical properties due to their variable mineral composition. In order to accurately model zones of serpentinite, their composition must be known, primarily by recovering samples by dredging or drilling. As more studies are completed, and a broader database constructed, it may be possible to distinguish bulk serpentinite assemblages from the observed physical properties.

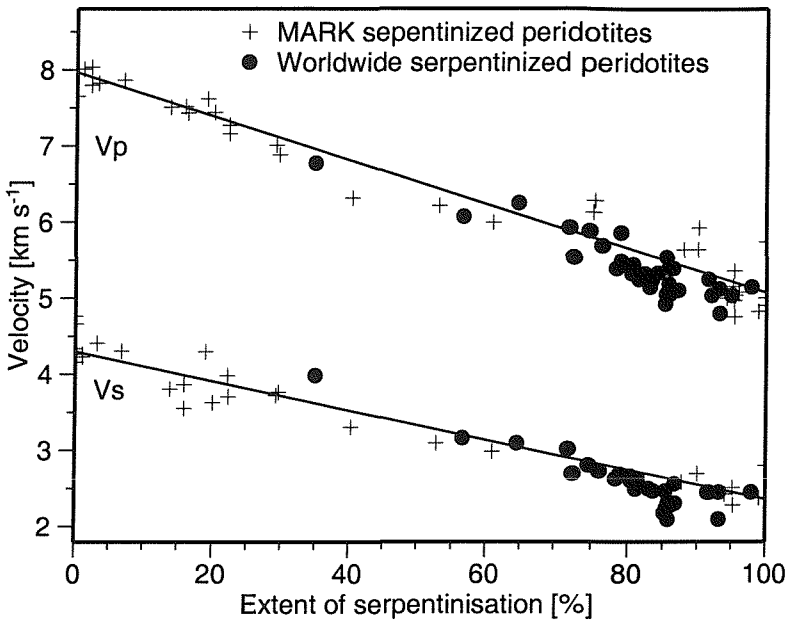

Figure 2.11: Empirical relationship of V_p and V_s with extent of serpentinisation. Worldwide serpentinite measurements are taken from Christensen (1966), Christensen (1972), Christensen (1978), Christensen and Salisbury (1972) and Kroenke et al. (1976). After Miller and Christensen (1997).

2.3.2 Physical properties of serpentinite

Seismic velocities

An empirical relationship has been defined between seismic velocity and extent of serpentinisation for a worldwide compilation of serpentinite samples (Miller and Christensen, 1997). Velocities decrease with serpentinisation, ranging from 8 km s^{-1} for unserpentinised mantle to 5 km s^{-1} for 100% serpentinisation (Figure 2.11). Low velocities of ~4.3 km s^{-1} have been observed at the top of serpentinite within a zone of exhumed mantle at the Southern Iberia Abyssal Plain and were interpreted as as result of intense brecciation of the serpentinite (Dean, 1999), which is encouraged by fracturing of hydrated rock.

The Poisson's ratio of serpentinite has been estimated by laboratory measurements of V_p and V_s (e.g., Miller and Christensen, 1997) and typically ranges from 0.30 to 0.38. For P-wave velocities in the range 4.5-6 km s^{-1}, serpentinite can be distinguished from thinned continental crust, basalt and gabbro (Section 6.2; Figure 6.5).

Magnetic properties

Rock magnetisation is most commonly contained within magnetite, an iron-oxide mineral with a large magnetic susceptibility (~6 SI), allowing strong magnetisations to be stored. The formation of magnetite during serpentinisation has been simply explained by the reaction

olivine + H_2O = serpentine ± brucite ± magnetite (Oufi et al., 2002),

but is complex and depends on the interaction between iron in the serpentinite and oxygen within the fluid (O'Hanley, 1996). Variations in magnetite content may result in large differences in the observed magnetisation for serpentinites at different locations (e.g., Beard, 2000; Zhao, 1996; Oufi et al., 2002).

Magnetisations of 10-20 A m^{-1} , similar to those typically observed in oceanic basalts, have been measured in serpentinites from ODP Site 920 on the Mid-Atlantic Ridge (Cannat et al., 1995) and at the Southwest Indian Ridge (Sauter et al., 2004), but contrast with serpentinites from Site 1070 where magnetisations of <1.2 A m^{-1} are recorded (Zhao et al., 2001). Oufi et al. (2002) suggest there is a non-linear relationship between magnetic susceptibility (K) and extent of serpentinisation, where K remains low during early serpentinisation and increases rapidly once serpentinisation increases beyond ~75%. These changes are related to the iron content of serpentinite and could be encouraged by prolonged contact with seawater which would allow serpentinisation to continue, the destabilisation of iron-rich serpentine (>6% FeO) to iron-poor serpentine (2-3% FeO) and the crystallisation of magnetite from the free iron (Oufi et al., 2002).

Attenuation

Attenuation is often estimated from multichannel seismic data (e.g., Spudich and Orcutt, 1980; Hobbs, 1990; Boillot et al., 1995) and generally decreases with depth within the Earth (inverse of Q), from Q_p =~300 in shallow crustal layers to Q_p =~1000 for the upper mantle (Table 2.2). The attenuation of serpentinite is strongly frequency dependent and has a $Q_p = 800 - 950$ for seismic frequencies of ~10 Hz.

Table 2.2: Quality factor estimates for sediment and various crustal types. Modelling of oceanic crust (Spudich and Orcutt, 1980) was insensitive to variations in Q_p: the estimate shown here is if all attenuation is due to shear losses. Low Q values equate to high attenuation. Measurements were made from multichannel seismic data except for the serpentinite measurements of Kern et al. (1997), which were conducted in lab conditions with a source frequency of 2 and 1 MHz for P- and S- waves respectively and indicate a strong frequency dependence of the quality factor, underestimating Q for typical deep crustal seismic frequencies.

Layer	Q_p	Q_s	Source
Sediment	100–200		Boillot et al. (1995)
Continental crust (whole crust)	400		Hobbs (1990)
	600–675		Boillot et al. (1995)
Upper continental crust	300–400		Braile (1977), Tittmann (1977)
Lower continental crust	500±200		Hobbs (1990)
	400–1000		Tittmann (1977)
Oceanic crust	~450	100–225	Spudich and Orcutt (1980)
Serpentinised peridotite	800–950		Boillot et al. (1995)
	60–200	50–130	Kern et al. (1997)
Upper mantle	1000		Boillot et al. (1995)

Chapter 3

Ray theory for wide-angle seismic modelling

Wide-angle modelling within this thesis was carried out using ray theory. This chapter describes the method used and the assumptions and limitations of this method.

The desired result from modelling of wide-angle seismic data is a velocity model that allows computed arrivals to match the observed instrument records. The method applied here follows that of Zelt and Smith (1992) and uses ray theory (e.g., Červený et al., 1977; Aki and Richards, 1980; Lay and Wallace, 1995) to fit arrival traveltimes. Geometrical spreading is incorporated within ray theory and, combined with the consideration of attenuation along the ray path (e.g., Červený et al., 1977), allows additional amplitude constraints to be provided by generating synthetic seismograms (Zelt and Ellis, 1988; Zelt and Forsyth, 1994).

Modelling can be carried out either by the forward method, where modifications to the model are user-controlled between each iteration, or the inverse approach where model adjustments are automated by minimising a penalty function according to some user-defined criteria that controls model perturbations. The non-linear nature of the inverse traveltime problem requires an iterative procedure to be followed, with the forward step completed following each inversion to update the model and calculate statistics for the rays traced. A brief discussion of solutions to the forward and inverse problems, the penalty function applied and model parametrisation within *RAYINVR* (Zelt and Smith, 1992) follows.

3.1 Forward step

If we consider a ray normal to a three-dimensional wavefront, an isotime surface away from a source and described by the traveltime function $T(\boldsymbol{x})$ (Figure 3.1), and with ray path $\boldsymbol{x}$: at any point along its path the ray travels a step length, ds, at an angle, θ, from the vertical (Figure 3.2). The ray can be separated into its component directions (dx_x, dx_y, dx_z), termed *directional cosines*, and must satisfy the subsidiary relation (Equation 3.1), a three-dimensional trigonometric identity.

$$\left(\frac{\partial x_x}{\partial s}\right)^2 + \left(\frac{\partial x_y}{\partial s}\right)^2 + \left(\frac{\partial x_z}{\partial s}\right)^2 = 1 \quad , \tag{3.1}$$

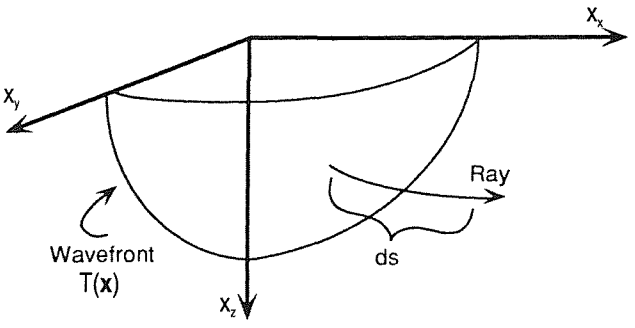

Figure 3.1: Schematic diagram of a three-dimensional wavefront. The ray is normal to the wavefront with length ds. After Lay and Wallace (1995).

At any point the ray is orientated normal to the surface of the wavefront (Figure 3.1) and distance travelled in any component direction, $\frac{\mathrm{d}x_i}{\mathrm{d}s}$, is proportional to the gradient of the wavefront in that direction, $\frac{\partial T(\boldsymbol{x})}{\partial x_i}$ $(i = x, y, z)$. Equation 3.1 can be re-written as

$$\left(k\frac{\partial T(\boldsymbol{x})}{\partial x_x}\right)^2 + \left(k\frac{\partial T(\boldsymbol{x})}{\partial x_y}\right)^2 + \left(k\frac{\partial T(\boldsymbol{x})}{\partial x_z}\right)^2 = 1 \quad , \tag{3.2}$$

where k is a constant of proportionality which, if equal to $v(\boldsymbol{x})$ where v is the velocity field, allows Equation 3.2 to be re-arranged into the *eikonal equation*:

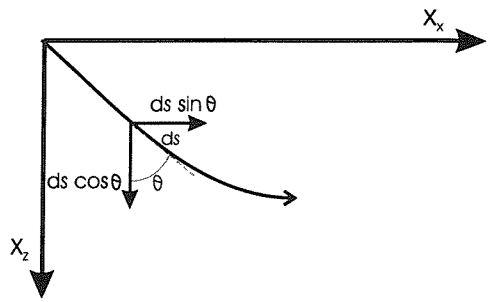

Figure 3.2: Instantaneous separation of a ray into its horizontal and vertical component directions. ds is the step length and θ is the angle of the ray path from the vertical.

$$\left(\frac{\partial T(\boldsymbol{x})}{\partial x_x}\right)^2 + \left(\frac{\partial T(\boldsymbol{x})}{\partial x_y}\right)^2 + \left(\frac{\partial T(\boldsymbol{x})}{\partial x_z}\right)^2 = \frac{1}{v(\boldsymbol{x})^2} \quad . \tag{3.3}$$

The *eikonal equation* is a partial differential equation that relates rays to the velocity field within the model. It can also be derived directly from the wave equation (see Appendix 3: Shearer, 1999) to give the general form:

$$\mid \boldsymbol{p} \mid^2 = \mid \nabla T \mid^2 = \frac{1}{v^2} \quad , \tag{3.4}$$

where v is the wave speed, T the traveltime function and $\boldsymbol{p}$ the slowness vector, which is given by the gradient of the traveltime function and describes the direction of the ray. A high frequency approximation must be explicitly made because the wave equation includes gradient terms in the Lamé parameters (constants that describe the relationship between stress and strain, or rigidity, for the material) that vary with $1/\omega$, tending to zero as the frequency increases. This high frequency approximation assumes frequencies are sufficiently high that the higher order terms are unimportant and can be neglected. In real-earth terms the *eikonal equation* approximates the wave equation as long as the change in velocity gradient over one wavelength is small compared to the velocity, an assumption that is valid for typical crustal velocities (Lay and Wallace, 1995). In regions of strong velocity gradients (e.g., at boundaries between materials of differing velocities) this approximation fails, but the problem can be separated into regions where the ray approximation is valid and the solutions recombined. Snell's law is applied at interfaces to calculate the initial conditions for the ray path segment after the interface.

Equations 3.1 and 3.3 can be combined to form the *normal equations* which describe the wave surface in its three component dimensions:

$$\frac{1}{v}\frac{\mathrm{d}x_x}{\mathrm{d}s} = \frac{\partial T(\boldsymbol{x})}{\partial x_x} \quad , \tag{3.5a}$$

$$\frac{1}{v}\frac{\mathrm{d}x_y}{\mathrm{d}s} = \frac{\partial T(\boldsymbol{x})}{\partial x_y} \quad , \tag{3.5b}$$

$$\frac{1}{v}\frac{\mathrm{d}x_z}{\mathrm{d}s} = \frac{\partial T(\boldsymbol{x})}{\partial x_z} \quad . \tag{3.5c}$$

In a model containing velocity gradients, the principle of conservation of horizontal slowness along the ray path causes the orientation of the ray to change with position: the ray-bending effect. Strictly speaking, horizontal slowness is conserved along a ray path in the presence of vertical velocity gradients only; lateral velocity gradients result in a change of horizontal slowness along the ray path, which may take a more complex route through the subsurface. To consider how the normal equations change along the ray path we take the derivative of Equations 3.5a–3.5c with respect to $\mathrm{d}s$ to produce a second-order differential equation for $\boldsymbol{x}$, the *raypath equation.*

$$\frac{\mathrm{d}}{\mathrm{d}s}\left(\frac{1}{v(\boldsymbol{x})}\frac{\mathrm{d}(\boldsymbol{x})}{\mathrm{d}s}\right) = \nabla\left(\frac{1}{v(\boldsymbol{x})}\right) \quad . \tag{3.6}$$

Considering only the horizontal (x_x) and vertical (x_z) dimensions, Equation 3.6 can be expanded to give

$$\frac{\mathrm{d}}{\mathrm{d}s}\left(\frac{1}{v}\frac{\mathrm{d}x_x}{\mathrm{d}s}\right) = \frac{\partial}{\partial x_x}\left(\frac{1}{v(\boldsymbol{x})}\right) \quad , \tag{3.7a}$$

$$\frac{\mathrm{d}}{\mathrm{d}s}\left(\frac{1}{v}\frac{\mathrm{d}x_z}{\mathrm{d}s}\right) = \frac{\partial}{\partial x_z}\left(\frac{1}{v(\boldsymbol{x})}\right) \quad . \tag{3.7b}$$

Equations 3.7a and 3.7b describe the change in orientation of a ray as it experiences a velocity gradient, or step, and can be considered a generalised version of Snell's law for geometrical optics (Officer, 1974).

Expansion of Equation 3.7a and 3.7b, substituting ray orientation, θ, for ray step length, $\mathrm{d}s$, and allowing vertical and horizontal velocity variations, $v(x_x, x_z)$, results in two pairs of differential equations that describe the change in ray position and orientation with model

location (Equations 3.8a, 3.8b) (e.g., Zelt and Smith, 1992). These derivations require nested application of the chain, product and quotient differentiation rules and are not reproduced here due to space limitations. Further discussion of the methodology applied to reach these solutions can be found in Červený et al. (1977)[1].

$$\frac{\mathrm{d}x_z}{\mathrm{d}x_x} = cotan\ \theta\,, \qquad \frac{\mathrm{d}\theta}{\mathrm{d}x_x} = \frac{\left(\frac{\partial v}{\partial x_z} - \frac{\partial v}{\partial x_x}\ cotan\ \theta\right)}{v}\quad , \tag{3.8a}$$

$$\frac{\mathrm{d}x_x}{\mathrm{d}x_z} = tan\ \theta\,, \qquad \frac{\mathrm{d}\theta}{\mathrm{d}x_z} = \frac{\left(\frac{\partial v}{\partial x_z}\ tan\ \theta - \frac{\partial v}{\partial x_x}\right)}{v}\quad . \tag{3.8b}$$

For near horizontal rays Equation 3.8a is solved with x_x as the variable; when the ray path is near vertical Equation 3.8b is solved with x_z as the variable. These equations can be solved using the Range-Kutta method as they are functions of one independent variable and contain first-order derivatives only. This method is computationally accurate and efficient, but requires initial conditions to be supplied:

$$x_x = x_{x0}, \quad x_z = x_{z0}, \quad \theta = \theta_0,$$

where the point (x_{x0}, x_{z0}) is the source location and θ_0 is the ray take-off angle.

The ray is defined at a number of points along its path, the step length, that depends on the user specified value (α). For $\alpha = 0.025$ to 0.1 this approximation results in a traveltime error of 2-10 ms (Zelt and Ellis, 1988). An α value of 0.03 was used in this study, towards the lower end of the tested range, with no significant increase in computation time and a resultant traveltime error of ~2 ms.

The total traveltime for each ray can be calculated by integrating along the ray path, s, through the velocity field $v(x_x, x_z)$

$$t = \int_s \frac{1}{v(x_x, x_z)}\mathrm{d}s \quad , \tag{3.9}$$

however in practice, traveltime is summed along its path for each ray segment, s_i

$$t = \sum_{i=1}^{n} \frac{s_i}{v_i} \quad . \tag{3.10}$$

[1]The author declines to reproduce the full derivation.

The principle of traveltime reciprocity is applied, allowing rays to emerge from the instrument and be traced to their surface shot points. Minimum and maximum ray take-off angles are determined iteratively and rays are traced between these two values. Ray endpoints may not match observed data points exactly, so traveltimes are linearly interpolated between endpoints to the required distances. This shooting method is more robust and less computationally intensive than two-point ray tracing (Zelt and Smith, 1992) and remains valid as long as enough rays are traced to sample lateral velocity variations within the model. To minimise the scattering and focussing of ray paths caused by discontinuities in velocity or velocity gradient, model boundaries are smoothed prior to ray tracing: boundaries are sampled into closely spaced linear segments and a three-point averaging filter is applied to produce a smoothed interface (Zelt and Smith, 1992). This smoothing compensates for any artificially sharp model boundaries that are introduced by the model, preventing geometrical shadow zones at the surface, allowing more data to be used, and improves model stability during inversions (Zelt and Smith, 1992).

3.2 Inverse step

The traveltime for a ray through the velocity model can be easily calculated by Equation 3.10 as a linear combination of 1/velocity for each ray path step. Traveltime inversion, predicting the velocity field from the observed traveltimes, is however a non-linear problem because the ray path is itself velocity dependent. In order to linearise this problem Equation 3.10 is expanded using a Taylor series, assuming a starting model and dropping higher order terms. The linearised equation to be solved then becomes

$$\boldsymbol{A}\ \Delta \boldsymbol{m} = \Delta\ \boldsymbol{t} \quad , \tag{3.11}$$

where $\boldsymbol{A}$ is the partial derivative matrix and describes the distance travelled at any point within the model space, $\Delta \boldsymbol{m}$ is the model adjustment vector and $\Delta \boldsymbol{t}$ is the traveltime residual vector calculated from the starting model for this iteration. An iterative inversion approach is required to keep model adjustments within the region of linearity about the current model, so that progressive convergence to the model with minimum global misfit is achieved and the final model is not distorted by tending towards a local minimum (Shaw and Orcutt, 1985; Hobro, 1999).

For a simple least-squares solution to this equation to be unique every model parameter must be uniquely constrained by the data, a situation that does not exist for real earth

problems, where data tend to be noisy and provide dense ray coverage in some regions and little in others. *RAYINVR* is designed to work with an under-parametrised model; additional constraints to the solution are required to maintain model stability during the inversion and are incorporated as regularisation terms in the function to be minimised, which then takes the form

$$\|\boldsymbol{A}\,\boldsymbol{m} - \Delta\boldsymbol{t}\|^2 + \lambda_d^2\,\|\Delta\boldsymbol{m}\|^2 + \lambda_s^2\,\|\boldsymbol{L}\,\Delta\boldsymbol{m}\|^2 \quad . \tag{3.12}$$

The first term describes the least-squares misfit to the data; the second and third terms damp model perturbations and smooth the perturbed model respectively, representing the damped least-squares (Aki and Richards, 1980; Zelt and Smith, 1992) and smoothed least-squares (Constable et al., 1987; Bruguier, 1997) solutions. The damped least-squares solution (*DMPLSTSQR*) is controlled by λ_d ($\lambda_s = 0$), the weighting of the damping term, which regulates the trade-off between model misfit and model perturbation within each iteration. High damping does not prevent a rough, or oscillatory, model from being produced, but damps parameter adjustments within each inversion step, resulting in an updated model that is similar to the input model. Using a damped least-squares solution, unsampled regions are unperturbed and remain equal to the starting model. Zelt and Smith (1992) describe stability problems with this solution in the presence of large lateral velocity gradients.

In the smoothed least-squares solution (*SMOOTHLSQR*) λ_s controls the weighting of model misfit against model roughness and $\lambda_d = 0$. $\boldsymbol{L}$ is an approximation to the Laplacian which describes the difference between a model node and an average of the surrounding nodes. The smoothness constraint is applied to the updated model and not the perturbations, hence is less dependent on the input model than the damped least-squares solution and unconstrained regions are smoothed by surrounding, constrained, areas. By maintaining layer smoothness (limiting lateral gradients) the instability during inversion caused by large lateral gradients can be avoided. Smoothing is applied in the horizontal direction only, at incremental depths to allow for lateral variations in velocity gradient.

A balance must be reached between model misfit and model roughness. Possible solutions range from smooth models that do not have a good fit to the observed data to oscillatory models with a minimum misfit (Figure 3.3). The optimal, or best-fit, model is situated between these extremes where the model is fairly smooth and there is a reasonable fit to the data (Shearer, 1999). The λ_d or λ_s value is user specified at each inversion step and

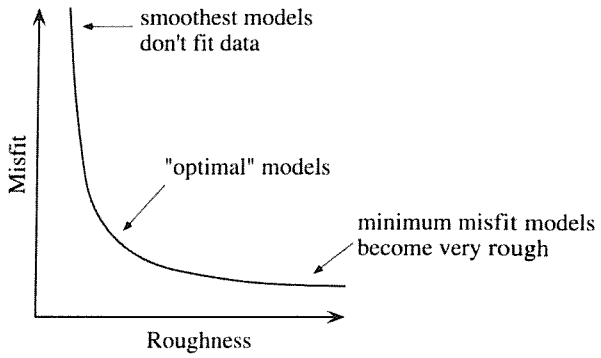

Figure 3.3: There is a trade off between model roughness and misfit to the observed data such that smooth models have a poor fit and minimum misfit models become oscillatory. The best-fit model is located between these extremes. From Shearer (1999).

usually starts with large values to allow rapid convergence, within the region of linearity from the current model (Shaw and Orcutt, 1985), to the first-order model fit (with minimum structure in the *SMOOTHLSQR* case) and progressively decreased to smaller values to allow finer adjustments (or increased roughness) and convergence to the best-fit model. Uncertainties of the data are estimated and statistical analysis attempted to help select the best-fit model (Section 5.1).

3.3 Model parametrisation

In order to solve the *ray equations* (Equations 3.8a and 3.8b) and determine initial model adjustments during the inverse step a starting velocity model is required. The choice of starting model can have significant influence on the model development so a simple model is preferred; *a-priori* information can be incorporated within the model at this stage e.g., interfaces from a seismic reflection profile.

Velocity models are constructed as a series of layers defined by boundary nodes at the top of a layer and linearly interpolated between them; the base of the layer is assumed to coincide with the top of the layer beneath, to prevent empty space from being introduced to the model. A horizontal boundary is required to indicate the base of the model. Boundary nodes can be placed anywhere within the model space as long as they do not cross existing layer boundaries, this approach allows nodes to be closely spaced in well constrained

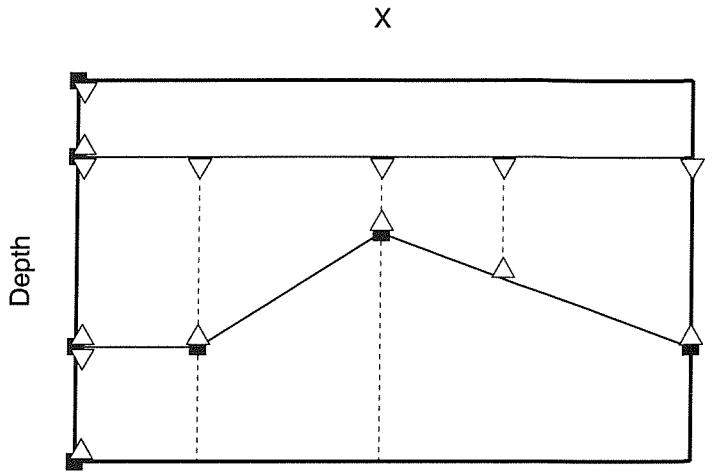

Figure 3.4: *RAYINVR* velocity models are defined by boundary nodes (squares) at the top of a layer and velocity nodes at the top (inverted triangles) and bottom (triangles) of a layer. The model is broken up into trapeziums at these velocity and boundary nodes (dashed lines) and velocities linearly interpolated within each trapezoid. Layer 1 has a laterally constant velocity, defined at the left of the model only; layer 2 velocities are defined at multiple X positions and can vary laterally. The base of layer 2 is defined by the layer 3 boundary and varies across the width of the model.

regions, or areas of complex topography, and a greater node spacing in poorly constrained regions. Horizontal layers can be defined by a single node at 0 km model distance (Figure 3.4) and pinch-outs can be included within the model by making the layer thickness zero for part of its width. Layer pinch-outs allow large lateral variability within the model without introducing modelling instabilities, but there must be strong evidence for such features (e.g., at continental margins a change in velocity structure from continental to oceanic crust may be considered abrupt) as they are a user-introduced structure and not necessarily required by the data. Velocity values are defined at the top and bottom of each layer (Figure 3.4). The velocity gradient can be zero for a layer and lateral variations in velocity and/or velocity gradient are allowed. Velocities are interpolated linearly between nodes for both the upper and lower boundaries. Top and bottom velocity nodes do not have to be defined at identical X coordinates, but practical experience suggests it is more efficient to have identical upper and lower node positions to give greater control over the velocity gradient within the layer.

Chapter 4

Goban Spur: data acquisition and processing

4.1 Data Acquisition: *RRS Charles Darwin* cruise 124

During September and October 2000 *RRS Charles Darwin* cruise 124 (CD-124) carried out a geophysical study at the Goban Spur margin with the principle aim of identifying the nature of basement in this region from seismic refraction surveying (Minshull, 2000). Gravity and echosounder data were continuously recorded during the study period and magnetic data were collected using a towed magnetometer. During a period of extremely poor weather and sea conditions, detailed swath surveying of the seabed was carried out, enabling identification of seven previously unidentified basement highs. A total of 24 ocean bottom instruments was deployed as part of the wide-angle seismic survey but only seven recorded data that were useful for this work. For a list of all instruments and sensors deployed see Appendix A.

4.1.1 Sea-bed mapping

A hull mounted Simrad EM12 multibeam echosounder was used during the cruise to acquire swath images of depth to seabed with a 20 m resolution. Conversion from time to depth was made according to a velocity function based on historical measurements of water column temperature and salinity from the National Oceanographic Data Centre (NODC) database. Ocean conditions were found to be consistent with this database by temperature measurements made with expendable bathythermographs (XBT) sampling to a maximum depth of 1870 m during this cruise (Table 4.1). The temperature-depth profiles recorded for each XBT are shown in Appendix B.

Table 4.1: Sippican XBT deployments during cruise CD-124. T5 and T7 probes have maximum depths of 1870 m and 780 m respectively.

XBT No	Day of year	Time	Type	Latitude N	Longitude W	Water depth [m]
1	269	0935	T5[1]	49°15.1′	12°25.4′	1138
2	269	1310	T5[2]	49°05.3′	12°58.6′	2162
3	269	2002	T5	48°45.6′	14°06.9′	4503
4	269	2219	T5	48°39.2′	14°30.1′	4640
5	270	2142	T5	48°30.7′	13°26.9′	4398
6	278	0705	T7	49°14.6′	12°24.9′	1128

[1]Reached seabed
[2]Recorded as T7

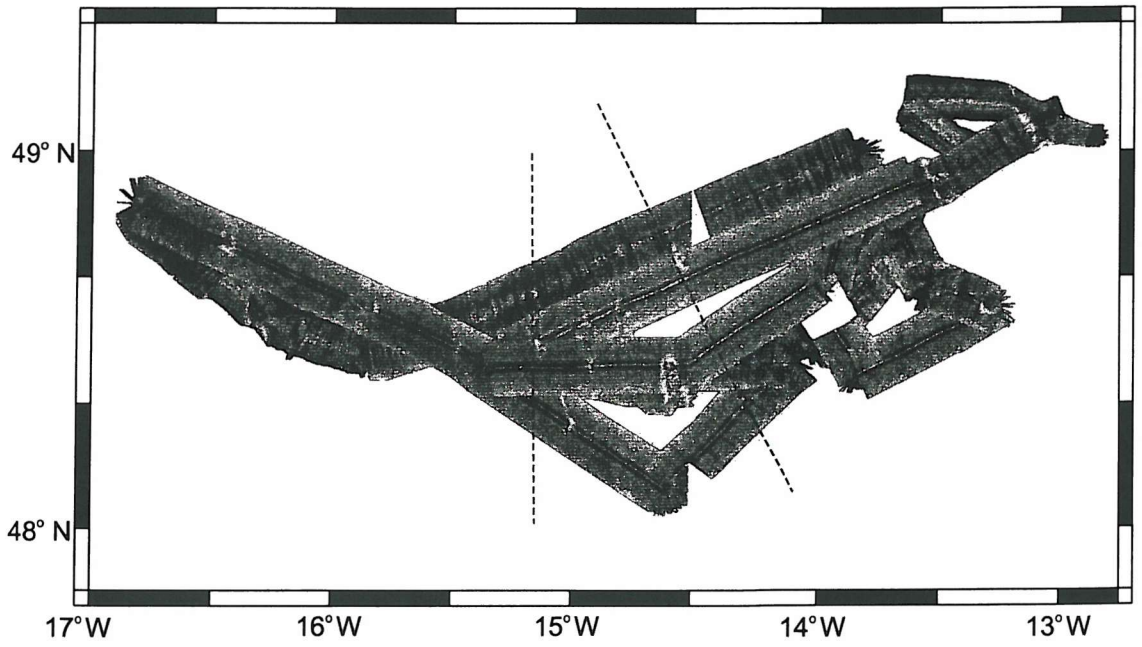

Figure 4.1: Backscatter image recorded with the hull-mounted swath bathymetry system. Seven previously unidentified basement highs can be seen penetrating the seabed between 14°and 16° W, with a change in orientation from margin parallel to north-south at 14°45′ W. The basement high successfully dredged in this study can be seen at 48°30′ N, 15°10′ W.

The poor sea conditions during part of this experiment resulted in some swath tracks displaying a large amount of noise caused by ship roll. Careful selection of the best available data had to be made to allow a composite image to be produced; a backscatter amplitude image is shown in Figure 4.1. Depth values were exported and these bathymetric data merged with data from an earlier swath test cruise, *RRS Charles Darwin* 116 (CD-116), to produce a detailed bathymetric contour map of the study region. Seven previously unidentified basement highs, >200 m above the surrounding abyssal plain, have been mapped and provide interesting targets for future exploration. A change in orientation of these basement highs can be observed around 14°45′ W from a strike of 330°-150° (approximately margin parallel) to 0°-180°. Bathymetric data were resampled at 0.25′ (~300 m) resolution, surfaced and contoured using packages from the *Generic Mapping Tools* (*GMT*) suite (Wessel and Smith, 1991) to produce a map for the swath study area (Figure 4.2). An accurate bathymetric map for the wider region was produced by merging this with bathymetry from the GEBCO database (Fisher, 1997) (Figure 4.3).

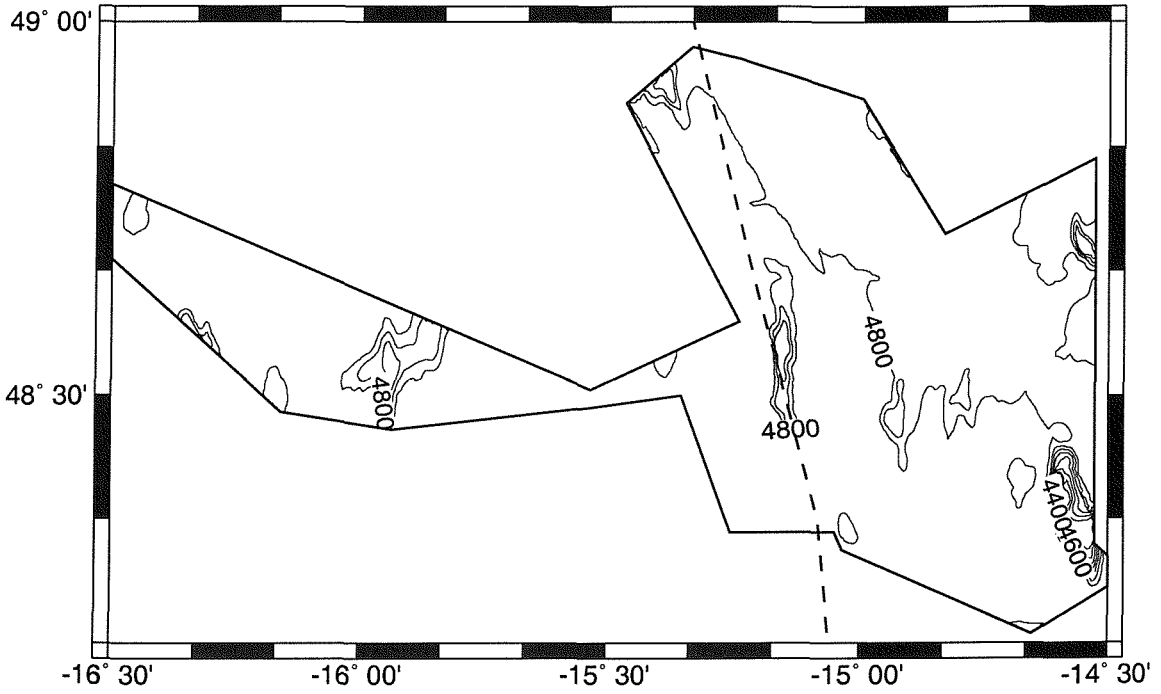

Figure 4.2: Swath bathymetry from CD-116 and CD-124. Contour interval 100 m, the dashed line shows the position of marine magnetic anomaly 34r. Seven previously unidentified basement highs can be seen, striking ~330°-150°east of 14°45′ W and north-south west of this point.

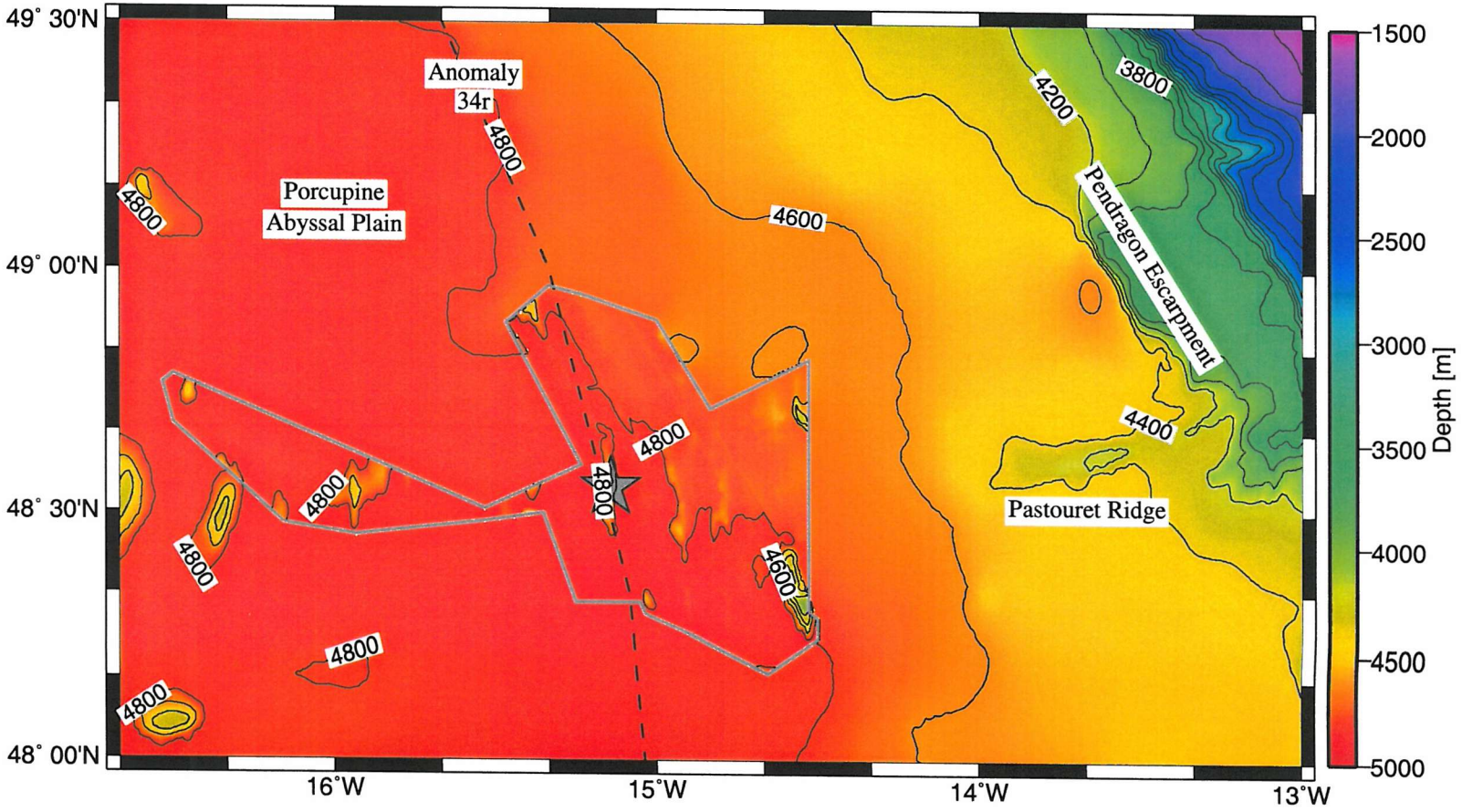

Figure 4.3: Bathymetry for the Goban Spur region from swath data on CD-116 and CD-124 (within grey box) merged with GEBCO bathymetry for more regional coverage. Contours plotted every 200 m depth. The dredge site (grey star), first marine magnetic anomaly, 34r, (dashed line) and named topographical features are shown. Surfacing was carried out with a smoothed solution to the gridding equation (a tension factor of 0.35) (Smith and Wessel, 1990) to compensate for the ship roll within the CD-124 dataset.

4.1.2 Dredging

One dredge of a prominent basement high over marine magnetic anomaly 34r (Figure 4.3) was attempted, unfortunately the ship became anchored and the 'weak link' broke with the loss of the dredge basket. A later dredge, during *RRS Discovery* 255, was successful and resulted in the recovery of some soft sediment and dolerite. This dolerite is enveloped by 2-4 cm of manganiferous crust and is significantly altered (R. Taylor, pers. comm). Rare earth and major element analysis of these dolerite samples has been carried out by Dr. Rex Taylor (SOC) and implies they were derived from an N-MORB (Normal Mid-Ocean Ridge Basalt) source, with extents and depths of melting typical of a normal ridge segment (R. Taylor, pers. comm).

More detailed geochemical analysis of these samples are not included here as they are not within the scope of this project. Melt source and depth of melting are important considerations for developing an accurate model of late stage rifting and continental break-up however, as discussed in Section 6.2.4, further studies are required to place these results in their regional context.

4.1.3 Seismic source

The seismic source used during CD-124 for wide-angle data collection was a 14-gun array deployed as four beams, each with three guns, and two single large volume guns. Only 12 guns were fired at any one time, with a total capacity of 6286 in^3 ($\sim$112 L). One gun failed immediately on deployment and was replaced with a spare gun of a similar volume on the same beam, a final gun was held in reserve and not required (Figure 4.4). The beams were towed at a depth of 6-8 m and the single guns at 15-17 m; it was planned to tow the array deeper, at $\sim$20 m, to minimise surface interactions with the bubble pulse however due to time limitations during shooting no attempt was made to adjust these depths. Source modelling predicts only a small change in the resultant waveform due to this depth change (Figure 4.5*c*); the frequency content is predicted to form a broader spectrum, but with reduced amplitudes at low frequencies. This array design was specifically chosen for it's strong low frequency waveform with a peak around 8 Hz and minimum bubble pulse predicted by source waveform modelling (Figure 4.5). A similar source arrangement was successfully used on cruise *RRS Discovery* 215 (DY-215) to the Southern Iberia Abyssal Plain and shown to allow good signal penetration to deep crustal levels suitable for large scale seismic refraction studies (Dean et al., 2000).

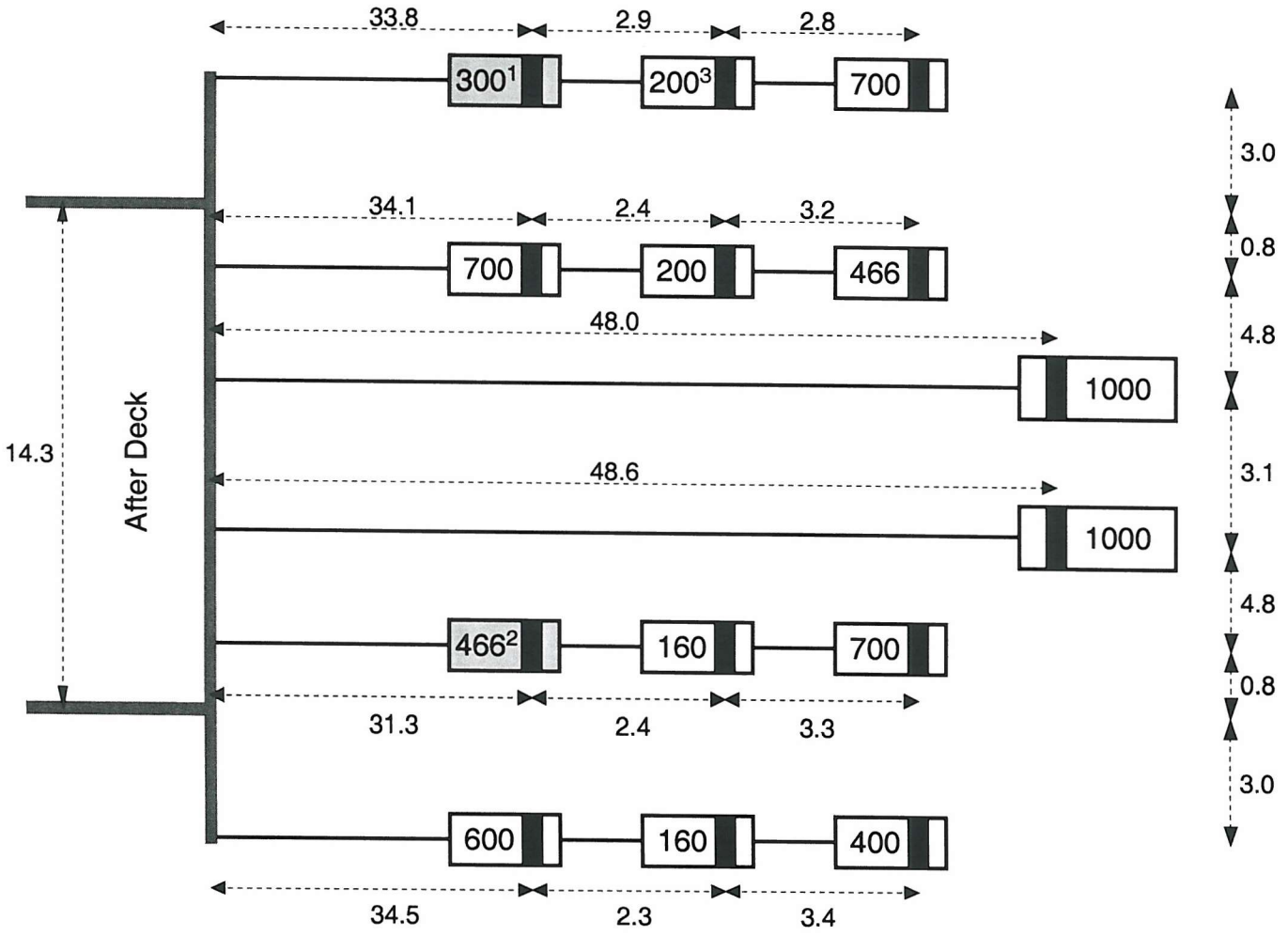

Figure 4.4: Schematic diagram of the airgun array used in the wide-angle experiment. White guns are those used during the experiment, grey indicate those not used within the array. Gun volumes in in^3 are shown. [1] = Solenoid failed immediately, [2] = unused spare gun, [3] = replacing failed gun on same beam ([1]). Distances are quoted in m.

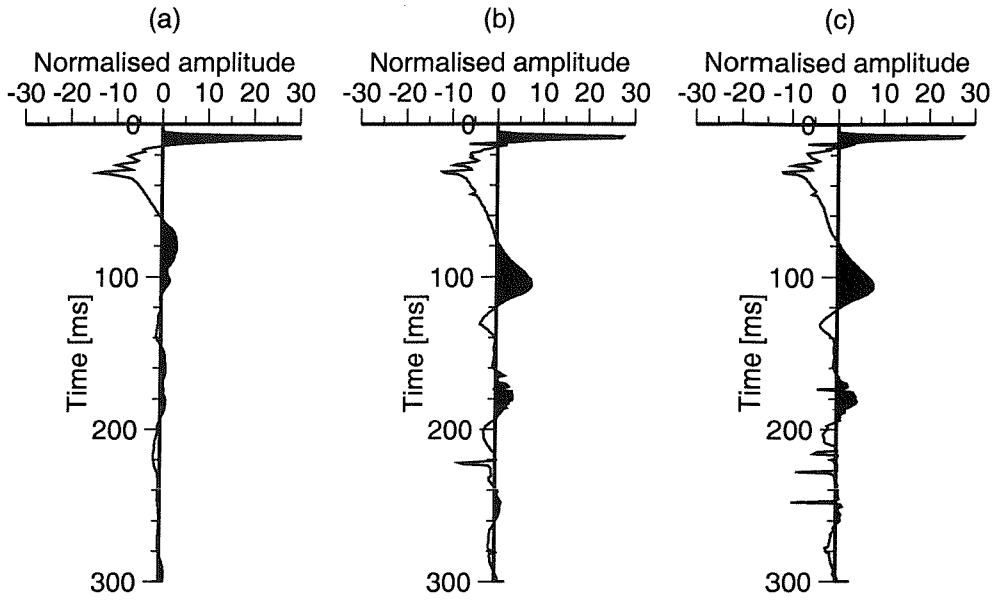

Figure 4.5: Predicted far-field source waveform (Hardy, 1991) from the deployed airgun array without (a) and including (b) modelling of bubble pulse interactions. The waveform is minimum phase, with a period of ~100 ms and a low amplitude following wave train. The predicted wavelet from an identical array towed at the planned depth of 20 m is shown in (c): there is little effect on the resultant waveform due to towing the array shallower than planned.

4.1.4 Wide-angle seismic experiment

Wide-angle seismic refraction data acquired during CD-124 was recorded on ocean bottom seismograph (OBS) and ocean bottom hydrophone (OBH) instruments provided by GEOMAR (Kiel, Germany). Only the hydrophone channel was used (Section 4.5) and all instruments will be referred to as OBH within this thesis. A mixture of sensors were used: the hydrophone channel was recorded using a hydrophone or broadband 'Cox/Webb' differential pressure gauge, with either 'Owen' or 'Webb' geophone packages for those instruments including a seismometer (Table 4.2). The 'Owen' sensor consists of a small three-component geophone package deployed on a 1.5 m arm while the 'Webb' sensor is a three-component broadband seismometer contained within a 17 inch (~43 cm) glass sphere on a 3 m arm. For both setups the arm was arranged so that the geophone sensor is deployed outside the influence of possible noise sources from the main instrument body. Wind speeds of 60-70 knots and a swell of 15-20 m during the study period severely reduced shooting time to 12 hours, a distance of approximately 100 km at 4.5 knots average speed, and meant that not all instruments could be recovered during the cruise period.

Table 4.2: Ocean bottom instruments used in this study. The model of hydrophone or geophone sensor deployed is listed as well as the sampling interval used in recording. Water depths are from the hull-mounted echosounder and are corrected for variations in water velocity using Carter's Tables (Carter, 1980). Instruments 2016 and 5001 are from the Horsefield et al. (1994) experiment (Figure 4.6; Section 4.4).

Inst. No.	Hyd channel	Geophone channel	Sampling interval [ms]	Water depth [m]	Deployment location	
					Latitude N	Longitude E
2016	Hyd	yes	13.3	3610	48°56.56′	-13°29.04′
5001	Hyd	yes	13.3	4520	48°54.07′	-13°36.79′
6	Hyd	–	10	3679	48°58.37′	-13°21.38′
8	DPG	Webb	10	4512	48°52.08′	-13°44.35′
9	Hyd	–	10	4535	48°48.76′	-13°55.74′
10	Hyd	Webb	10	4527	48°45.55′	-14°06.93′
11	DPG	–	10	4538	48°42.54′	-14°18.49′
13	Hyd	Owen	10	4747	48°36.22′	-14°41.24′
15	DPG	–	10	4840	48°29.71′	-15°03.76′

Ten instruments were on timed releases and had to be left floating at sea; three of these turned up on the Cornish and Breton coasts over the following months. Eight instruments were left on the seabed at the end of this experiment and were recovered by a later cruise aboard a trawler *The Cornishman*.

Table 4.3: Sonobuoy deployment locations and recording frequencies. Locations are marked as the grey inverted triangles in Figure 4.6.

Sonobuoy number	VHF channel	Frequency [MHz]	Depth [ft]	Recording channel	Deployment location	
					Latitude N	Longitude E
2	10	169.000	400	3	48°31.72′	-14°56.76′
3	5	165.250	400	-	48°34.06′	-14°48.44′
4	24	167.875	400	2	48°34.40′	-14°47.24′
5	13	171.250	400	3	48°37.81′	-14°35.10′
6	4	164.500	400	2	48°41.04′	-14°23.82′
7	30	172.375	400	3	48°44.24′	-14°12.59′
8	10	169.000	400	2	48°47.49′	-14°00.86′

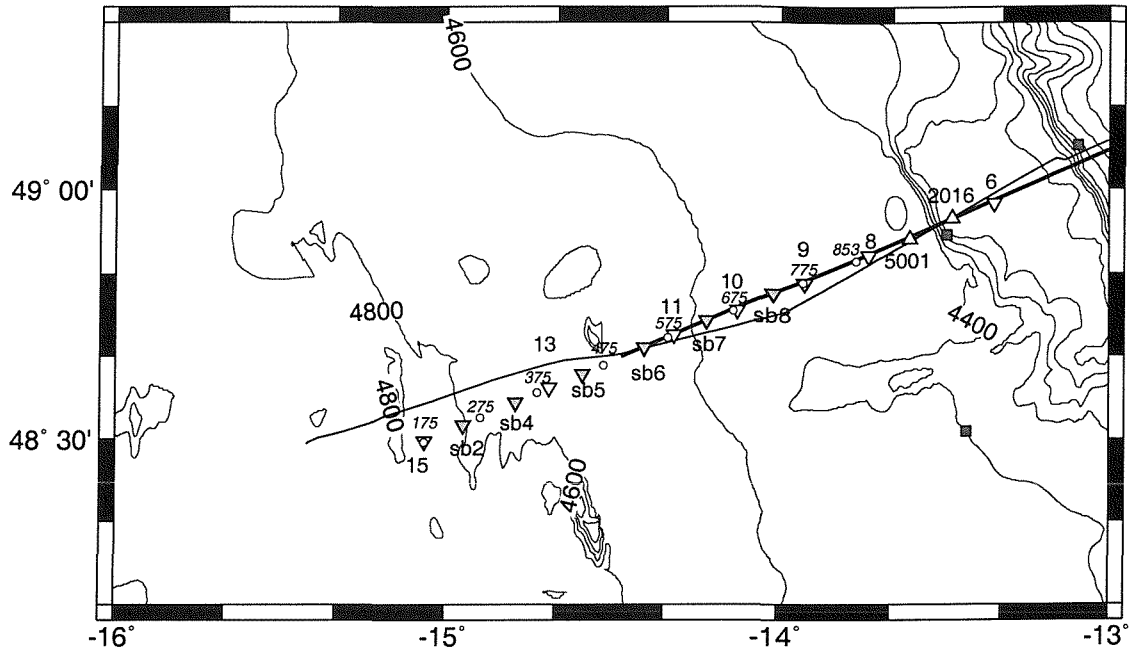

Figure 4.6: Experiment arrangement for CD-124. Ocean bottom instruments are indicated by open inverted triangles, and open triangles (Horsefield et al. (1994) experiment), grey inverted triangles mark sonobuoy deployment locations. All instruments are labelled. DSDP Leg 80 drill Sites are plotted as grey squares. BIRPS seismic reflection line WAM (black line) and the wide-angle line from the Horsefield et al. (1994) experiment (bold line) are also plotted. Shot points from this study are numbered and marked by the small circles; first shot is 175.

A total of 7 OBHs were recovered, spaced at 15-30 km intervals along a line across the margin, positioned to extend existing wide-angle studies further seaward and lying approximately coincident with the deep crustal seismic reflection line, WAM (Figure 4.6). Seven sonobuoys (SB) were deployed at equal intervals between the OBHs to increase data coverage along the line (Table 4.3, Figure 4.6). Sonobuoy signals were received through VHF aerials located on the ship's mast and digitally recorded in SEG-D format with a sampling interval of 4 ms and a record length of 30 s. Only two sonobuoy data streams could be recorded at any one time; with instrument deployments every 15 km the instrument being recorded must be changed at around 30 km offset. This was approximately the limit of useful data observed so no information was being discarded. The transmitter on SB 3 appeared to fail on deployment so SB 4 was immediately deployed, resulting in no significant loss of data coverage.

4.1.5 Underway data

Gravity surveying

Shipborne gravity data was acquired using a LaCoste and Romberg gravity meter sampling every 10 s during the cruise (Figure 4.7). Base ties were taken at the beginning and end of the cruise from a base station at Southampton and a correction for instrument drift during this period was made (Table 4.4). Latitude (ψ) corrections were applied using the WGS84 reference spheroid (Mittermayer, 1969), to account for the effect of an ellipsoidal Earth; the Earth's greater equatorial than polar radius means that points on the equator are further from the centre of mass and gravity increases poleward. The latitude correction also accounts for an increase in angular velocity from zero at the poles to a maximum at the equator: variations in the resultant centripetal acceleration cause gravity to increase poleward. An Eötvös correction was applied to compensate for the effect of the ship moving over the Earth's surface. The ship track during the experiment did not allow a statistical meaningful crossover analysis to be applied (Figure 4.7).

Instrument drift during the 13 day study period can be calculated using Equation 4.1, where Δg_{meter} is the change in measured gravity at the shipboard meter (meter reading × calibration constant) and Δg_{height} is the correction for the expected change in measured

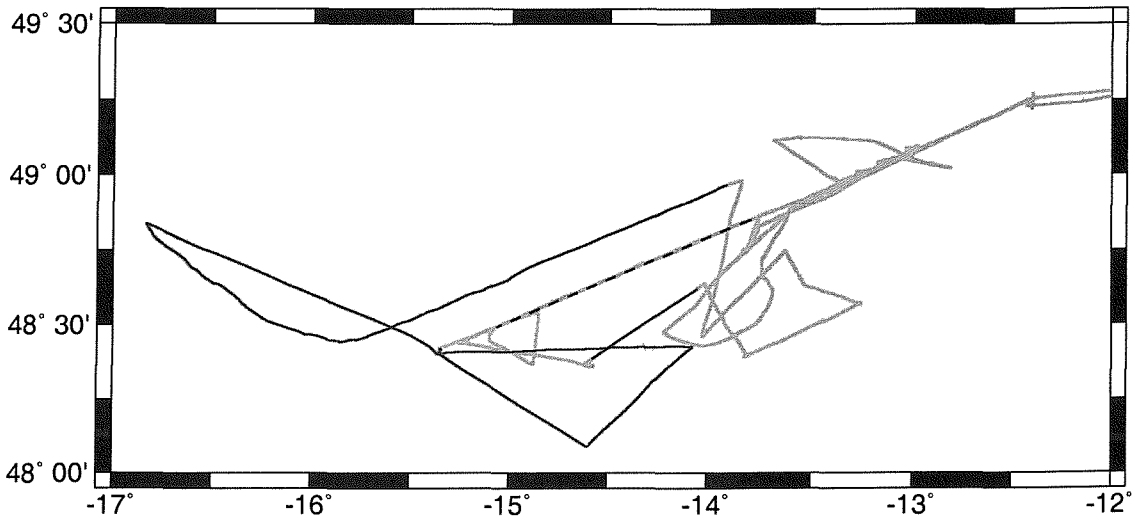

Figure 4.7: Underway data recording during CD-124. Grey lines are ship tracks: gravity measurements were made every 10 s during the cruise and black lines indicate magnetic profiles. The dashed line shows the location of the wide-angle seismic line.

Table 4.4: Gravity base ties and instrument drift over the study period. Differing tidal conditions during base station readings result in a change in meter height relative to the base station.

	Start	End	Change
Day/Time	267/0900	280/0753	
$g_{basestation}$ [mGal]	981,114.42	981,114.42	
Shipboard meter reading[1]	12348.4	12347.7	-0.7
Δg_{meter}	–	–	-0.70
Meter height above base station [m]	-2.02	-2.30	-0.28
Δg_{height} [mGal]	–	–	0.08

[1]Calibration constant = 0.9967 mGal division^{-1}

gravity due to the shipboard meter being at a different height. The drift was found to be -0.78 mGal over 13 days, assuming linear drift this equates to -0.0025 mGal hour^{-1} (Table 4.4).

$$\text{Drift} = \Delta g_{meter} - \Delta g_{height} \quad \text{mGal.} \tag{4.1}$$

To construct a shipborne gravity profile along the full length of the wide-angle line, the most suitable data must be chosen from the various ship tracks during the study period. The seismic line was sailed over twice: during instrument deployment and shooting. Measurements made during shooting were cut short due to deterioration of the sea conditions which caused cross-coupling of the gravity meter (due to ship roll) to become very significant (e.g., +50 mGal; day 277, 1600). A cross-coupling correction was applied, but the uncertainty in these measurements becomes greater than the expected amplitude of anomalies and the calculated free-air anomaly (FAA) became oscillatory over small length scales (grey line: Figure 4.8). Gravity measurements made during the instrument deployment period are used as this profile extends over the full length of the wide-angle line and was made during a period of calm sea conditions. Repeated acceleration and deceleration between OBH deployment locations is experienced by the gravity meter and caused the recorded gravitational acceleration to be overprinted by this effect. The correction to remove this effect was determined according to the accelerations experienced by the gravity meter and was automatically applied during the FAA calculation, removing this effect almost entirely (to within ~1 mGal) (Figure 4.8). These shipborne data closely fit the FAA derived from satellite gravity measurements (4.17 mGal RMS misfit; Figure 4.8).

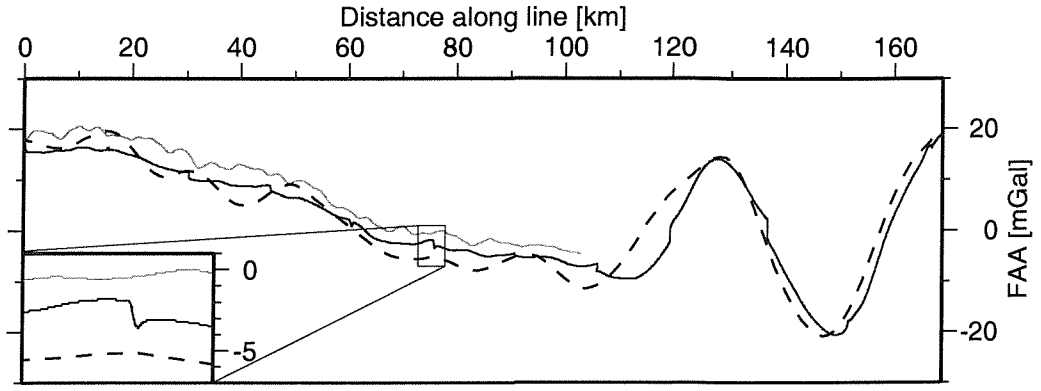

Figure 4.8: Free-air gravity anomaly along the wide-angle seismic line studied here. Measurements were made with a shipboard LaCoste and Romberg gravity meter during OBH deployment (black), during seismic shooting (grey) and compared to satellite gravity extracted along the seismic line (dashed line) (Sandwell and Smith, 1997). A RMS misfit of 4.17 mGal exists between the shipborne and satellite derived gravity measurements. The box indicates the measurements shown within the inset. Gravity measurements along the line were cut short when the line was ended early due to poor sea conditions. Inset: Enlargement of gravity measurements around an OBH deployment location. Although corrections are applied for the ship's acceleration and deceleration, a small effect ($\leq$1 mGal) remains.

Magnetic surveying

Magnetic data were collected on a Varian V75 magnetometer, towed ~160 m behind the ship; two ship lengths separation between the ship and magnetometer results in an error in the measurements of ~10 nT (Bullard and Mason, 1961). Magnetic anomalies were computed relative to International Geomagnetic Reference Field (IGRF) (Peddie, 1983). Measurements were made along a transect between the OBH 15 deployment and the dredge site, and across marine magnetic anomaly 34r (Figure 4.7). No magnetic profile was made directly along the seismic line; the closest is parallel to, but 10 km north of, the line and stops at 90 km distance along the seismic line due to the deteriorating weather.

Magnetic anomalies were extracted from the North Atlantic magnetic grid with a 2′ resolution and sub-sampled every 5 km (Verhoef et al., 1996). Comparison of the gridded magnetic anomaly along the seismic line and along the shipborne magnetic profile track shows only small changes in general appearance and imply that lateral variability is small over 10 km distance along margin strike (Figure 4.9). These grid anomalies show a RMS misfit of 96 nT to the shipborne data; the largest difference (120 nT) occurs in the magnitude of anomaly 34r at -10 km (Figure 4.9). This may be partly attributed to along-strike

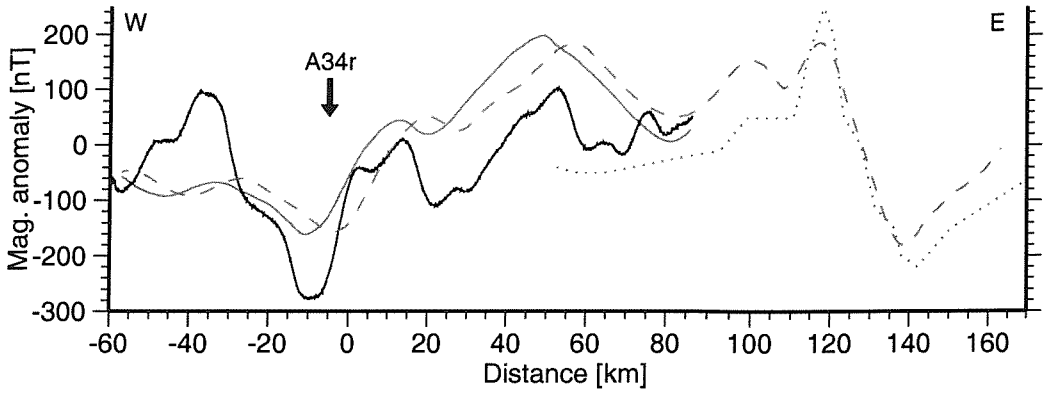

Figure 4.9: Comparison of shipborne magnetic anomaly (black) with the anomaly extracted from the North Atlantic magnetic anomaly grid along the same profile (grey) and along the full length of the wide-angle model line, 10 km to the south (grey, dashed). The magnetic anomaly used in previous modelling (Louvel et al., 1997) is given by the dotted line and shows a rapid decrease to 0 nT anomaly not seen in the datasets here. There is a large RMS misfit (96 nT) between the shipborne and gridded data but the general features are consistent between both. Position is given as distance along the seismic line.

variations within the resolution of the magnetic grid: e.g., anomaly 34r is narrower and weaker 10 km north of the seismic line (Figure 4.10). Many features appear to be shifted ~5-10 km east (Figure 4.9), most likely due to the obliqueness of the profile or the features themselves: this can be considered an estimate of the lateral uncertainty of these data. A gradual decrease in magnetic anomaly is observed from -13°30′ to -15° (200 to -50 nT), in both the gridded and shipborne data, giving confidence in features of the gridded dataset. This gently decreasing magnetic anomaly west of the continental slope is at odds with the rapid trend to ~0 nT west of the continental slope shown by Louvel et al. (1997) (Figure 4.9). The magnetic profile tracks used to compile the Verhoef et al. (1996) grid between 12° and 16° W are held by the British Geological Survey and remain unpublished for commercial reasons; data points may be widely spaced and amplitudes reduced by smoothing between observation points. The absolute amplitudes within the shipborne dataset are probably more accurate, but for completeness over the study line, the magnetic anomaly over the foot of the continental slope, unsampled by the shipborne magnetic profile, must be considered. To allow this, the anomaly extracted from the North Atlantic magnetic grid will be fitted during modelling and the shipborne data will be plotted but not directly analysed. Due to the uncertainties present within these anomalies the main task will be fitting gross anomaly features, which are consistent across datasets, rather than exact amplitude matching.

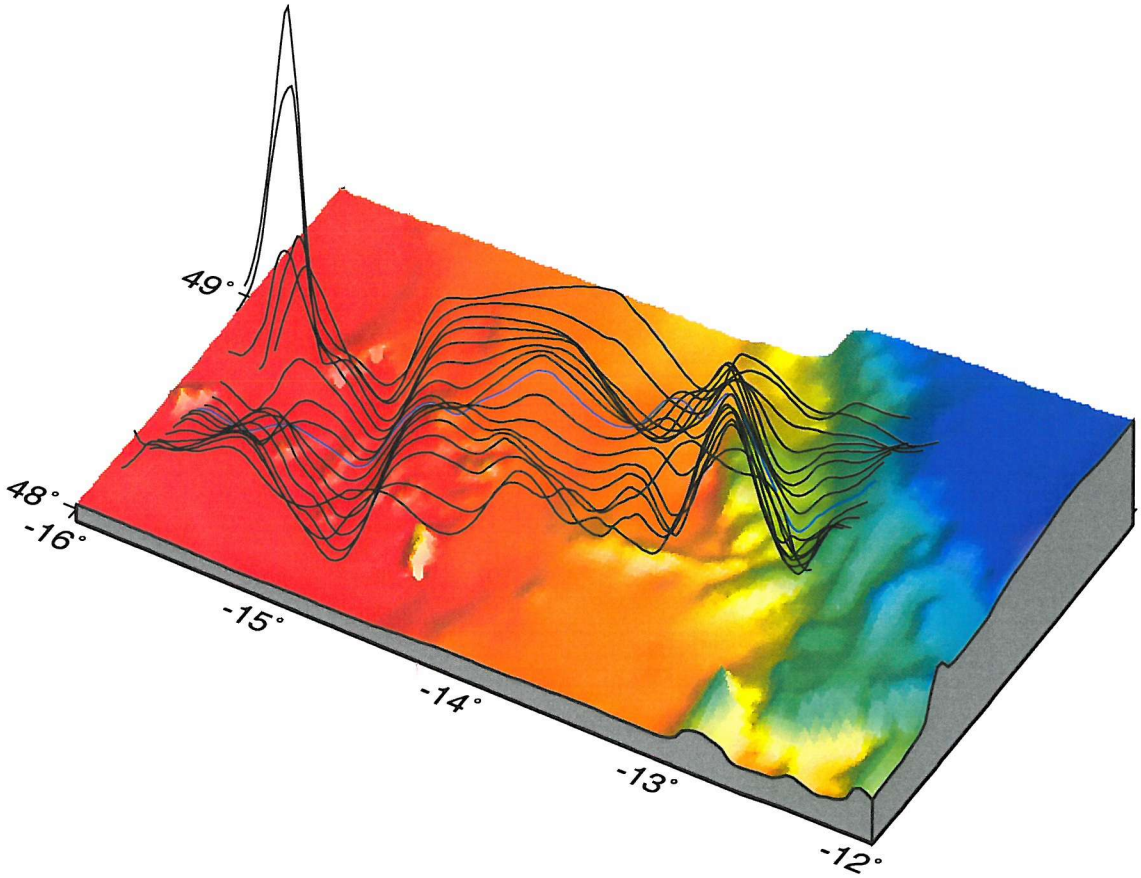

Figure 4.10: Magnetic anomalies extracted every 5 km across the Goban Spur margin overlain on the bathymetry. The blue line indicates the magnetic anomaly over the seismic line in this study. Anomaly 34r can be seen as a large negative anomaly at ~15° W and changes shape with latitude: as you progress north, anomaly 34r becomes narrower compared to the south. The anomaly is generally lower amplitude around the seismic line, increasing in amplitude to the north and south.

4.2 OBH data processing

4.2.1 Instrument relocation

OBH data were read off the instrument data cards and converted to SEG-Y format using the ship's navigation and shot times. No bulk static shifts were required to these data. Corrections for internal clock drift and trigger delay (Section 4.2.2) were made at this stage. Instrument relocation was carried out in an in-line direction only by picking the near-offset (<3 km) direct arrival and iterative adjustment of the instrument location until the direct arrival hyperbola became symmetrical either side of the instrument. A crossing line, or near pass, would be required to accurately relocate the instrument in three dimensions. A water velocity of 1.51 km s^{-1} is assumed, consistent with the velocity profile expected for this region from the comparison of XBT profiles with the assumed velocity-temperature structure (Figure 4.11), and results in an error of <2 ms for offsets <3 km (Figure 4.11*c*). Relocations were made to $\frac{1}{10}$ minute accuracy and little repositioning of the instruments on the seabed was required. Errors in positioning of the OBHs are incorporated into the modelling uncertainty and considered in Section 5.1.3.

4.2.2 Timing corrections

The internal clock in each OBH was monitored against the GPS clock and any drift in the instrument clock was corrected for. The time offset between the internal and GPS clocks were recorded before (t_{before}) and after deployment (t_{after}) and, assuming a linear drift during the deployment period ($T_{deployment}$), a time correction (t_{drift}) was made to each instrument for the time passed since the start of the deployment (T) according to Equation 4.2.

$$t_{drift} = t_{before} + \left(\frac{t_{after} - t_{before}}{T_{deployment}} \times T \right) \quad \text{ms.} \tag{4.2}$$

Corrections for the internal clock drift are applied, not to the instrument clock itself, but by changing the time at which samples are extracted relative to the instrument clock, hence are positive when the instrument clock is fast compared to the GPS standard. This is the opposite convention to that expected when corrections are applied directly to the data. Those instruments recovered after the cruise end (15, 13 and 9) had insufficient battery power to run for the duration and no drift calculation was possible. Known clock

Table 4.5: Internal clock drift during the survey is variable, ±100 ms. Late recovery of instruments 15, 13 and 9 made it impossible to calculate the clock drift. Rather than attempt to apply an unknown correction this error is incorporated into the modelling uncertainties.

Instrument	Clock drift during deployment [ms]
11	-91
10	20
8	115
6	-10

drifts during the shooting period have a wide range of values (Table 4.5), so no drift is assumed. During the shooting period, clock drift is consistently within ±12 ms if linear drift is assumed (Figure 4.12); this is incorporated within the modelling uncertainty for instruments uncorrected for clock drift (Section 5.1.3).

During acquisition an artificial delay of ~50 ms was introduced between the gun trigger and the shot instant, considered to be the first peak of seismic energy. This gave the gun controller time in which to fire each airgun within the array to produce the optimum tuned wavelet. In practice a delay of 48 ms was observed between the GPS trigger time and onset of the source waveform and this correction, $t_{trigger}$, was applied to these OBH data (Equation 4.3).

$$t_{trigger} = -48 \quad \text{ms.} \tag{4.3}$$

The total correction to be applied is

$$t_{total\_corr} = t_{drift} + t_{trigger} \quad \text{ms.} \tag{4.4}$$

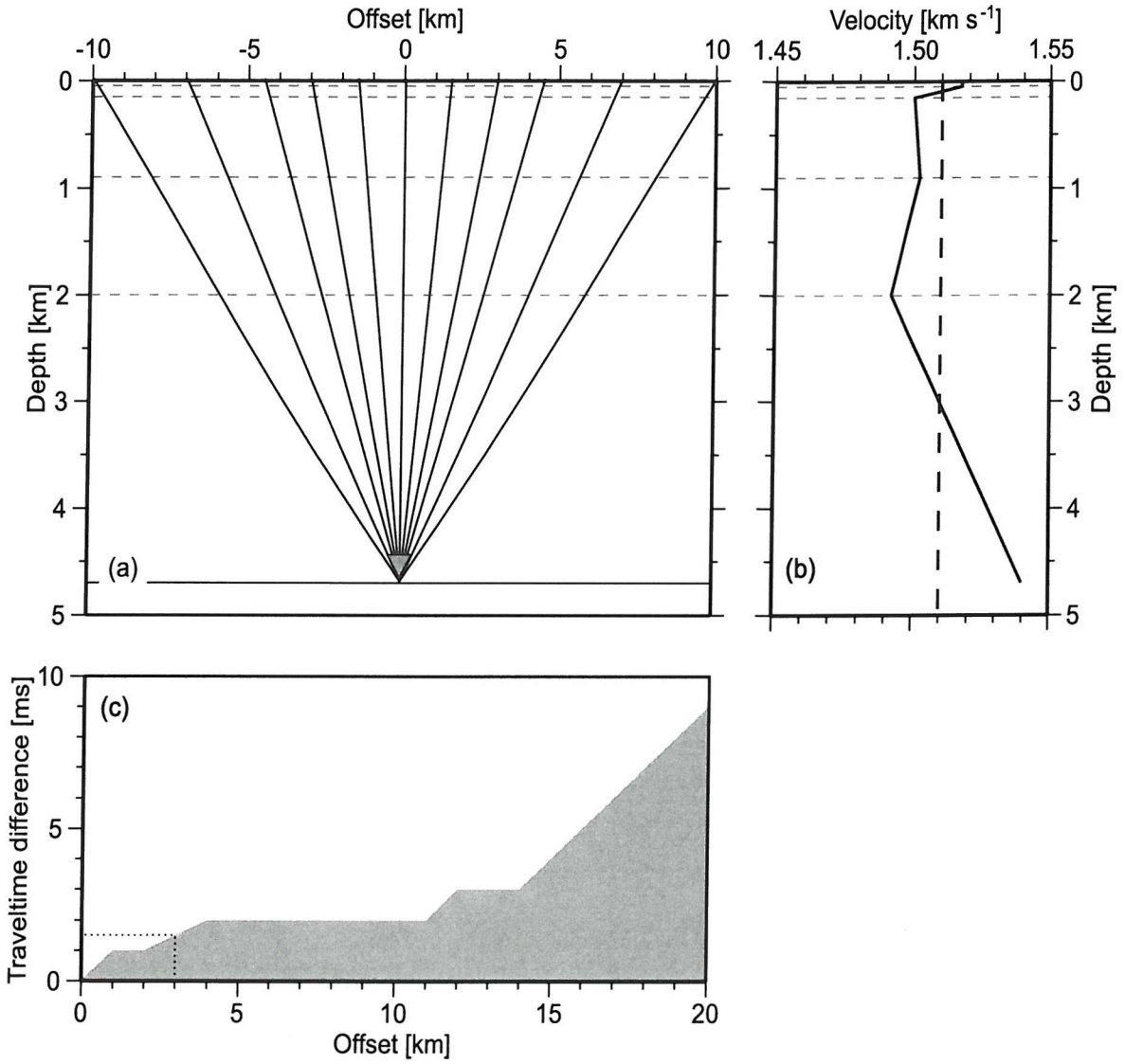

Figure 4.11: (a) Rays traced through the water column velocity structure in (b) for an ocean bottom instrument at 4.7 km depth (grey inverted triangle). This is the approximate depth of the abyssal plain at Goban Spur; seven of the nine instruments modelled in this study are in water depths of 4.5-4.8 km. Layers within the water column are indicated by dashed horizontal lines and the seabed by a solid line. (b) The water column velocity structure is taken from the NODC database for the Goban Spur region during September-October. XBT readings were made to ground-truth the database, to a maximum depth of 1.87 km. A constant water velocity of 1.51 km s^{-1} is shown by the vertical dashed line and underestimates velocities in some parts while over estimating others. (c) The traveltime misfit due to assuming a constant water velocity of 1.51 km s^{-1} compared to the observed velocity structure is <3 ms for offsets <12 km.

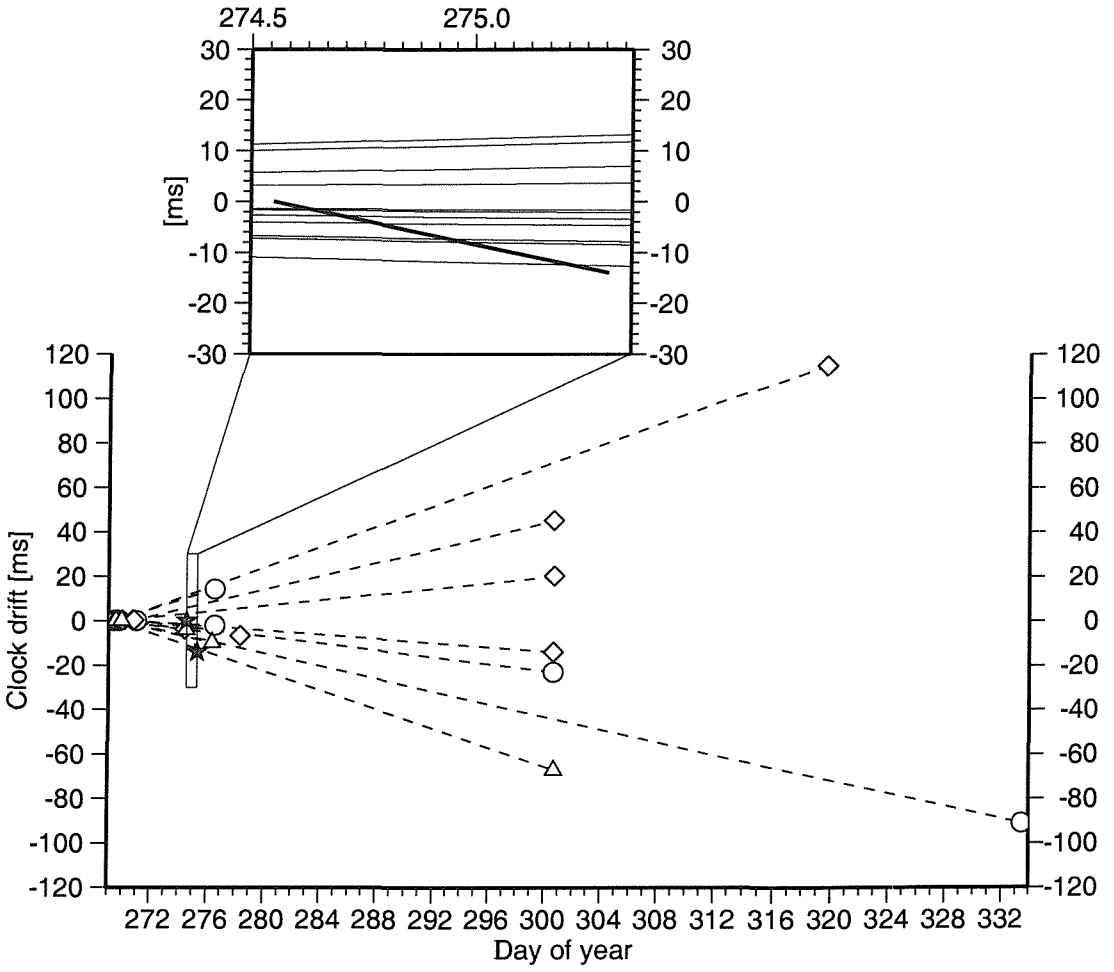

Figure 4.12: The internal clock drift for the ocean bottom instruments (dashed lines) and gun trigger (solid line) during this study. Start and end drift points are marked by according to instrument package by diamonds (OBS), triangles (OBH), circles (DPG) and grey stars (gun trigger). The shooting duration is enlarged with tick marks every hour and clock drift plotted in detail (instruments are solid lines, the trigger in bold); clock drift is within ±12 ms for all instruments during this period.

4.2.3 Filtering

Each OBH is designed to record seismic frequencies in the range 3-100 Hz (DPG instruments can operate in an expanded range of 0.1 Hz to 4.5 kHz (Bialas and Flueh, 1999)). With a sampling frequency of 10 ms (Table 4.2) this equates to a Nyquist frequency of 50 Hz; frequencies above this limit are aliased and removed from the dataset during recording. Figure 4.13*a* shows an unfiltered example record from instrument 11 which is observed to contain frequencies of 1-50 Hz (Figure 4.13*b*); the peak in energy at low frequencies (1-5 Hz), corresponding to a period of 0.2-1 s, is most probably low frequency wave noise

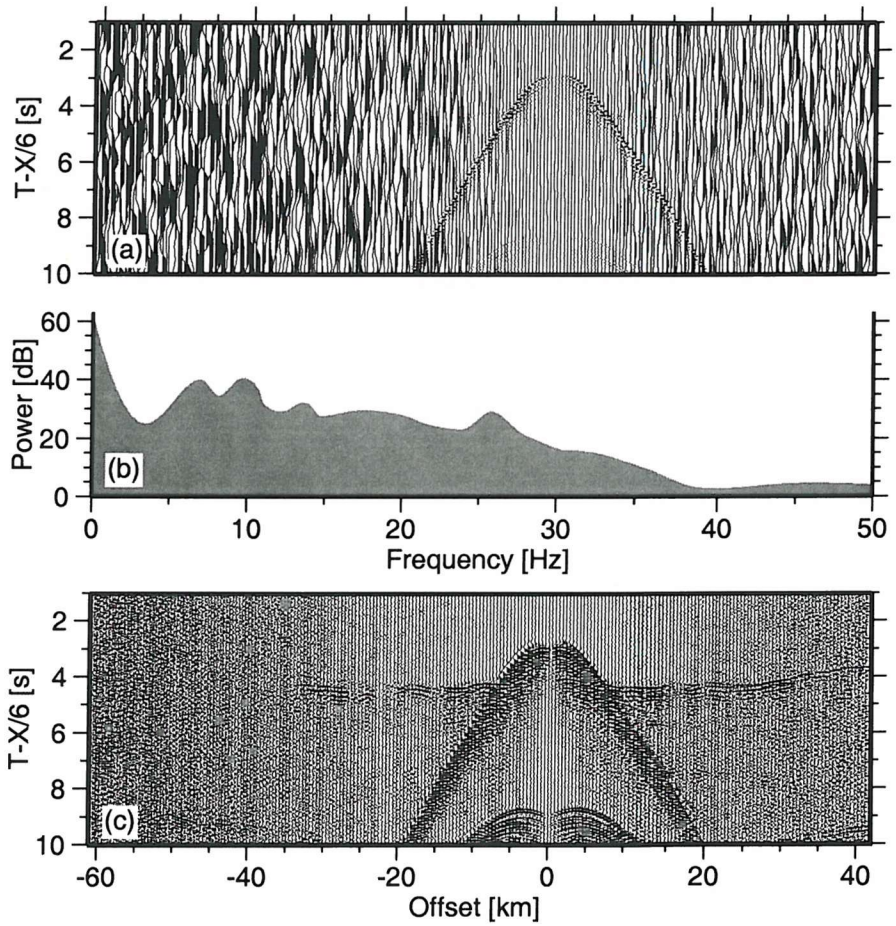

Figure 4.13: (a) Unfiltered data record for instrument 11. (b) Frequency content for instrument record shown in (a). See text for a discussion of the frequency content. (c) Instrument 11 with the final bandpass filter applied (3-5-15-25 Hz) allows arrivals to be identified to ~50 km offset.

(Webb, 2002). Energy at high frequencies is likely related to short period waves and reverberating energy within the water column. At abyssal water depths the instruments are shielded from wind-induced high frequency wave noise, but stormy sea conditions during shooting input greater amounts of wave energy and probably disrupted the oceanic layering to increase noise levels observed at the instrument. Figure 4.13*c* shows instrument 11 with the best bandpass filter applied: arrivals can now be observed out to ~50 km offset.

Filters were tested at a series of frequency bands (e.g., Figure 4.14); low frequencies allow arrivals to be observed at greater offsets with a lower resolution (longer period), but high frequencies introduce noise from non-seismic sources. The final bandpass filter was designed by visual inspection of the resultant section and chosen to have frequency bounds of 3-5-15-23 Hz (Figure 4.13*b*).

4.3 Sonobuoy processing

Digitally recorded in SEG-D format, the sonobuoy records were converted to SEG-Y, had offsets written into the trace headers and a static correction applied. The direct water wave was picked with a zero phase bandpass filter applied and interpolated and/or extrapolated from pick locations. The zero phase filter added a delay to the first break which varied between +10–20 ms. A time correction was applied to the picks to compensate for this filter effect and the gun trigger delay of 48 ms (Equation 4.5). This correction ($t_{correction}$) is negative and must be subtracted from the picked traveltimes.

$$t_{correction} = -\left(t_{filter} + t_{trigger}\right) \quad \text{ms.} \tag{4.5}$$

Source-receiver offset was calculated from the corrected traveltime according to Equation 4.6, assuming a water velocity of 1.51 km s^{-1} and correcting for the disparity in depth between the seismic array (13 m) and the sonobuoy hydrophone (123 m) (Figure 4.15).

$$\text{offset} = \sqrt{(t_{corrected}\ [\text{s}] \times 1510\ [\text{m s}^{-1}])^2 - 110^2\ [\text{m}]} \quad \text{m.} \tag{4.6}$$

Static corrections (Equation 4.7) were applied to the seismic data to correct to the sea surface datum, correcting for gun and hydrophone depths ($t_{surfacedatum} = +91$ ms) and for the trigger delay.

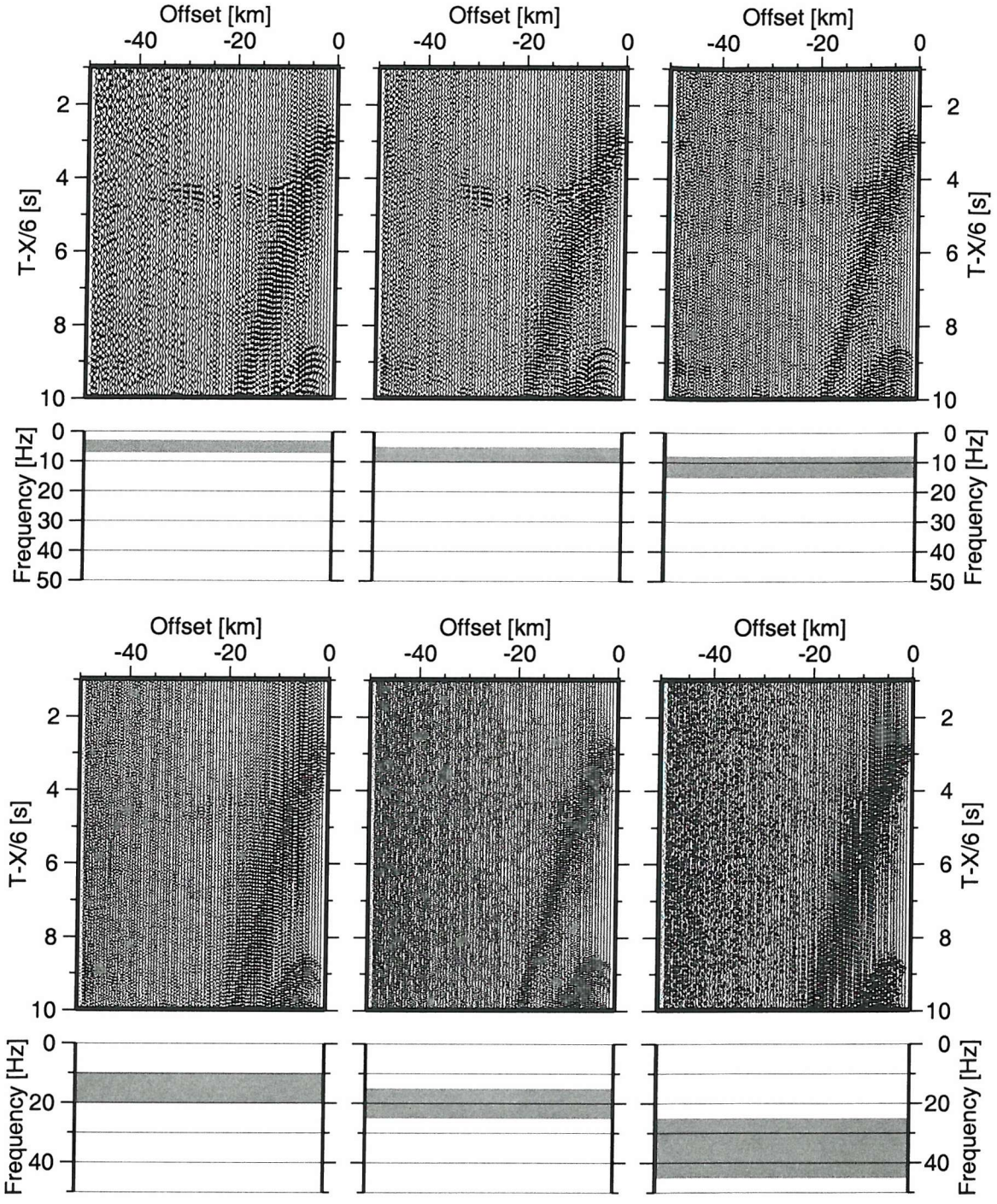

Figure 4.14: Test filter panels for OBH 11. Bandpass filter frequency ranges are shown beneath each section. Low frequencies <5 Hz allow signals to be observed at far offsets, but with a lower resolution. Arrivals are difficult to identify at frequencies >30 Hz where high frequency noise is introduced.

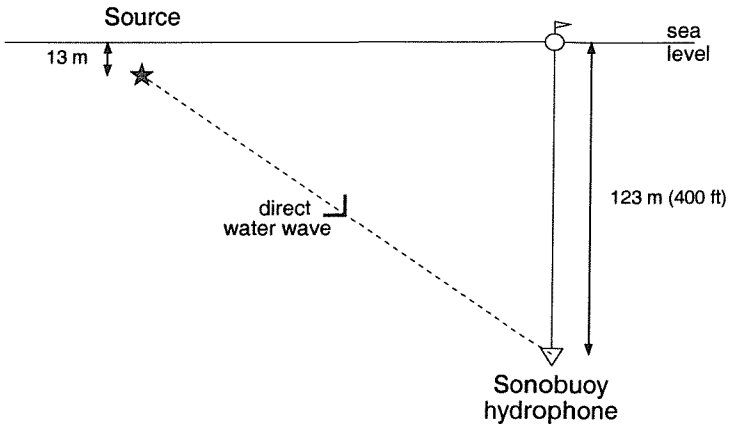

Figure 4.15: Geometry for the water wave received at the sonobuoy hydrophone. A static correction is made to correct the source and receiver depths to the sea surface datum.

$$t_{static} = +t_{surfacedatum} - t_{trigger} \quad \text{ms.} \tag{4.7}$$

Sonobuoys are deployed and persist within the surface layer of the ocean where they experience wind and wave effects which cause the instrument to drift during the experiment. This drift results in a difference between the offset calculated from the water wave (actual ship–instrument distance) and the offset calculated from the ship–deployment location distance. If the traveltime error due to this drift $\ll$ picking uncertainty, this drift can be considered insignificant.

The instrument is first projected back onto the seismic line, equating source-receiver offset with distance along the line (Figure 4.16). The difference between the deployment location and projected position, ε, is the error due to instrument drift; the traveltime error due to this drift is given by

$$tt_{error} = \frac{\varepsilon}{velocity} \quad \text{ms.} \tag{4.8}$$

Figure 4.17 shows the error due to drift during the experiment for sonobuoys 6 and 7.

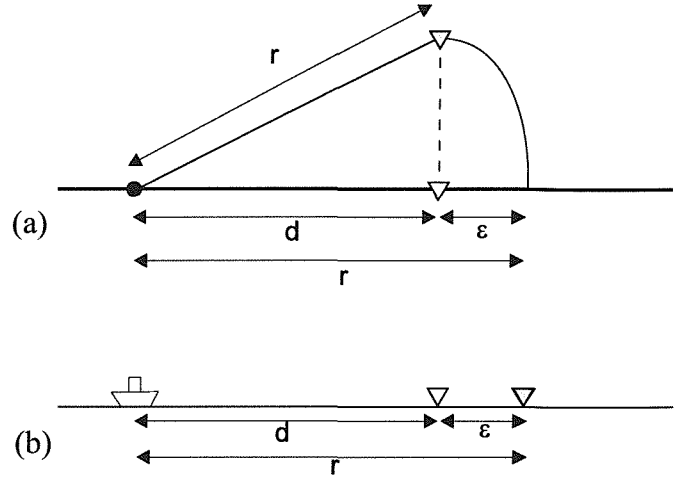

Figure 4.16: Sonobuoy drift during the survey in (a) plan view and (b) cross-section. The black circle is the ship location, grey inverted triangle the instrument location and white inverted triangle the instrument deployment location. Distance along the line is assumed to equal the shot–deployment distance (d), but the instrument drift causes a error in the instrument location (ε = r - d) when relocated back onto the line.

Drifts of up to 1.8 km are observed after 3 hours (180 shots at a shot interval of ~60 s), corresponding to traveltime errors of up to ~300 ms. By relocating the sonobuoys every 40 shots this error can be reduced to $\leq$300 m, a traveltime error less than the picking uncertainty of 50 ms (Figure 4.17). A velocity of 4 km s^{-1} is assumed, valid for crustal phases observed at a minimum offset of ~5 km. At greater offsets the velocity increases and the corresponding traveltime error due to instrument drift becomes smaller.

4.4 Existing OBH data

The CD-124 experiment provides detailed instrument coverage over the abyssal plain, but in order to produce a transect extending seaward from continental crust, instruments from the Horsefield et al. (1994) experiment were incorporated into this modelling procedure. Horsefield et al. (1994) instruments 5001 and 2016 were digital ocean bottom seismographs (DOBS) from the Institute of Oceanographic Sciences Deacon Laboratory (now part of Southampton Oceanography Centre) and were fitted with a hydrophone and three-component geophone (Table 4.2) and located at model distances of 115.359 and 127.993 km, immediately seaward of the continental slope and over the basalt body. A sampling interval of 13.333 ms corresponds to a Nyquist frequency of 37.5 Hz for these

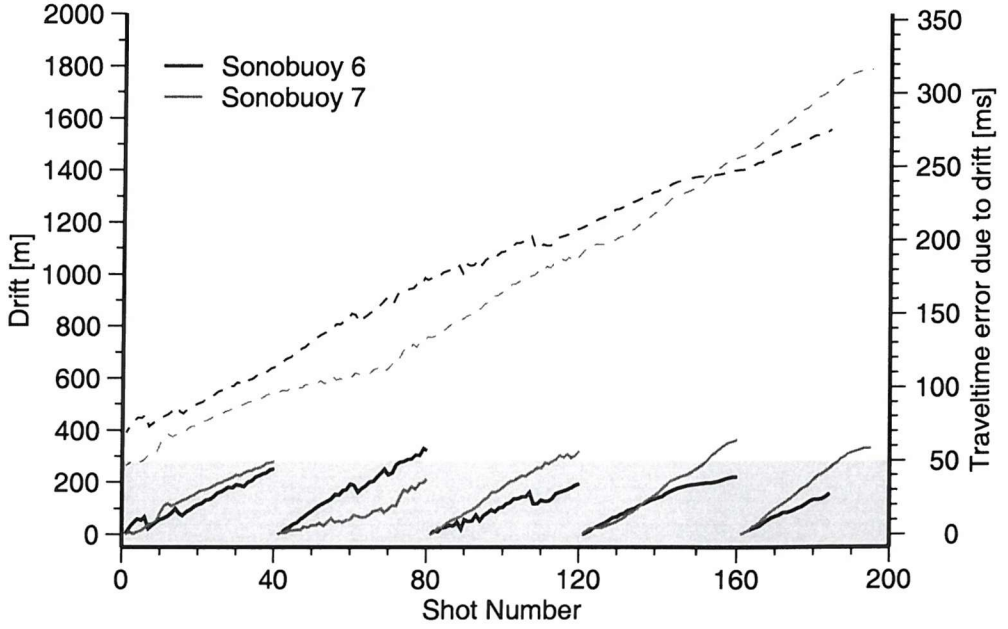

Figure 4.17: Error due to sonobuoy drift during the experiment. A crustal velocity of 4 km s^{-1} is assumed for all traveltime error calculations, which can be considered a maximum error: higher velocities at greater offsets reduce the corresponding traveltime error. Dashed lines show the error before relocation, solid lines after relocation every 40 shots, for sonobuoys 6 (black) and 7 (grey). The shaded region indicates an error <50 ms, the approximate picking error for these instruments. The traveltime error due to sonobuoy drift after relocation is $\leq$ the picking error.

datasets. The source for this experiment was a 8000 in^3 array (eight 1000 in^3 airguns) fired every 120 s giving an approximate shot interval of 300 m.

The vertical geophone on both instruments recorded clear arrivals out to ~50 km (Figures 7, 8: Horsefield et al., 1994); the hydrophone channel also recorded useful data out to ~50 km offset (Figure 4.18), including converted S-waves, and was used for consistency with other instruments modelled in this study.

4.5 Data Quality

All channels recorded data, however the geophone channels exhibit a much lower signal to noise ratio (SNR) than the hydrophone channel (e.g., Figure 4.19) hence data from the hydrophone channel was used in this thesis. Low SNR on the geophone sensor may be

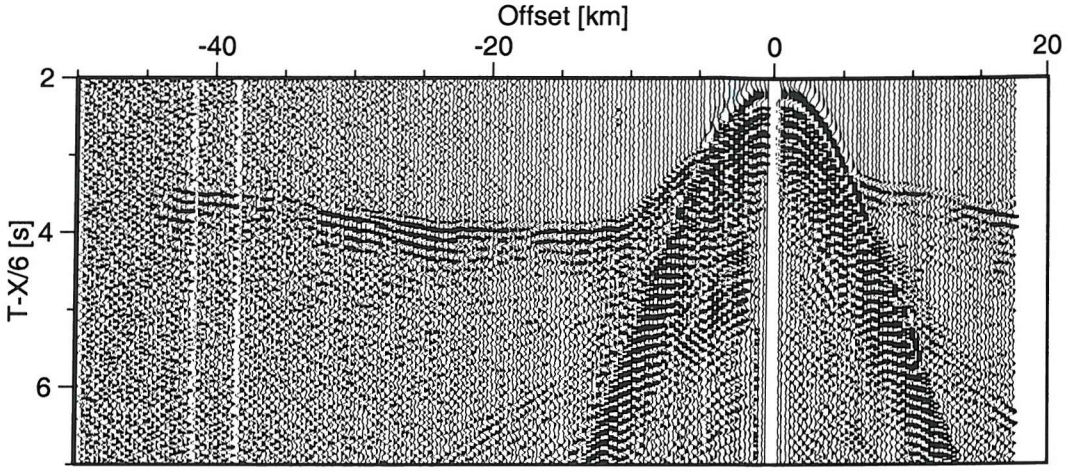

Figure 4.18: Example instrument 2016 from the Horsefield et al. (1994) experiment. The hydrophone channel is shown here and used in this study. A 2-4-15-20 Hz bandpass filter and data reduction at 6 km s^{-1} have been applied. These instruments (5001 and 2016) have a lower resolution than the CD-124 instruments due to a doubled shot interval (~300 m). Arrivals can be identified to ~50 km offset.

due to poor coupling between the geophone and seabed or, as this was the first deployment with this instrument and recorder combination, the gains may have been incorrectly set prior to deployment. The second possibility seems more likely as the poor SNR is repeated across all geophone sensors and there is no reason to expect poor coupling in the soft sediment at Goban Spur: geophones in the Horsefield et al. (1994) experiment show clear signals. Some arrivals are visible on the vertical geophone (e.g., Figure 4.19) however this is often limited to the direct arrival only and is always much lower quality than the comparable hydrophone channel.

The DPG is a broadband hydrophone package suitable for recording teleseismic arrivals as well as controlled source seismic data. No difference in recording quality is expected between OBH and DPG instruments for controlled source seismic frequencies, and none is seen (Figure 4.20). Both OBH and DPG sensors recorded arrivals out to ~70 km offset e.g., DPG 15 (Figure 4.20*a*); OBH 9 (Figure 4.20*b*), largely limited by the length of the seismic line shot. Data are recorded up to 135 km offset on OBH 6, however picked arrivals are restricted to ~80 km (Figure 4.20*c*). No arrivals can be identified on DPG 5 (Figure 4.20*d*) or instruments more distant from the shooting profile so instruments 5 to 1, with a minimum offset >50 km, are not included within this modelling.

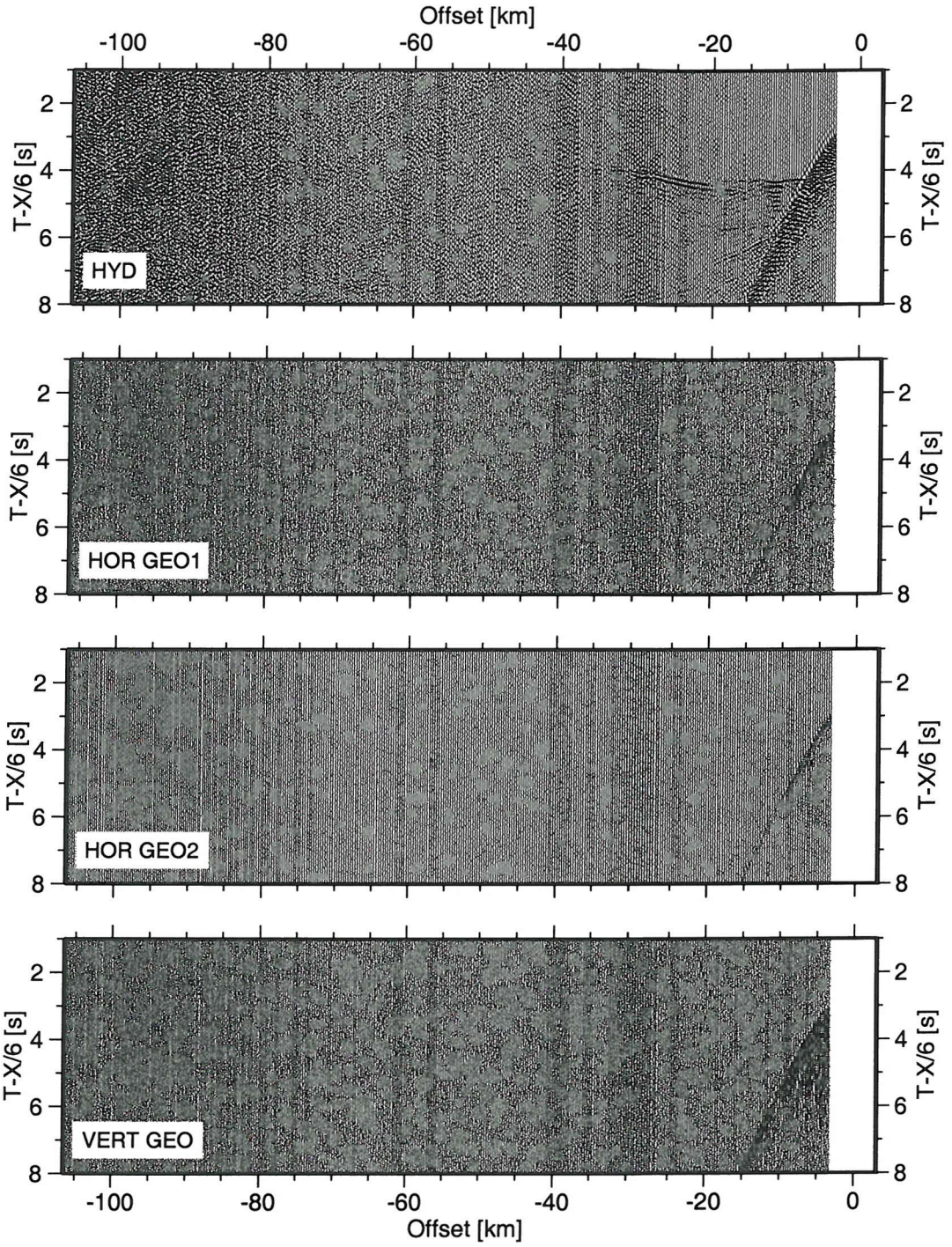

Figure 4.19: Hydrophone and geophone channels of instrument 8. First arrivals can be identified to >60 km offset on the hydrophone channel but only the direct arrival can be seen on the vertical geophone. Horizontal geophone records have even poorer signal to noise ratios. This poor recording may be caused by incorrectly set gains for this instrument-recorder combination; three component geophones successfully recorded arrivals from a nearby location in an earlier study (Horsefield et al., 1994).

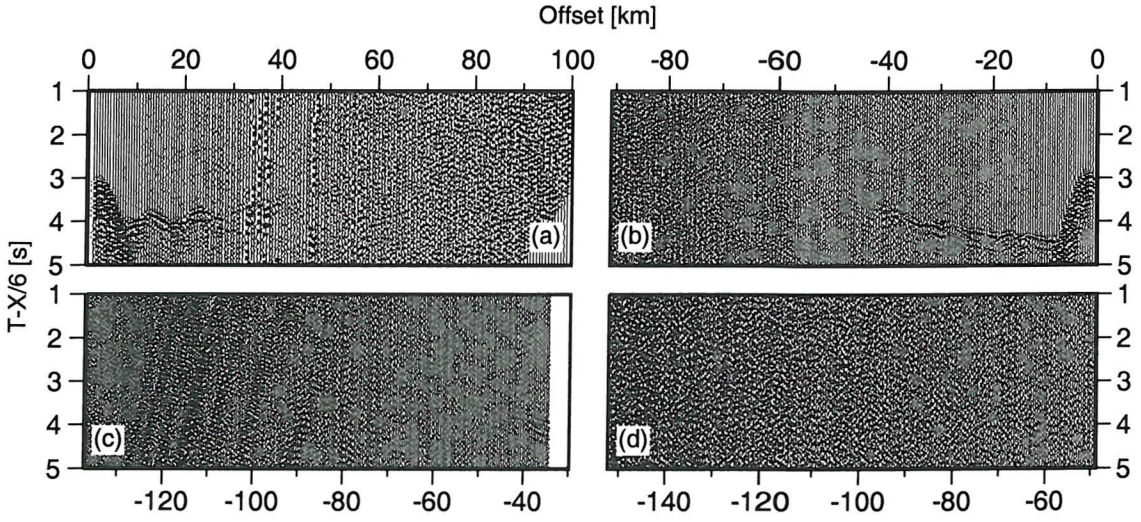

Figure 4.20: Instrument records from (a) DPG 15, (b) OBH 9, (c) OBH 6 and (d) DPG 5. Data quality is good on both hydrophone and DPG sensors. Arrivals can be identified on instruments 15 to 6, the minimum offset for instrument 5 (~50 km) coincides with low amplitude arrivals on other instruments which makes them hard to identify. Instruments 5 to 1, with minimum offsets >50 km, are not incorporated within the modelling.

A number of near normal incidence reflections can be observed on these data at offsets ±6 km. Deeper reflections with higher apparent velocities are visible on most instrument records e.g., 28 km offset on DPG 15 (Figure 4.21).

There is a change in appearance of crustal arrivals, visible either side of instrument 11 located at 60 km (Figure 4.22), from clearly separable phases defined by gradient changes at model distances <60 km, to arrivals with a continuous increase in apparent velocity with depth. These arrivals at distances >60 km appear to form a single phase but exhibit amplitude variations with offset that are diagnostic of changes in velocity gradient with depth. Amplitude variations are used to define different phases consistently during picking and for the modelling procedure.

A similar procedure was followed to define the best filter for the Horsefield et al. (1994)

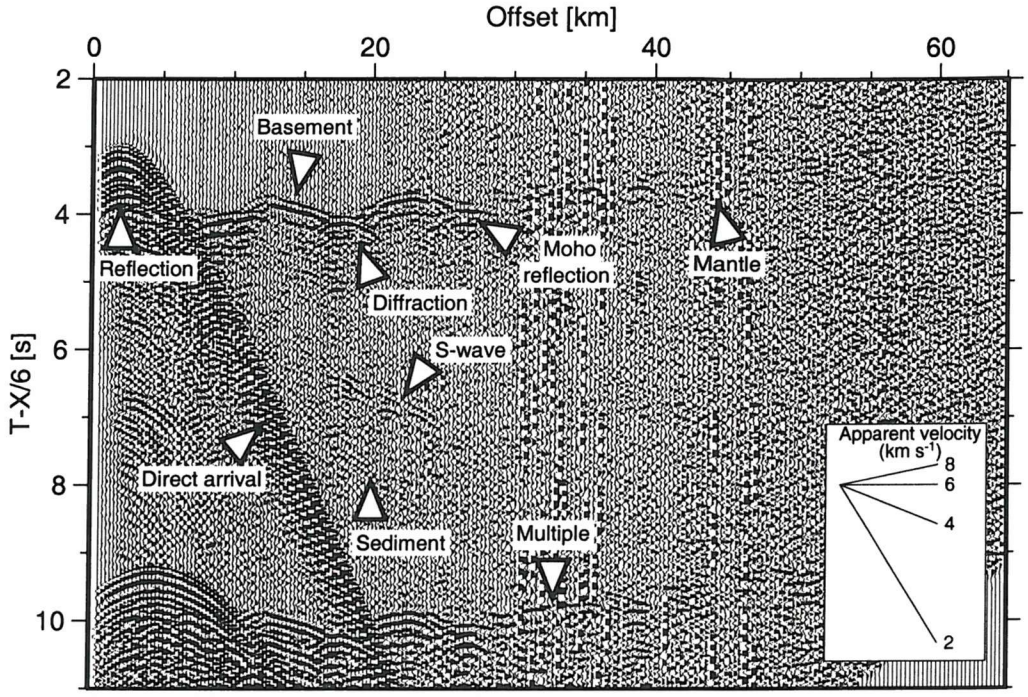

Figure 4.21: Hydrophone record section of instrument 15, located at the seaward end of the survey line. A 3-5-15-23 Hz bandpass filter and gain proportional to offset have been applied, with time reduced at 6 km s^{-1}. Only one sediment arrival is observed, due to the thin sedimentary cover at this location. Basement arrivals are generally high amplitude although basement topography in this region causes diffractions and lower amplitude arrivals to appear due to defocussing of energy through basement highs. Mantle refractions have low amplitudes and can be picked to >65 km offset.

instruments: 2016 and 5001. A bandpass filter with frequency bounds of 2-4-15-20 Hz was found to produce the best image and allow arrivals to be observed to ~50 km (Figure 4.18).

Sonobuoy data quality is generally good with arrivals visible out to ~30 km offset (Figure 4.23). As the swell picked up during shooting the sonobuoy antenna occasionally got lost in the swell at large offsets, reducing data quality. Sonobuoys are military built hardware primarily for the detection of marine acoustic signals such as submarines hence their operational frequency range is not ideal for controlled source seismology. With the application of a suitable filter it is possible to markedly improve the observed SNR; a minimum phase bandpass filter with frequency bounds of 3-5-25-35 Hz was found to result in the clearest image. High frequency wave noise prevents near offset reflections from being clearly identified within these data (Figure 4.24).

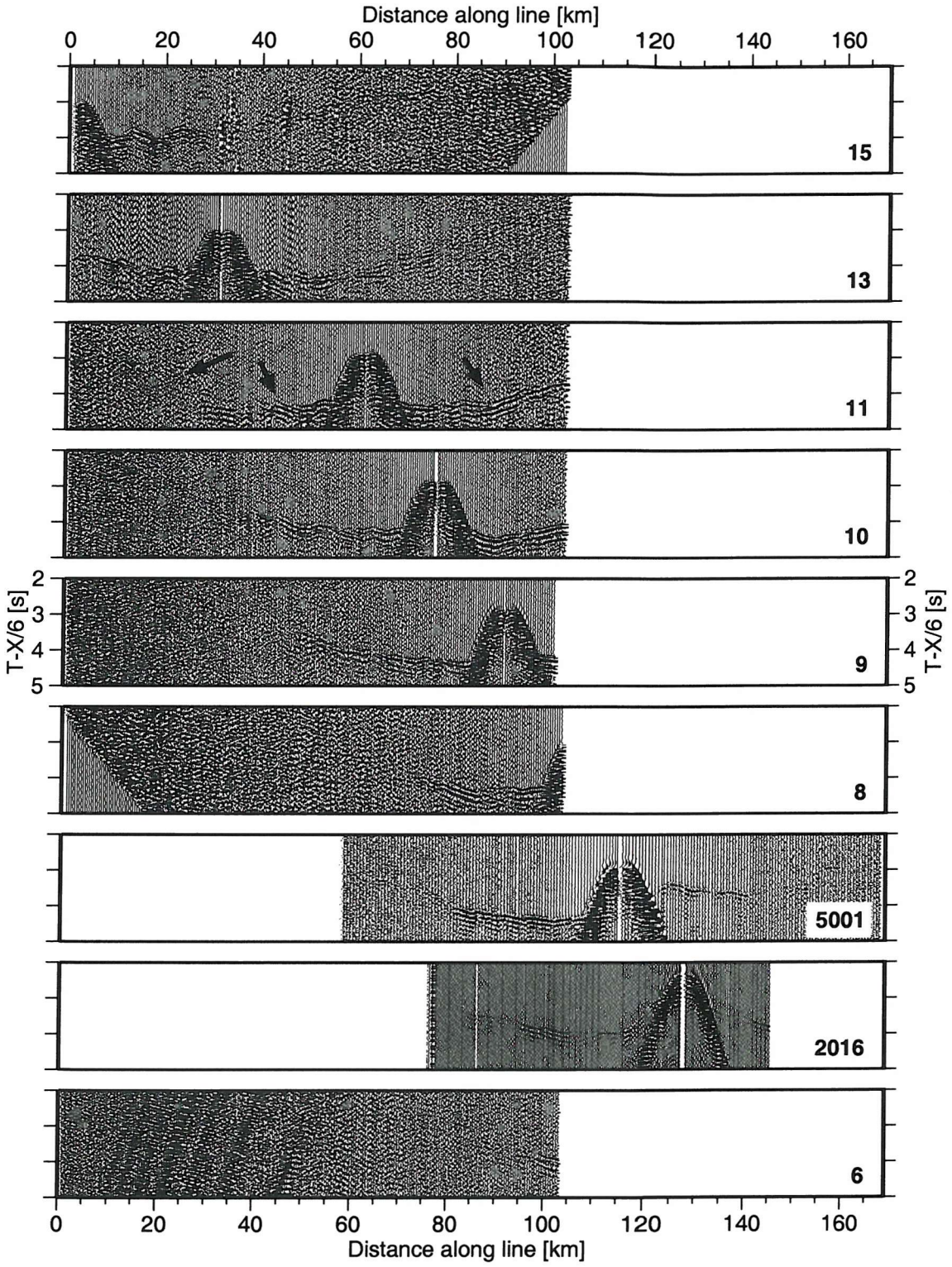

Figure 4.22: Crustal phases for all instruments positioned along the velocity model line. Note the change in appearance around 60 km, particularly clear on instrument 11, from two distinct phases at <60 km to one phase, with a more gradual increase in velocity, for >60 km as indicated by the arrows.

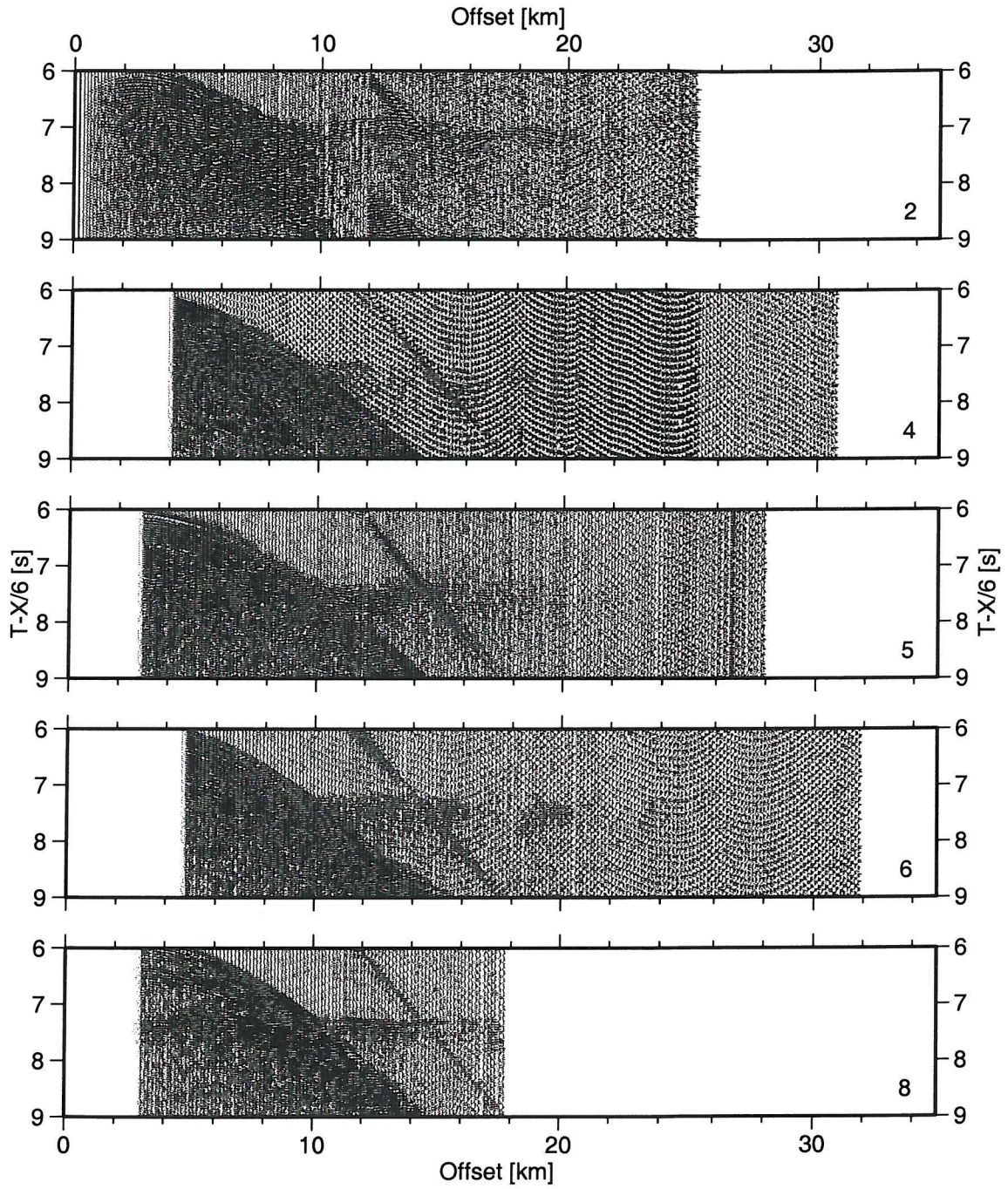

Figure 4.23: Crustal arrivals for sonobuoys 2–8. A bandpass filter with frequency bounds of 3-5-25-35 Hz and gain increasing with offset have been applied; the sections are reduced at 6 km s^{-1}. Arrivals are recorded to a maximum offset of ~25 km.

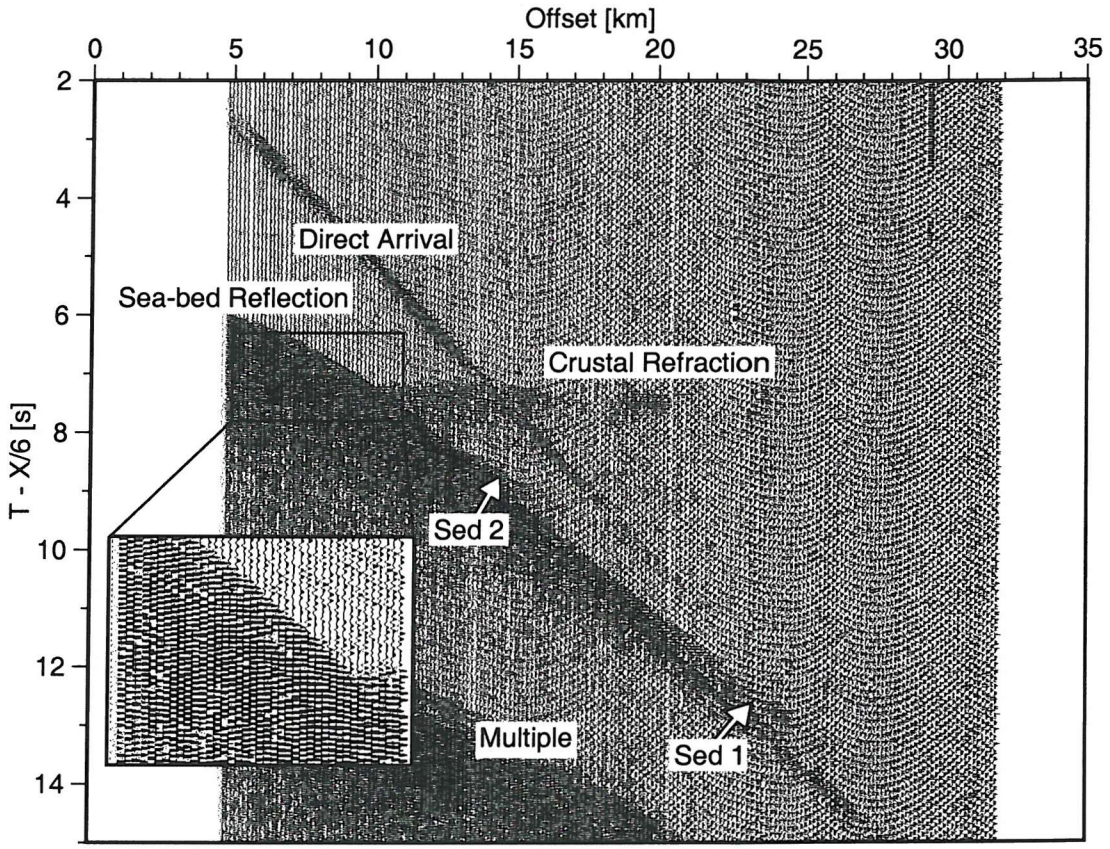

Figure 4.24: Interpretation of sonobuoy 6, located at 55 km model distance. Plotting parameters are as for Figure 4.23. Inset shows an enlargement of near-offset arrivals: crustal refractions can be identified as second arrivals but no near-offset reflections are clearly visible.

Chapter 5

Goban Spur: geophysical modelling

5.1 Wide-angle velocity modelling

The interpretation of wide-angle refraction and reflection data to construct a model of velocities within the subsurface can be carried out by ray-tracing through a predicted earth structure (velocity model) to match observed and predicted traveltimes. Inverse modelling using the *RAYINVR* package (Zelt and Smith, 1992) was carried out here and consists of two steps: the forward step, where ray-tracing is carried out and the model misfit calculated, and the inverse step, where model adjustments are made (Section 3). Inversion was attempted for both velocities and interfaces separately as part of an iterative procedure.

5.1.1 Modelling strategy

A minimum structure modelling strategy (e.g., Zelt, 1999) was designed to produce a model that contains the fewest features required to explain the observed data. Traveltime modelling provides a non-unique solution, but a minimum structure model prevents unnecessary features being introduced and the data being over interpreted. Constraints from seismic reflection profiles are incorporated into the model where the presence of structures is clearly defined e.g., the basalt body at 120 km model distance. Observed arrivals were assigned a phase, a layer where the ray turns or reflects from the base, and each layer is then modelled in turn following a 'layer stripping' approach. Progressively deeper phases are modelled while holding the overlying layers fixed until all data have been fitted. Model smoothness was allowed to decrease with depth in order to prevent lateral velocity variations within the shallow structure propagating to the predicted deeper structure. Velocities within individual layers were modelled by an iterative procedure: inversion was

carried out firstly with a fixed velocity gradient followed by an adjustment of the lower velocity nodes only and this procedure was repeated with a reduced smoothing constraint as described above. Inversion of upper velocity nodes within a layer was found to be less stable and rarely used. By this approach the best fit velocities and velocity gradient for a layer could be obtained.

5.1.2 Stopping Criteria

The normalised misfit (χ^2) is a commonly used statistical measure of observed data (t_{iobs}) fit to a predicted distribution (t_{icalc}) according to Equation 5.1 (Staples, 1997; Shearer, 1999). In the case of traveltime modelling, observed data are the picked traveltimes; the predicted distribution is calculated by ray tracing and is the predicted traveltime for each pick; the uncertainty assigned to the ith pick is given by unc_i and n is the number of successfully traced rays.

$$\chi^2 = \frac{1}{n-1} \sum_{i=1}^{n} \frac{(t_{icalc} - t_{iobs})^2}{unc_i^2} \quad . \tag{5.1}$$

A χ^2 of 1 describes a model that fits exactly to the assigned uncertainties while $\chi^2 \gg 1$ describes a poor fit to the data and $\chi^2 < 1$ that the model has been over-fit to the data. To change the recovered χ^2 value either the model or the assigned uncertainties can be adjusted; to use the normalised misfit as a measure of model fit it is important to realistically define the uncertainties assigned to each phase (Section 5.1.3). Stopping criteria of χ^2=1-1.5 were desired, although geometrical and smooth model constraints prevented this misfit being reached for all phases (Section 5.1.8). Rays should be traceable to all picks (Zelt, 1999) and models which could not fulfil this constraint were discarded. Due to the ray-tracing approach used here the geometry of layer pinch-outs may restrict the arrival of rays at the surface for some offsets. Often small (<0.5 km) geometry changes would be required to enable rays to be traced and in these cases the model was considered to satisfy these data and accepted, even though rays may not reach the surface for a specific phase in the preferred model.

5.1.3 Uncertainty analysis

The modelling procedure applied here requires an uncertainty to be assigned to each traveltime pick to weight the inversion towards well constrained data and allow a statistical

calculation of the model misfit at each step. It is impractical to assign uncertainties to each pick individually within such a large data set hence generalised equations are determined for refracted arrivals according to the following assumptions and errors. The majority of data has an uncertainty <63 ms. Near-offset reflections are assigned a constant picking uncertainty of 55 ms, approximately equivalent to half a wave period for these arrivals.

Uncertainty in the instrument clock

Drift of the internal clock during the deployment period is corrected for during preliminary processing by assuming linear drift between deployment and recovery (Section 4.2.2). There is an inherent timing uncertainty present due to the digitising process, given by the sampling interval of these instruments so a minimum uncertainty of 10 ms was assumed. Instruments 15, 13 and 9 could not be corrected for internal clock drift, but as clock drift is consistently within ±12 ms during the shooting period (Figure 4.12) this is incorporated into the uncertainty assigned to picks for these instruments.

Uncertainty in bathymetry and water velocity

Bathymetric uncertainty depends on the error due to assuming a constant water velocity of 1.51 km s^{-1} as well as the assumed shot depth (13±1 m) and instrument height above the sea-floor (1 m). Water column velocities were derived from XBT temperature profiles and consistent with the assumed seasonal velocity-depth profiles. It was shown earlier (Section 4.2.1) that the uncertainty due to assuming a constant water velocity structure is <3 ms for abyssal water depths (Figure 4.11).

Uncertainty in shot location

The modelling technique assumes that the positions of the shot and receiver within the model are well known. Instrument locations are constrained by analysis of the direct arrival at near offsets, with the shot location assumed to be in the centre of the airgun array (Figure 4.4), ~36 m behind the ship's stern. The ship to airgun array distance is known to within ±0.5 m, much smaller than the accuracy of the GPS system which is taken to be 10 m. A 10 m error in horizontal positioning results in a traveltime uncertainty of 7 ms through the water column which, assuming horizontal layering of structures, becomes less significant (~1 ms) for crustal phases at increasing offset as raypaths through the water

column become near-vertical and seismic energy travels deeper, through higher velocity material, reducing the traveltime error due to uncertainty in horizontal (shot) positioning (e.g., Equation 5.2).

Uncertainty in instrument location

After deployment at the sea surface the OBH makes a controlled descent to the seabed, during which ocean currents cause the instrument to drift from the deployment location. Instrument drift is corrected for by instrument relocation according to near-offset observations of the direct arrival (Section 4.2.1). Repositioning back onto the experiment line is achieved by approximating source-receiver offset to distance along the line (Figure 5.1), but the error, and traveltime uncertainties, due to this assumption must be considered (Equations 5.2 and 5.3).

$$\text{uncertainty}_{in-line} = \frac{\text{error}_{in-line}}{\text{velocity}} \quad \text{ms.} \tag{5.2}$$

$$\text{uncertainty}_{off-line} = \frac{\text{offset} - \left(\text{offset}^2 - \text{drift}^2_{off-line}\right)^{\frac{1}{2}}}{\text{velocity}} \quad \text{ms.} \tag{5.3}$$

The in-line error is dependent only on the error in positioning measurements and the accuracy of the relocation technique. The differential GPS system operated during this experiment can be considered accurate to ~10 m, more accurate than the relocation which was carried out to $\frac{1}{10}$ of a minute (~100 m at 48°30′ N). The resultant in-line traveltime uncertainty is significant at all offsets and ranges from 25 ms at 5 km offset to 12.5 ms at >30 km offset (Table 5.1).

$\text{Uncertainty}_{offline}$ is the uncertainty in in-line position due to off-line drift and is highly offset dependent; as source-receiver distance increases, the off-line drift becomes a less significant proportion of measured offset and the velocities sampled are higher, resulting in a reduced traveltime uncertainty for a given drift (Equation 5.3). Instrument 10, where off-line drift is greatest, has a maximum uncertainty of ~8 ms for offsets <5 km (Table 5.2). Considering all instruments, the traveltime uncertainty for crustal arrivals due to off-line drift is <4 ms and quickly becomes insignificant ($\ll$1 ms) at increasing offsets (Table 5.3).

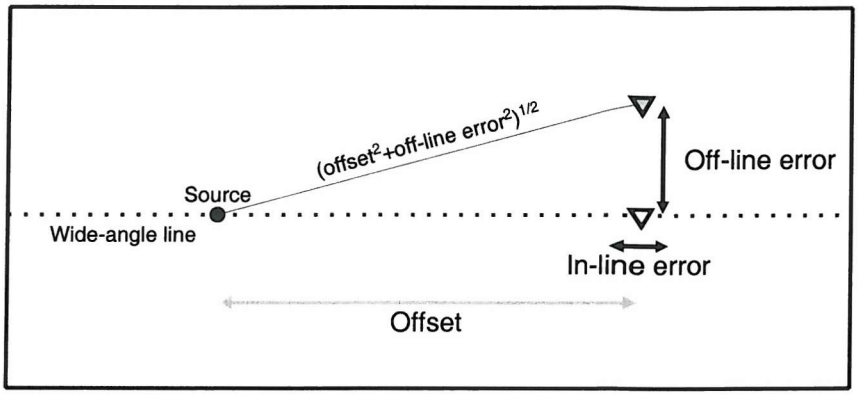

Figure 5.1: The traveltime error due to in- and off-line instrument drift. The instrument (grey triangle) is assumed to lie on the line (white triangle) and the traveltime uncertainty due to the in- and off-line errors is calculated from the source-receiver offset (Equations 5.2, 5.3).

Flat earth assumption

The curvature of the earth's surface can described by an ellipsoid and source-receiver offsets are calculated over this surface. Seismic energy travels along the shortest path between the source and receiver, resulting in an overestimation of source-receiver offset. At 48°30′ N the overestimation becomes significant at large offsets however the CD-124 dataset is recorded at offsets $\leq$100 km, which corresponds to an error of <1 m. Assuming crustal velocities of 4 km s^{-1} the travel time uncertainty due to this error is ~0.2 ms.

Table 5.1: In-line traveltime uncertainties decrease with offset as raypaths penetrate deeper and travel through higher velocity material. Velocities are estimated from the gradient of refracted arrivals on the instrument sections. In-line uncertainties range from 25-12.5 ms for crustal arrivals, but are significant at all offsets.

Offset [km]	Velocity [km s^{-1}]	uncertainty$_{in-line}$ [ms]
<5	2	50
5	4	25
10	6	16.6
30	8	12.5

Table 5.2: Traveltime uncertainty due to off-line drift for instrument 10; this instrument had the greatest off-line drift of 401 m and gives a maximum uncertainty estimate. Traveltime uncertainty decreases with offset, as the drift becomes a smaller proportion of source-receiver distance and the raypaths sample higher velocities.

Offset [km]	Velocity [km s^{-1}]	$Drift_{off-line}$ [m]	$uncertainty_{off-line}$ [ms]
<5	2	401	~8
5	4	401	4
10	6	401	1
30	8	401	$\ll$1

Table 5.3: Traveltime uncertainty due to off-line drift estimated for all instruments at 5 km offset and crustal velocities of 4 km s^{-1}. At longer offsets this uncertainty reduces further for the reasons given in Table 5.2. Off-line drift is calculated from the source-receiver offset observed at the closest pass to the instrument and ranges from 29-400 m; no shots were recorded directly over instruments 8 and 6 so they were assigned a maximum estimate of $\leq$400 m.

Instrument	Offset [km]	Velocity [km s^{-1}]	$Drift_{off-line}$ [m]	$uncertainty_{off-line}$ [ms]
15	5	4	29	0.02
13	5	4	243	1.5
11	5	4	54	0.07
10	5	4	401	4
9	5	4	153	0.6
8	5	4	$\leq$400	$\leq$4
6	5	4	$\leq$400	$\leq$4

Picking uncertainty

Picking uncertainty is a measure of the difficulty in identifying the onset of an arrival within the seismic data. The minimum uncertainty is limited by the sampling interval of these data, 10 ms, and increases with offset as the SNR decreases. At far offsets the first break of an arrival can be identified to within one wave cycle (110 ms). A linear increase in uncertainty with offset was applied, according to Equation 5.4. This is a simple scheme that can be quickly applied, but is valid as the SNR tends to decrease smoothly with offset

(Figure 4.21) and behaves consistently across all ocean bottom instruments in this survey (e.g., Figure 4.20).

$$\text{picking uncertainty} = \begin{cases} 10 + \text{offset} & \text{if offset} < 100 \text{ km} \\ 110 & \text{if offset} \geq 100 \text{ km} \end{cases} \text{ ms.} \tag{5.4}$$

There is an increased minimum picking uncertainty of 20 ms for Horsefield et al. (1994) instruments (5001 and 2016) to account for a lower SNR than the CD-124 instruments.

The picking uncertainty for sonobuoys ranges from 40 to 130 ms between 0 and 30 km offset (10 + 3×offset [ms]). The SNR is very poor at far offsets due to wave noise and the lower sensitivity of these instruments to low frequencies than the OBH.

Table 5.4: Contributing factors to traveltime uncertainty for OBHs in this study. Uncertainty in the internal clock is given for those instruments that have been corrected for clock drift as well those that were not.

Contributing factor		Uncertainty [ms]
Picking uncertainty		10-110
Instrument location:	In-line	12
	Off-line	4
Instrument clock		10/12
Flat earth assumption		0.2
Bathymetry and water velocity		<3
Shot location		1

Combination of uncertainties

The final uncertainty to be assigned to each pick is calculated by a combination of the individual uncertainty terms, summarised in Table 5.4, summed with the offset dependent picking uncertainty. The uncertainty functions are given below, separate functions are required for those OBH corrected for internal clock drift (11, 10, 8 and 6) and those for which this correction could not be made (15, 13 and 9).

For instruments 11, 10, 8 and 6:

$$\text{uncertainty} = 40 + \text{offset [km]} \quad \text{ms.} \tag{5.5}$$

For instruments 15, 13 and 9:

$$\text{uncertainty} = 42 + \text{offset [km]} \quad \text{ms.} \tag{5.6}$$

For instruments 5001 and 2016 (Horsefield et al., 1994):

$$\text{uncertainty} = 50 + \text{offset [km]} \quad \text{ms.} \tag{5.7}$$

For sonobuoys 2, 4, 5, 6 and 8:

$$\text{uncertainty} = 40 + 3 \times \text{offset [km]} \quad \text{ms.} \tag{5.8}$$

5.1.4 Model parametrisation

The wide-angle model was built of layers each with boundary and depth nodes defined across its width (Section 3.3). The layer stripping approach followed here allowed a simple model to be built, with layers extending across the full model width, and new layers were added only when a single layer cannot satisfactorily explain the lateral velocity or depth

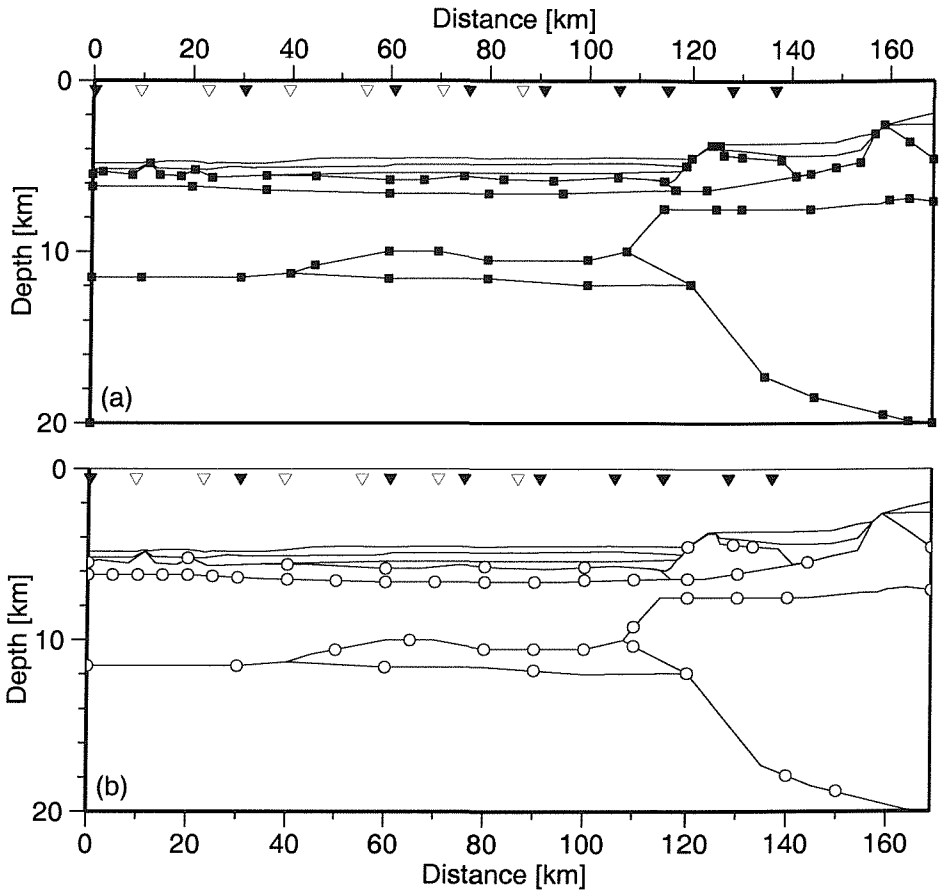

Figure 5.2: Parametrisation of basement and upper mantle layers in the final wide-angle model. (a) Depth nodes are shown as black squares for crust and mantle layers. (b) Velocity nodes (open circles) are shown for the top of each layer only: base nodes are defined at identical distances. Model layers are shown as black lines, sonobuoys as open triangles and OBHs as black triangles.

variations (e.g., the deep layer from 40 to 120 km pinches out in either direction). A thin, ~1 km, upper basement layer is required between 0 and 120 km to fit crustal arrivals with low basement velocities which cannot be explained by a single velocity gradient layer within this region. The Horsefield et al. (1994) velocity model was used to define the initial position of the continent-ocean boundary and was further adjusted to fit these data.

Boundary nodes were positioned every 2-30 km across the model (Figure 5.2*a*); the node spacing is small in regions of complex topography where constraints from multichannel seismic (e.g., the basalt body at 120 km) or from pull-up in the wide-angle data (e.g.,

ridges at 10 km) can be included and tends to increase with depth beneath top basement as boundaries become less well constrained. The Moho is defined by depth nodes every ~20 km. Initial model parametrisation followed Zelt (1999) with a node spacing of 20-30 km, approximately equal to the instrument spacing (Figure 5.2*a*); nodes were added where required to fit these data.

The spacing of velocity nodes varies widely (Figure 5.2*b*) and depends on the number of rays turning within the model layer. Seaward of the continental slope, velocity nodes are positioned widely, every 20 km, as not all instruments sample this thin layer. Upper basement beneath this has a dense node array, from 5 to 10 km, to constrain lateral velocity variations within the densely sampled basement. Deep layers have an increased node spacing, from 10 to 30 km. There are few instruments, and poor ray coverage, towards the east of the model (120-169 km), regular velocity nodes are required to give control over lateral variations in velocity gradient within the rapidly thinning layer (Figure 5.2*b*).

5.1.5 Instrument and model fit

The final P-wave velocity model has an overall RMS misfit of 80 ms between all observed and calculated traveltimes, ranging from 63 to 115 ms for individual phases, and a χ^2 of 1.414. Statistics for each model layer are shown in Table 5.5. Figure 5.3*a* shows the number of rays passing through each 1×0.5 km model cell. The absolute ray count should not be taken as the uncertainty of values within the cell being measured. Ray counts are high along narrow paths focusing towards each instrument, but the velocity constraints that can be derived from these rays is poor. Such rays tell us that the total traveltime along the ray path is consistent with these data. There is no weighting applied to distinguish between rays that turn within a layer or ones that are passing through. Figure 5.3*a*, *b* show relative model constraints very well: the model has dense ray coverage between 0 and 120 km but us much less well constrained from 140 to 169 km, where rays turn in the mantle but only pass through continental crust. The ray coverage and traveltime misfit for all ocean bottom instruments used to produce this model are shown in Figures 5.4-5.8.

5.1.6 Wide-angle velocity model

The final P-wave velocity model (Figure 5.9) can be divided into three regions on the basis of the exhibited velocities:

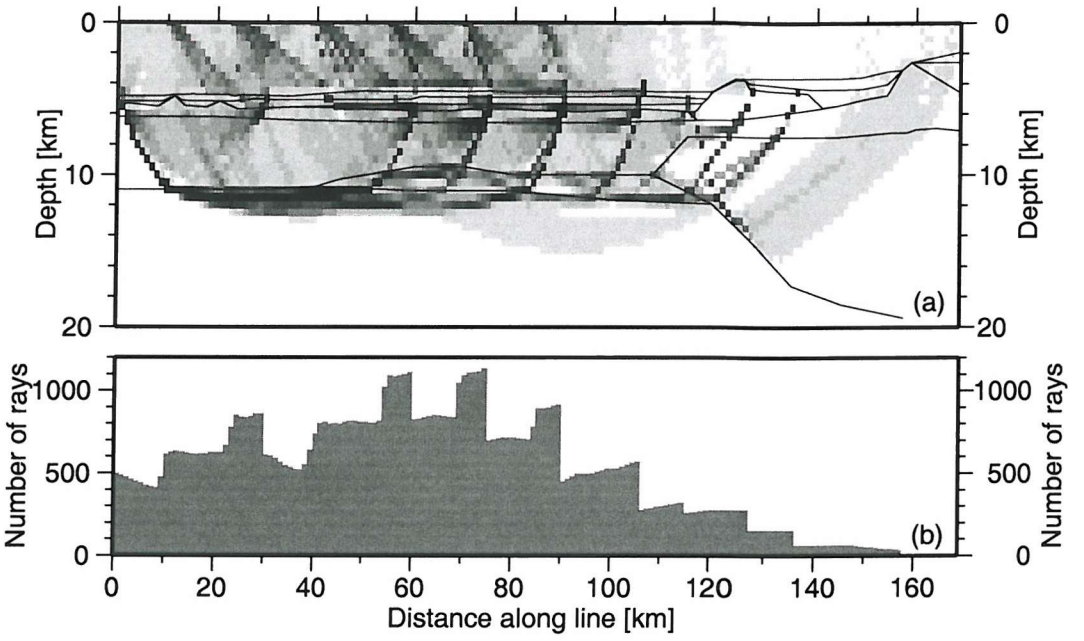

Figure 5.3: (a) Ray density through the velocity model. 1×0.5 km cell size is used. Cells are shaded based on the number of rays passing through it from white (no rays) to black for >100 rays. (b) The number of rays counted in 1 km wide bins through the velocity model. There is dense ray coverage within the intermediate zone but poor coverage through continental crust.

1. Thinned continental crust.
2. Intermediate zone with high velocity layer (7.2-7.6 km s^{-1}).
3. Intermediate zone; velocities ~7 km s^{-1} at base, but no high velocity layer.

The thinned continental crust on this profile consists of two layers broadly defining an upper (5.2-5.8 km s^{-1}) and lower continental crust (6.6-6.9 km s^{-1}); an absence of middle continental crust is due to the sparse ray coverage and the desire for a minimum structure model (Figure 5.10). A model incorporating 2 km thick middle continental crust, with velocities of 6.4-6.7 km s^{-1} is also consistent with these data (Figure 5.11) but not required by them. The modelled velocities are consistent with seismic refraction studies of full thickness continental crust in the English Channel where lower crust with a uniform velocity of 6.7 km s^{-1} extends from ~15 km depth to the Moho at ~35 km (Grandjean et al., 2001) and the two-layer reflectivity structure observed on seismic reflection line WAM (Cheadle et al., 1986; Peddy et al., 1989; Pinet et al., 1991).

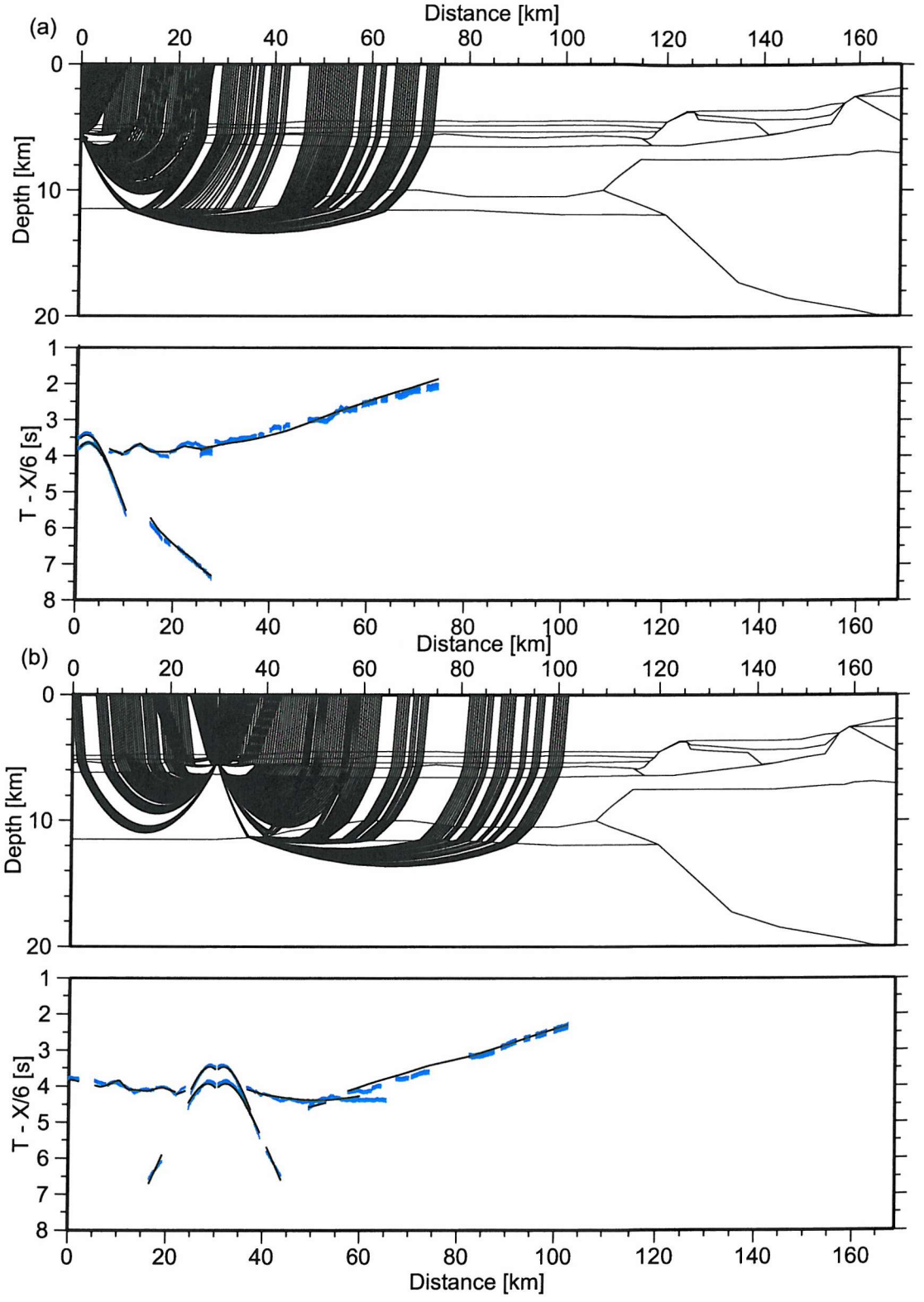

Figure 5.4: Ray coverage and arrival misfit for (a) instrument 15 and (b) instrument 13. All phases are traced, including S-waves, and every other ray is plotted. Instrument picks and calculated traveltimes are reduced at 6 km s^{-1}. The vertical height of the pick bar is equal to the uncertainty assigned to the pick.

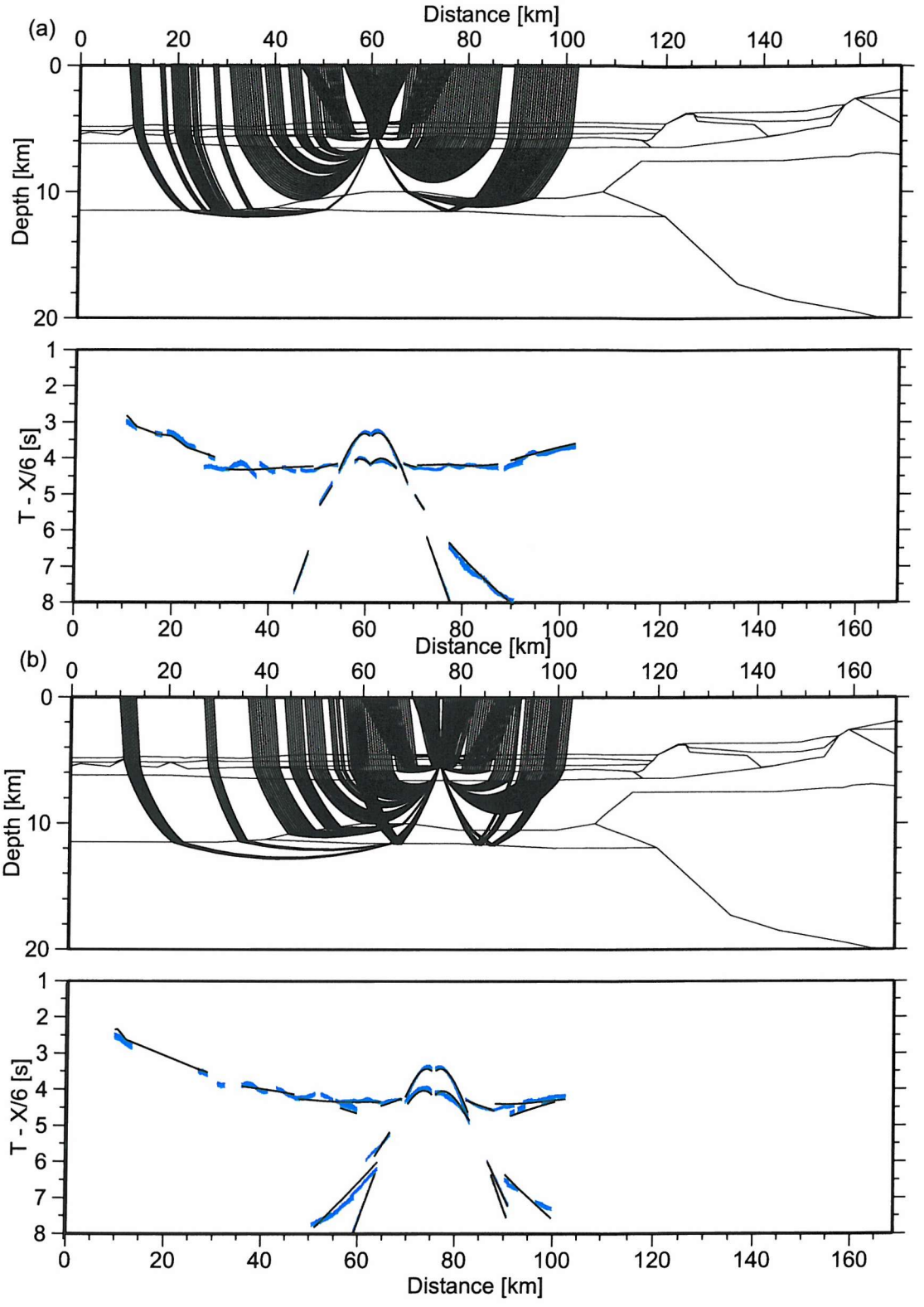

Figure 5.5: Ray coverage and arrival misfit for (a) instrument 11 and (b) instrument 10. Plotting details are as for Figure 5.4.

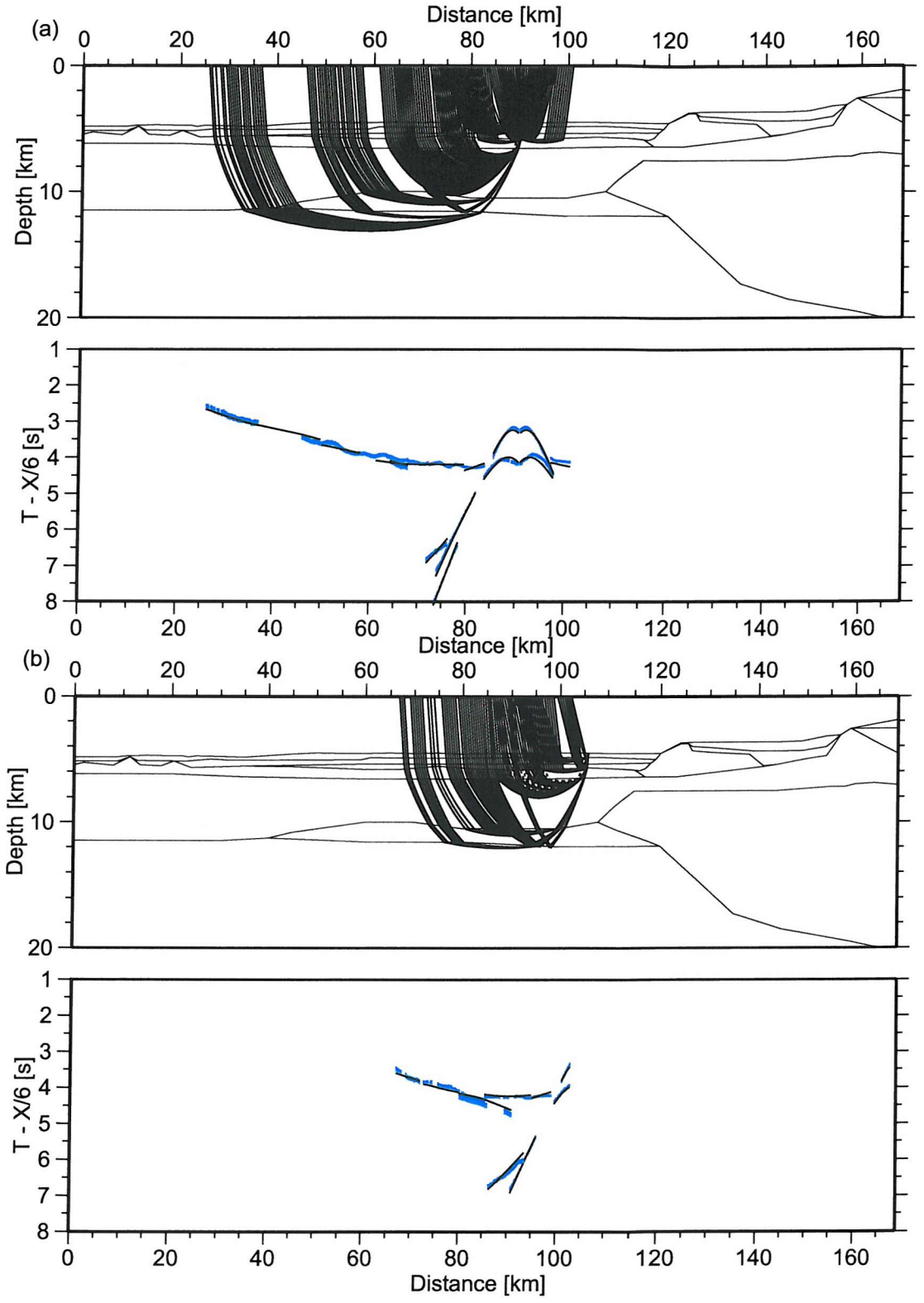

Figure 5.6: Ray coverage and arrival misfit for (a) instrument 9 and (b) instrument 8. Plotting details are as for Figure 5.4.

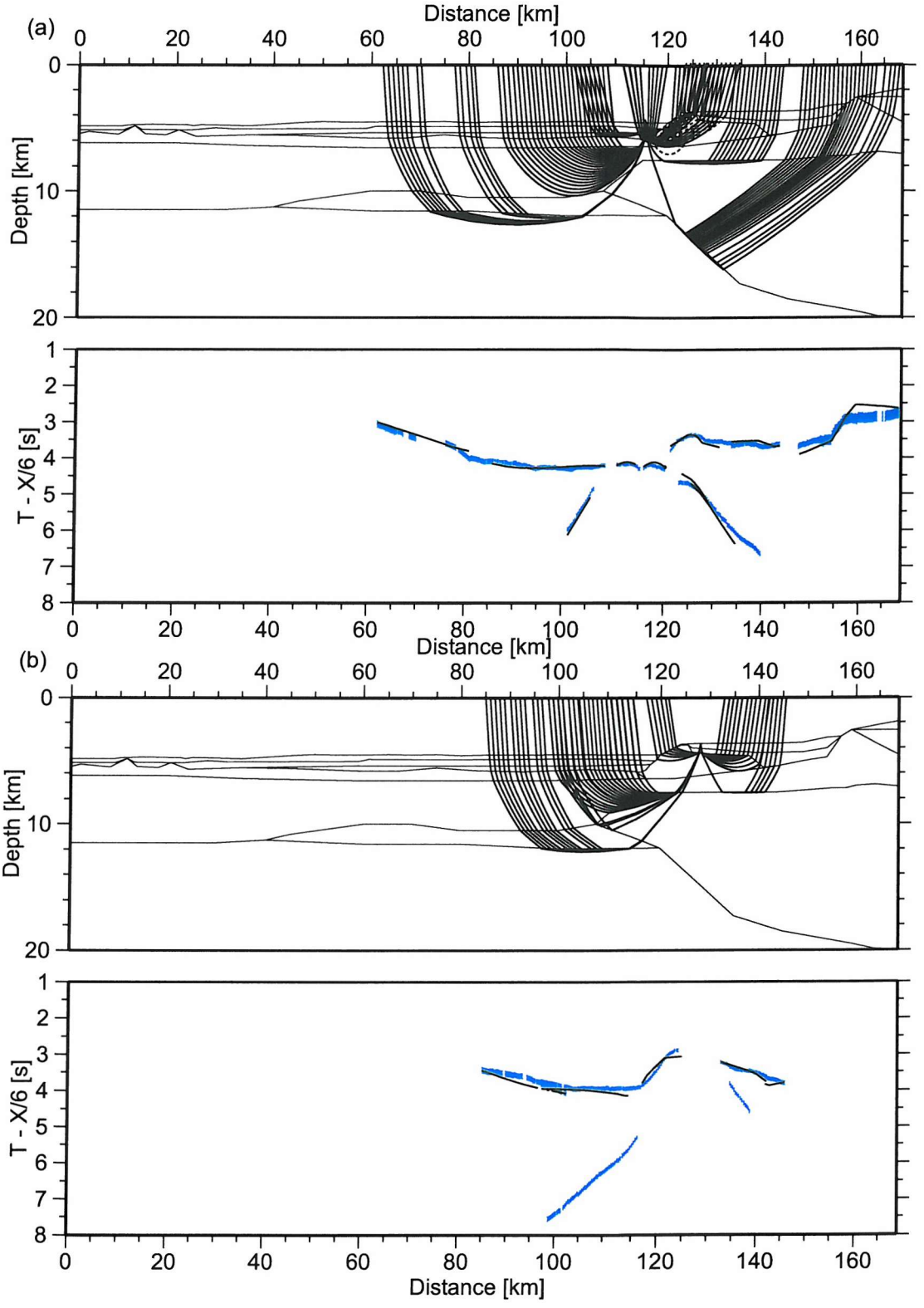

Figure 5.7: Ray coverage and arrival misfit for (a) instrument 5001 and (b) instrument 2016. Plotting details are as for Figure 5.4.

Table 5.5: Model fit to data for individual refracted and reflected phases and for the whole model. All phases are refractions unless otherwise specified.

Phase	No. picks	No. rays traced	RMS misfit [ms]	χ^2
Sediment	560	558	77	1.336
Basalt body	98	88	90	2.363
Continental crust	111	104	99	2.001
Transitional basement	1674	1512	73	1.554
High velocity layer	250	247	63	0.835
Mantle	830	822	115	1.607
Intra-sediment reflection	422	417	63	1.321
Basement reflection	419	413	66	1.287
Moho reflection	211	196	113	1.922
Overall model	5601	5365	80	1.414

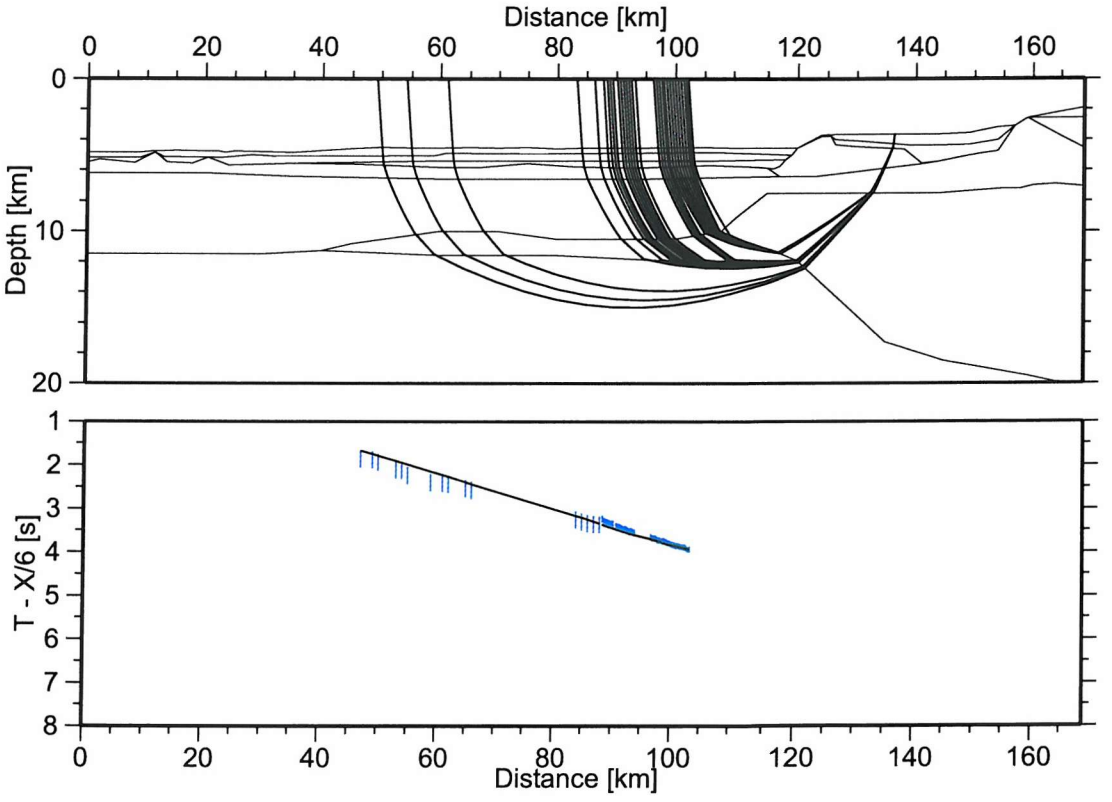

Figure 5.8: Ray coverage and arrival misfit for instrument 6. Plotting details are as for Figure 5.4.

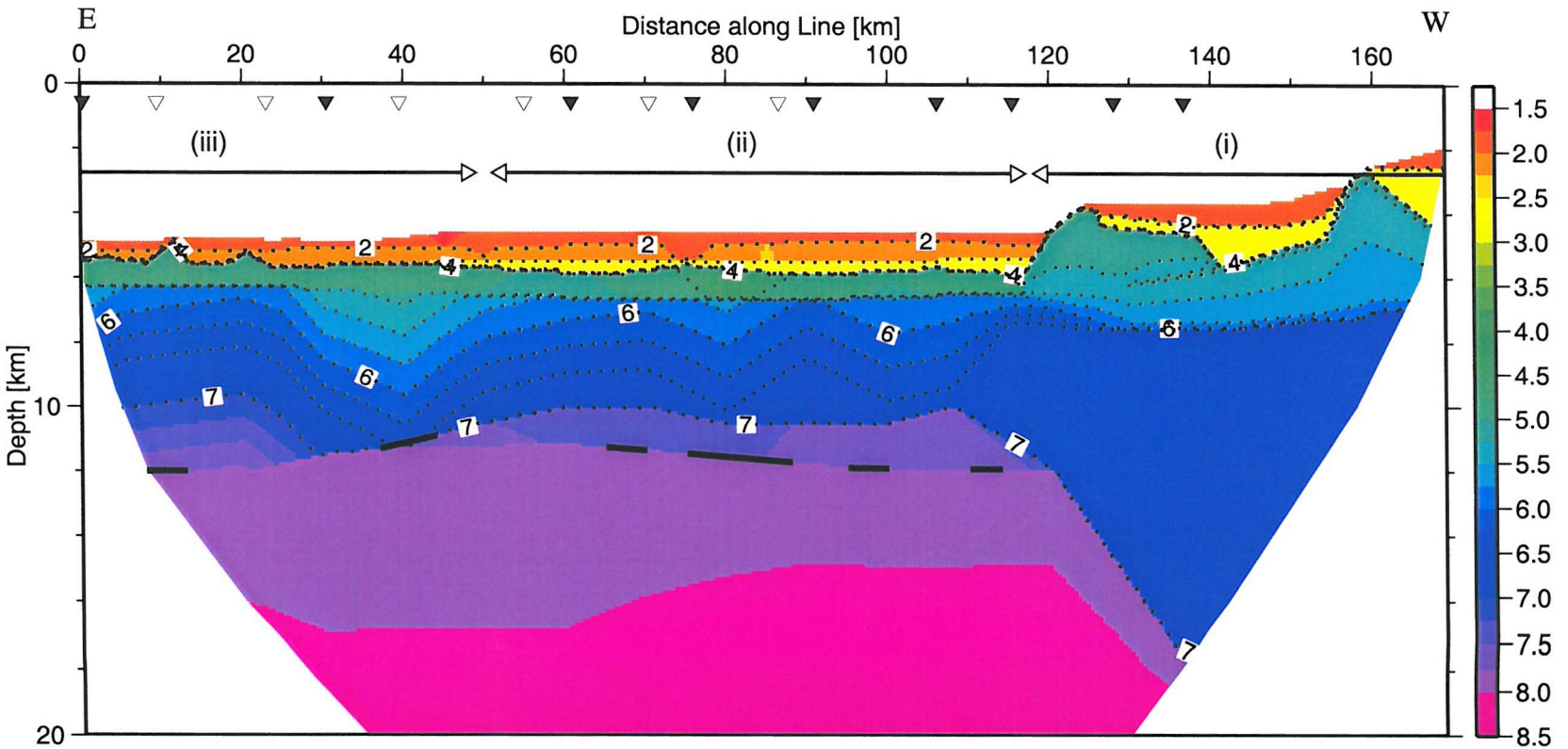

Figure 5.9: P-wave velocity model along the wide-angle line. Scale shown in km s^{-1}; velocities from 4 to 6.5 km s^{-1} are contoured every 0.25 km s^{-1}. Instrument positions are indicated by black (OBH) and white (sonobuoy) inverted triangles at the top of the model. Wide-angle Moho reflections are shown by solid black lines. The model is divided into three regions (see text) and plotted with 4x vertical exaggeration.

The lower continental crust is constrained by turning rays from instruments 5001 and 2016, while the upper layer velocity is unconstrained by turning rays but required to provide the correct traveltime delay and assumed to be laterally constant (Figure 5.10). The velocity jump between upper and lower continental crust does not produce any observable reflections but is required to fit the traveltimes through this region. PmP traveltimes from instrument 2016 (Figure 5.10) are consistent with reflections from either the base of thinned continental crust or the adjacent high velocity layer beneath region (ii). It is not clear where the greatest velocity contrast exists because the velocities at the base of thinned continental crust are poorly constrained. These arrivals are modelled as reflections from the base of the high velocity layer for consistency with modelling of PmP on other instruments. Mantle turning rays from instrument 5001 (Figure 5.10) and gravity modelling provide important constraints on the depth to continental Moho.

The basalt body (Section 1.3) can be clearly seen lying over thinned continental crust from 120-140 km model distance, with velocities of 4.95-5.35 km s^{-1}. Arrivals from this body have been interpreted as turning in a strong velocity gradient ($\sim$0.25 s^{-1}) within the basalt, but the traveltimes are also consistent with reflections from the base of this body. The second interpretation is not favoured due to the low, and in part negative, velocity contrast observed at this boundary.

The intermediate zone exhibits velocities of 4.5 km s^{-1} at top basement across its whole width. These low velocities are required to fit shallow turning rays but increase rapidly with depth to $\sim$5.8-7 km s^{-1}. A low velocity gradient of 0.1 s^{-1} is observed within the top 1 km with a higher gradient of 0.5 s^{-1} beneath. It was initially assumed that velocities were continuous with depth and the interface between low and higher basement velocities represents a change in velocity gradient, but the preferred model has a velocity jump of 0.7 km s^{-1} as such a model provides a significantly better fit to these data. Between 40 and 120 km a high velocity layer (7.2-7.6 km s^{-1}) exists $\sim$5 km into basement; the velocities and velocity gradient are well constrained by dense ray coverage throughout this zone (Figure 5.12).

Velocities $\sim$7 km s^{-1} are also predicted from 0-30 km model distance deep within basement. Turning rays here have a higher amplitude, comparable to the shallower basement refractions and in contrast to the low amplitudes generated through the high velocity layer (Figure 5.13). This region is sampled by rays from two instruments, 15 and 13, but not well sampled below $\sim$10 km depth (Figure 5.14). The high velocities are unconstrained

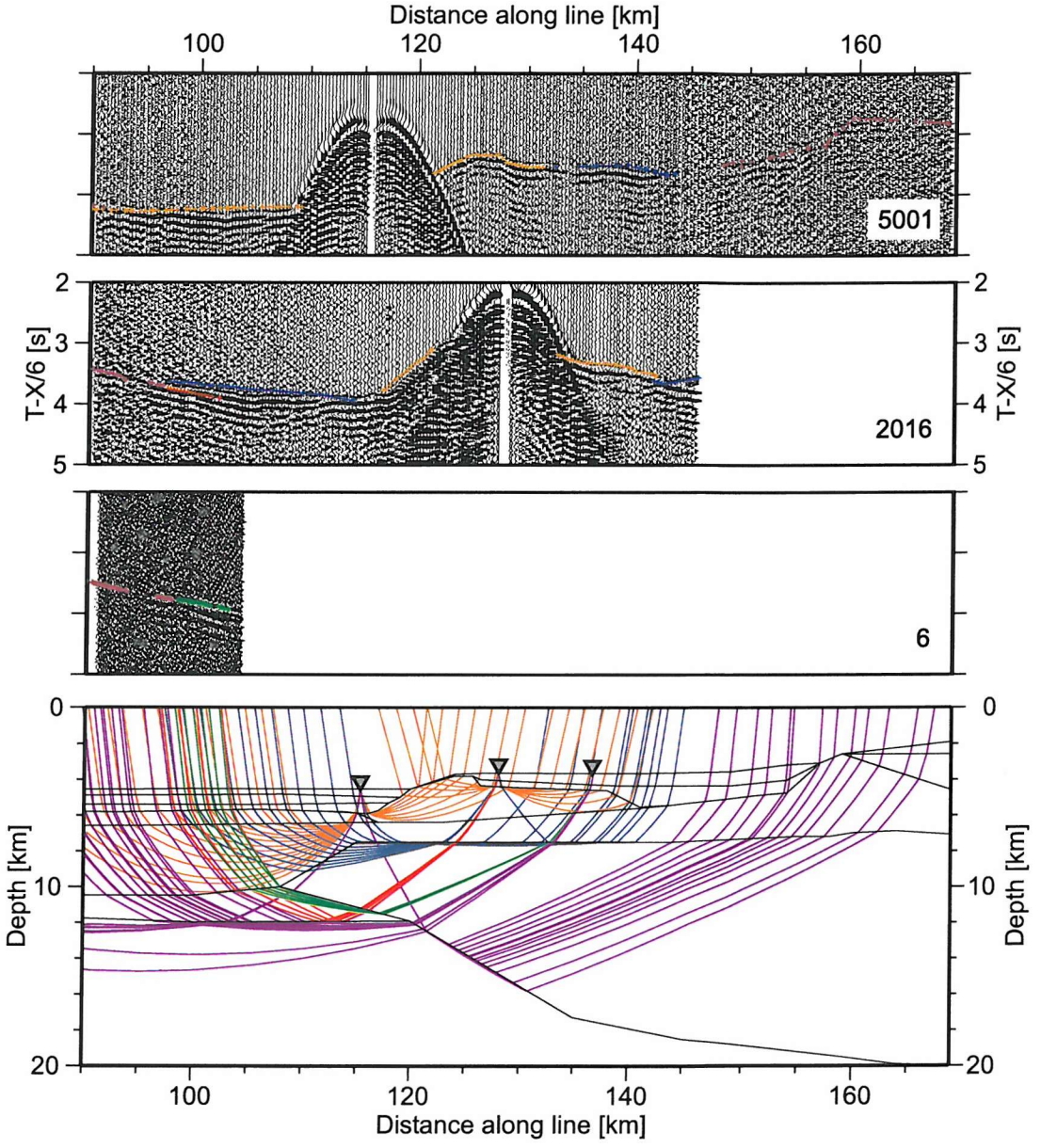

Figure 5.10: Ray coverage from model distance 90-169 km. Rays are shown from instruments 5001, 2016 and 6 (inverted triangles), sampling the basaltic body and upper intermediate crust (orange), lower continental crust (blue), high velocity lower crust (green) and mantle (purple). Deep reflections (red) are consistent with traveltimes of arrivals from either the base of thinned continental crust or the base of the 7.2-7.6 km s^{-1} layer; the preferred model has them coming from the high velocity layer for consistency with other instruments across the intermediate zone. Picks are overlain on the instrument sections.

within this part of the model and arise from assuming a constant velocity gradient within the crust.

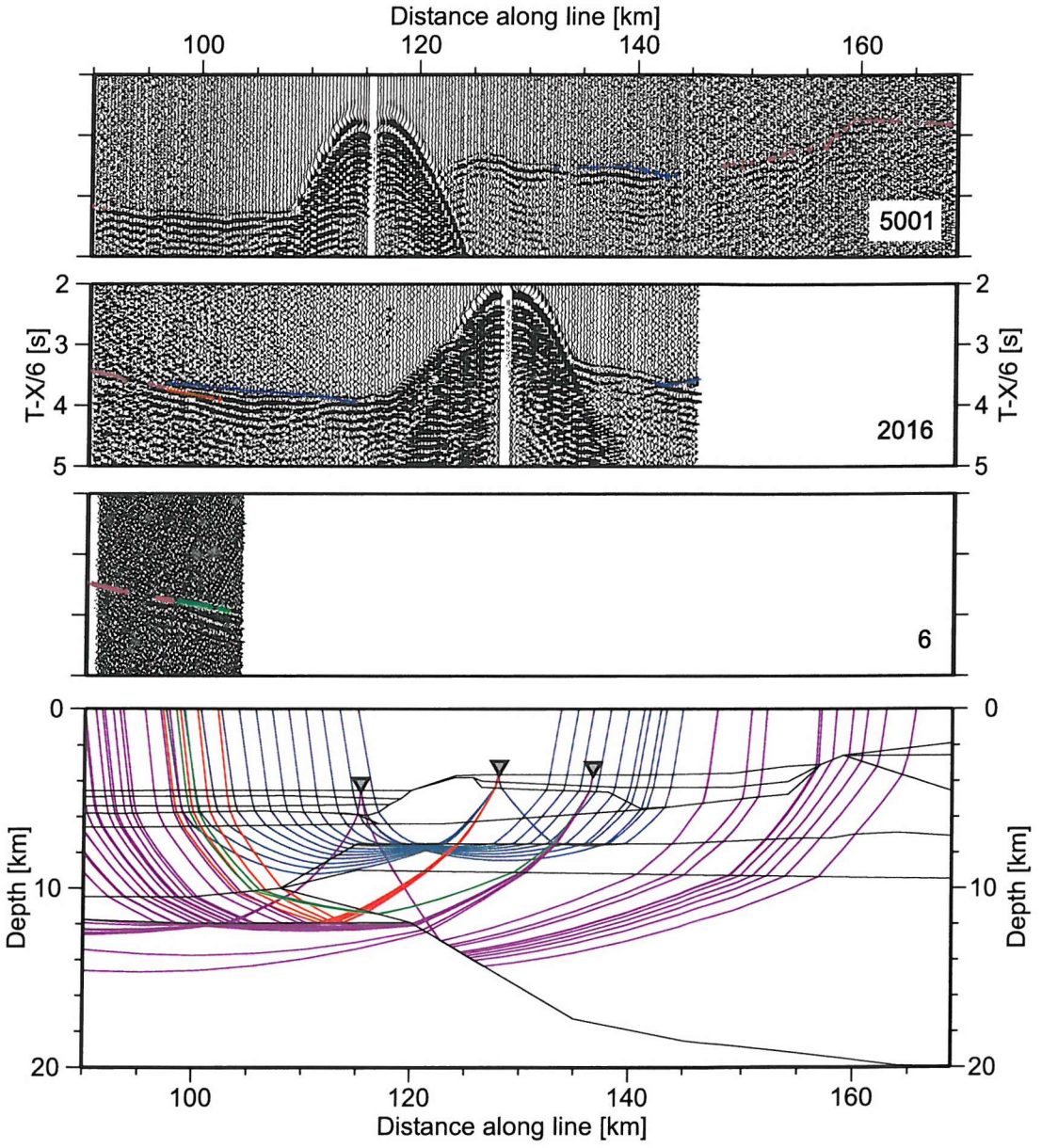

Figure 5.11: Velocity model including a middle continental crust layer. This 2 km thick layer has velocities of 6.4-6.7 km s^{-1} with a 7-7.4 km s^{-1} lower crust beneath. The final RMS misfit is 156 ms for this model, compared to 137 ms for the two-layer continental crust model. Only rays that pass through the continental crust are shown. No forward or inverse modelling was attempted for velocities within the lower crust of the three layer continental crust model.

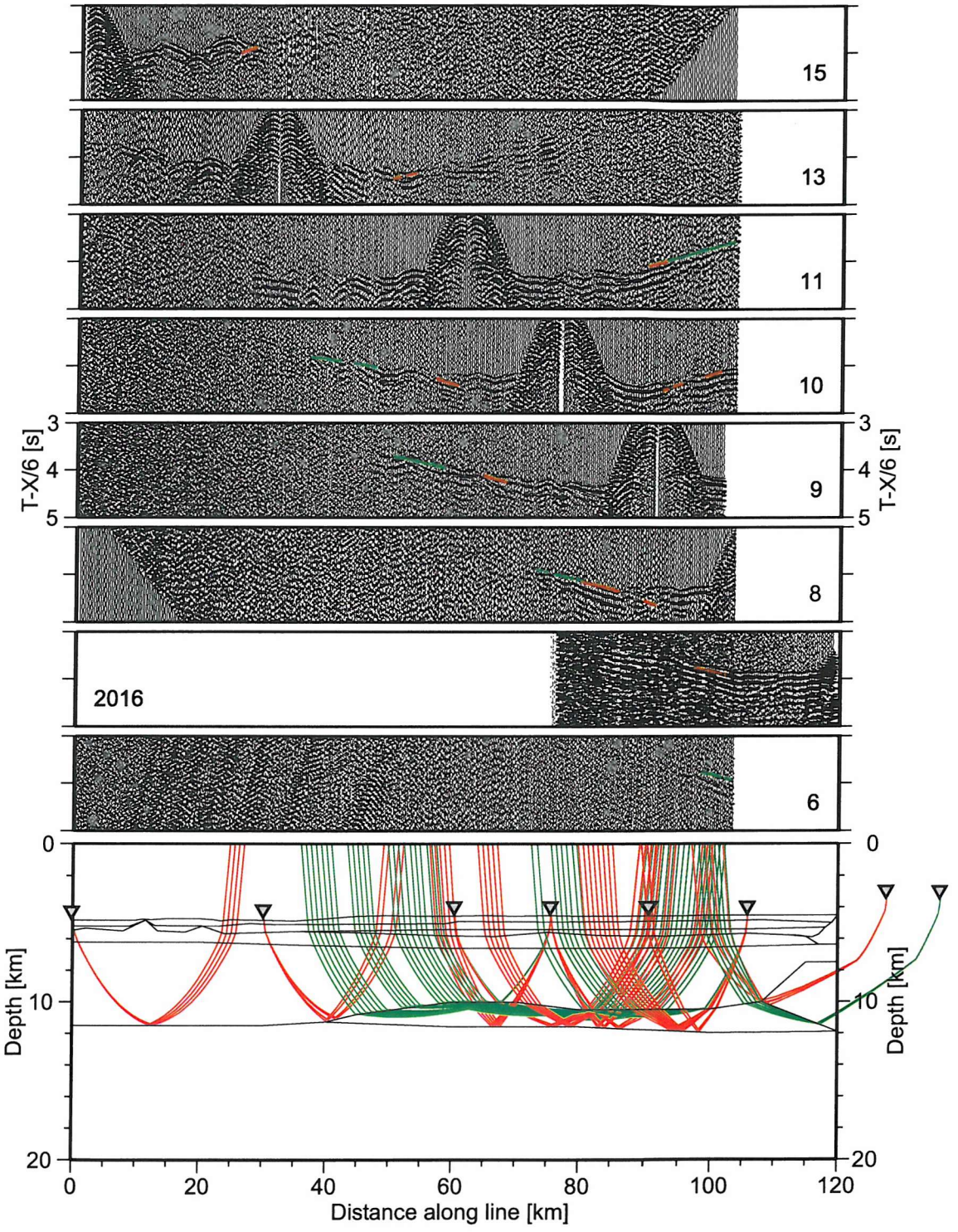

Figure 5.12: Ray coverage through the high velocity lower crust (green) and Moho reflections (red) from model distance 0-120 km. Every fifth ray shown from instruments 15, 13, 11, 10, 9, 8, 2016 and 6 (inverted triangles). Picks are overlain on the OBH sections; the sonobuoys do not provide any constraints on these deep layers.

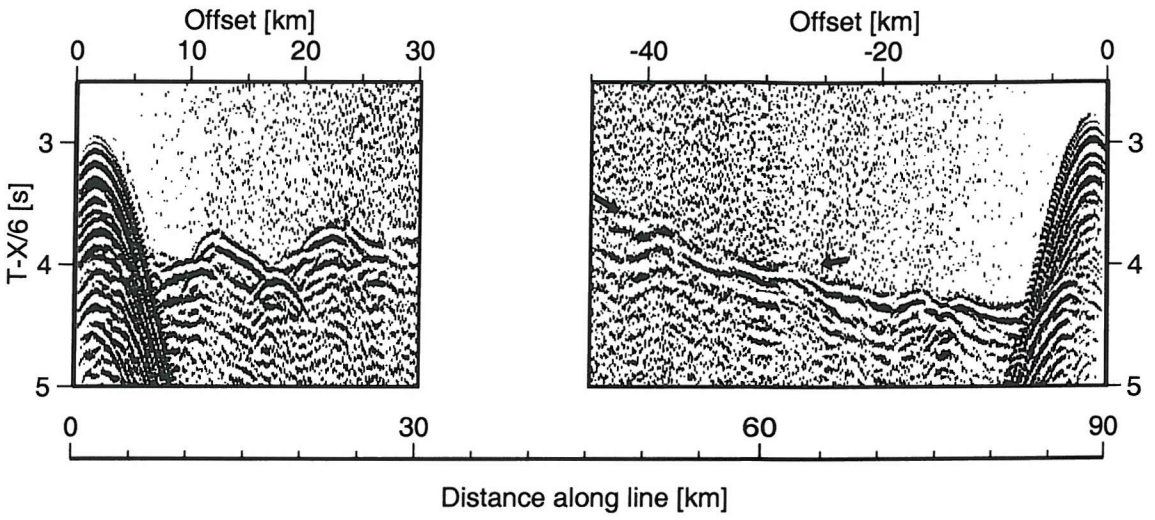

Figure 5.13: Arrivals with apparent velocities >7 km s^{-1} have high amplitudes at <30 km model distance and lower amplitudes between 40 and 120 km model distance (indicated by black arrows). Instruments shown are 15 and 9, located at 0 and 90 km model distance respectively.

Deep reflections from beneath intermediate basement appear on most instruments between 0 and 120 km. Traveltime modelling shows that these come from ~12 km depth (Figure 5.12) and represent the upper boundary of a region with normal mantle velocities of 8.0 km s^{-1}, both where the high velocity layer exists and where it is absent. During modelling this interface was kept smooth to enable turning rays in the low velocity gradient mantle beneath to be traced without the geometrical restrictions of an undulating Moho topography. This resulted in a higher χ^2 value than a model in which the Moho undulates, but is justified because the depiction of the Moho as a single interface is a simplified representation of what is likely to be a complex, laterally varying transition zone. Normal mantle velocities of 7.95-8.0 km s^{-1} underlie the whole model.

The intersection between upper and lower continental crust and intermediate basement has few rays passing through it (Figure 5.10). At ~120 km model distance three layers come together and pinch out forming the separate upper continental crust, lower continental crust and high velocity intermediate crust layers. Separate layers are required to allow the lateral velocity variations, but the complexity of the velocity model prevents rays from turning in this region. Interfaces were adjusted within this region to allow rays to be traced to all observation points, but there is considerable uncertainty in layer geometry and the modelled interfaces should not be taken as exact lithological boundaries.

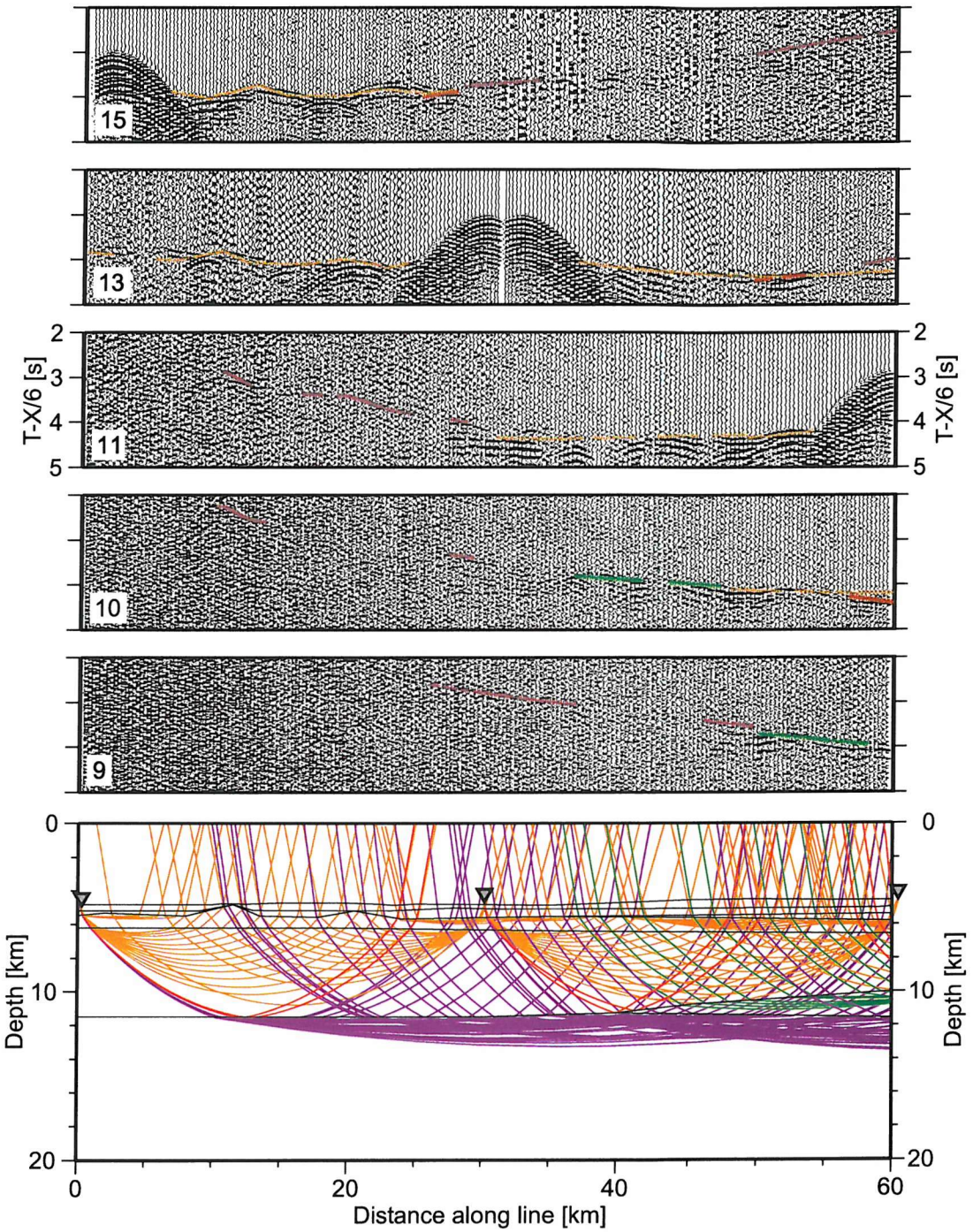

Figure 5.14: Ray coverage from 0 to 60 km model distance. Every tenth ray is plotted; rays turn within upper basement (orange), high velocity lower crust (green) and mantle (purple). Moho reflection (red) comes from the base of the basement layer. OBH 15, 13 and 11 are shown as grey inverted triangles; OBH 10 and 9 are located at 75 and 90 km model distance respectively. Picks are overlain on the instrument records.

5.1.7 S-waves

P to S converted waves can be observed on instruments 15, 11, 10, 9, 8 and 5001 (e.g., Figure 4.21). They appear later than the basement arrivals, with an apparent velocity of $\sim$3.5 km s^{-1}. They also have a strong amplitude, similar to that of upper basement and dissimilar to that of sediments observed elsewhere. Due to a thin sedimentary cover and a low sediment velocity the large velocity step at top basement makes this the most likely location for conversion to occur.

RAYINVR achieves S-wave traveltime modelling by setting user-defined values of Poisson's ratio in each model trapezoid and allowing the S-wave velocity to be defined from the P-wave velocity model. Poisson's ratio must be given for all trapezoids through which rays pass and the converting interface also specified. This approach does not allow an automated inversion of the S-wave traveltimes and Poisson's ratio values must be adjusted by the user between each iteration; forward modelling of Poisson's ratio at top basement was carried out. A best fit was achieved with an RMS misfit of 123 ms and rays turning in the layer 1-6 km beneath top basement for which Poisson's ratio remained fixed at 0.285-0.29 across the entire model width. To fit the delay time of these arrivals the final model shows Poisson's ratio at top basement decreasing seaward from 0.36 to 0.28 (Figure 5.15). The greatest lateral change occurs from 0.35 to 0.285 between 20 and 50 km model distance. Poisson's ratio was fitted to the nearest 0.01 from 50-120 km, but between 0 and 50 km an adjustment of 0.005 was found to improve the fit significantly.

5.1.8 Model resolution and uncertainty analysis

Lateral resolution

The spatial resolution of seismic data is limited by expansion of the wavefront as it travels through the earth away from a point source and described by the width of the Fresnel zone. The width of the first Fresnel zone is defined as the area over which the path lengths differ by less than $\lambda/2$. For path distances, d, $\gg$ the wavelength, λ, the radius, r, of the first Fresnel zone is given by

$$r \approx \sqrt{d\lambda/2} \quad . \tag{5.9}$$

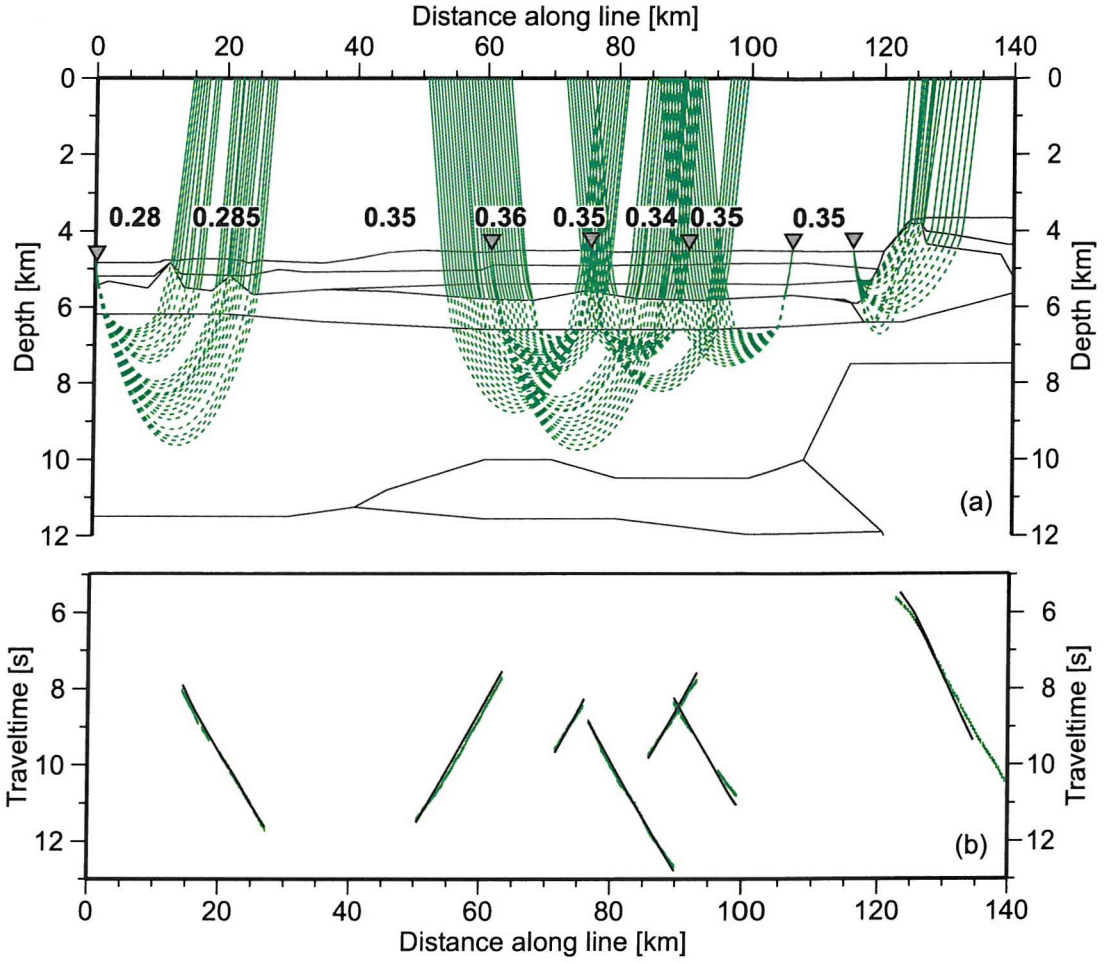

Figure 5.15: (a) Ray coverage for converted P- to S-waves, every 2^{nd} ray plotted. Solid lines are when ray is travelling as a P-wave, dashed when travelling as an S-wave; conversion occurs at top basement. S-waves turning within the basalt body (120 km) convert at the top of this body which was assigned a Poisson's ratio of 0.28. Instrument locations are shown as grey inverted triangles and the final Poisson's ratio values for top basement are given above their correct model distance. (b) Fit of these modelled rays to the observed picks, shown unreduced. Vertical height of the picks equals their assigned uncertainty.

For normal incidence experiments the path length can be approximated as the depth to the reflector, but for ray tracing the path length must be estimated, taking account non-vertical paths and ray bending. The Fresnel zone radius describes the spatial resolution of the model normal to the ray path. Variability on a length scale significantly smaller than the first Fresnel zone radius will not be resolved; small anomalies that reduce the travel-

time along the ray path may be observed, but those that retard the ray will be discarded due to the requirement for a minimum traveltime.

For the wide-angle experiment here the Fresnel zone radius at the Moho is ~4.5 km, assuming a path length of 20 km, a frequency of 8 Hz at the Moho and a P-wave velocity of 8 km s^{-1}. The Fresnel zone radius at top basement is much smaller, ~1 km, assuming a higher frequency of 20 Hz, a path length of 10 km and a velocity of 4 km s^{-1}. We could not expect to resolve features with dimensions smaller than these values.

Uncertainty of the velocity model

The F-test statistical analysis (e.g., Press et al., 1992) was applied to model parameters to provide an estimate of the uncertainty in the final velocity model for interfaces and velocities. Moho depth was tested by moving the entire boundary. Velocities were tested by adjusting individual parameters while maintaining the velocity gradient within the layer. Perturbed models are considered different from the final model when the variation in χ^2 is significant at the 95% confidence limit. The velocity uncertainty in intermediate basement is estimated at ±0.04 km s^{-1} (Figure 5.16*a*), in the lower basement layer at ±0.08km s^{-1} (Figure 5.16*b*) and in the upper mantle at -0.19 to +0.04 km s^{-1} (Figure 5.16*c*). The preferred upper mantle velocity is slightly higher than the χ^2 minima as this results in more traveltime picks being reached by ray tracing. Based on the F-test, the uncertainty on Moho depth is -0.7 to +0.6 km (Figure 5.16*d*) but if models in which ray tracing fails for a significant number of picks are discarded, the uncertainty is reduced to -0.4 to +0.6 km. These estimates assume there is no error in the overlying velocity structure. When uncertainties of the overlying velocities are considered with the depth uncertainty, the uncertainty in the Moho depth increases to -0.4 to +0.65 km. These values are calculated by adjusting the model parameters within the allowed velocity and depth bounds, and forward modelling to calculate the overall uncertainty.

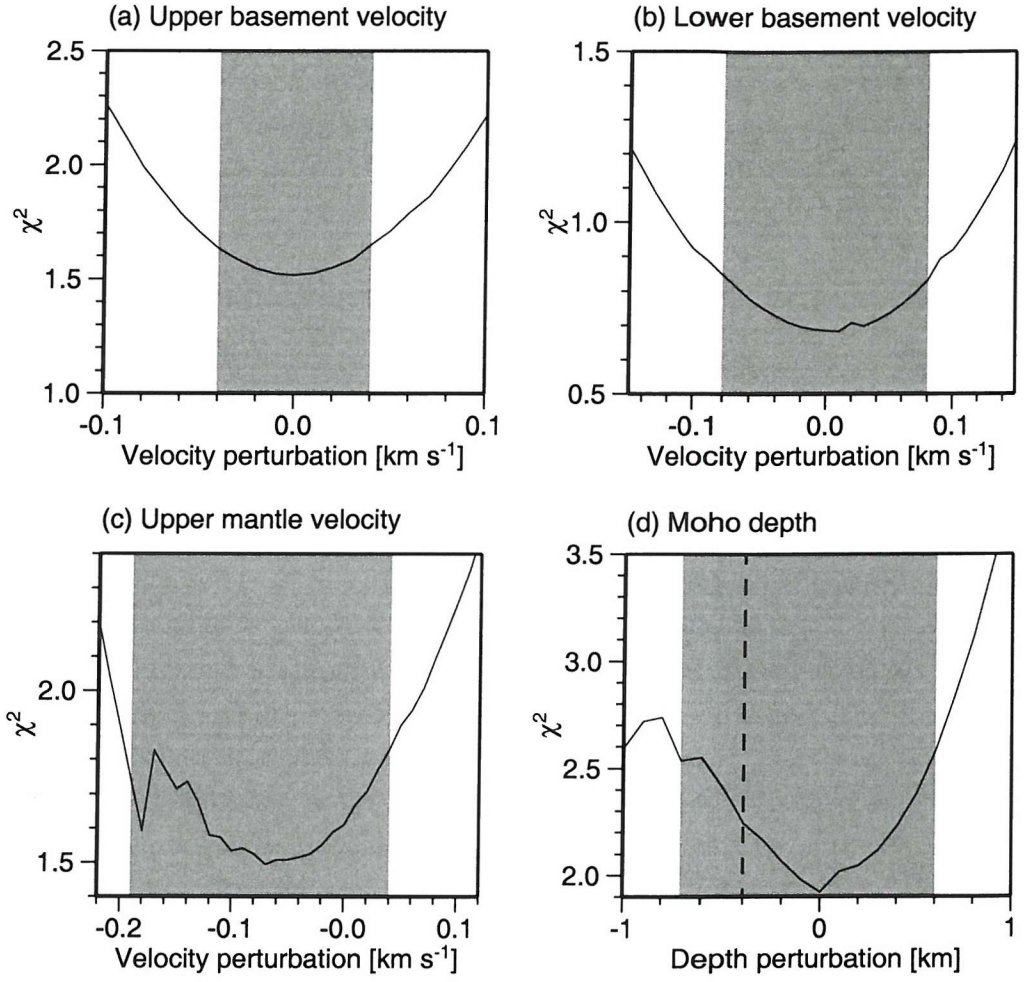

Figure 5.16: Uncertainty in (a) upper basement velocity in the intermediate zone, (b) lower basement velocities (high velocity lower crustal layer), (c) upper mantle velocity and (d) Moho depth. The perturbed model is considered different from the final model when the variation in χ^2 value is significant at the 95% confidence limit of the statistical F-test (e.g., Press et al., 1992), represented by the shaded areas. The dashed line in (d) indicates the limit that maintains ray coverage through the rest of the model: as the Moho depth is reduced layers above are pinched out and rays cannot be traced to arrivals observed from overlying layers.

5.2 Gravity data

5.2.1 Conversion of velocities to densities

The observed gravity anomaly along the wide-angle line can be utilised to make an independent test of this velocity model. A direct conversion of velocities to a densities was made according to a fourth-order polynomial fit to the empirical relationship of Ludwig et al. (1970). For density, ρ, in $\times 10^3$ kg m^{-3} (Mg m^{-3}) and P-wave velocity, V_p, in km s^{-1} the relationship is given by

$$\rho = -0.6997 + 2.2302V_p - 0.598V_p^2 + 0.07036V_p^3 - 0.0028311V_p^4 \quad . \tag{5.10}$$

This relationship is based on experimental data from unconsolidated sediments and sedimentary, metamorphic and igneous rocks made by various authors between 1938 and 1965. It is well defined for P-wave velocities of 4-6.5 km s^{-1}, for oceanic crust and serpentinite samples (Figure 5.17). Velocity-density relationships for abyssal plain sediments, marine turbidites and sedimentary rocks were considered by Hamilton (1978) (Figure 5.17) and should closely represent the sediments expected at a rifted continental margin. Velocity and density measurements of sediments recovered from DSDP Sites 548-551 are overlain in Figure 5.17. Densities are underestimated by the Ludwig et al. (1970) curve; the Hamilton (1978) curve fits observations better, but is not applicable for crustal velocities (>4 km s^{-1}) so is not preferred for use in whole model velocity-density conversion. For sediment velocities of 2-2.5 km s^{-1} observed in the velocity model presented here, the error in predicted density due to Equation 5.10 is $\sim$0.2 $\times 10^3$ kg m^{-3}. Water and upper mantle densities were assumed to be 1.033 and 3.330 $\times 10^3$ kg m^{-3} respectively.

A density model is produced using this velocity-density relationship (Figure 5.18); the FAA calculated from this model has a RMS misfit of 10.97 mGal compared to the satellite derived gravity anomaly. There is a close fit to the observed anomaly over thinned continental crust, supporting the simple two-layer continental crust model and the predicted depth to continental Moho. However there is significant misfit (>15 mGal) to the observed anomaly seaward of the continental slope. Between 0 and 80 km the FAA decreases in a regular way that may be related to earth structure deeper than this model e.g., variations in lithospheric thermal structure normal to the margin. The best-fit slope of this decrease is calculated and a correction applied to remove this long wavelength feature (dashed line: Figure 5.18). There is still a close fit to the continental crust anomaly and the fit further seaward is improved between 0 to 50 km, but remains poor between 50 and 110 km.

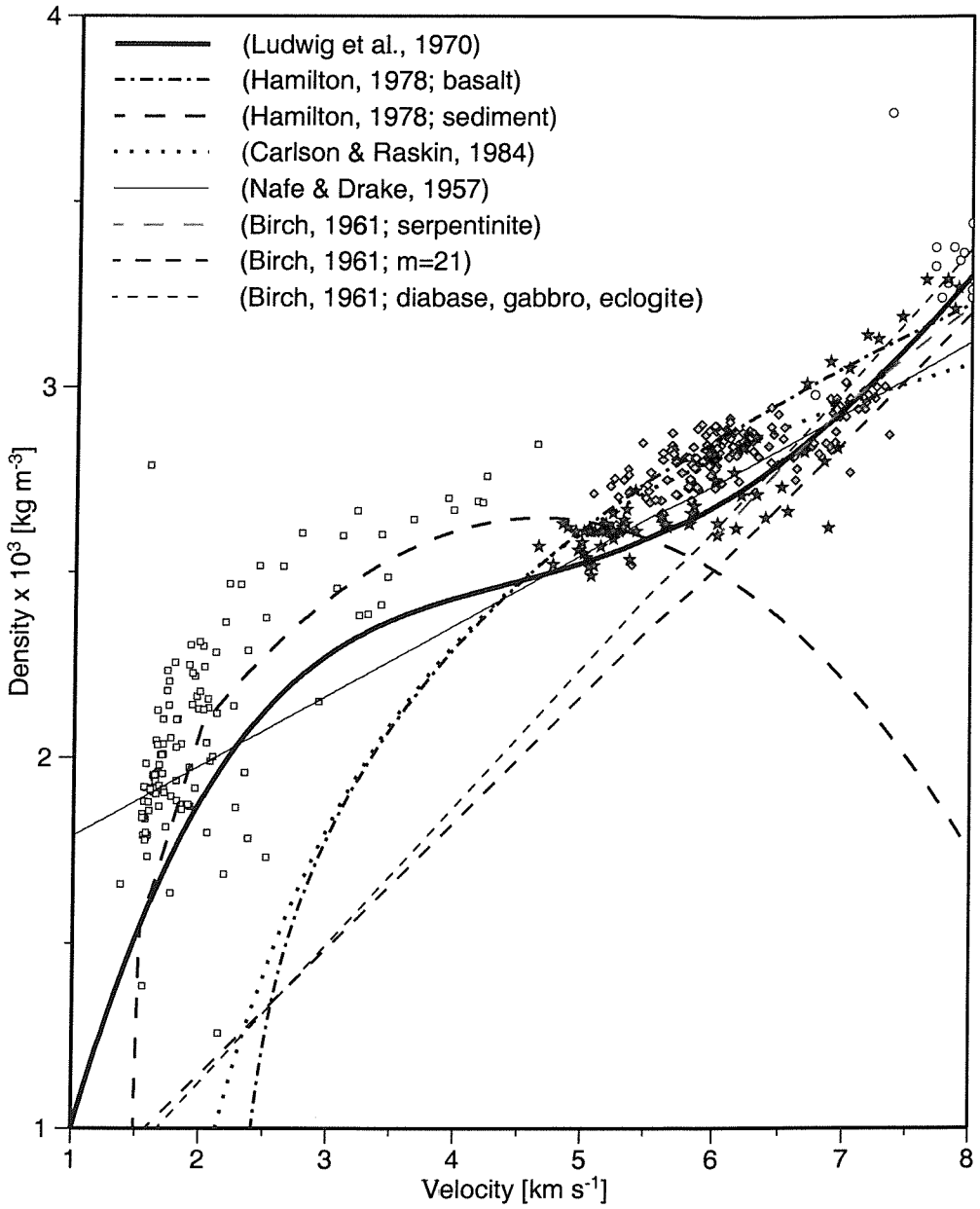

Figure 5.17: Velocity-density relationships from lab measurements of core samples. The polynomial fit to the relationship of Ludwig et al. (1970) was used in this study and shows a reasonable fit to mafic (grey diamonds), ultramafic (white circles) and serpentinite (dark grey stars) samples. Data for serpentinite samples are taken from Christensen (1966), Christensen (1978) and Miller and Christensen (1997). Sediment samples from DSDP Leg 80 at Goban Spur are shown by light grey squares. The Ludwig et al. (1970) relationship consistently underestimates sediment densities but is a much improved fit compared to the commonly applied relationship of Birch (1961) for diabase, gabbro and eclogite; $\rho = 0.375 + 0.375V_p$, which considerably underestimates the density of mafic rocks and serpentinites in the velocity range 4.5-6 km s^{-1}. The Birch (1961) m=21 relationship is for a mean atomic weight of 21.

Large misfit coincides with the region of high velocities deep within basement where the predicted FAA is greater than the observed. These high velocities likely represent altered peridotites with a low extent of serpentinisation; although the velocity-density relationship appears consistent with serpentinite samples, at higher velocities the predicted density tends to be lower than the sampled density. Serpentinite with V_p >7 km s^{-1} has not been densely sampled, but the scatter of observed data points about Equation 5.10 is $\sim 0.1 \times 10^3$ kg m^{-3} (Figure 5.17). In order to test the impact of these errors within the deep structure, the velocity to density conversion was repeated with constant densities of 2.88, 2.95, 3.01 and 3.08 $\times 10^3$ kg m^{-3} (equivalent to velocities of 6.8, 7.0, 7.2 and 7.4 km s^{-1}

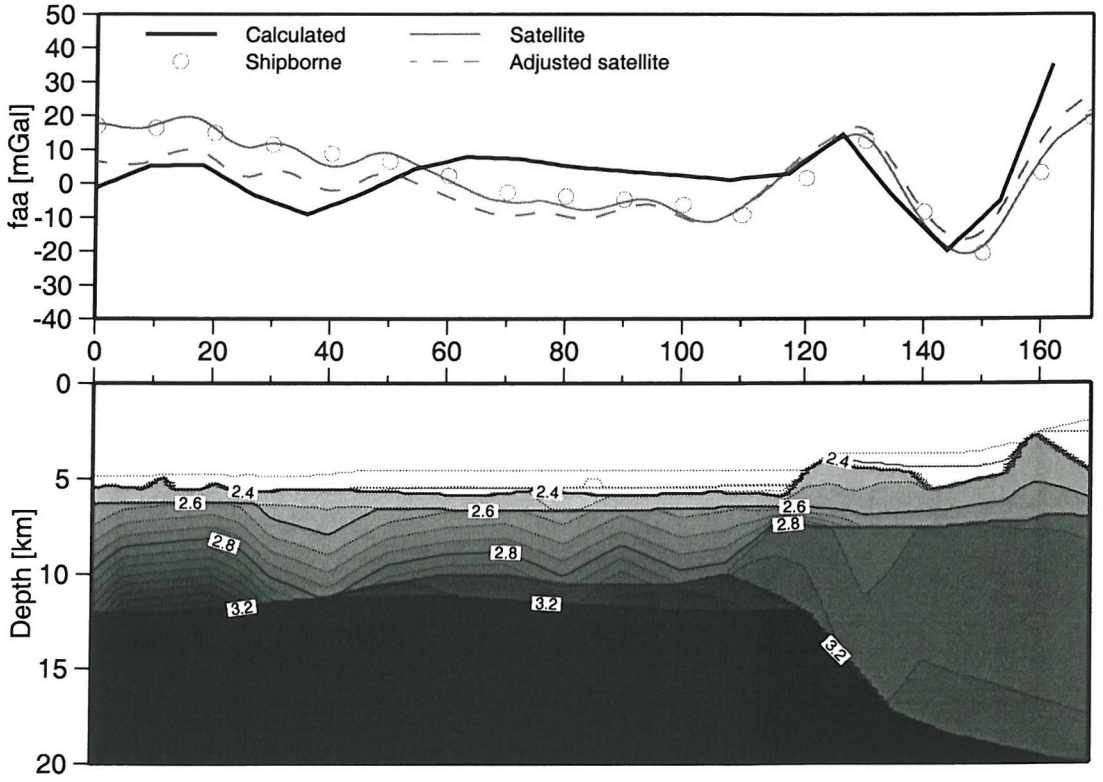

Figure 5.18: Conversion of the wide-angle velocity model to density by a fourth order polynomial fit (Equation 5.10) to the relationship of Ludwig et al. (1970). Symbols and lines are as indicated in the key; the satellite anomaly is adjusted assuming a regional gravitational trend due to deeper structure than constrained by this model. The equation applied for the linear correction was $FAA = 11.294 - 0.1054 \times distance$ [km]. The RMS misfit, measured against the satellite derived gravity anomaly, is 10.97 mGal and is halved by applying a regional correction, but significant misfit remains between 50 and 110 km.

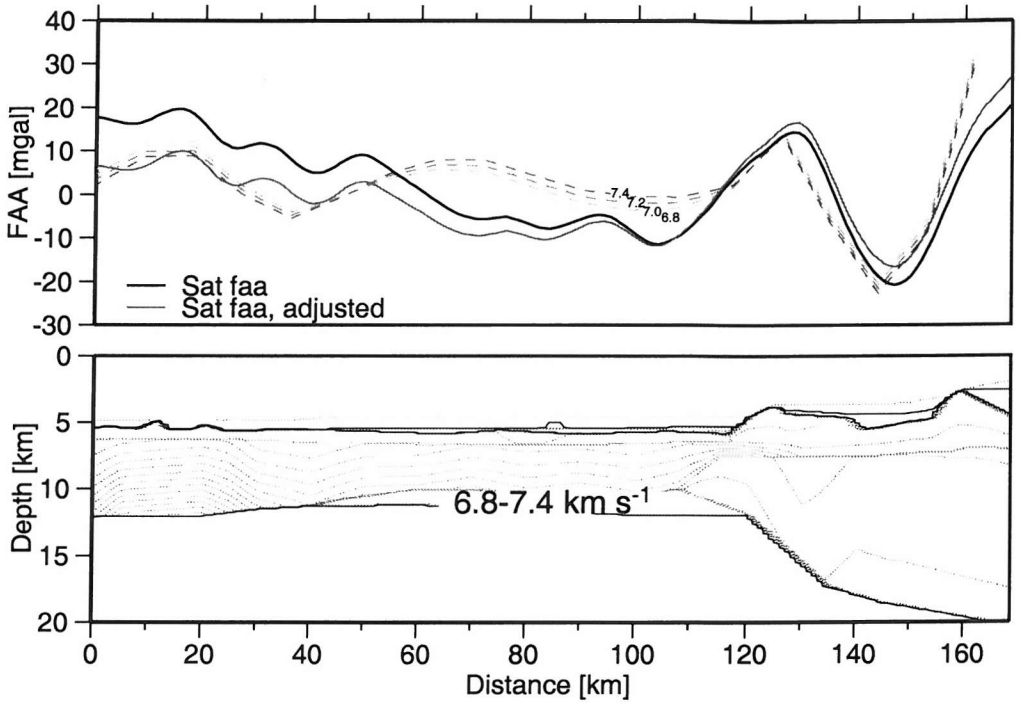

Figure 5.19: Gravity models testing the impact of possible over-estimation of density within the high velocity lower crust. Constant densities of 2.88, 2.95, 3.01 and 3.08 $\times 10^3$ kg m^{-3} were assigned to this layer, calculated using Equation 5.10 and assuming velocities of 6.8, 7.0, 7.2 and 7.4 km s^{-1}respectively. This adjustment improves the model fit but significant misfit remains.

respectively) assigned to the high velocity layer (Figure 5.19). A lower density within this layer reduces the misfit between 50 and 120 km model distance, but is not satisfactory.

5.2.2 Gravity modelling

To improve the fit and explain some features of the observed gravity data two dimensional gravity forward modelling was carried out following the approach of Talwani et al. (1959). Constant density bodies were defined based on average velocities within model layers and the velocity-density relationship previously defined (Equation 5.10); density adjustments of up to $\pm 0.1 \times 10^3$ kg m^{-3} were allowed, based on the uncertainty in velocities and in the density conversion, to produce the final model in Figure 5.20.

Modelling was carried out incrementally starting with a single crustal layer of constant density (Figure 5.21*a*). Basement and Moho depths were taken from the wide-angle model

and the basalt body and the high density (velocity) layer between 40 and 120 km were added (Figure 5.21*b*). A lateral density contrast within basement is required; the best fit to the observed FAA is with a density change at 40 km model distance (Figure 5.21*c*, *d*).

An RMS misfit of 4.34 mGal was achieved for the final model (Figure 5.20). A two layer continental crust was found to describe the relative thinning of upper and lower continental crust better than a single density layer; a slightly lower density of 2.35 $\times 10^3$ kg m^{-3} was required for the basalt body to fit the continental slope anomaly, within the range of observed densities (2.2-2.7 $\times 10^3$ kg m^{-3}) at DSDP Site 551 (de Graciansky and Poag, 1985). An average density of 2.65 $\times 10^3$ kg m^{-3} overlies the high velocity layer, with a greater average density of 2.74 $\times 10^3$ kg m^{-3} required between 0 and 40 km. The high velocity layer has a density of 3.10 $\times 10^3$ kg m^{-3}, lower than in some alternative models, and best constrained by closely fitting the continental slope anomaly.

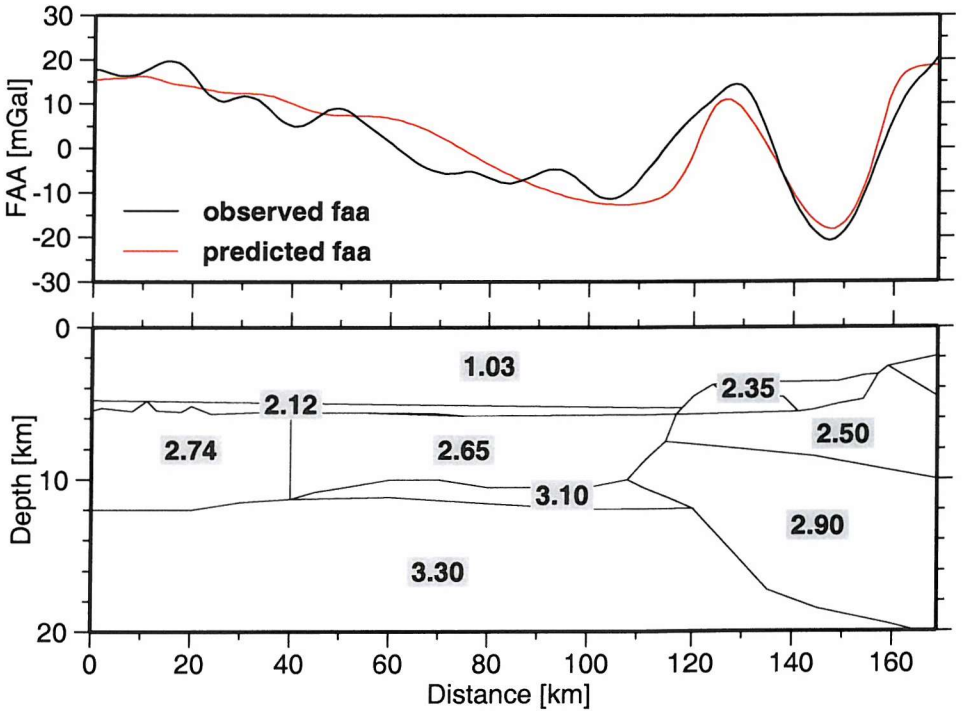

Figure 5.20: Final density model from gravity forward modelling. Model bodies are based on the wide-angle velocity model with densities overlain in $\times 10^3$ kg m^{-3}. There is a close fit between the predicted and observed free-air anomalies (RMS misfit of 4.34 mGal).

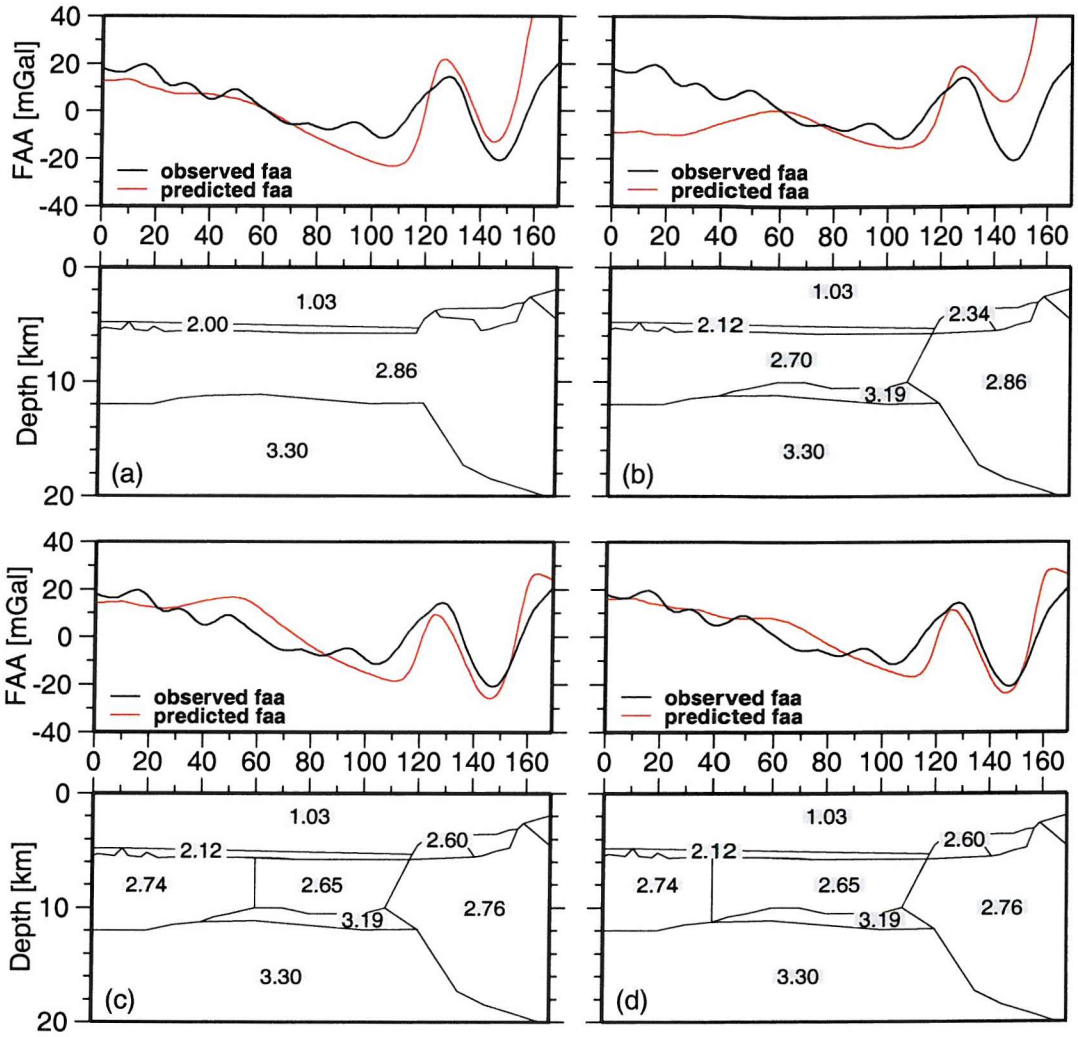

Figure 5.21: Alternative gravity models produced by forward modelling. Densities are given in $\times 10^3$ kg m^{-3}. (a) Minimum structure model with a constant density for the whole crust. A reasonable fit to these data was achieved, but this model discards some information such as the presence of the basalt body and crustal lithology changes observed on seismic data. (b) Introduction of the high density (velocity) lower layer to the intermediate zone, which has a constant upper layer density. There is a large misfit between 0 and 60 km. Continental crust density is unchanged from (a) but the basalt body is introduced. (c) and (d) include lateral variations in density within the intermediate zone and are examples of testing for the location of this boundary. The best fit (6.56 mGal) occurs with a density contrast situated at 40 km. Each layer density was forward modelled to produce the best fit to the observed data within ranges of expected values. Best fit densities for the basalt body vary from 2.34 to 2.60 $\times 10^3$ kg m^{-3} and depend strongly on the density assigned to deeper layers. A density of 3.19 $\times 10^3$ kg m^{-3} is required for the high velocity lower crust, greater than predicted from the velocity model (e.g., Figure 5.19), but may still represent low density mantle or serpentinite.

5.3 Multichannel seismic data

Deep seismic reflection line WAM (Western Approaches Margin) was acquired in 1985 by BIRPS (British Institutions Reflection Profiling Syndicate) and ECORS (Étude de la Croûte continentale et Océanique par Réflexion et réfraction Sismiques) and extends for 645 km from 30 km thick continental crust in the east (Pinet et al., 1991) to oceanic crust in the west; WAM is not straight and not exactly coincident with the wide-angle profile, with a maximum offset of ~50 km at the western end (Figure 4.6). The profile was recorded to 15 s two-way traveltime (TWT) using a 3 km streamer with 60 geophone groups and a ~50 m shot spacing. A standard processing sequence was applied consisting of spherical divergence corrections, velocity analysis, normal moveout correction, mute, stacking and deconvolution. These data are resampled to 8 ms at an early stage of the pre-processing, which gives a Nyquist frequency of 62.5 Hz for this dataset. Full details of the acquisition and pre- and post-stack processing applied are given by Klemperer (1989).

Depth migration of line drawings from the time section was carried out by Peddy et al. (1989), according to the method of Raynaud (1988), allowing the Moho depth to be estimated from the base of lower crustal reflectivity. A full depth migration was attempted by Louden and Chian (1999) using the velocity model of Horsefield et al. (1994) (Figure 5.22) but suffers from large amounts of waveform stretching at the base of the sedimentary column due to a large velocity gradient. Prior to this study velocities are poorly constrained seaward of the continental slope.

It was considered most important to produce an accurate map of depth to basement so that basement relief could be quantified along this line. To achieve this without the artifacts introduced by Louden and Chian (1999), depth migration was carried out with a smoothed velocity model based on the wide-angle velocities (Figure 5.23). Initial depth migration at water velocity accurately located the sea-bed; incorrect positioning of the sea-bed interface within the model would result in distortion of this reflector due to the velocity jump present here. The rest of the velocity model was built in depth, based on the wide-angle velocity model and smoothed over 200 CDPs (5 km) horizontally and 400 m vertically. Before migration the water column velocity is reset to 1.48 km s^{-1}, chosen to be slightly lower than actual water velocities to prevent over-migration of the sea-bed reflection. Sediment velocities between 0 and 120 km distance through the migration velocity model closely match wide-angle velocity depth profiles taken at the same locations (Figure 5.23) so top basement should be correctly located within the migrated section.

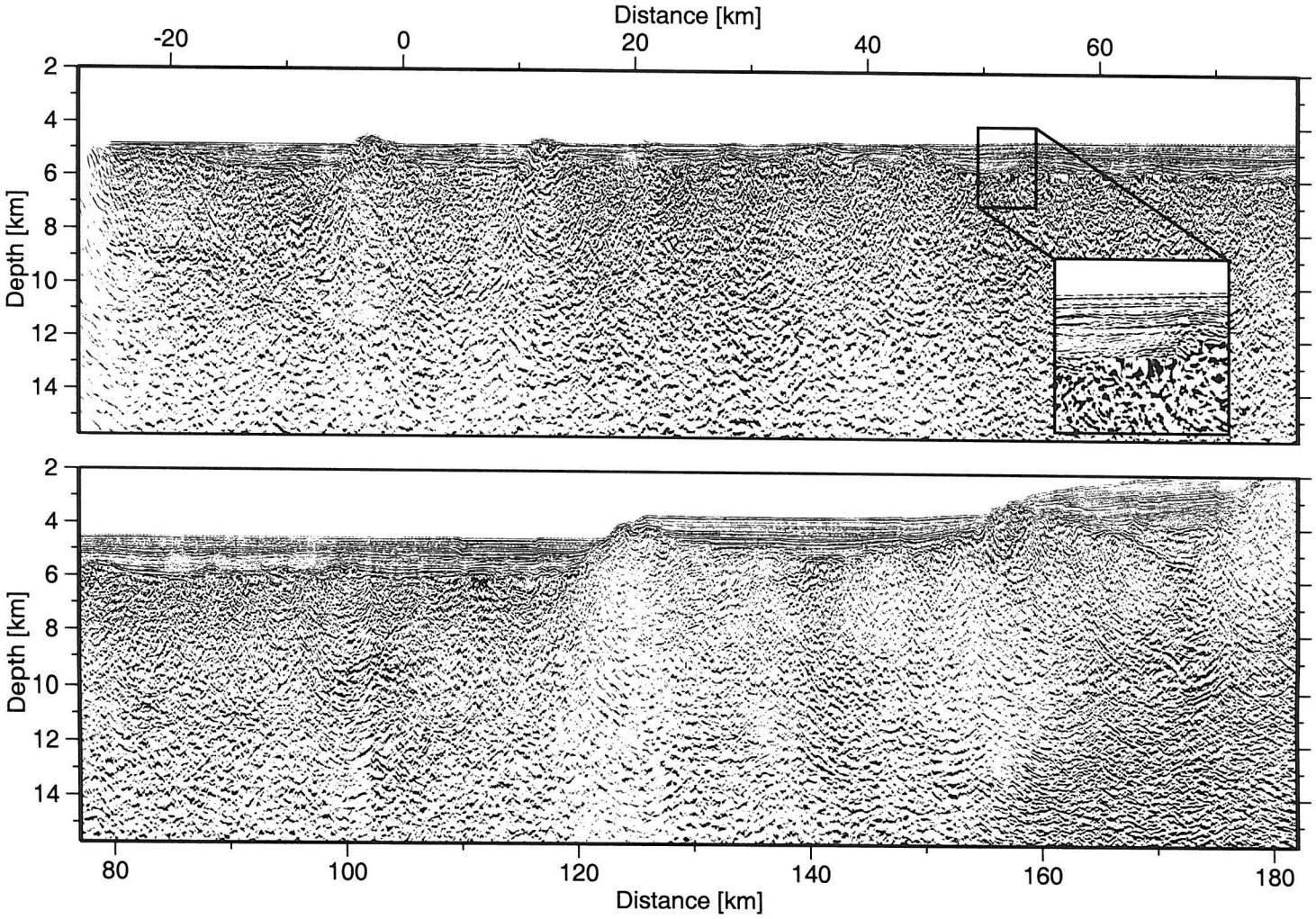

Figure 5.22: Louden and Chian (1999) depth migration of WAM (2× vertical exaggeration). Enlarged box shows the distortion of top basement caused by this migration and the difficulty in picking the reflector accurately.

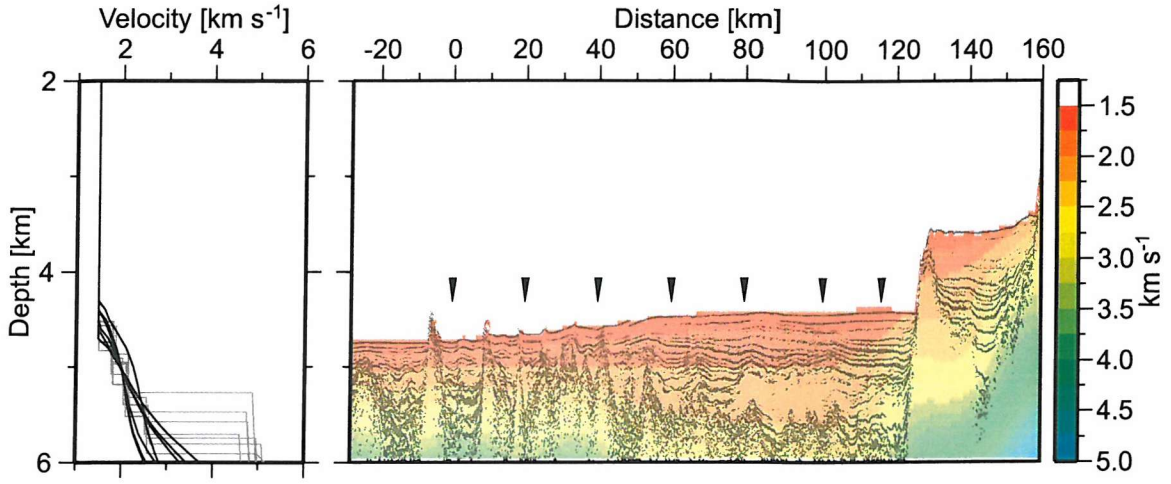

Figure 5.23: Migration velocity model for the depth migration of WAM. A smooth velocity model was applied with no velocity steps beneath the seabed. 1-D velocity-depth profiles at model locations indicated by black inverted triangles are shown in the left panel (black lines). Sediment velocities used in the migration closely match wide-angle sediment velocities (grey lines). Velocity steps from ~2 km s^{-1} to >4 km s^{-1} occur at different depths but are indicative of changes in depth to basement along the line. Basement velocities are underestimated in the migration velocity model, ~4 km s^{-1} (green colour) is reached 0.5-1 km into basement and will result in incorrect positioning of some deeper events.

The velocity step at top basement is smoothed and true basement velocities (>4 km s^{-1}) are reached 0.5-1 km into basement (Figure 5.23), this will result in under-migration and incorrect positioning of energy within basement.

Kirchoff depth migration (Section 7.1.4) was applied to the stacked time section with a maximum frequency of 62 Hz and a maximum dip to migrate of 60°. The migration aperture controls the lateral width over which diffractions can be collapsed within the section; it is important to use a wide enough panel to include all diffracted energy but over realistic distances (e.g., energy cannot have come from 100 km away and panels that include this should not be tested). There are substantial computational time costs to increasing this parameter so a migration aperture of 4 km was used, slightly larger than the calculated Fresnel zone radius (Section 5.1.8) ~5 km into basement of 1.5 km (depth=9 km, velocity=5 km s^{-1}, f=25 Hz).

Basement picks from the depth migration were separated into two regions corresponding

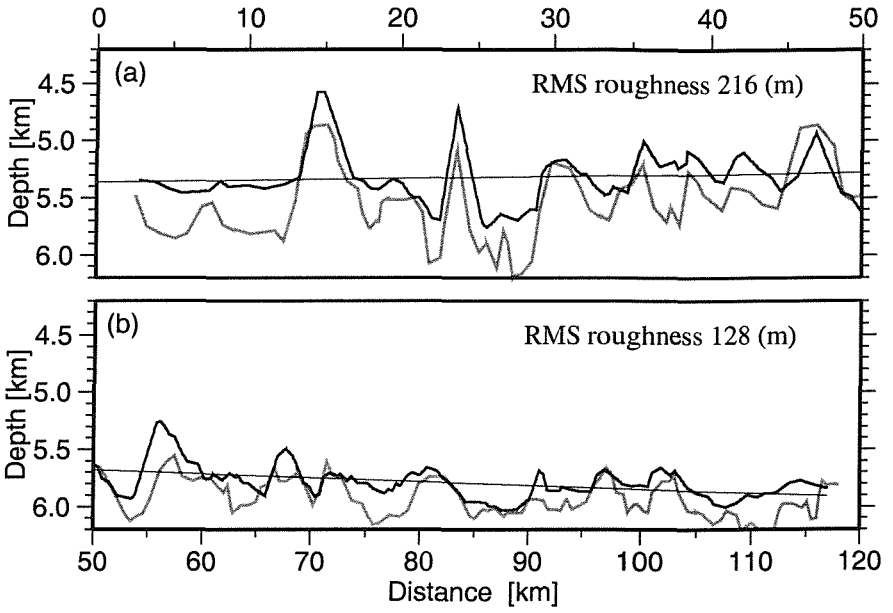

Figure 5.24: Basement picks from the WAM depth migration (black line) at wide-angle sediment velocities (Figure 5.23) for (a) 0-50 km and (b) 50-117 km. Linear trends are plotted for each panel and the RMS misfit about this line given. Basement picks from the (Louden and Chian, 1999) migration are also shown (grey line). Although there is some disagreement in absolute depth the relative variations in basement topography are comparable between the two migrations.

to changes in basement relief, from 0 to 50 km and 50 to 117 km. No picks were made for the basement ridge that overlies anomaly 34r. Best fit lines through these picks were derived and the RMS roughness about this line calculated (Figure 5.24). There is an increase in roughness from 128 m for the smooth basement to 216 m for the region of ridges and increased relief. Basement picks were also made for the Louden and Chian (1999) migration and compared with those made here. Although there is some disagreement in absolute basement depth, both migrations show comparable topography and roughness values.

Although the depth migration detailed above produces a clear and correctly located image of top basement it is less satisfactory for detailing deep structure; migration at high velocities results in considerable waveform stretching and loss in apparent vertical resolution. Previously clear features such as the reflector at the base of the basalt body (125-140 km) are only just visible on the migrated section (Figure 5.25) and not at all visible on the

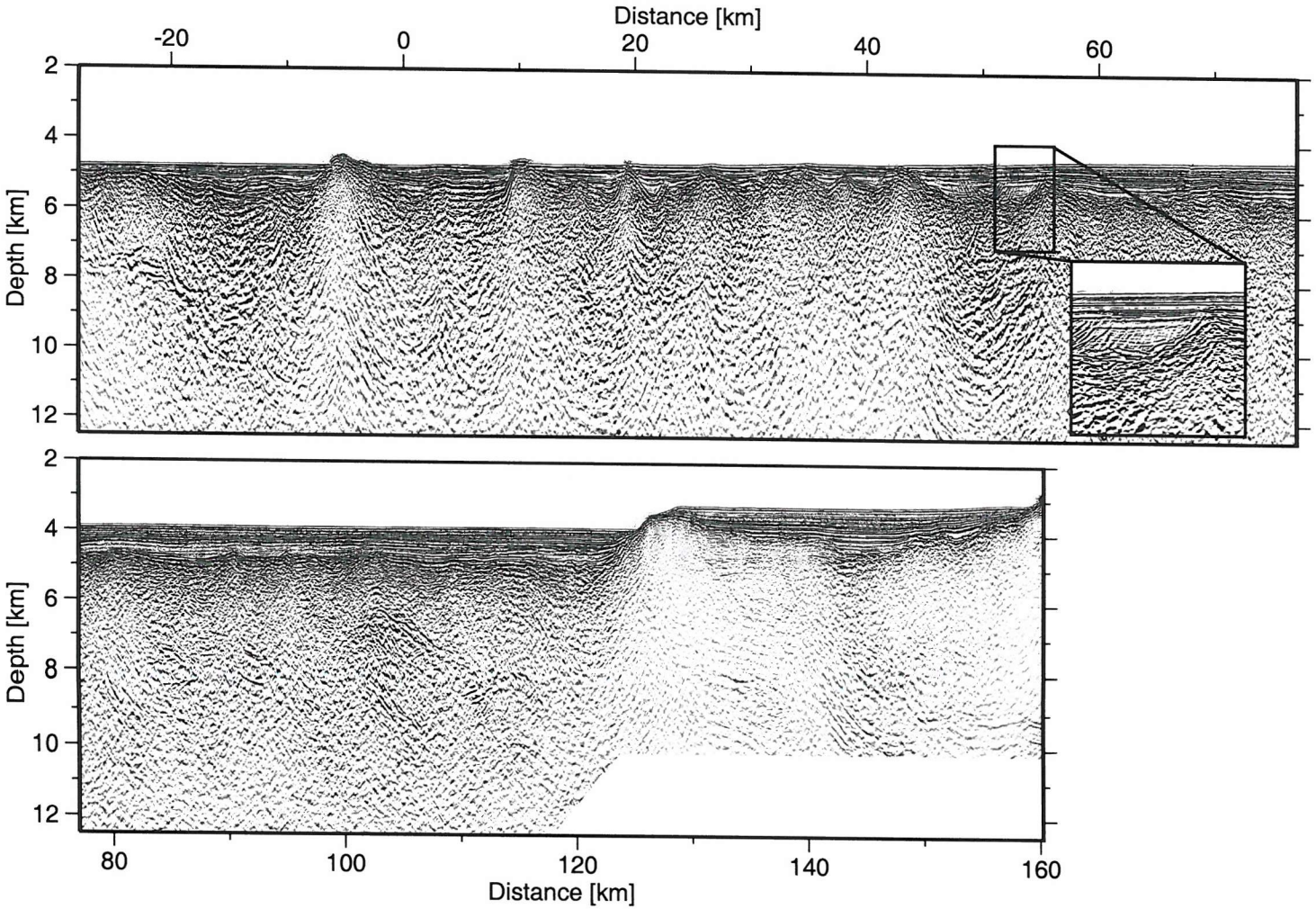

Figure 5.25: WAM depth migration with a smoothed wide-angle velocity model (Figure 5.23). 2× vertical exaggeration. A much clearer image of top basement has been achieved (see inset) compared to the Louden and Chian (1999) migration (Figure 5.22). There are suggestions of a dipping reflector at 8 km depth (-23 to -16 km) and a possible Moho reflection from -20 to 0 km. Patches of reflectivity can be seen within basement from 0 to 120 km (e.g., 7 km depth at 115 km) but in general the image is poorer than the time section (Figure 5.26).

Louden and Chian (1999) migration (Figure 5.22). This sub-basement reflection is clearly visible on the time section (Figure 5.26), migrated at water velocity (1.48 km s^{-1}) to suppress diffractions, which will be used for the description of margin features that follows.

At the foot of the continental slope the basaltic body can be clearly delineated between 120 and 140 km. Beneath the basalt is a zone of low signal to noise ratio which due to its clear distinction from the basalt above is interpreted as thinned continental crust. Reflective lower continental crust extends beneath the basalt body, being at least 1 s TWT thick at 127 km distance. West of this, from 50-120 km, is a 70 km wide zone of low basement relief. Basement here is generally unreflective with isolated patches of reflectivity 1-1.5 s TWT beneath top basement and occasional reflectors deeper, at possible Moho depths (8.5-9 s TWT) (Figure 5.27c). The most continuous of these reflectors is ~6 km long at 100 km distance and 8.5 s TWT (~7 km) (Figure 5.27*c*), with a dip of ~10°. This event does not coincide with a layer boundary in the wide-angle velocity model and is not associated with any wide-angle reflections; its position ~1 km beneath top basement, close to the change in basement velocity gradient, suggests some relationship with this feature as a hydrothermal alteration front (e.g., Bull and Scrutton, 1992), serpentinisation front (e.g., Minshull et al., 1998) or deep intrusions.

From 0 to 50 km is a region of increased topographic expression that is ~400 m shallower than the adjacent smooth basement. Swath bathymetric data acquired during this study and these multichannel seismic data show that this zone consists of closely spaced ridges (5-10 km apart), some of which pierce the sea-bed and exhibit margin parallel trends while others are oblique to the margin, sub-parallel to magnetic anomaly 34r (Figures 4.3, 5.26). These ridges are bounded by reflectors dipping to the west at 40-60°, estimated from depth migration of these data (Figures 5.25, 5.27*b*). There has been some disruption of the sediments over the ridges resulting in chaotic areas, seismically transparent when compared to the surrounding sediment, which are themselves overlain by continuous reflectors (Figure 5.27*b*).

Definitive oceanic crust is marked by magnetic anomaly 34r, located at -2 km, and corresponds with a broad (~8 km wide) basement high (Figure 5.27*a*). To the west of this, basement appears rough and generally unreflective. A weak reflection Moho appears from -17 to -27 km at ~8.3-8.5 s TWT, shallower than the wide-angle Moho predicted to be at ~9 s TWT from a time conversion of the velocity model (Figure 5.9).

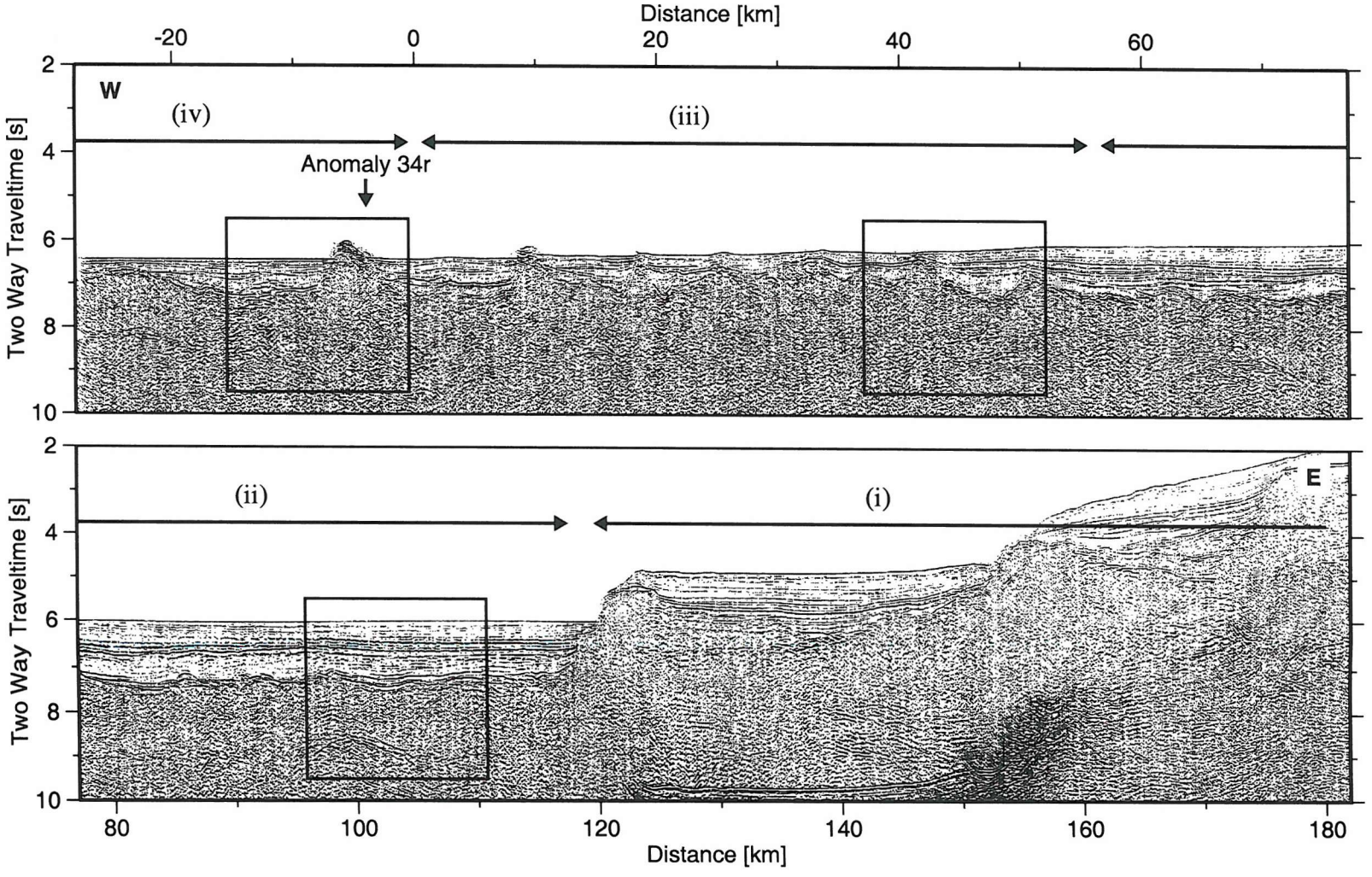

Figure 5.26: WAM seismic reflection profile, migrated at water velocity (1.48 km s^{-1}), and plotted with a 2-4-25-35 Hz bandpass filter applied. Numbered regions indicate (i) thinned continental crust, (ii) intermediate zone with smooth basement, (iii) intermediate zone with ridges and (iv) oceanic crust. Marine magnetic anomaly 34r is located at -2 km. The numbering of regions follows the zones defined in the wide-angle velocity model (see text and Figure 5.9). Enlarged panels (black squares) are shown in Figure 5.27.

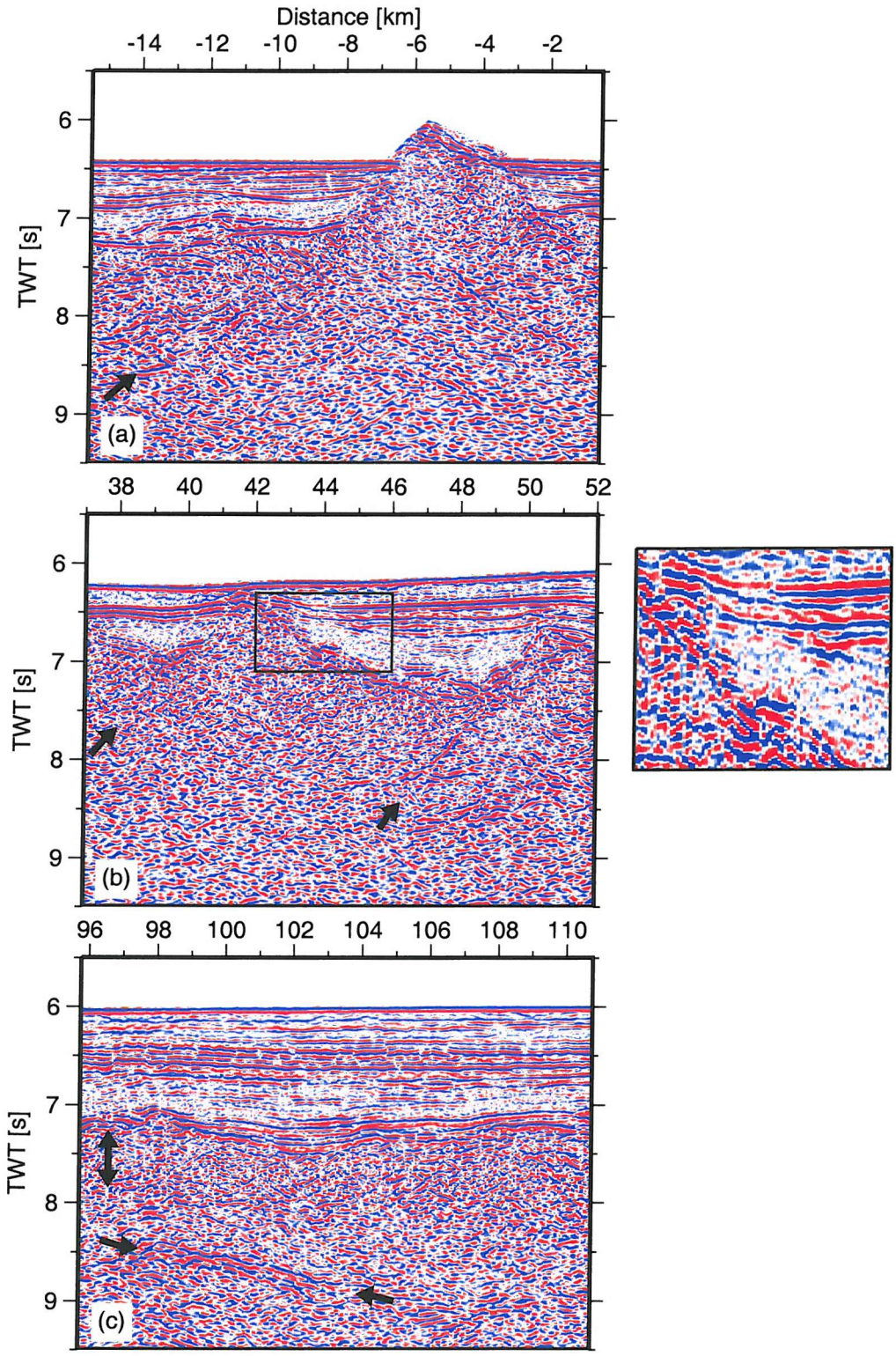

Figure 5.27: Enlarged panels of WAM indicated in Figure 5.26. (a) oceanic crust at anomaly 34r with a westward dipping bounding fault, (b) intermediate zone (i) where ridges are bounded by faults dipping to the west and (c) intermediate zone (ii) with low relief and unreflective basement. Arrows indicate reflection events referred to in the text, double-ended arrow indicates seismically transparent region; reflection Moho first appears west of panel (a) (Figure 5.26 at ~8 s TWT, -20 km). The enlargement in panel (b) illustrates the seismically transparent region overlying the ridges.

5.4 Magnetic modelling

Two-dimensional magnetic forward modelling was carried out according to the method of Talwani (1965) by defining polygons with a constant magnetisation and summing their individual magnetic fields. Oceanic crust (west of anomaly 34r), the intermediate zone and the basaltic body overlying continental crust were assumed to have attained their magnetisation during the late Cretaceous at approximately their present latitude; remanent magnetisation was assigned an inclination and declination of 64.5° and -10.4° respectively (Louvel et al., 1997) for normal polarity blocks. Induced magnetisation was assumed to be negligible compared to the remanent component. The final fit to these data is not very good (Figure 5.28*a*); in order to match the anomaly exactly the model must be very complicated and we are only interested in interpreting the major features, which we have confidence in, so a simple model is preferred.

The anomaly from 120 to 150 km is associated with the basaltic body over continental crust and the sharp increase in depth to basement at the foot of the continental slope, from 3.5 to 5.5 km. Best fit is attained here with a magnetisation of 3.5 A m^{-1} for the basalt body. The base of this magnetised body corresponds to the reflector that marks the top of continental crust (120-140 km: Figure 5.26) and implies that there is limited intrusion beneath this body; small volumes of intruded material are allowed within this model as the contribution to the total anomaly decreases with depth of the magnetised body.

Top basement in the intermediate zone was found to mark the top of the magnetic layer; depth to this interface was taken from the velocity model and the thickness as well as magnetisation of this layer were varied to find the best fit. Top basement is constrained every ~15 km by wide-angle reflections, with an uncertainty of ±200 m, and interpolated linearly between nodes. Between 0 and 60 km, top basement consists of a series of small ridges (<5 km width) which are clearly visible on WAM, but cannot be accurately projected onto the magnetic (wide-angle seismic) line; an average depth is assumed by smoothing between wide-angle basement reflections. Basement depth over the ridges varies by ±70 m, calculated from basement picks of the WAM depth migration (Figure 5.24*a*), considerably less than the absolute uncertainty in basement depth. As the ridge separation is approximately equal to the grid sampling interval the magnetic signature from these ridges has been smoothed in the observed anomaly, so this linear interpolation is valid and will help prevent over-fitting of these data. From 60 to 120 km top base-

ment is flat, a valid approximation within ±200 m (Figure 5.24*b*). The intermediate zone anomaly can be fit by a 4-5 km thick magnetic layer with a low magnetisation ≤ 1 A m^{-1} (e.g., Figure 5.29*a*) or a much thinner layer (1-2 km) with a higher magnetisation. The preferred model has a 1 km thick magnetic crust with a magnetisation of 3 A m^{-1} from 90-120 km as this provides a substantially closer fit to the continental slope anomaly at 118 km. A decrease in magnetisation seaward best fits the decreasing magnetic anomaly. The magnetic layer is assumed not to vary greatly in thickness due to the lateral continuity of the velocity model between 40 and 120 km.

An increase in thickness of the magnetic layer to ~2 km between 10 and 40 km is required to match the slope of these data with a magnetic polarity reversal (anomaly 34r) at

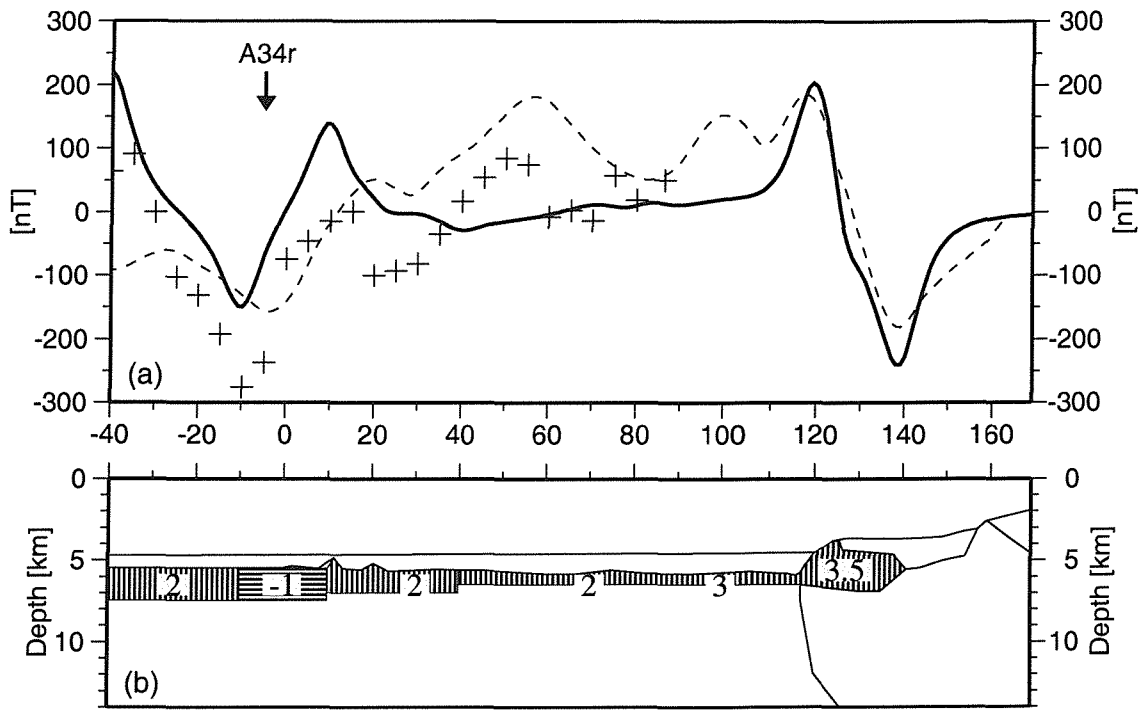

Figure 5.28: Final magnetic model. (a) Fit of calculated anomaly (black line) to the shipborne (crosses) and North Atlantic grid (dashed line) magnetic anomalies. There is a good fit to the major features of this profile: the continental slope anomaly; the increasing anomaly from 20-110 km; anomaly 34r. Short wavelength anomaly features (~10-20 km width) are not well matched in this model. (b) The final model. Normal and reverse polarity blocks are shown with vertical and horizontal bars respectively. Magnetisation within each model block is given in A m^{-1}.

10 km. Assuming an interval of 4 m.y. for anomaly 34r (Cande and Kent, 1992; Gradstein et al., 1994), the width of the reversely magnetised block is consistent with a half-spreading rate of 5 mm yr^{-1}, comparable to that estimated for the intermediate zone. Anomaly 33n and a normal polarity field is modelled from -10 km to the edge of the model; a spreading rate of ~6 mm yr^{-1} is predicted for early definite oceanic crust, within the range of 2-8 mm yr^{-1} estimated by Cande and Kristoffersen (1977).

The model presented here includes only a thin magnetised layer near top basement; the addition of a more weakly magnetised layer (<0.5 A m^{-1}) beneath it, to Moho depths, does not improve the fit, but is consistent with these data (Figure 5.29*b*). Assigning a magnetisation to the continental crust slightly improves the fit to the observed anomaly (Figure 5.30). A magnetisation of 0.2 A m^{-1} gives the best fit to these data and requires a small decrease in the magnetisation of the basalt body to 2.9 A m^{-1}. As the improved fit is localised to the continental slope anomaly this feature has been omitted from the final magnetic model presented to produce a simpler model and focus on the greater intensity variations within the intermediate zone basement.

Induced magnetisations of a similar magnitude for the sediments have also been considered. These require a small equivalent decrease in basement magnetisation, but have no other impact on the model produced. As their influence is much less than the resolution of these data, sediment magnetisations are not included within the final model.

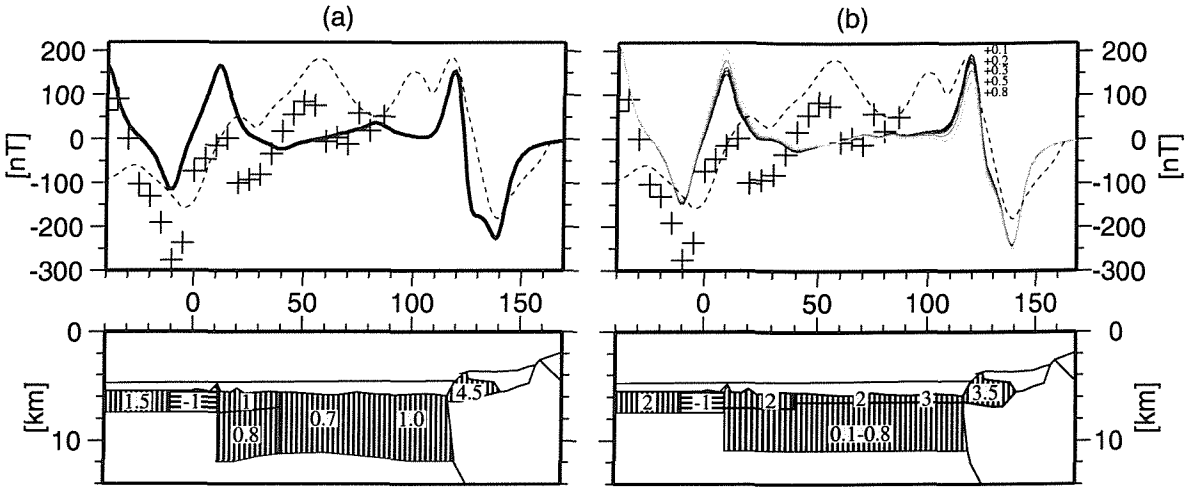

Figure 5.29: (a) Alternative model with a 5 km thick magnetised layer for the intermediate zone; a low magnetisation <1 A m^{-1} is required for 10-120 km. (b) Model designed to test the addition of a deeper layer with a low magnetisation beneath a thin magnetic crust. The model is identical to that shown on Figure 5.28 with the addition of a deeper magnetised body from 10-120 km. Magnetisations of this body are varied from 0.1-0.8 A m^{-1} (always positive) and have little effect on the predicted anomaly. Plotting parameters are the same as for Figure 5.28.

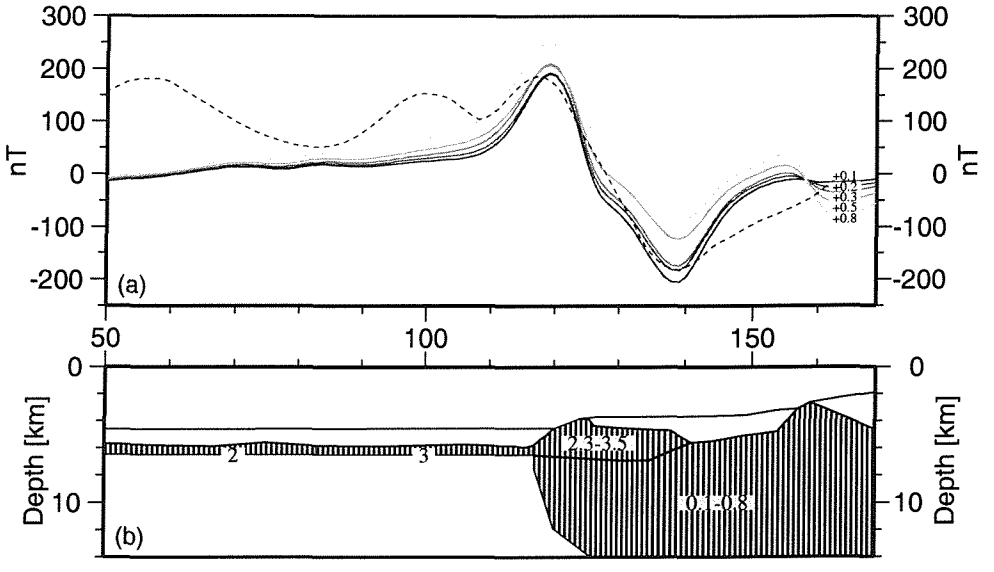

Figure 5.30: Magnetised continental crust test. The model is shown from 50-169 km. Continental crust was assigned a magnetisation of 0.1 to 0.8 A m^{-1} and the magnetisation of the basalt body was adjusted accordingly to produce the best fit to these data; a range of 2.3-3.5 A m^{-1} was required. The best fit is with a magnetisation of 0.2 A m^{-1} and 2.9 A m^{-1} for the continent and basalt respectively. No distinction is made between the magnetisation of upper and lower continental crust as the contribution of deep crust is small compared to the anomaly being considered.

Chapter 6

Goban Spur: conjugate margin and discussion

6.1 Geophysical studies of the conjugate margin

6.1.1 Flemish Cap

Goban Spur is conjugate to the northern margin of Flemish Cap (Section 1.3.3; Figure 1.16). The reconstruction to pre-rift position is unaffected by the identification of a zone of serpentinite as the most seaward location of continental crust is unchanged in the new crustal model; it may, however, be incorrect to describe the reconstruction as the arrangement at magnetic anomaly 34.

MCS line 85-3 (Figure 6.1) was recorded in 1985 across the northern margin of Flemish Cap and offset by 50 km from line WAM in the reconstruction (Srivastava et al., 1988b), aligned with line CM-11. Pastouret Ridge, an elongate raised basement feature seaward of the continental slope, lies between CM-11 and WAM and has been interpreted as a reactivated oceanic fracture zone (Sibuet et al., 1985), but there is little evidence for widespread fracture zones at this latitude within the eastern North Atlantic, suggesting that any displacement across this fracture zone was small during early sea floor spreading. With the exception of Pastouret Ridge, there are no major transform faults on the European (Keen et al., 1989) or Canadian sides (Tankard and Welsink, 1987) between the two lines, so it is reasonable to assume that WAM and 85-3 are conjugate.

Layered lower continental crust can be identified on line 85-3 up to 1.0-1.5 km thick (Keen et al., 1989) extending from full thickness continental crust to highly thinned continental

crust at the foot of the continental slope (de Voogd and Keen, 1987). The continental Moho, defined by wide-angle seismic studies, coincides with the base of this layered reflectivity (Keen and Barrett, 1981; de Voogd and Keen, 1987) which, when depth converted, gives a crustal thickness of 28 km for Flemish Cap (Keen et al., 1989). Layered reflectivity beneath the Grand Banks extends deeper, suggesting a full crustal thickness of up to 40 km further to the west (de Voogd and Keen, 1987). Beneath the continental slope the Moho rises sharply from 28 to 20 km depth over ~25 km. Reflective layering is still visible in this region of thinning, strongly supporting the interpretation of this layering as a pre-rift feature, itself deformed during rifting (White and Peddy, 1990).

The most seaward continental block can be identified at 150 km distance. Keen and de Voogd (1988) locate the continent-ocean boundary at the edge of continental crust as a 30 km wide zone between 115-145 km. This zone coincides with a landward dipping reflector at ~130 km, widespread around the Flemish Cap margins, and a magnetic anomaly of ±100 nT (Keen and de Voogd, 1988; Srivastava et al., 1988b). These features have been interpreted as marking initial oceanic crust: 'crust with oceanic affinities dips down toward the continent' (Keen and de Voogd, 1988), but could also be produced by a dipping Moho (shallowing in a seaward direction) (e.g., Section 7.6.2). There is no significant basement topography associated with this landward dipping reflector and magnetic anomaly.

Srivastava et al. (1988b) carried out a detailed aeromagnetic survey over northern Flemish Cap and Newfoundland; the 'slope anomaly' at the foot of the continental slope is identified over a wide area from 42° to 48° N and marine magnetic anomaly 34r and 33 are located. Anomaly 34r is ~130 km seaward of the slope anomaly and anomaly 33 is a further 60 km seaward. From the magnetic modelling at Goban Spur it can be seen that the width of the negatively magnetised crust is given by the peak to trough distance for anomaly 34r (Figure 5.28). This distance is ~30 km at Flemish Cap (Srivastava et al., 1988b) which, assuming an interval of 4 m.y. for anomaly 34r (Cande and Kent, 1992; Gradstein et al., 1994), equates to an initial half spreading rate of 7.5 mm yr^{-1}. Considering the uncertainties in these measurements and the assumption of magnetised body width this spreading rate can be considered identical to that observed at Goban Spur (Section 5.4). Initial sea floor spreading within the North Atlantic was therefore roughly symmetric between Goban Spur and Flemish Cap at a full-spreading rate of 10-15 mm yr^{-1}.

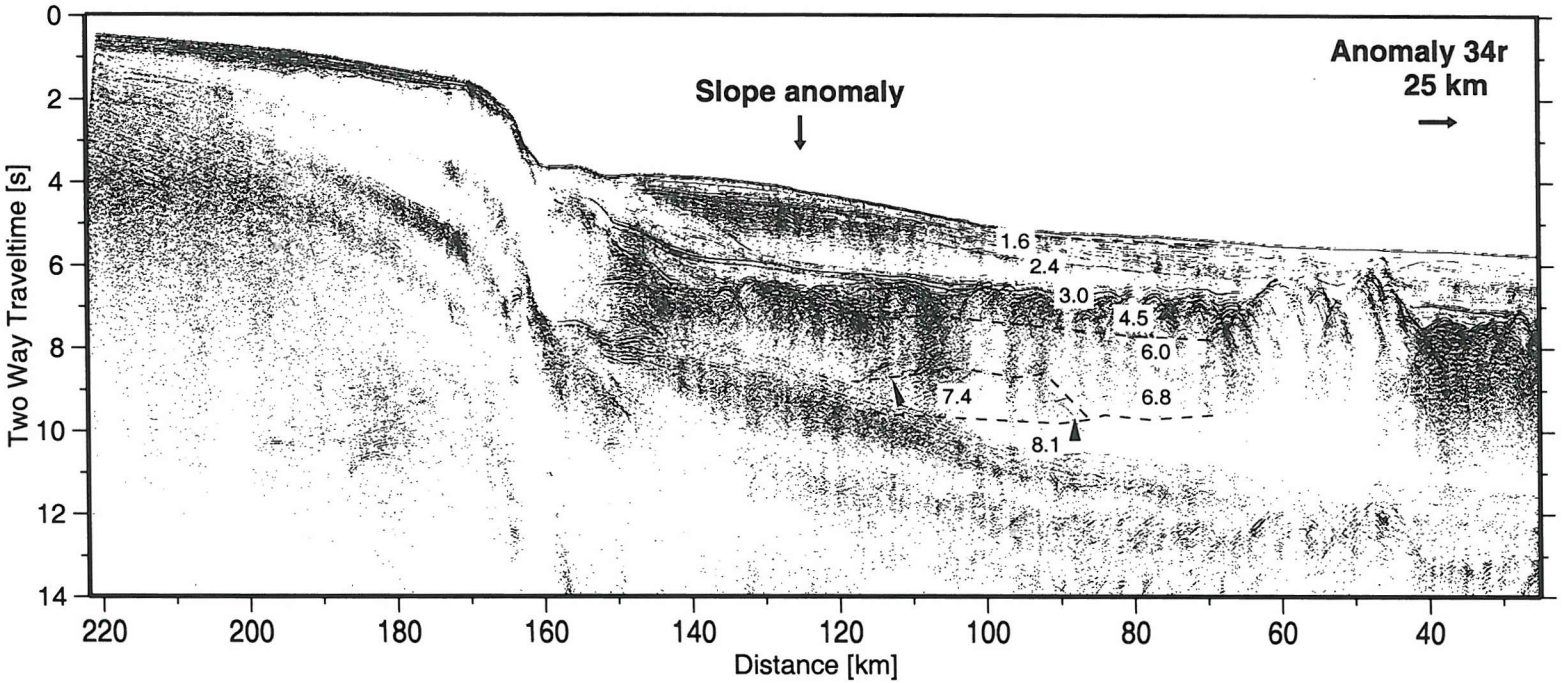

Figure 6.1: Line 85-3 over Flemish Cap extends from thinned continental crust in the west and finishes 25 km short of marine magnetic anomaly 34r. The location of the magnetic 'slope anomaly' identified by Srivastava et al. (1988b) at ~125 km is indicated by an arrow. The velocity model of Reid and Keen (1990) between 120 and 70 km is overlain; velocities are given in km s^{-1}. Distance [km] is given as distance landward from anomaly 34r. Dipping reflectors beneath the low relief basement are shown by black arrows and coincide with the top of the 7.4 km s^{-1} body.

Two regions between seaward-most continental crust and magnetic anomaly 34r can be distinguished by changes in basement relief. From 135 km to 60 km is a 75 km wide zone of low basement relief. Two dipping reflectors are imaged at 8.5-9.5 s TWT (expected Moho reflection time) at 110 and 80 km. These reflectors appear to bound a 7.4 km s^{-1} body (85-130 km distance: Figure 6.1) that was modelled in a wide-angle OBS experiment over the low relief basement (Reid and Keen, 1990). Suggestions of the oceanic Moho can be seen at 80 km (~9.5 s TWT), but a clear oceanic Moho is not observed on line 85-3. At 60 km two large ridges (50-60 km and 40-50 km) rise ~1 s TWT above the surrounding basement (Figure 6.1; Figure 7: Louden and Chian, 1999). Magnetic anomaly 34r is not reached along this line.

6.1.2 Conjugate margin pair

Keen et al. (1989) produced a model for the conjugate margin pair of Goban Spur and Flemish Cap, joined at the edge of continental crust, based on deep seismic reflection profiles WAM and 85-3 (Figure 6.2). This image should represent the situation immediately prior to break-up and gives insight into how the continental block has been extended and finally broken. Line drawings are less sensitive to the velocity model used in depth conversion than the seismic section would be, allowing a depth section to be produced for the Flemish Cap margin where velocity control is poor. To allow comparison of upper basement structure seaward of the continental slope, line 85-3 has been reversed and aligned with WAM at anomaly 34r (0 km) (Figure 6.3).

The two margins share many similarities in appearance. A distance of 120-130 km exists between the last continental fault block and marine magnetic anomaly 34r, divided into two regions. Immediately seaward of the continental slope is a 70-75 km wide region of low relief basement with no reflection Moho: a faint reflection Moho appears 70-100 km from the last continental fault block but there is no clear oceanic Moho until A34r (Figure 5.26; Louden and Chian, 1999). Seaward of this a 50-60 km wide region of higher relief basement displays ridges, ~5 km wide, within a region of elevated basement at Goban Spur (400 m above the adjacent low topography region) compared to Flemish Cap where there are fewer ridges each ~10 km in width.

Figure 6.2 illustrates some important differences between crustal thinning at Goban Spur and Flemish Cap. Upper and lower continental crust is thinned in approximately equal proportions at Goban Spur: reflective lower crust is visible throughout the thinned crust

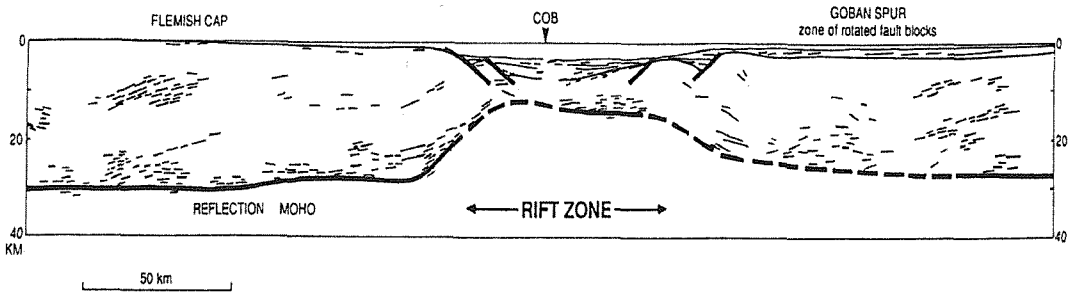

Figure 6.2: Line drawing of line 85-3 over Flemish Cap and line WAM over Goban Spur reconstructed at the most seaward observed continental crust on each margin (COB). Depth conversion of these line drawings was carried out using velocities of 1.5, 2.3 and 6.0 km s^{-1} for water, sediment and basement respectively. Reflection Moho is indicated by a solid black line, dashed where uncertain. From Keen et al. (1989).

region. Crustal thinning at Flemish Cap occurred at the expense of both upper and lower continental crust, but late stage thinning, as indicated by the rapid loss of layered lower continental crust, was by crustal necking over a narrow zone (Keen et al., 1989). There is a broader region of thinned crust at Goban Spur which Keen et al. (1989) suggest is caused by pure shear extension and final breakup offset towards Flemish Cap, leaving a wider zone of thinned continental crust at Goban Spur. Louden and Chian (1999) additionally consider the width of normal faulting within the upper crust, which occurs over ~150 km at Goban Spur and only ~50 km at Flemish Cap, to conclude that crustal thinning was fundamentally different at each margin and occurred over a narrower distance at Flemish Cap (20-30 km) compared to 60-80 km at Goban Spur.

6.2 Discussion: Goban Spur

6.2.1 Composition of the Intermediate zone

Thinned continental crust (120-169 km), a basaltic body (120-140 km) and definitive oceanic crust (<-2 km) can be clearly identified on the basis of their P-wave velocities, seismic reflection characteristics, magnetic anomalies and from sampling. However geological interpretation of the intermediate zone (0-120 km) is less clear-cut. The P-wave velocity structure is consistent with the presence of thinned continental crust, oceanic crust and/or serpentinised upper mantle, all of which can exhibit velocities in the range

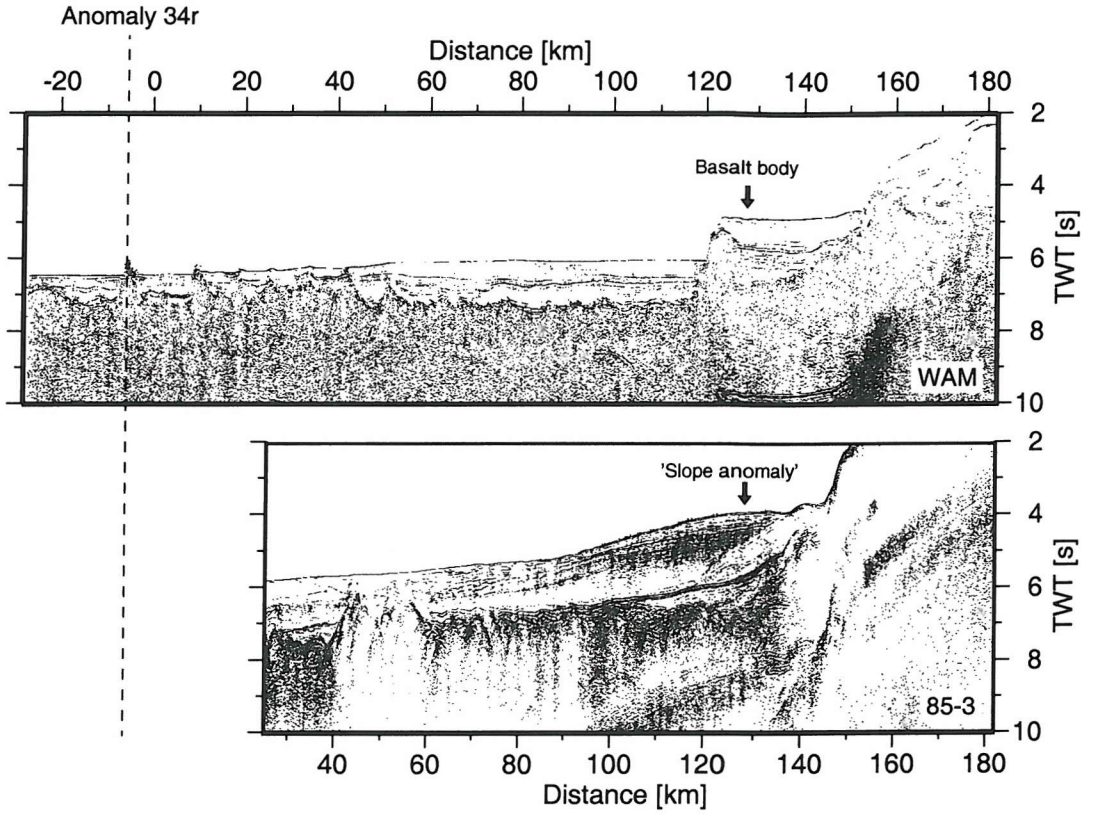

Figure 6.3: Seismic reflection lines across Goban Spur (WAM) and Flemish Cap (85-3) aligned at the first observable seafloor spreading anomaly, A34r. Line 85-3 has been reversed to allow comparison with WAM. There is a similar distance (120-130 km) between A34r and the seaward most continental crust at both margins; this distance is marked by the emplacement of a basaltic body at Goban Spur and a deep landward dipping reflector and magnetic anomaly at Flemish Cap. ~70 km of basement with a low topographic expression is visible on both margins seaward of the continental slope, further seaward there exists 50-60 km of higher relief basement before A34r is reached. See text for a further discussion.

4.5-6.5 km s^{-1} (e.g., Miller and Christensen, 1997; Dean et al., 2000). Typical velocity gradients have been described for thinned continental crust (Section 2.1) and oceanic crust, but these depend on the oceanic crustal composition (Section 2.2). Velocity gradients within zones of serpentinite are poorly known due to variations in extent of serpentinisation with depth (Section 2.3). Continental crust can be distinguished on the basis of crustal reflectivity and magnetisation, but oceanic crust and partially serpentinised peridotite can share similar physical properties. Densities of 2.5-3 $\times 10^3$ kg m^{-3} are consistent with both lithologies (Figure 5.17) and although not observed in all samples, high

magnetisations have been measured in serpentinite (e.g., Oufi et al., 2002) (Section 2.3) which prevents magnetisation from being used as a delimiter between these two interpretations. Difficulties in making a positive distinction are further exacerbated by the existence of a range of geologically valid compositions between the end-member types, e.g., oceanic crust at slow spreading rates can consist partly, or entirely of serpentinite (Cannat, 1993; Dick et al., 2003) and may present similar physical properties. Poisson's ratio shows a clear distinction between basalts and serpentinites and provides and important method for distinguishing the lithologies at Goban Spur. Each of the possible compositions for intermediate zone (ii) are dealt with in turn below.

Oceanic crust hypothesis

The intermediate zone does not fit the velocity-depth profile for normal oceanic crust (Figure 6.4): here we see an upper high velocity gradient zone ~5 km beneath top basement and high velocities (>7 km s^{-1}) from 5-7 km into basement. High Poisson's ratio values, >0.34, are not compatible with a basaltic composition of normal oceanic crust (Figure 6.5).

The observed velocity structure may be compatible with anomalous oceanic crust formed at faster or slower spreading rates. Using the empirical relationships between spreading rate and basement relief of Malinverno (1991) and Small (1994) (Section 2.2.2), the 70 km wide zone of low relief basement at the foot of the continental slope has a roughness (Figure 5.24) comparable to oceanic crust formed at spreading rates of >80 mm yr^{-1} (Malinverno, 1991) (Figure 2.10).

Fast spreading rates are generally associated with a magmatic crust ~6 km thick (Figure 2.8) (White et al., 2001) which could represent the upper basement layer in the velocity model (Figure 5.9); in this model the lower layer would most likely be a combination of partially serpentinised upper mantle and gabbroic melt products. Magnetic modelling could be satisfied by oceanic crust with a thin layer 2; most magnetic minerals within oceanic crust are concentrated within the upper levels of the crust, with a magnetisation 5-10 times greater than in the lower crust (Arkani-Hamed, 1988). The major problem with this interpretation is that it requires a spreading rate much faster than the 10 mm yr^{-1} (full-spreading rate) evidenced here immediately following anomaly 34r (Section 5.4). To form this low-relief crust at 80 mm yr^{-1} and maintain an average of 10 mm yr^{-1} a rapid change in spreading rate to very low values would be required after the formation of intermediate zone (ii). Such a large change in spreading rate has been observed at the Carlsberg Ridge (Mercuriev et al., 1996), but occurred there over several magnetochrons.

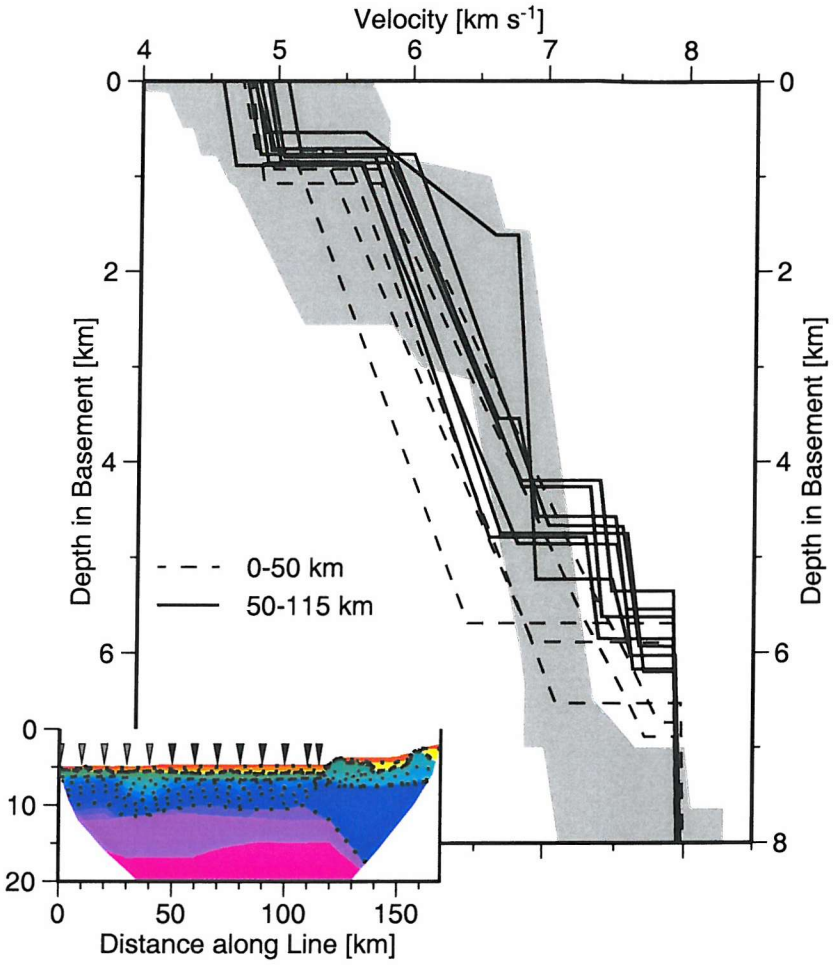

Figure 6.4: Velocity-depth profiles seaward of the continental slope. Locations of 1-D profiles are shown by grey (0-40 km) and black (50-115 km) inverted triangles in the inset, through intermediate zone (ii) (50-115 km) (black lines) and intermediate zone (i) (0-50 km) (dashed lines). The grey shaded region indicates the velocity bounds for normal oceanic crust aged 59-144 Ma (White, 1992).

It is probable that the spreading rate at Goban Spur remained approximately constant during this rifting and break-up period at an ultra-slow 10 mm yr^{-1}, so it is not possible to explain the low relief by fast spreading rates.

Oceanic crust formed at ultra-slow spreading rates (<20 mm yr^{-1}), outside the influence of mantle thermal anomalies, can be considered anomalous (Section 2.2.2) with variable volumes of melt and serpentinised upper mantle products forming the crust (e.g.,

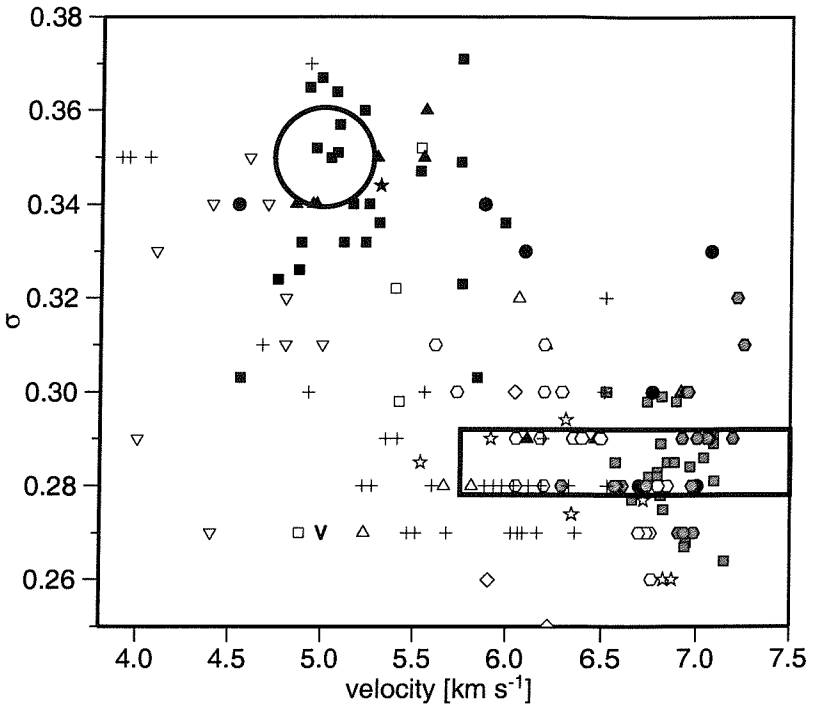

Figure 6.5: Poisson's ratio against P-wave velocity for serpentinites (black), basalts (white) and gabbro (grey) samples; crosses indicate altered basalts. Measurements from Miller and Christensen (1997) (squares), Christensen (1978) (triangles), Christensen (1966) (circles), Christensen and Shaw (1970) (diamonds), Salisbury and Christensen (1978) (hexagons), Planke et al. (1999) (inverted triangles), Christensen (1996) (stars), Johnston and Christensen (1997) (crosses) and seismically defined for basalts ('v') Minshull (1993) and made at 60 MPa (0.6 kbar), the approximate lithostatic pressure at 5 km below top basement, and ambient temperature except for Christensen (1996) and Johnston and Christensen (1997) which were made at 200 MPa. The range of V_p vs. Poisson's ratio for 50-120 km in the velocity model presented here (Figure 5.9) is shown for the upper 1 km only (black circle) and for the lower high velocity layer (black rectangle). There is considerable scatter in the data, but for V_p <6 km s^{-1} serpentinites can be clearly distinguished from basalts.

Cannat, 1993; Dick et al., 2003). The initial spreading rate at Goban Spur sits firmly within this classification. A very thin magmatic crust (~1 km), underlain by 5 km of serpentinised mantle, could fit the observed velocity and magnetic structure, but is incompatible with the modelled Poisson's ratio structure. Conversely a 1 km thick serpentinite upper layer underlain by magmatic material is consistent with the Poisson's ratio values, but does not fit the predicted magnetisation structure. To reconcile these competing geophysical observations I suggest that basaltic melt is distributed throughout a serpentinite upper layer ~1 km thick and underlain by 5 km of gabbro and/or serpentinised mantle.

This may allow strain focusing in the weaker serpentinite during extension, limiting stress build-up within the brittle crust. Brittle failure would occur more regularly, but cause smaller displacements which could assist the formation of relatively low relief at top basement. However, such a model does not provide major fluid pathways within basement to allow the extensive serpentinisation that we observe at depth. It is hard to understand how diffuse faulting through serpentinite would allow large volumes of fluid to penetrate deeply, as the serpentinisation process results in expansion of the altered rock and closure of the fluid pathways (Section 2.3). No major faults cut down from top basement through this region and I conclude that this region is not oceanic crust formed at an ultra-slow spreading rate. This argument is is supported empirically by the presence of 70 km of low basement relief that has not been observed elsewhere on ultra-slow spreading oceanic crust (e.g., Dick et al., 2003).

Highly thinned continental crust hypothesis

The presence of highly thinned continental crust forming a transition zone has been proposed at several margins e.g., Galicia Bank (Sibuet et al., 1995). P-wave velocities up to 5 km into basement on this line are consistent with those predicted for highly thinned upper continental crust (Whitmarsh et al., 1986), a conclusion supported by the absence of reflective lower crust in the intermediate zone. The lack of tilted fault blocks and continental layering observable on the seismic reflection section (Figure 5.26) strongly oppose this conclusion. Heat flow is lower than expected and suggests that, if the region consists of continental crust, Goban Spur was a lower plate margin in a simple shear rifting regime (Louden et al., 1991).

The high velocities at depth could in principle be attributed to underplating by highly fractionated ultramafic intrusives (e.g., White and McKenzie, 1989). However, in this case, such velocities would be associated with a much thicker extrusive layer than that observed. Therefore if the upper layer consists of thinned continental crust, we would interpret the layer beneath as serpentinised mantle. In general the basement from 50-120 km has a low topographic expression and appears mostly unreflective and dissimilar to the adjacent continent so we conclude that intermediate zone (ii) does not consist of thinned continental crust.

Exhumed mantle hypothesis

The presence of serpentinised peridotite at or near the top of basement of rifted margins has been described on the West Iberia margin on the basis of seismic reflection and wide-angle velocity models (Dean et al., 2000), drilling of basement highs (Whitmarsh and Sawyer, 1996; Whitmarsh and Wallace, 2001) and magnetic modelling (Russell and Whitmarsh, 2003). P-wave velocities range from 8.0 km s^{-1} for unserpentinised mantle to 5.0 km s^{-1} for 100% serpentinisation (Miller and Christensen, 1997). The observed velocities of 4.5-7 km s^{-1} fit within this range, slightly lower than predicted velocities at top basement may be attributed to intense fracturing and brecciation or further alteration of serpentine (Section 2.3).

Velocities of 7.2-7.6 km s^{-1} exist 5-8 km below top basement, comparable to the values (7.3-7.9 km s^{-1}) modelled 2.5-6 km into basement beneath the West Iberia margin (Chian et al., 1999; Dean et al., 2000) (Figure 6.6a). At both margins the high velocities coincide with regions of lower relief basement than the surrounding crust; ~100 km wide on IAM-9 (West Iberia) and ~70 km at Goban Spur. Whitmarsh et al. (2001a) interpret this low relief basement as a detachment zone along which mantle was exhumed. Localised roughness is considered to result from rafted fault blocks on the basis of continental material recovered from ODP drill Sites 901, 1065 and 1069 (Whitmarsh and Sawyer, 1996; Whitmarsh and Wallace, 2001) and their seismic reflection characteristics (Hölker et al., 2003). Similar features do not exist at Goban Spur where top basement of intermediate zone (ii) is continuous, smooth and unreflective.

Poisson's ratio is high through the top of intermediate zone (ii) from 50-120 km. This may indicate material with a lower rigidity such as serpentinite, for which Poisson's ratios of 0.32-0.38 predominate. Based on *in-situ* sampling and laboratory measurements made at 60 MPa and ambient temperature, serpentinite can be distinguished from basalts on the basis of their Poisson's ratio for V_p <6 km s^{-1} (Figure 6.5).

Magnetisations of ~3 A m^{-1} are consistent with remanent magnetisations recorded from individual serpentinite samples from the Mid-Atlantic ridge and the Hess Deep near the East Pacific Rise by Oufi et al. (2002) for serpentinisation >75%, and observed at the Southwest Indian Ridge (Sauter et al., 2004), but contrast with the zone of exhumed mantle off Iberia where low magnetisations (<1.2 A m^{-1}) have been observed (Zhao, 1996; Zhao et al., 2001; Russell and Whitmarsh, 2003) and with the ultra-slow spreading Gakkel Ridge, and segments of the Southwest Indian Ridge, for which weak magnetisations have also been

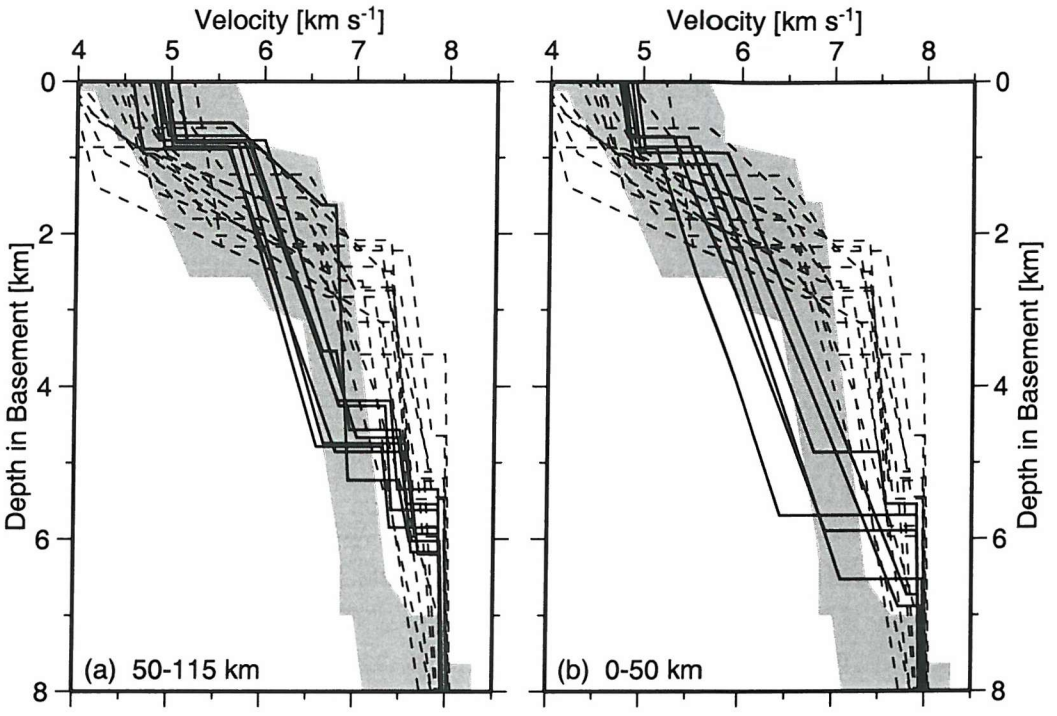

Figure 6.6: Velocity-depth profiles at Goban Spur for (a) Intermediate zone (ii) (50-115 km) and (b) intermediate zone (i) (0-50 km) compared to profiles through the Southern Iberia Abyssal Plain transition zone (dashed lines) (Chian et al., 1999; Dean et al., 2000). The grey shaded region indicates the velocity bounds for normal oceanic crust aged 59-144 Ma (White, 1992).

observed (Vogt et al., 1989; Dick et al., 2003). Due to the low sedimentation rate at Goban Spur immediately post rifting (1.3-13.5 m m.y.$^{-1}$: de Graciansky and Poag, 1985) the serpentinites observed here were in contact with seawater for a prolonged period, allowing the serpentinisation process to continue, resulting in the destabilisation of iron-rich serpentine (>6% FeO) to iron-poor serpentine (2-3% FeO) and the crystallisation of magnetite from the free iron (Oufi et al., 2002).

The exhumed mantle interpretation for intermediate region (ii) at Goban Spur fits the observed velocity structure by variations in the extent of serpentinisation with depth and can explain the high velocity layer 5-8 km into basement. Serpentinisation may be encouraged by water percolation along deeply penetrating faults as mantle is exhumed. Models considering mechanisms of final break-up are considered in Section 6.2.4.

6.2.2 Composition of intermediate zone (i) (0-50 km)

The P-wave velocity model shows upper basement to be laterally continuous from 0-120 km across the margin, but there are some important differences between the two regions that support a different interpretation for the crustal structure between 0 and 50 km.

At ~50 km basement abruptly changes depth, rising above the adjacent basement by ~400 m and with a much increased roughness of 216 m (Figure 5.24*a*). Poisson's ratio at top basement is 0.28-0.29 between 0 to 50 km. This is within the range of typical Poisson's ratio for layer 2 basalts (e.g., 0.27±0.01: Minshull, 1993) (Figure 6.5) or 100 Ma oceanic layer 2A (0.28: Johnston and Christensen, 1997; Shaw, 1994) and contrasts with the higher values identified between 50 and 120 km. The interpretation of upper basement as basaltic crust is supported by westward dipping faults that bound the ridges (Figure 5.27*b*) and resemble inward dipping faults from slow-spreading ridge axial regions. Mantle velocities are reached only 5 km into basement; the low crustal thickness is consistent with our earlier conclusion that this region was formed during a period of ultra-slow spreading with normal mantle temperatures.

The high velocity layer is not present in the velocity model between 0 and 40 km; the increased amplitude of arrivals from this region distinguish them from high velocity layer arrivals. Velocities of ~7 km s^{-1} are present at depth in this part of the velocity model which are sampled by two instruments, 13 and 15, but unfortunately ray coverage is not sufficient through this region to define the velocities and velocity gradient with much certainty and are therefore poorly constrained. Arrivals turning deep between 0 and 50 km have a high amplitude and are easily distinguished from the consistently low amplitude arrivals from the high velocity layer. A change in the appearance of crustal arrivals either side of instrument 11 from clearly separable phases defined by gradient changes at model distances <60 km to arrivals with a continuous increase in apparent velocity with depth (Section 4.5; Figure 4.22) is strong evidence for a lateral change in margin composition. A density change at 40 km is inferred from the gravity data (Figure 5.20), consistent with the disappearance of the high velocity layer.

6.2.3 Decompression melting during continental rifting

The 1 to 1.5 km thick basaltic body on the Goban Spur margin is best explained by decompression melting during extension. Its location at the foot of the continental slope implies

emplacement towards or at the end of continental rifting. Accurate dating is not yet available for these rocks due to extensive alteration, the earliest sediments overlying these basalts are late Cenomanian post-rift chalks (Site 551: de Graciansky and Poag, 1985). Contrary to previous interpretations this body does not represent the onset of sea-floor spreading (e.g., Horsefield et al., 1994); a 70 km wide zone of exhumed mantle with little or no evidence for melting has been identified seaward of this body.

An analysis of crustal reflectivity suggests that continental thinning occurred by pure shear at Goban Spur (Peddy et al., 1989) (Section 1.3). The presence of continental crust with a thickness of ~3.5-4 km implies whole crust stretching factors (β) of 8 to 10, an estimate that is supported by a whole crust stretching factor of 4-10 calculated by Davis and Kusznir (2004). The method of Bown and White (1995) was used to predict the amount of melt produced by decompression melting during pure shear extension assuming a rift duration of 14-22 m.y., β=8-10, an initial continental thickness of 125 km and an asthenospheric potential temperature of 1300° C. A melt thickness of 0.2-1.3 km is predicted (Figure 6.7), consistent with the observed melt volume over continental crust. This compares to similar calculations by Bown and White (1995) assuming a rift duration of 16-27 m.y. and β=3-5.5 that predict no syn-rift melting during extension at Goban Spur (Figure 6.7). The difference between these predictions is caused by the improved constraints within this thesis increasing the total amount of thinning required and decreasing the rift duration.

6.2.4 Melting during mantle exhumation and models of continental break-up

From the velocity model (Figure 5.9) a maximum melt thickness of 4 km throughout intermediate zone (ii) is calculated: assuming 25% melt products within the 1 km thick serpentinite upper layer and a magmatic composition for the remainder of upper basement (<4 km thick). This is a maximum estimate as Poisson's ratio values do not support the presence of seismically resolvable volumes of melt within the top 1 km of upper basement and magnetic modelling does not require magnetic crust beneath the top 1.5-2 km of basement. The high velocity lower crust is not believed to contain any melt products for the buoyancy reasons that follow and the magnetic modelling already referred to. The density of basaltic melt is dependent on the degree of fractionation, but a density of 2.8 $\times 10^3$ kg m^{-3} is close to the observed maximum (Figure 2: Hooft and Detrick, 1993); this density corresponds to a velocity of ~6.5 km s^{-1} in serpentinite. If melt was to have

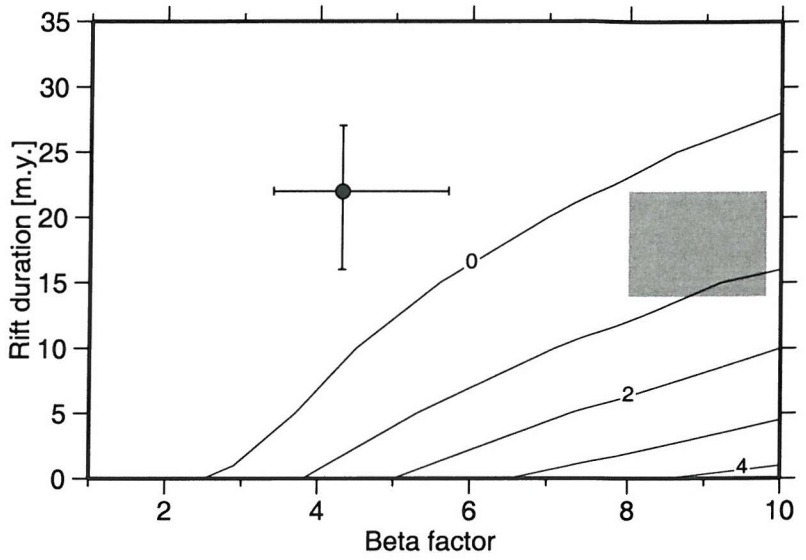

Figure 6.7: Variation of predicted melt thickness with stretching factor and rift duration. Continental lithosphere is initially 125 km thick and in thermal equilibrium with the underlying asthenosphere with a potential temperature of 1300° C. Final melt thicknesses are contoured every 1 km, rifting parameters for Goban Spur are shown by the grey box; a melt thickness of 0.2-1.3 km is predicted. The black circle, shown with error bars, gives the melt volume predicted using the rift parameters of Bown and White (1995).

pooled within the serpentinite basement its natural buoyancy level would be above the high velocity layer. No strong reflection event from ponded or intruded basalts can be identified at this level and reflections from the base of the high velocity layer are unlikely to be melt related due to the near mantle velocities observed at this depth. Melt volumes of ~4 km thickness are consistent with theoretical models of melt generation as a function of spreading rate at mid-ocean ridges (Figure 2.8). Even if this melt thickness is a gross over-estimate, recent work by Dick et al. (2003) has shown that at spreading rates <10 mm yr^{-1} amagmatic oceanic crust can be emplaced consisting largely of serpentinite, exhumed within oceanic core complexes and identified at several slow spreading mid-ocean ridges (e.g., Atlantis Bank: Dick et al., 2000). The relationship between mantle exhumation immediately post-rift and during ultra slow sea-floor spreading is not clear, but it seems likely that similar processes would operate under comparable extensional conditions.

This broad region of exhumed mantle was emplaced seaward of the continental slope and

the basalt body during a long period (~20 m.y.) of amagmatic extension. The lack of melt at Goban Spur can be explained by two reasons:

1. Asymmetric final break-up with melting focused on the Flemish Cap margin.
2. Symmetric break-up with no melting on either margin.

The evidence does not yet exist to conclude which of these mechanisms for the transition from continental rifting to sea floor extension was active between Goban Spur and Flemish Cap; however, a brief discussion of the models and their implications follows.

Asymmetric break-up

Late stage continental thinning occurred in an asymmetric manner with rapid necking at Flemish Cap and more gradual crustal thinning at Goban Spur (Section 6.1). If lithospheric thinning occurred by pure shear then lateral changes in Moho shape reflect the base lithospheric configuration; mantle upwelling would be focused on a narrower region at Flemish Cap (Figure 6.8*a*), which may allow less conductive cooling per unit of upwelling mantle, and encourage melting (Minshull et al., 2001). Mantle upwelling was spread over a broader region at Goban Spur which increased heat conduction and limited melt formation.

The basalt body was emplaced at the time of continental break-up; in an asymmetric model, following this initial pulse all other melt is restricted to the Flemish Cap margin where initial oceanic crust is formed (Figure 6.8*b*). Simple shear, or some detachment fault, is required to exhume mantle at Goban Spur and allow continued sea floor spreading at Flemish Cap. This detachment fault produces the low relief basement observed between 50 and 120 km on the Goban Spur margin. Any melt from the exhuming mantle rises and is emplaced on the overlying (Flemish Cap) margin.

Extension continues in this manner for ~20 m.y. resulting in oceanic crust on one half of the margin pair and exhumed mantle on the other (Figure 6.8*c*). Melt volume increases with time on the Goban Spur margin to produce 50 km of oceanic crust before anomaly 34r is reached; this corresponds to the region of ridges, but likely contains <4 km of melt products. There may be variations in the volume of melt produced throughout this time on the Flemish Cap margin that cannot be resolved with the present data. Due to the low extension rate it is possible that the crustal thickness is small and serpentinite comprises a substantial portion of the crust. An increase in full spreading rate after A34r allows increased melting and produces crust more comparable to 'normal' oceanic crust.

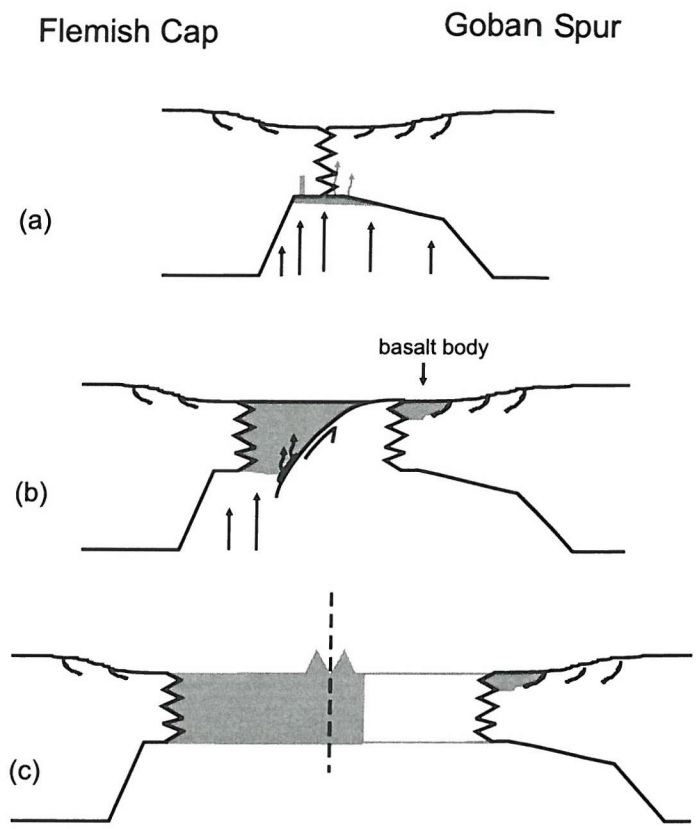

Figure 6.8: Asymmetric rifting between Goban Spur and Flemish Cap. (a) Asymmetric crustal thinning allows increased conduction and restricted melting beneath Goban Spur. Melt pools beneath the rift axis, is intruded, and the basalt body is emplaced during continental separation. (b) Top-to-the-west detachment fault exhumes mantle onto the Goban Spur margin. Melt is concentrated on the Flemish Cap margin where oceanic crust is produced (grey region). (c) Situation at anomaly 34r. 70 km of mantle has been exhumed at Goban Spur (white region in grey box) and 50 km of oceanic crust is produced further seaward before full sea-floor spreading begins at anomaly 34r.

The model in Figure 6.8 shows a top-to-the-west detachment exhuming mantle, but the observed features could equally be explained by a top-to-the-east detachment fault (Figure 6.9*b*). Extension is then initially focused on the eastern edge of the rift zone where mantle is exhumed by a top-to-the-east detachment; this fault would likely exist at the base of the crust as there is no evidence for faulting through or disruption of the lower continental crust. Little syn-rift melting occurred, intruding the base of thinned continental crust, and the basalt body is supplied by melting of the exhuming mantle at the base of the crust before it enters the brittle regime (Pérez-Gussinyé and Reston, 2001a); the basalt body may be constructed from multiple phases of melting and formed over several m.y. The

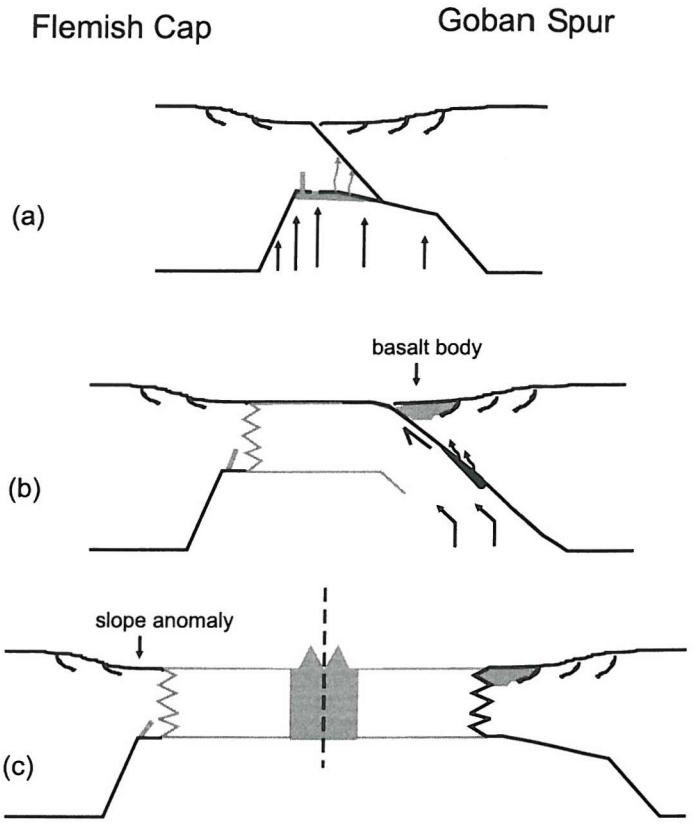

Figure 6.9: Alternative model for mantle exhumation at Goban Spur. A top-to-the-east detachment fault exhumes sub-continental mantle between Flemish Cap and Goban Spur (b). (c) The focus of extension jumps westward to the centre of the rift; seafloor spreading at an ultra-slow rate produces the 50 km wide region of ridges on both margins before full seafloor spreading begins at anomaly 34r.

earliest sediment deposited on the basalt body is late Cenomanian (Site 551: de Graciansky and Poag, 1985), some 10 m.y. later than post-rift sediment observed seaward of the basalt body at DSDP Site 550. In the top-to-the-west detachment model, melt is derived from the asthenosphere and should show no continental contamination, consistent with the results of Maury et al. (1985) which show a N-MORB signature. Melts forming the basalt body in the top-to-the-east detachment model may show continental contamination (Figure 6.9*b*), but the model does not necessitate this as the basalts could be directly emplaced on top of the continent.

A total of 140 km of mantle is exhumed before the locus of extension shifts to the center of this zone (Figure 6.9*c*) and symmetric spreading begins. Limited melting allows

early oceanic crustal accretion and the formation of the 50 km wide ridge region on both margins. The final situation leaves exhumed mantle at top basement at Flemish Cap and Goban Spur. Serpentinite at Flemish Cap is exhumed first and is likely to show a greater extent of serpentinisation that at Goban Spur. A difficulty with this model is that sediments onlap westwards onto top basement across intermediate zone (i) and (ii) (Figure 5.26), suggesting that older sediments are situated nearest to the continental slope. Late Albian to middle Cenomanian mudstones recovered at Site 550 overly basalt, not serpentinite, and can be considered synchronous with melting and not mantle exhumation at this location; a degree of along-margin variability in melting is required by these data and is compatible with this model.

The landward dipping reflector and magnetic 'slope anomaly' observed at Flemish Cap (Section 6.1) may be associated with the formation of oceanic crust at Flemish Cap and emplacement of the basalt body on Goban Spur in the top-to-the-west detachment model; with top-to-the-east detachment faulting they may represent small volumes of syn-rift melting intruded into the lower crust.

Symmetric break-up

The observed features can also be explained by a model of symmetric sea-floor extension similar to that proposed by Davis and Kusznir (2004); this is supported by the obvious symmetry between top basement structures visible on the MCS data on both margins (Section 6.1; Figure 6.3). Asymmetry in mantle upwelling during late stage continental rifting is allowed, but not required, in this model; the low extension rate may allow sufficient cooling to impede melt production beneath both margins. Some melt is produced and pools at the base of thinned continental crust, before being intruded and eventually extruded to produce the basalt body (Figure 6.10*a*). The landward dipping reflector and magnetic anomaly at Flemish Cap may be related to this melting event; a near vertical dyke intruded beneath Flemish Cap will rotate to dip landward once the margin has undergone post-rift thermal subsidence. It is not clear whether post-rift subsidence alone in enough to account for the observed angle of dip, intrusion may occur along a zone of weakness, parallel to the dipping base of thinning crust.

Extension continues symmetrically about the Mid-Atlantic Ridge at 10 mm yr^{-1} (f.s.r.); sea floor spreading is initiated, but at an ultra-slow spreading rate which allows the formation of thin crust consisting largely of serpentinite with few melt products (Figure 6.10*b*).

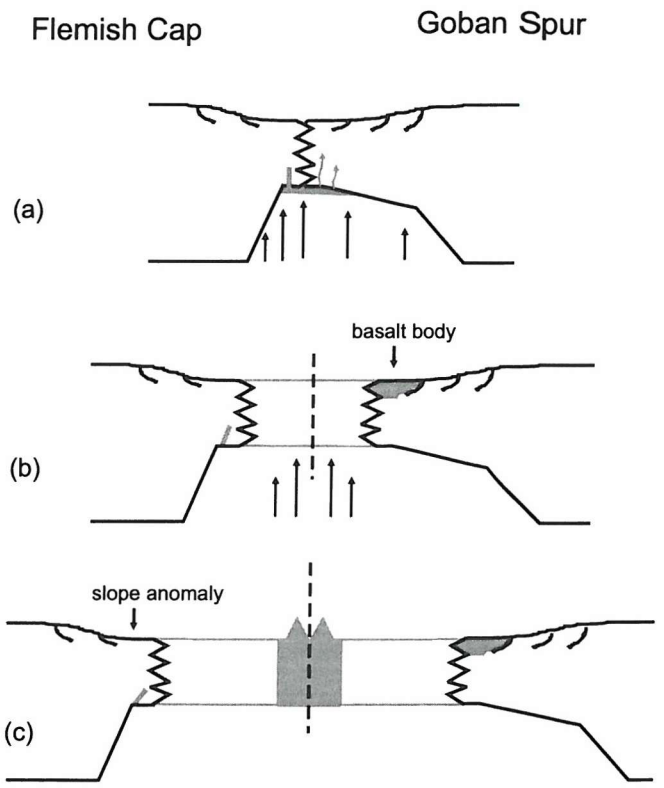

Figure 6.10: Symmetric spreading model for extension between Flemish Cap and Goban Spur. (a) Decompression melting beneath the rift axis allows limited melt to pool at the base of the crust. Intrusion occurs at the base of the crust on both margins. (b) Melt migrates to the surface at Goban Spur, forming the basalt extrusives at the foot of the continental slope. Symmetric spreading continues at 10 mm yr^{-1} (f.s.r.) to emplace 70 km of serpentinised peridotite (white in grey box) on both margins. (c) 50 km of oceanic crust with an increased magmatic content (grey) is emplaced before anomaly 34r is reached.

Sea floor spreading forming significant volumes of magmatic crust begins after 70 km of serpentinite have been emplaced on both margins (Figure 6.10*c*). The spreading rate probably remains unchanged, not increasing until anomaly 34r is reached. This zone of increased magmatism is equivalent to intermediate zone (i) at Goban Spur and suggests a basaltic/serpentinite composition for initial oceanic crust. Melting models (Figure 2.8) predict a 2-5 km thick magmatic crust for a spreading rate of 10 mm yr^{-1}, consistent with the presented wide-angle velocity model (Figure 5.9).

Further studies are required in order to distinguish between these rifting models. A detailed examination of the crustal structure at Flemish Cap should be made; a wide-angle survey with dense instrument coverage was carried out during 2002 (*CCGS Hudson*

cruise 2002-11) which, when modelled, will give excellent constraints on crustal velocities and allow more accurate migration of existing MCS data. Detailed magnetic (Srivastava et al., 1988b) and satellite derived gravity data (Sandwell and Smith, 1997) also exist over this region. Accurate dating of extrusive volcanics from the dredge site (anomaly 34r) and DSDP Site 551 would confirm the relative timing of volcanic activity; when combined with detailed geochemical analysis, the transition between sub-continental and N-MORB melt sources might be defined.

6.3 Goban Spur conclusions

A wide-angle seismic survey combined with normal incidence seismic data, gravity and magnetic modelling from the Goban Spur rifted margin and integrated with basement sampling from DSDP Leg 80 leads to the following conclusions.

1. A 70 km wide zone of exhumed mantle is identified between thinned continental and oceanic crust. This zone exhibits very low basement relief, P-wave velocities of 4.5-7.6 km s^{-1} and high Poisson's ratio (0.34-0.36) within the top 1 km of basement.

2. Observed velocities correspond to extent of serpentinisation 100-50% up to 5 km beneath top basement and <25% from 5-8 km into basement.

3. Magnetisation is strongest within the top 1-1.5 km of basement, 2-3 A m^{-1}. We attribute this to intense serpentinisation during a prolonged contact with seawater which encouraged the formation of magnetite by destabilisation of serpentinite to a less iron-oxide rich form.

4. Initial oceanic crust was first formed 70 km west of the continental slope and extends for 50 km. This crust is anomalously thin, ~5 km, and defined by small (~5 km wide, ~500 m high) ridges bounded by westward dipping faults, an absence of clear normal-incidence Moho reflections and velocities >7 km s^{-1} at depth. Normal oceanic crust is indicated by marine magnetic anomaly 34r, 120 km west of the continental slope and the appearance of a seismic reflection Moho.

5. The observed melt volume at the foot of the continental slope can be explained by decompression melting during thinning with β=8-10.

6. Continental break-up may have occurred in a symmetric or asymmetric manner. Potential models for margin development are presented, but insufficient evidence is available to conclude which mechanism operated between Goban Spur and Flemish Cap.

Chapter 7

Continental rifting at the North Biscay margin

The North Biscay margin bounds the western segment of the European plate within the Bay of Biscay and was formed by Cretaceous rifting and sea-floor spreading along an east-west ridge connected to the developing Mid-Atlantic Ridge by a triple junction at 14° W and 48° N (Section 1.4). The region has experienced a complex geological history and there is considerable uncertainty in the pre-drift position of the continents (Section 1.4.2). This study will examine two seismic reflection profiles across the North Biscay margin and attempt to constrain the timing of tectonic events here. The S-reflector (Section 1.4.5) will be examined and compared to a similar feature observed at the Galicia Bank margin and its role in continental rifting and break-up considered.

7.1 Multichannel seismic processing

7.1.1 Acquisition parameters

The *Continental Margin* (CM) survey was carried out in 1977 along transects across the UK and Irish continental margins from 56° N to ~47° N. A total of ~4350 km of multi-channel seismic data were acquired with the vast majority of these data located across the Porcupine and Goban Spur margins in the North Atlantic and the westernmost portion of the North Biscay margin in the Bay of Biscay (Figure 7.1). Multichannel lines CM-13, 14 and 15 have a ~100 km separation along the margin with an orthogonal line, CM-16, parallel to the margin to tie the lines together (Figure 1.9). Previous geophysical studies have been focused along CM-14, coinciding with velocity models from wide-angle studies

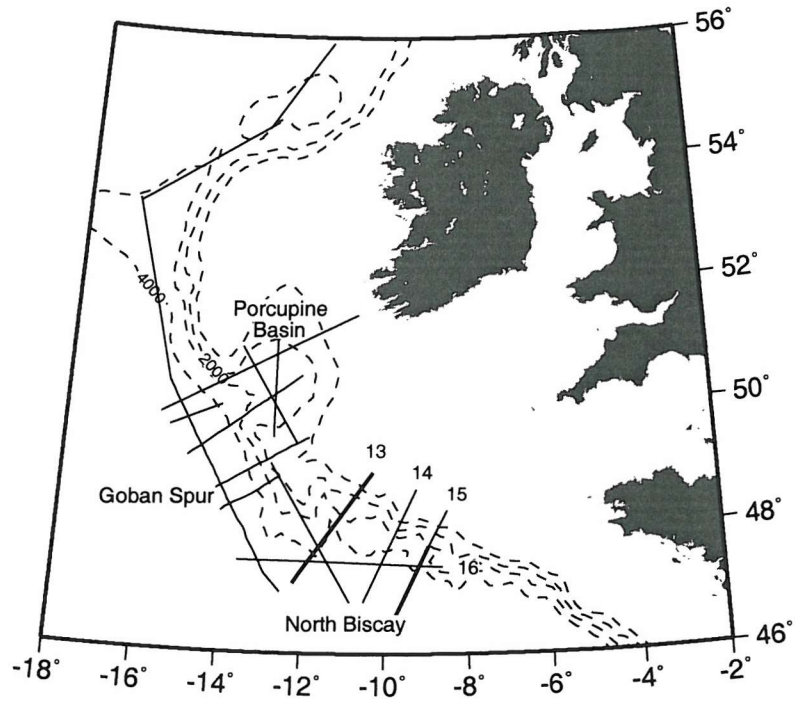

Figure 7.1: Seismic lines shot during the *Continental Margin* (CM) survey. Lines shown in bold are re-processed in this thesis. Bathymetric contour interval is 1 km.

(Figure 1.22; Avedik et al., 1982; Ginzburg et al., 1985; Whitmarsh et al., 1986). Lines CM-14 and CM-16 had a standard processing sequence applied at the time of acquisition and the resulting stacked sections were used for comparison.

The CM data were acquired using an airgun source of total array volume 1511 in^3 at 1800 p.s.i., sufficient for good energy penetration and imaging within basement. The shot interval was 50 m; a towed streamer with 48 hydrophone groups recorded arrivals at offsets between 275 m and 2625 m (Figure 7.2). The data were binned with a CDP spacing of 25 m and a maximum fold of 24. The data were recorded in SEG-C format with a sample interval of 2 ms. A bandpass filter with a high cut of 124 Hz and a low cut of 8 Hz was automatically applied during recording to remove high and low frequency wave and ship noise. This low cut improves the SNR within the sedimentary column by removing the low frequencies and does not reduce the image quality within basement where high amplitude reflections are recorded at 7-9 s TWT on portions of these data (e.g., Avedik et al., 1982). Following acquisition, these data were converted to SEG-Y format and subsampled at

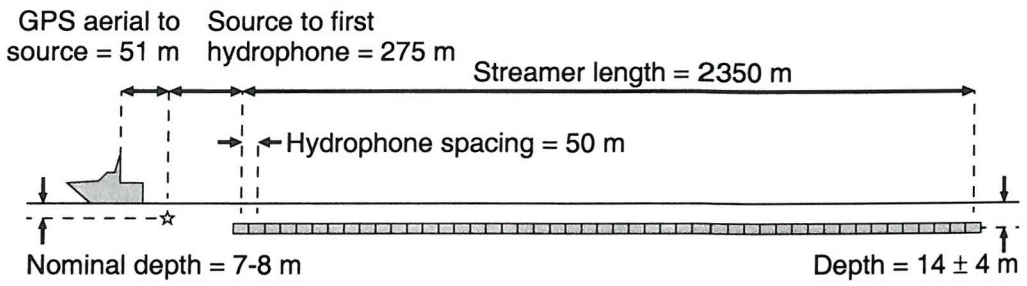

Figure 7.2: Source and hydrophone layout for the CM experiment. The source location (star) marks the centre of the airgun array and was towed shallower than the streamer. An identical survey arrangement was used for all CM lines.

4 ms; this corresponds to a Nyquist frequency of 125 Hz so no further high cut filters were required to prevent aliasing of these data.

Lines CM-13 and CM-15 were selected for further study because they appear to show features of interest that have been missed by the concentration of studies along the profile CM-14. Lateral changes observed between the profiles may be important for constraining margin development. Given the finite time period available and the concentration of geophysical studies along CM-14, it was not chosen to re-examine this line in detail. Lines CM-13 and CM-15 were reprocessed to provide a digital dataset to which multiple removal, migration and amplitude analysis techniques could be applied.

7.1.2 Standard processing sequence

A standard processing sequence was designed for the CM dataset (Figure 7.3) and successfully applied to CM-13 and CM-15. The desired final output were migrated sections in time and depth. A discussion of the processing procedure follows.

Pre-processing: Static corrections, trace editing and geometry installation

Field data were recorded with repeating three-digit shot numbers and with the seabed reflection relocated between 0 and 1 s TWT; the correct shot numbers were written into the trace headers and a shift applied to restore the first break to the correct water-bottom time in pre-processing. Fourteen auxiliary channels (49-62) were excluded and bad shots

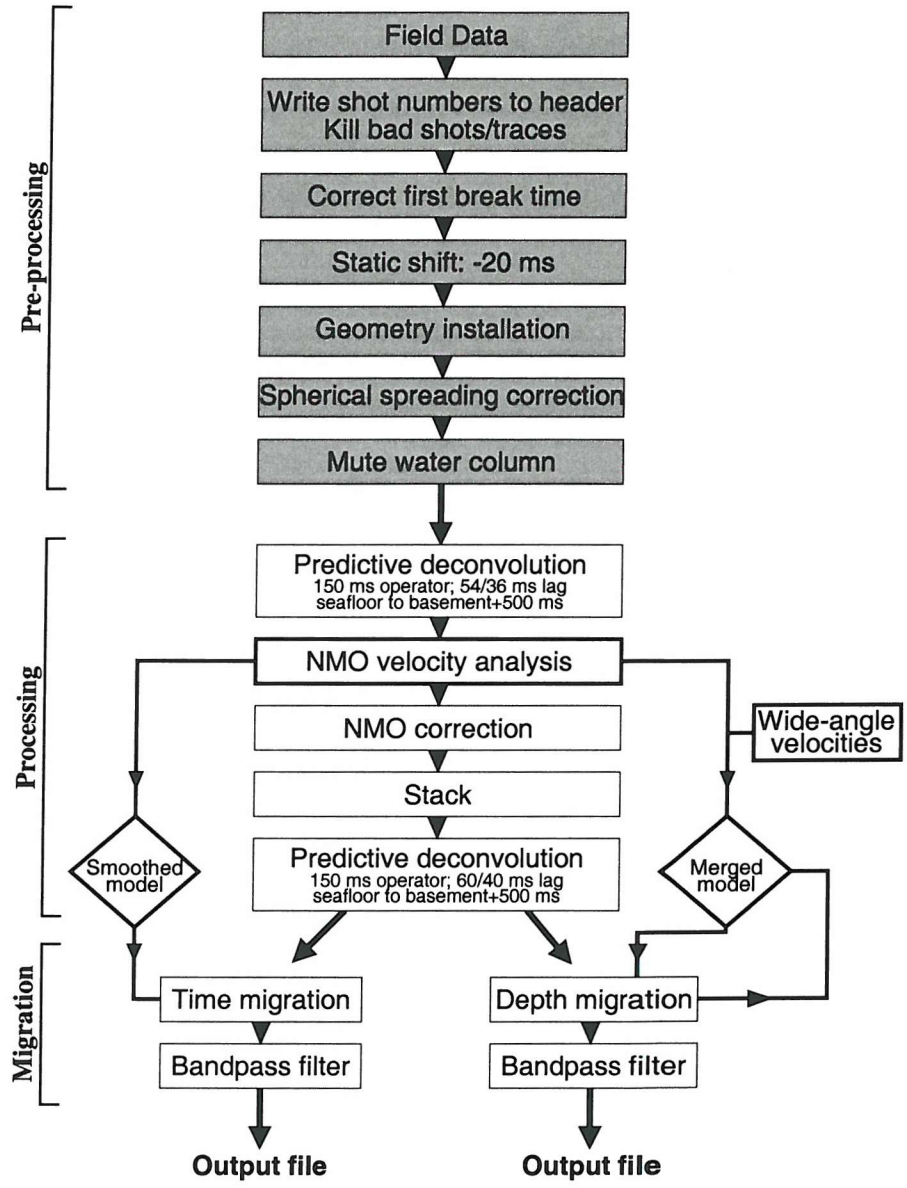

Figure 7.3: The processing sequence applied to the CM data in this study. Pre-processing steps (grey boxes) were completed in the shot domain and processing steps (white boxes) in the CDP domain or post-stack. Times quoted for predictive deconvolution are for the design window only and applied to the entire dataset; longer lag times were used in the shallow water regions where a higher amplitude sea-bed reflection is present with a longer period. An outer trace mute was applied during NMO correction to compensate for waveform stretching. Time migration was carried out using a smoothed stacking velocity model; depth migration required an iterative procedure to define the velocity model, at each step interfaces become more closely aligned with reflection events.

or traces were manually identified and killed (Figure 7.4). Geometry installation included writing the source-receiver offset into the trace header and calculating the CDP number according to the equation

$$\text{CDP No.} = (48 - \text{channel}) + ((2 \times (\text{shotpoint} - (\text{first\_shot} - 1))) - 1) \quad . \tag{7.1}$$

For CM-13, first_shot=1 so Equation 7.1 becomes

$$\text{CDP No.} = (48 - \text{channel}) + (2 \times \text{shotpoint}) - 1 \quad . \tag{7.2}$$

A spherical spreading correction was applied to recover true amplitudes. Amplitude decay was assumed to be due to expansion of a three-dimensional wavefront away from a point source as it passes through the subsurface, and was shown by Newman (1973) to be proportional to $1/v^2 \times t$, where v is the velocity and tends to increase with depth through the earth and is a function of time, t. This assumption is strictly only valid for a horizontally stratified earth as it does not compensate for the focusing and defocusing effects of lateral variations, but this approximation was shown to be valid for most real earth conditions by Hardage (1985). The velocity model necessary to accurately compute the spherical spreading correction is estimated by stacking velocity analysis; an initial pre-processing iteration is completed to determine this correction, followed by a second iteration which includes the spherical spreading correction. The water column was muted during pre-processing to remove spurious noise spikes.

Deconvolution before stack

Predictive deconvolution was applied pre-stack (DBS) in the shot domain to attempt removal of oscillatory multiples, particularly within the sediment column. A 150 ms operator with 54/36 ms lag was designed on the sediment column, from the sea floor to 500 ms beneath the basement reflection, and applied to the entire trace. Longer lag times (54 ms) were used where the seabed reflection has a high amplitude and longer period (shallow water) with a shorter lag applied to the rest of the dataset. A lag of 4 ms is equal to the sampling frequency and corresponds to spiking deconvolution however the seabed waveform is strongly minimum phase, not zero phase, and the lag must be at least equal to the period of the seabed reflection to enable accurate forward prediction. DBS was most effective on near-offset traces (Figure 7.5) and allowed improved arrival identification during velocity analysis.

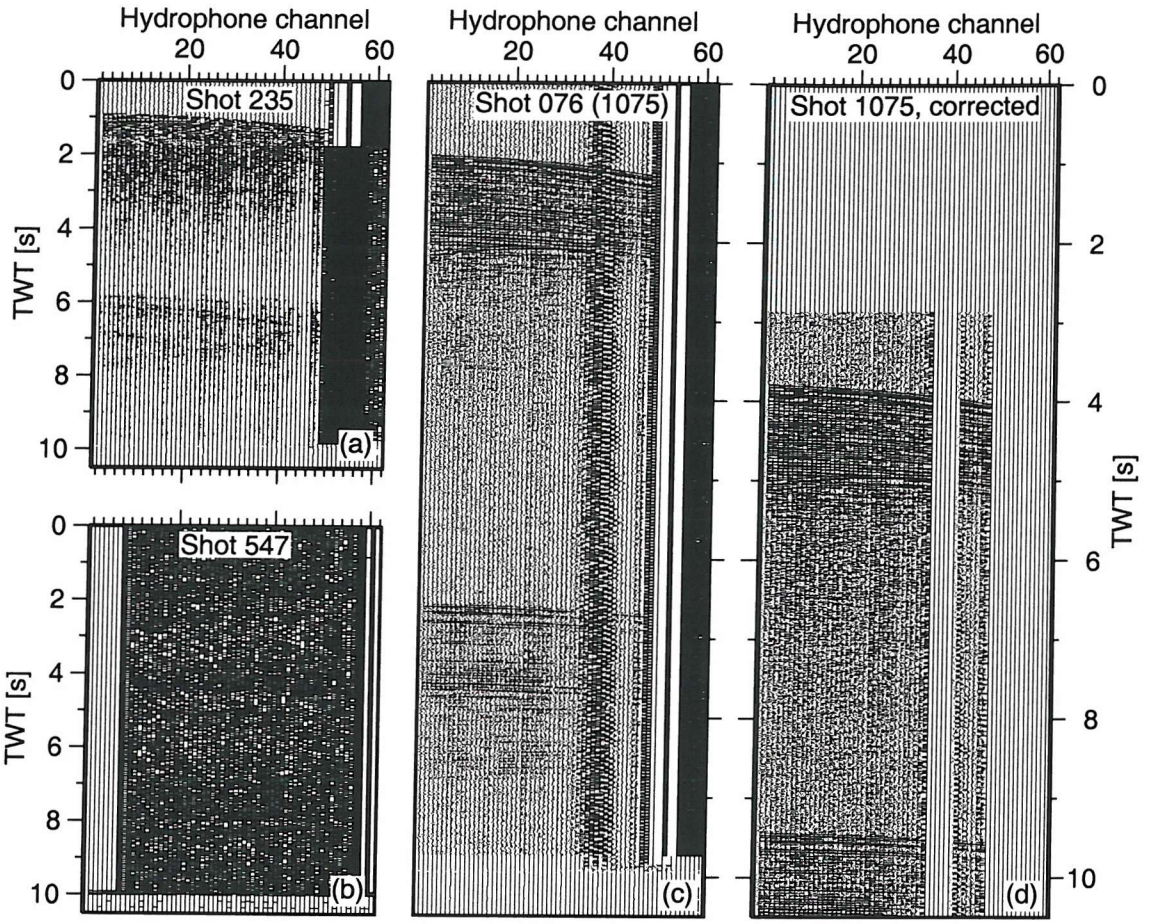

Figure 7.4: Examples of noisy data where (a) first break is present, but at a later time all channels abruptly stop recording strong arrivals and are overprinted by high frequency noise at, in this case, 1.6 s TWT. (b) All channels record high amplitude noise and no useful signal. Traces were killed if noisy along their entire length and a surgical mute applied if some signal was present on the trace. (c) Shot 1075 (originally recorded as 076) has six noisy traces within the gather (36-41); channels 49-62 are auxiliary channels and not used in this survey. The first break is adjusted to between 0 and 1 s TWT during recording to maximise the storage of subsurface data for a fixed trace length and must be corrected for during pre-processing. (d) Corrected shot 1075. Bad traces have been killed or muted and a static correction applied to position the first break at the correct time. These shots are taken from line CM-15. The majority of shots recorded clear arrivals on all (1-48) hydrophone channels.

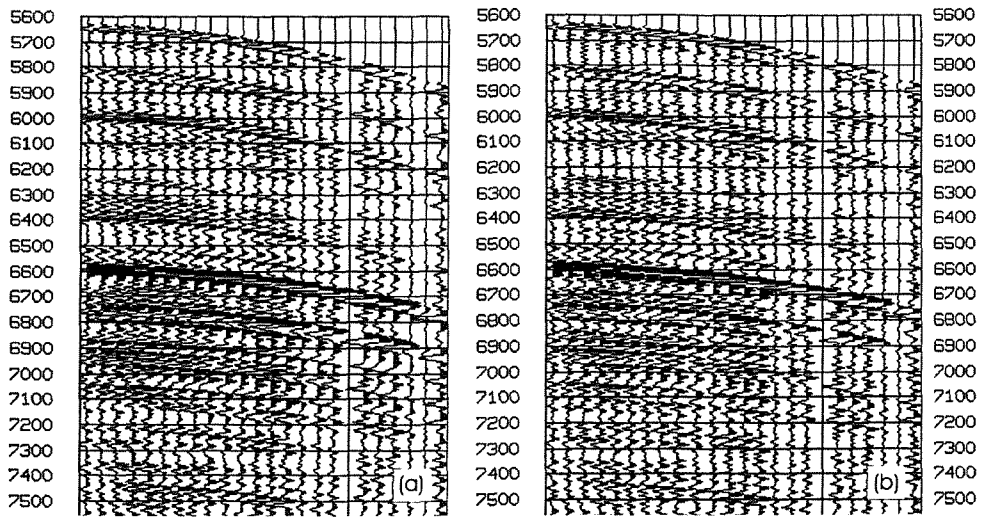

Figure 7.5: (a) CM-15 shot gather for SP 5200 and (b) the identical shot gather with predictive deconvolution before stack applied. The deconvolution operator is 150 ms long with a lag of 36 ms, designed over the sediment column and applied to the entire trace. Improvement can be seen at near offsets where multiples have been diminished e.g., at 6950 ms.

NMO and stacking velocity analysis

Velocity analysis was carried out every 100 CDPs (~2.5 km) and linearly interpolated between sample locations. Stacking velocity analysis determines a RMS velocity-time function for CDP gathers based on the normal moveout (NMO) of reflections with increasing offset. Semblance plots are produced for NMO corrected traces at a range of velocities: high coherency for a time-velocity pair identifies the ideal stacking velocity for the reflection event at that time (Yilmaz, 1987). Positive breaks were picked as the onset of an arrival; where maximum coherency was for negative amplitudes an adjustment was made by close examination of the corrected gather. The NMO correction stretches each trace by an amount increasing with offset, so that when the correct velocity is applied the corrected event appears at the same time on each trace. Some common sense must be applied during stacking velocity analysis: the water column multiple produces a strong reflection event with a low apparent velocity. Velocity tends to increase with depth so velocities ~1.5 km s^{-1} beneath the seabed are unlikely to be real events and were not picked as such. Multiples with more complex paths are also present and care was taken to avoid picking them as primary arrivals. Stacking velocity analysis provides velocity control on the material above the picked event only. Reflections are generally sparse within basement

hence stacking velocity analysis provides little control on basement velocities and other constraints (e.g., velocities from wide-angle modelling) were used.

For a horizontally stratified subsurface the NMO traveltime correction, Δt_{nmo}, for a reflection recorded at offset, x, is given by

$$\Delta t_{nmo} = t(0) \left\{ \left[1 + \left(\frac{x}{v_{nmo}\ t(0)} \right)^2 \right]^{\frac{1}{2}} - 1 \right\} \quad , \tag{7.3}$$

where t_0 is the two-way traveltime at zero offset (normal incidence: $x = 0$) and v_{nmo} is the NMO velocity of the reflector. Assuming the offset is small compared to the depth of the reflector, v_{nmo} closely approximates the RMS velocity at the reflector (Yilmaz, 1987). For a layered velocity model, the interval velocity (v_{int}) within a layer, n, can be calculated from the RMS velocity at the layer according to the Dix equation (Equation 7.4) (Dix, 1955).

$$v_{int} = \left(\frac{v_{rms_n}^2\ t_n - v_{rms_{n-1}}^2\ t_{n-1}}{t_n - t_{n-1}} \right)^{\frac{1}{2}} \quad . \tag{7.4}$$

The NMO correction stretches each trace so that arrivals from horizontal reflectors appear flat within a CDP gather; waveform stretching can be large at far offsets, particularly in shallow water depths, and introduces noise to the section when stacked. To reduce signal degradation during stack, waveforms with >30% stretching are muted during the NMO correction: this harsh mute does not reduce the quality of the stack because the muted events are generally shallow, where there is good energy penetration and reflections have higher amplitudes and are well constrained at near offsets.

Stack and deconvolution after stack

These NMO corrected data were stacked within each CDP gather; amplitudes from all offsets within the gather are summed and the mean taken to give a single amplitude for the trace. Coherent arrivals interfere constructively while noise, both random and multiples, should interfere destructively, increasing the SNR.

Predictive deconvolution after stack was applied in a similar manner to DBS with a prediction lag of 60 ms in shallow water regions and 40 ms elsewhere. The operator, of length 150 ms, was designed on the sedimentary column and applied to the entire trace. Decon-

volution parameters were designed by testing on a small stacked panel and then applied to the entire dataset; small improvements in image quality are observed with decreased ringing through the sedimentary column (Figure 7.6).

7.1.3 Time migration

A post-stack Kirchhoff time migration was applied to these stacked data to collapse diffractions and improve the clarity of the resultant image. Post-stack time migrations are computationally fast and are not highly dependent on the velocity model used (Larner et al., 1981) allowing for quick and simple improvements to be made. The Kirchhoff time migration is compared to the Kirchhoff depth migration and relative advantages and disadvantages discussed in Section 7.1.4. The migration velocity model was based on the stacking velocities (Equation 7.4) and smoothed over 200 CDPs (5 km) horizontally and 0.5 s vertically; a smooth velocity model is essential to allow diffractions to be accurately collapsed. The migration velocity models for CM-13 and CM-15 are shown in Figures 7.7 and 7.8, overlain on the migrated sections and were applied at 90% of the velocity function to prevent over migration. This migration is successful at collapsing diffractions without introducing artifacts (migration smiles) to the section and significantly improves image quality within the sediment column and basement (Figure 7.6).

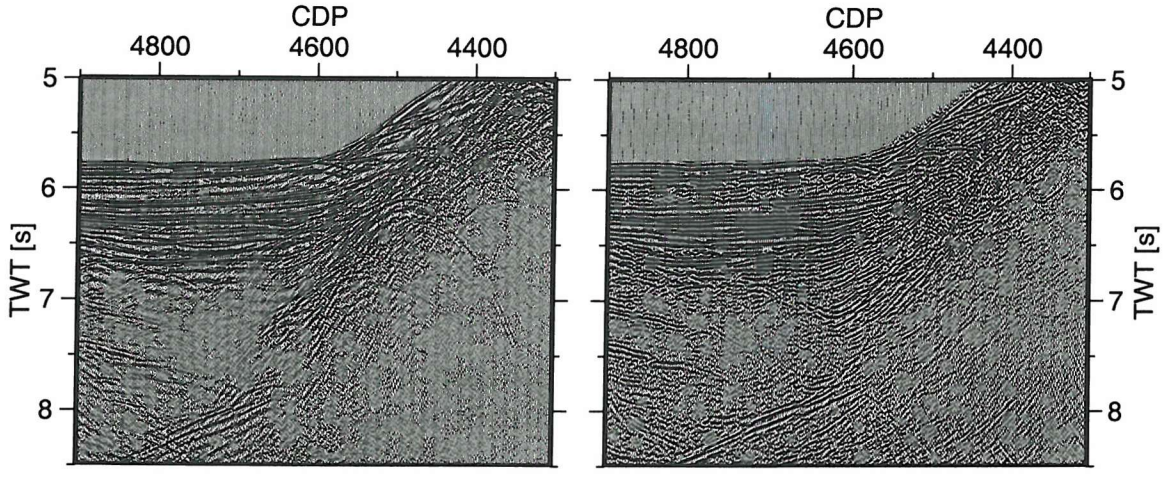

Figure 7.6: Panel of CM-15 (a) brute stack and (b) identical panel after deconvolution and post stack time migration with a bandpass filter with frequency bounds of 2-4-25-40 Hz applied. Ringing has been reduced within the sedimentary column improving the clarity of sediment reflectors. Diffractions have been successfully collapsed and reflectors within basement show greater lateral continuity.

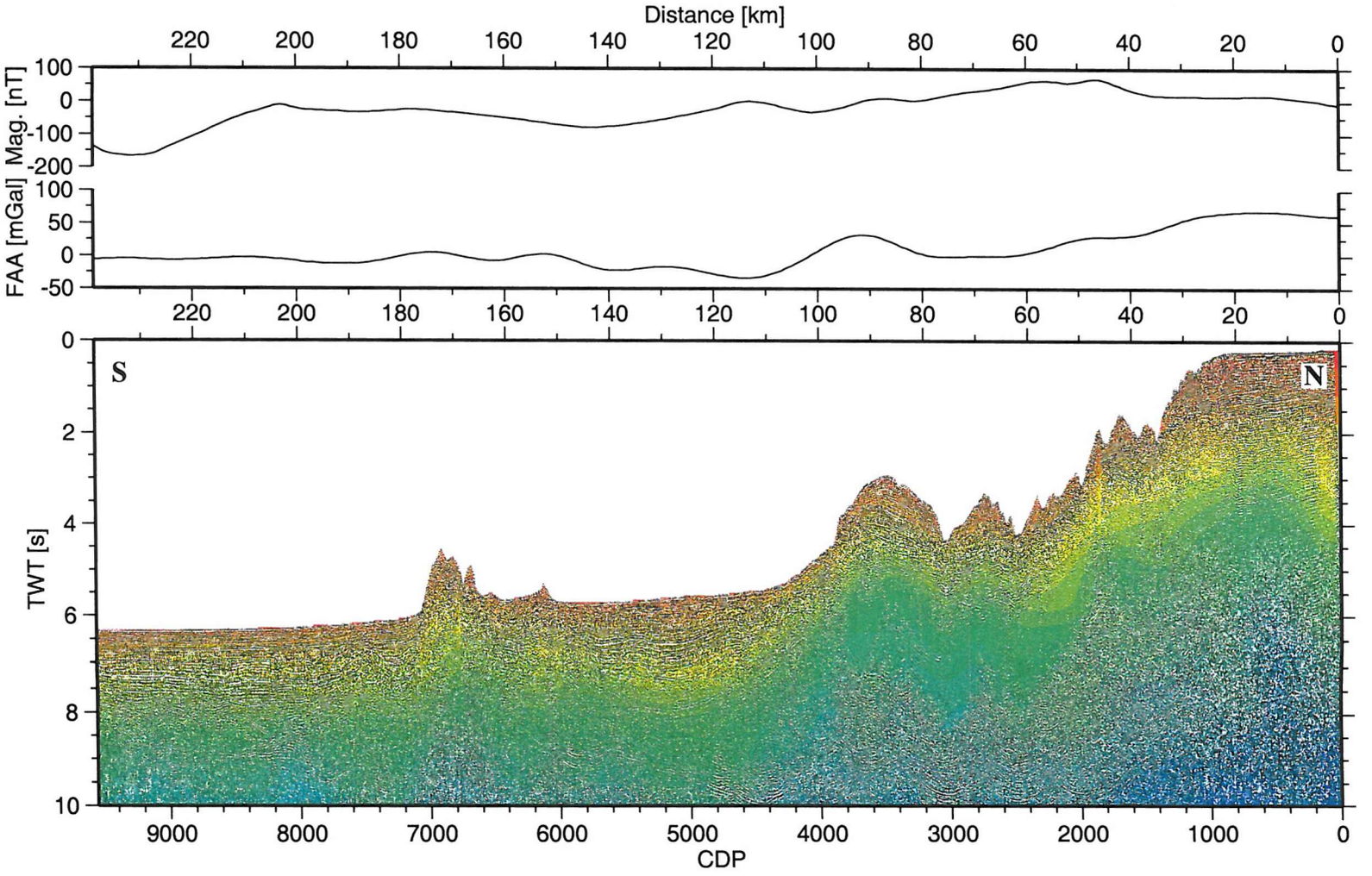

Figure 7.7: Time migration of line CM-13 overlain by the migration velocity model. Velocities were derived from analysis of normal moveout and smoothed over 200 CDPs horizontally and 0.5 s vertically. Gravity and magnetic anomalies along the line are small; the first marine magnetic anomaly is at ~220 km. An identical velocity scale was used as for CM-15 (Figure 7.8).

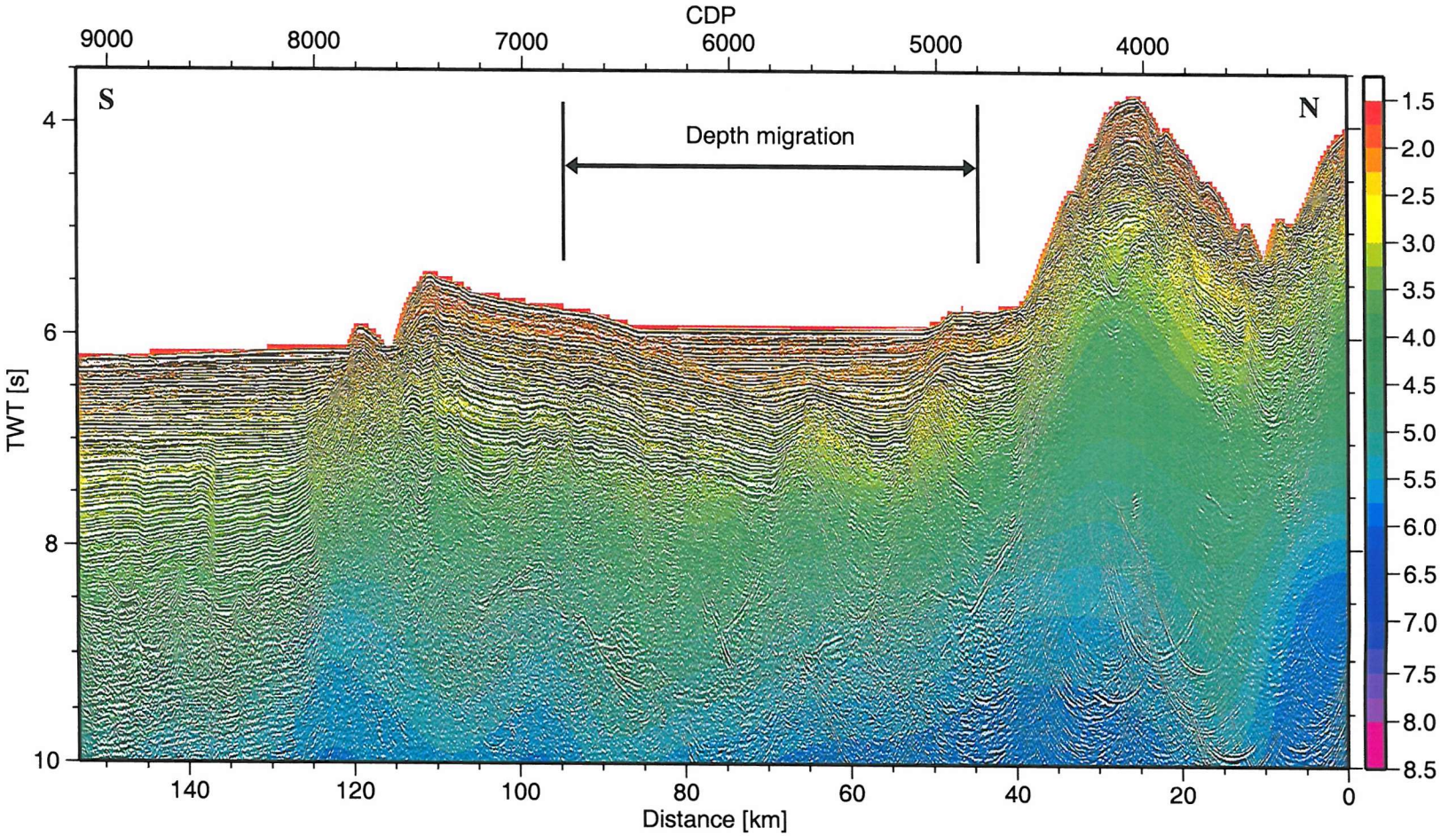

Figure 7.8: Time migration of CM-15. The migration velocity model is overlain; velocities were determined by stacking velocity analysis and smoothed over 200 CDPs horizontally and 0.5 s vertically. The panel selected for depth migration is shown within the vertical bars.

7.1.4 Depth migration

Depth migration of these seismic lines was attempted to produce a section where the geometry of reflectors better represents that of the subsurface by correctly locating energy within the section. This method assumes that the migration velocity model closely approximates the real earth. An iterative procedure (Figure 7.3) was used to define an accurate migration velocity model; after each iteration, the velocity interfaces become more accurately aligned with the corresponding reflectors. An accurate velocity model and depth migration were produced within six iterations, a procedure that takes considerable computational and user time to complete.

The Kirchhoff depth migration can be applied to data to collapse diffractions and reposition energy into its correct location. A summation of amplitudes is performed along the path of diffraction hyperbolae and the energy repositioned at the location and time of the apex of the hyperbolae (Figure 7.9). The shape of the diffraction hyperbolae used for summation are determined by solving the wave equation for the given velocity model. True amplitudes are calculated before migration is attempted (Section 7.1.2).

If the velocity varies with depth only, diffractions will have an approximately hyperbolic shape except at their far flanks (Yilmaz, 1987) and the apex of the diffraction curve will be located directly over the diffractor (Figure 7.9*a*, *b*). If horizontal velocity variations are introduced then the diffraction curve becomes asymmetric and the apex will be offset from the diffractor (Figure 7.9*c*, *d*) (Larner et al., 1981). Kirchhoff time migration assumes hyperbolic moveout so the diffraction will not be completely collapsed and energy is repositioned at an incorrect apex location (Judson et al., 1980; Yilmaz, 1987). Depth migration significantly improves on time migration by including a *thin lens term* (Claerbout, 1976) as well as a *diffraction term* in the differential equation used to solve the wave equation, accounting for distorted and non-hyperbolic moveout on diffraction curves. Time migration includes the diffraction term only and assumes hyperbolic moveout. Depth migration can therefore collapse non-hyperbolic diffractions and migrate energy to the correct lateral position, recovering the true geometry of reflection events.

The most significant difficulty in correctly positioning energy within the section is the correct choice of velocities. True subsurface velocities correctly locate events within the section, but may not collapse diffractions effectively; to produce the best image, velocities should be chosen that collapse diffractions clearly and closely approximate the observed interval velocities. Stacking velocity analysis provides good velocity control within the

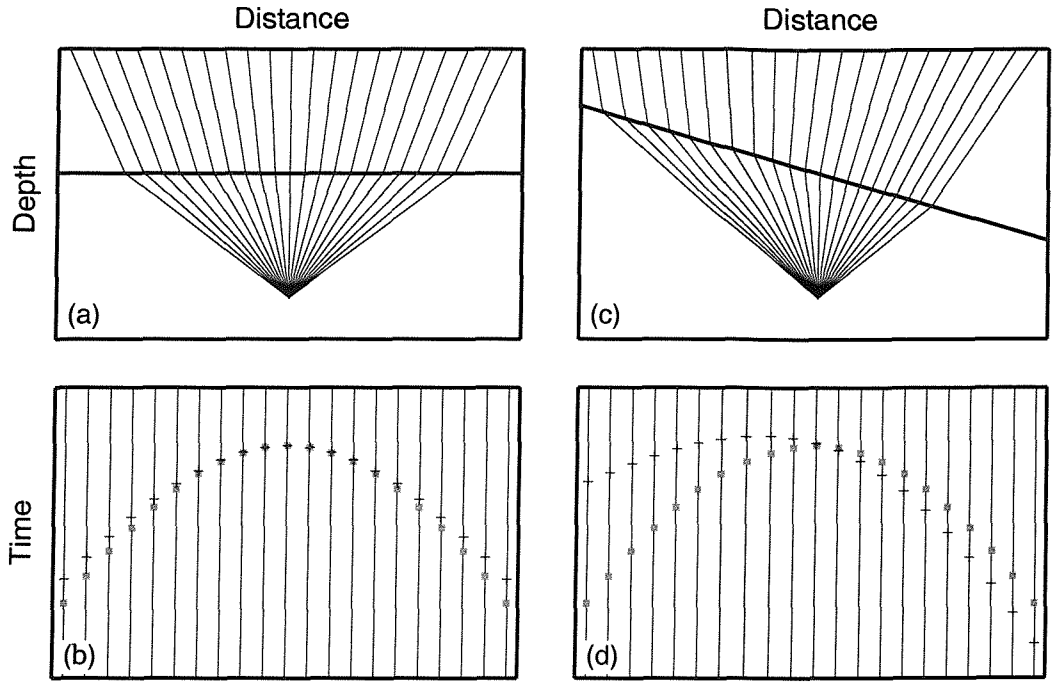

Figure 7.9: (a) Ray paths from a point diffractor to the surface through an overburden with laterally homogenous velocities. (b) The traveltime curve for the raypaths in (a) is symmetric about the diffractor and is nearly hyperbolic (grey squares) at all but far offsets. (c) Raypaths from a point diffractor through laterally varying velocities. (d) The traveltime curve for (c) is highly asymmetric and the apex positioned away from the diffractor. From Dean (1999).

sediment column where reflections are high amplitude and laterally coherent, but poor constraints on basement velocities, where reflections tend to be lower amplitude and less coherent. The depth migration velocity models were constructed as a series of layers defined by sediment intervals, each with a constant interval velocity. Wide-angle velocities along CM-14 (Avedik et al., 1982; Ginzburg et al., 1985; Whitmarsh et al., 1986) were incorporated into the migration velocity model to better constrain the basement velocities. A linear velocity gradient within basement was assumed for CM-13 and a constant velocity assigned to basement for CM-15 to enable more rapid production of the migrated section.

The Kirchhoff depth migration algorithm in *ProMAX* can reposition energy located at dips of up to, and beyond, 90° by using a ray tracing technique. There is a significant computational cost to migrating such high dips and the steepest dipping reflection events visible on the profiles presented within this thesis are typically basement features with

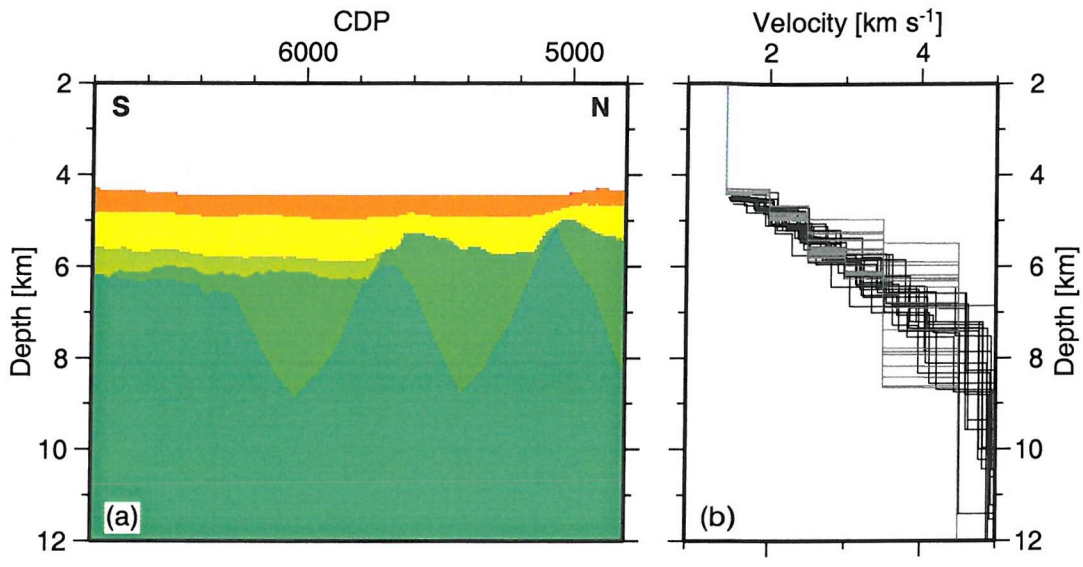

Figure 7.10: (a) Depth migration velocity model for the CM-15 panel from CDP 4800-6800. Four sedimentary layers were defined with constant velocities of 2, 2.5, 3 and 3.5 km s^{-1}; basement is assigned a constant velocity of 4.5 km s^{-1}. (b) Velocity-depth profiles every 100 CDPs through the migration velocity model (grey lines) closely match stacking velocities through the same region (black lines). RMS stacking velocities have been converted to interval velocities using the Dix equation and depth converted before plotting. The constant velocity layers defined in the migration velocity model are a good approximation to the observed velocities. The depth migrated panel is shown in Figure 7.11.

dips <60°, so it was chosen to migrate dips of up to 80°. A migration aperture of 8 km and a maximum frequency of 62 Hz were used. Migration velocities were applied at 100% of the depth migration velocity model.

CM-15 depth migration velocity model

Based on the previously completed time migration, a panel from CDP 4800-6800 was selected to show the relationship between continental fault blocks and the S-reflector within basement. Four sedimentary layers (Section 1.4.4) were defined within the migration velocity model (Figure 7.10). Two post-rift layers corresponding to Eocene to recent (units 1a-b, 2a-d: Montadert and Roberts, 1979) and Cretaceous (units 3, 4a-b: Montadert and Roberts, 1979) units were assigned interval velocities of 2.0 and 2.5 km s^{-1} respectively. A third layer is does not extend across the full width of the model, pinching out towards

the north, and was assigned a velocity of 3 km s^{-1}. Tilted fault block infill was assigned a velocity of 3.5 km s^{-1} and includes syn-rift sediment where present (Figure 7.10). The Pre-rift sedimentary packages are considered part of basement for the purposes of velocity definition as the base of pre-rift sediments cannot always be clearly imaged. The depth migrated panel is shown in Figure 7.11.

Sediment velocities were based on wide-angle and stacking velocity analysis; *in-situ* velocity measurements at Site 400 (Figure 1.20) were made through the post-rift sequences to 778 m beneath the seabed (Montadert and Roberts, 1979) and are consistent with the velocities assigned to the upper two layers. Comparison of velocity-depth profiles taken every 100 CDPs through the migration velocity model with the stacking velocities show that the constant interval velocity assumption closely approximates the observed sediment velocities for this line (Figure 7.10*b*). Some misfit is present at the change to velocities >4 km s^{-1}, but this can be attributed to the variation in depth to basement over the continental fault blocks that is corrected for by accurately picking top basement within the velocity model.

Basement was assigned a constant velocity of 4.5 km s^{-1} to enable more rapid development of the velocity model compared to more complex models. This velocity is consistent with the 4.2-4.9 km s^{-1} range estimated for upper basement from wide-angle sonobuoy, ocean-bottom instrument and expanding spread surveys (Avedik and Howard, 1979; Ginzburg et al., 1985), so the depth to the S-reflector, taken as the base of the 4.9 km s^{-1} layer (Avedik and Howard, 1979), will be accurate. The assumed model underestimates the velocity beneath S and will, therefore, underestimate the dip of any reflection events beneath S.

CM-13 depth migration velocity model

Sediment layers on CM-13 were defined by tracing reflectors from DSDP Site 400 along CM-15 and the margin parallel line CM-16. The same reflectors were observed on CM-15 and CM-13 with no large change in thickness of sedimentary packages along the margin.

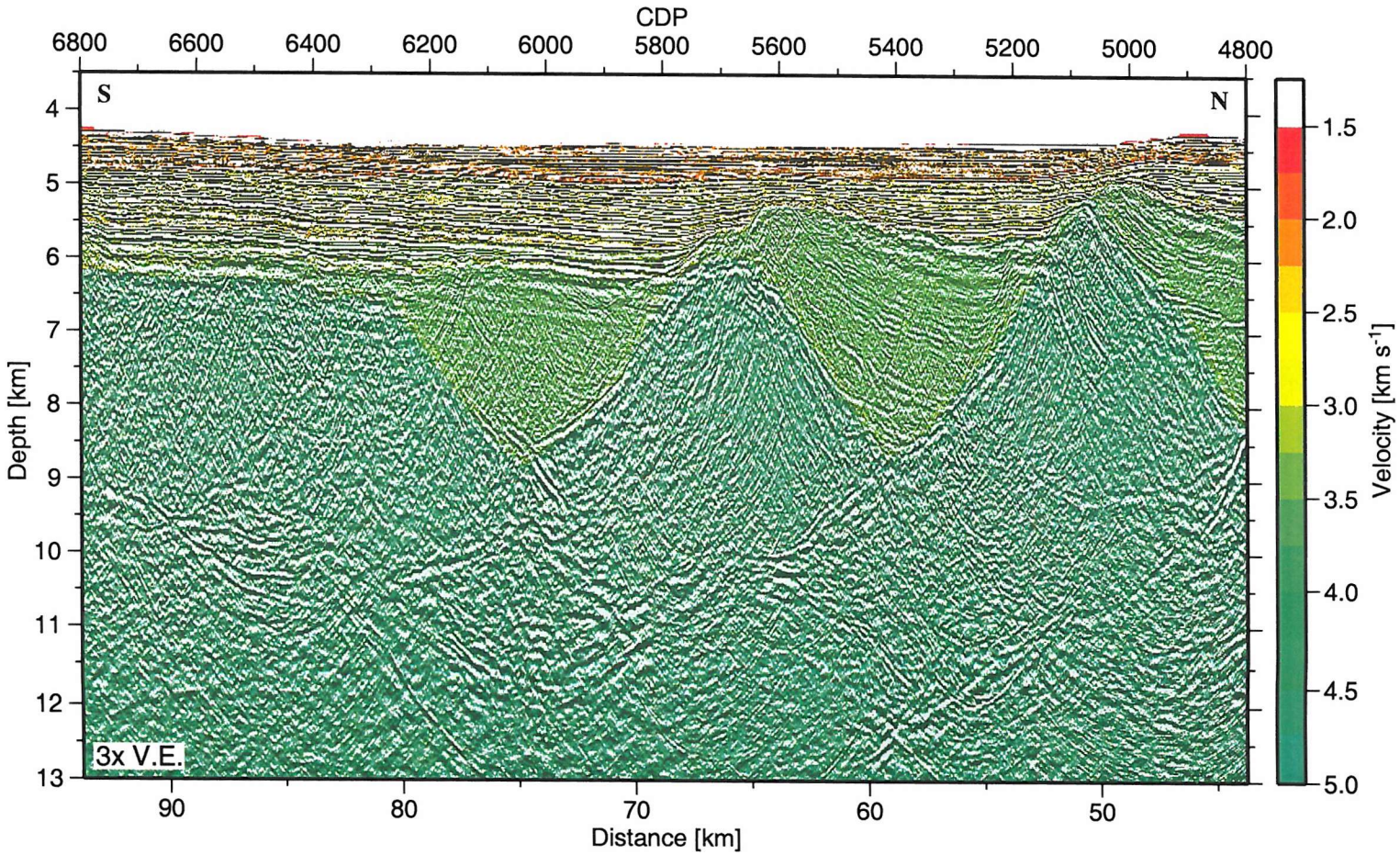

Figure 7.11: Depth migrated panel of CM-15 from CDP 4800-6800 with the depth migration velocity model overlain. Faults bounding tilted blocks appear listric and sole out onto a reflector that rises southward. Between CDP 6200 and 6800, basement loses its tilted block structure and becomes seismically transparent, but the deep intra-basement reflectivity is present and remains continuous.

Depth migration of CM-13 was carried out on the entire line. The velocity model was built in depth with four sedimentary layers assigned constant velocities of 2, 2.5, 3 and 3.5 km s^{-1}. Basement was assigned velocities increasing from 4 km s^{-1} at the top to 8 km s^{-1} at 12 km model depth, with a laterally variable velocity gradient that depends on the depth of top basement and was assumed to increase linearly with depth. To maintain a laterally consistent top basement velocity across substantial basement topography, *ProMAX* requires the velocity model to be built as a series of polygons, each with small change in basement depth. Assuming top basement is at 5 km depth, a 200 m change in basement depth within a polygon equates to a lateral velocity variation of ~0.1 km s^{-1} (Figure 7.12), this was the maximum lateral variation allowed within a polygon. The resultant velocity model is smooth within basement where depth to basement varies smoothly (Figure 7.13). A total of ~140 polygons were required to build the basement velocity model and velocities beneath 12 km depth were fixed at 8 km s^{-1}.

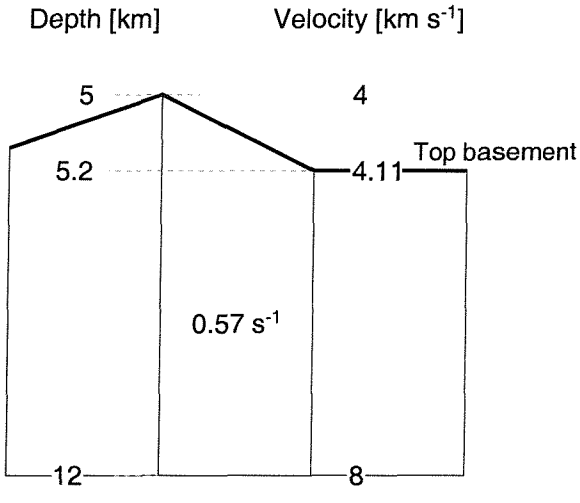

Figure 7.12: The CM-13 depth migration velocity model is constructed using polygons within basement with <200 m lateral variation in basement depth. Assuming a velocity gradient of 0.57 s^{-1} (top basement at ~5 km depth) and that 8 km s^{-1} is reached at 12 km depth a 200 m change in basement depth results in a velocity variation of 0.1 km s^{-1} at top basement.

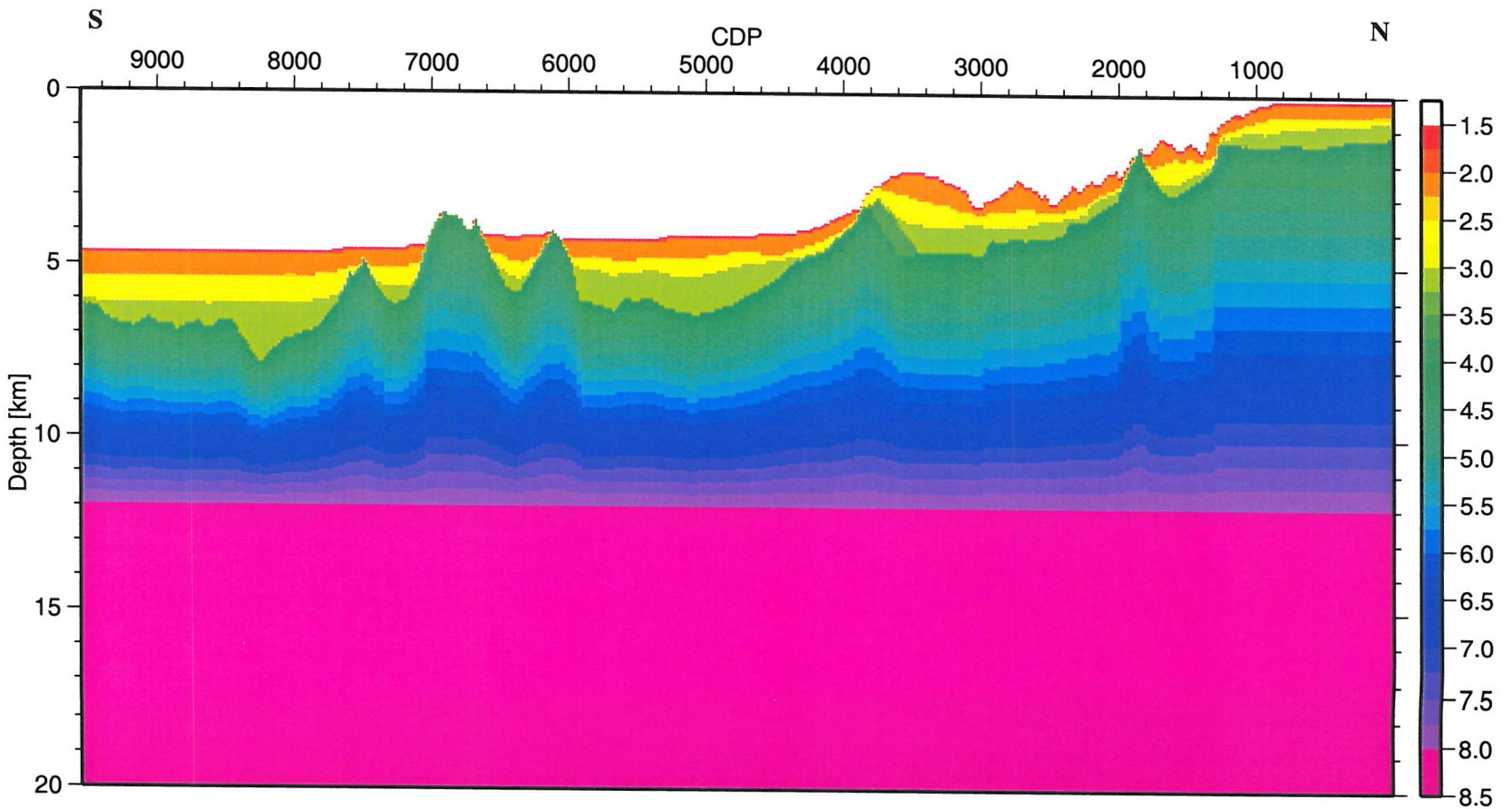

Figure 7.13: The CM-13 depth migration velocity model is constructed of three post- and syn-rift sedimentary layers (2, 2.5 and 3 km s^{-1}). One pre-rift sediment layer with a migration velocity of 3.5 km s^{-1} is identified over a tilted fault block at CDP~3600. A velocity of 1.48 km s^{-1} is assigned to the water column. This figure is sampled every 20 CDPs along the line, a coarser sampling than the model used for migration which is sampled every 2 CDPs laterally and 50 m vertically.

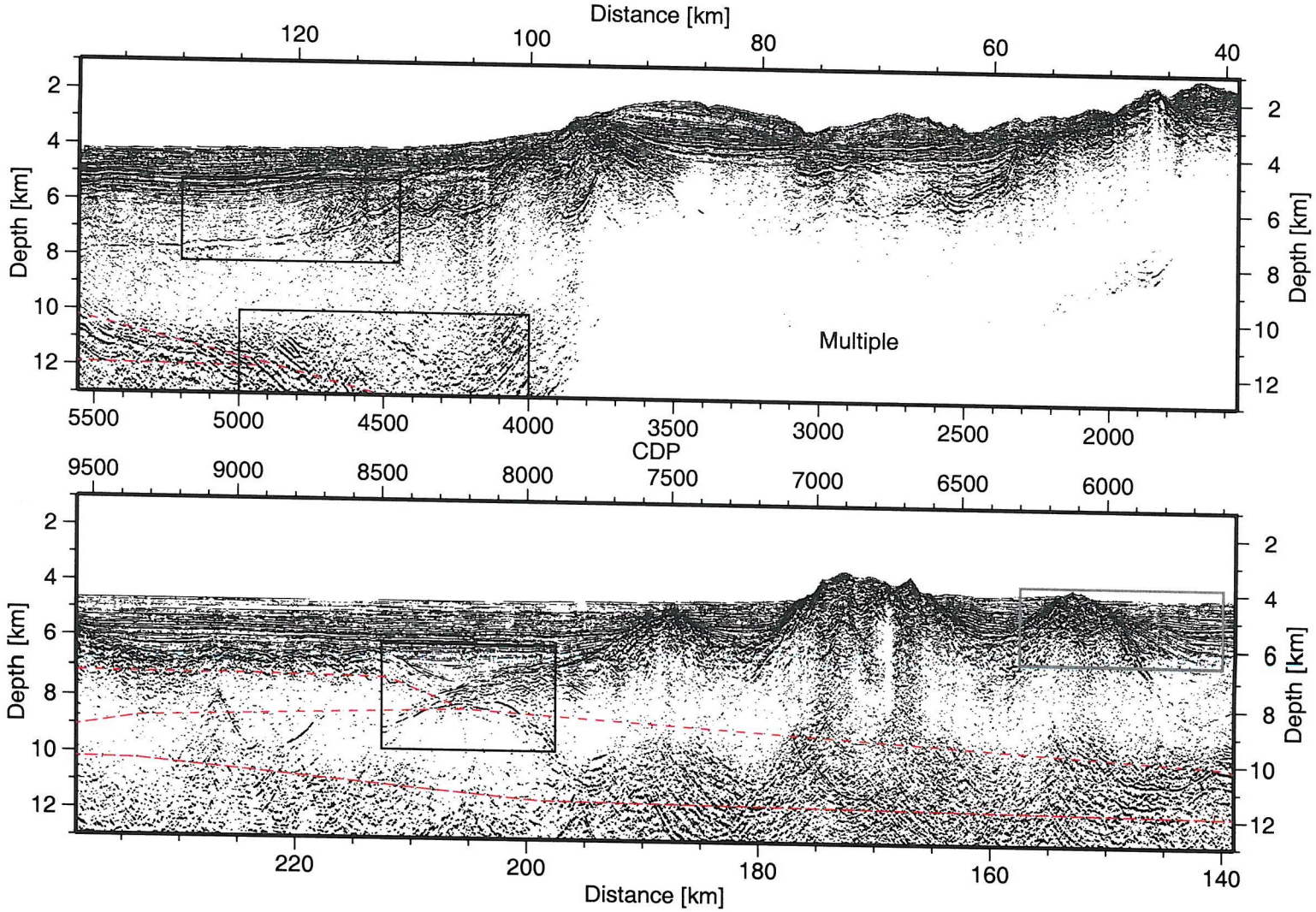

Figure 7.14: CM-13 depth migration. AGC has been applied with an 8 s window and the water bottom multiple muted between 40 and ~100 km. The grey box is enlarged in Figure 7.18 and black boxes are enlarged in Figure 7.20. Red dashed lines correspond to deep density boundaries from gravity modelling (Figure 7.16). These panels have a vertical exaggeration of approximately 2.4.

7.2 Gravity Modelling along CM-13

7.2.1 Initial model

The initial density model was designed to be as simple as possible to test the first-order fit of margin features (Figure 7.15*a*). Seabed and top basement boundaries were picked on the depth migrated section and imported as boundaries to the starting gravity model; depth to Moho was taken from gravity modelling along CM-14 (Ginzburg et al., 1985) and projected along the margin to CM-13. A mean crustal density of 2.86 $\times 10^3$ kg m^{-3} was used based on gravity modelling along CM-14. Sediment densities of 2.2 and 2.36 $\times 10^3$ kg m^{-3} correspond to layer velocities of 2.35 and 3.32 km s^{-1} (Ginzburg et al., 1985) and are consistent with stacking velocity analysis along this line. The sediment column is modelled as a single layer with a density of 2.25 $\times 10^3$ kg m^{-3}; this approximation is supported by stacking velocity analysis that shows the ratio of low to high density sediments does not vary widely along the line, so the average density remains approximately constant. Water and mantle densities of 1.03 and 3.30 $\times 10^3$ kg m^{-3} were assumed. The first-order fit of this model to the margin is reasonable, successfully reproducing the anomaly related to crustal thinning beneath the continental slope, but, because of the very large density contrast at top basement, the modelled anomaly is highly dependent on basement topography. The predicted anomaly over the basement high between 140 and 190 km is too large (Figure 7.15*a*) and the fit to full thickness continental crust is poor.

7.2.2 Model development and alternative models

Figures 7.15*b* and 7.15*c* improve the fit by the addition of a two-layer continental crust, with densities of 2.6 and 2.96 $\times 10^3$ kg m^{-3} estimated from wide-angle velocities, and a lateral change in density at 200 km distance where crust is assumed to have a thickness of 5 km. The continuation of lower continental crust densities beneath 180-210 km improves the fit to the observed anomaly (Figure 7.15*b*), but is geologically unlikely as this requires a seaward thickening of the lower continental crust. Figure 7.15*c* improves the fit over the continental anomaly at ~100 km by including smooth variations in Moho depth, preferred to models with a more rapid zone of crustal thinning (Figure 7.15*a*, *b*) and includes more realistic continental thinning at the seaward end of the profile where lower crust pinches out progressively seaward. A large misfit between 200 and 240 km is reduced slightly by a decrease in the density of the body between 200 and 240 km to 2.8 $\times 10^3$ kg m^{-3}, but remains >20 mGal.

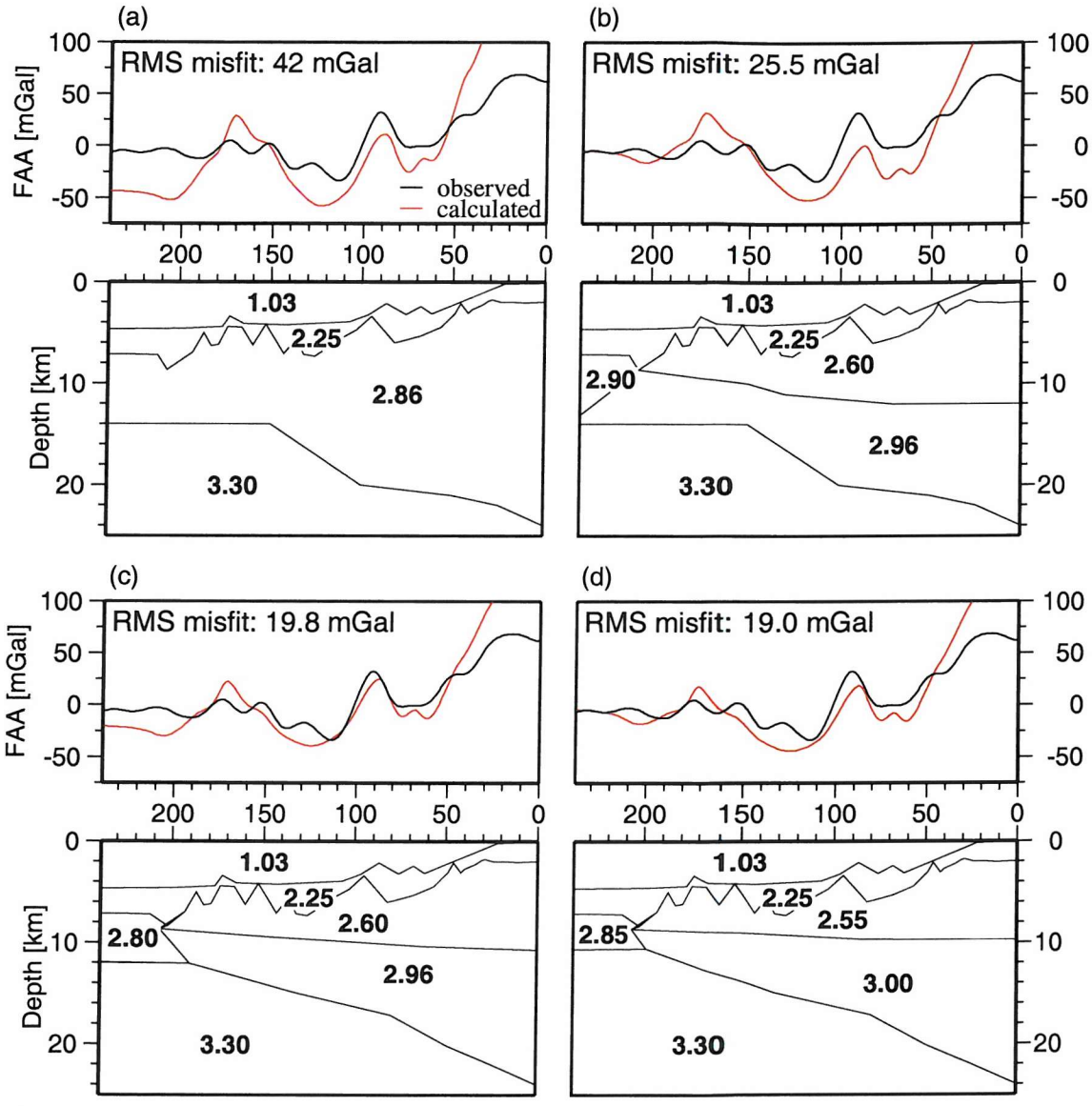

Figure 7.15: Alternative gravity models. (a) Initial model assuming single layer crust with an average density. (b) Two-layer continental crust assuming average densities based on the CM-14 wide-angle velocity model. The transition to oceanic crust at ~210 km is assumed to dip southward with the reflector on CM-13 (Figure 7.14). (c) The transition to oceanic crust dips landward, a more realistic model than (b) because lower continental crust is not required to thicken seaward. (d) Thin (<4 km) initial oceanic crust is modelled between 200 and 240 km distance. Lower continental crust requires a higher density to fit the observed anomaly. Densities are overlain in $\times 10^3$ kg m^{-3} and have been forward modelled in (b-d) to provide the best fit. The models were extended 500 km in either direction from the region of interest to minimise the influence of edge effects.

A thin, 3-4 km thick, crust is tested between 190 and 240 km in Figure 7.15*d*. The best fit is attained with a density of 2.85 $\times 10^3$ kg m^{-3} for this seaward crust, 2.55 for upper continental crust and 3.0 $\times 10^3$ kg m^{-3} for lower continental crust; the magnitude of the predicted anomaly between 150 and 200 km is reduced, providing a much closer fit to the observed anomaly.

Previous models have assumed equal thinning of upper and lower continental crust with both present to the continent-ocean transition, supported by wide-angle velocity modelling along CM-14. The presence of deep reflectivity at ~120 km on CM-13 that disappears southward may suggest the disappearance of lower crust before the ocean-continent boundary is reached (Figure 7.14). To test this hypothesis lower crust was assumed to pinch out at ~140 km, where the deep reflectivity disappears, and the Moho assumed to be located at the base of upper continental crust. Forward modelling of crustal thickness at the seaward end of the line predicts crust <2 km thick with an average density of 2.7-2.85 $\times 10^3$ kg m^{-3} (Figure 7.16), consistent with previous modelling.

The addition of a low density body beneath the Moho further reduces the misfit to the observed anomaly between 150 and 240 km (Figure 7.16*b*). The addition of such a body was initially suggested by the improved fit in Figure 7.15*b* where lower continental crust is present across the full model width, but this model provides a geologically reasonable explanation. A density of 3 $\times 10^3$ kg m^{-3} best fits the anomaly with an upper layer density of 2.85 $\times 10^3$ kg m^{-3} from 200 to 240 km. The best fit model has an RMS misfit of 15.8 mGal to the observed free-air anomaly with maximum misfit of ~30 mGal at 20 km model distance. Model misfit remains large between 0 and 110 km distance and may be related to differential crustal thinning within the continental crust that is poorly constrained by these data. Gravity is under-predicted over basement lows and over-predicted at basement highs by ~20 mGal (e.g., at 20 and 70 km distance) which may indicate that, assuming a two-layer crust approximates the real earth, the upper-lower crust interface parallels top basement. A similar effect may be the result of 3-D effects, where offline basement highs act to increase the observed gravity anomaly over troughs and inversely decrease the anomaly observed over peaks when they are surrounded by low basement topography. This may be a significant effect over the North Biscay margin because the bathymetric contours do not always parallel the gravity profile; a 100 m topographic variation would cause a ~7.5 mGal change in the gravity anomaly, although this amount decreases with distance offline.

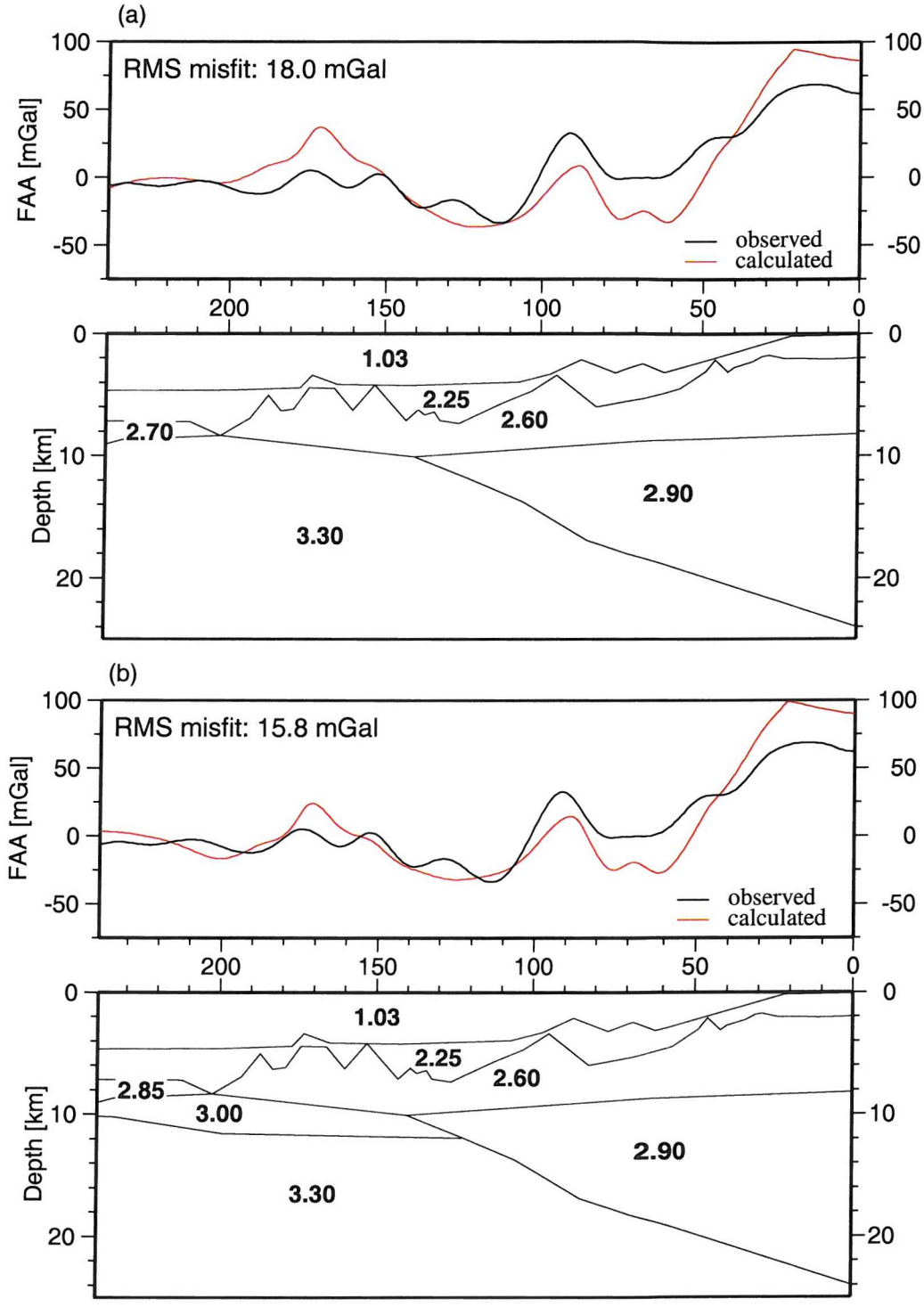

Figure 7.16: (a) Gravity model along CM-13 with preferential thinning of the lower continental crust and <2 km thick crust south of 200 km distance. Moho is constrained by deep reflections at 120 to 145 km and 200 to 215 km distance. (b) Final gravity model. Model boundaries are as for (a) with the addition of a low density mantle layer between 120 and 240 km. Upper crust between 200 and 240 km requires a higher density of 2.85 $\times 10^3$ kg m^{-3} to fit these data. Densities are overlain in $\times 10^3$ kg m^{-3}; the models are extended in either direction by 500 km to reduce edge effects.

Following gravity modelling, the model interfaces were overlain onto the seismic line. The top of the low density body coincides with dipping reflectors from 200 to 215 km and 120 to 150 km (Figure 7.14); the base of this body coincides with some sub-horizontal reflectivity between 130 and 150 km distance (Figure 7.14). This is strong supporting evidence for the presence of the low density body in this location and for the cause of these reflectors to continue between 150 and 200 km where the deep reflections are not observed. This body may be poorly imaged due to the re-emergence of basement topography, causing a decrease in energy penetration by increased attenuation and scattering, rather than changes in the physical properties of the body.

7.3 CM-13 analysis

Line CM-13 extends from the continental shelf to the abyssal plain with an increase in water depth from ~100 m to 4 km along the line. Gravity and magnetic anomalies are small along the line, the first marine magnetic anomaly, at or slightly younger than M0 (Sibuet and Collette, 1991), is located at 220 km (Figure 7.7). The depth migrated seismic section (Section 7.1.4; Figure 7.14) will be considered during the following discussion of margin features.

Upper basement from 0 to ~200 km (CDP 1-8000) consists of seven structures 10-15 km wide and 2-5 km high, typical of continental fault blocks. Pre-rift sediments (Unit 5: Figure 7.17) are identified over one fault block, at ~95 km (CDP 3700), where they are ~1 km thick with northward dipping layering, parallel to the top of the underlying fault block.

One syn-rift sediment package (Unit 4a: Figure 7.17) is evident, at ~145 km (CDP 5800) (Figure 7.14), with a maximum thickness of 0.5 km and divergent layering away from the fault block crest that indicates syn-rotational deposition (Figure 7.18). Post-rift sediments at this location are horizontal and onlap the syn-rift sediments to the south. The thin extent of syn-rift sediment suggest that there was a low sedimentation rate during rifting; there is no evidence for post-rift disruption of the sedimentary column that may act to disperse or recycle the syn-rift sediment layering. It is possible, although unlikely, that syn-rift sedimentation was limited to a small region of the margin through either a spatially variable sedimentation rate or multiple rift phases with a time-dependent sedimentation rate. If rifting occurred progressively seaward, the observations presented here suggest an

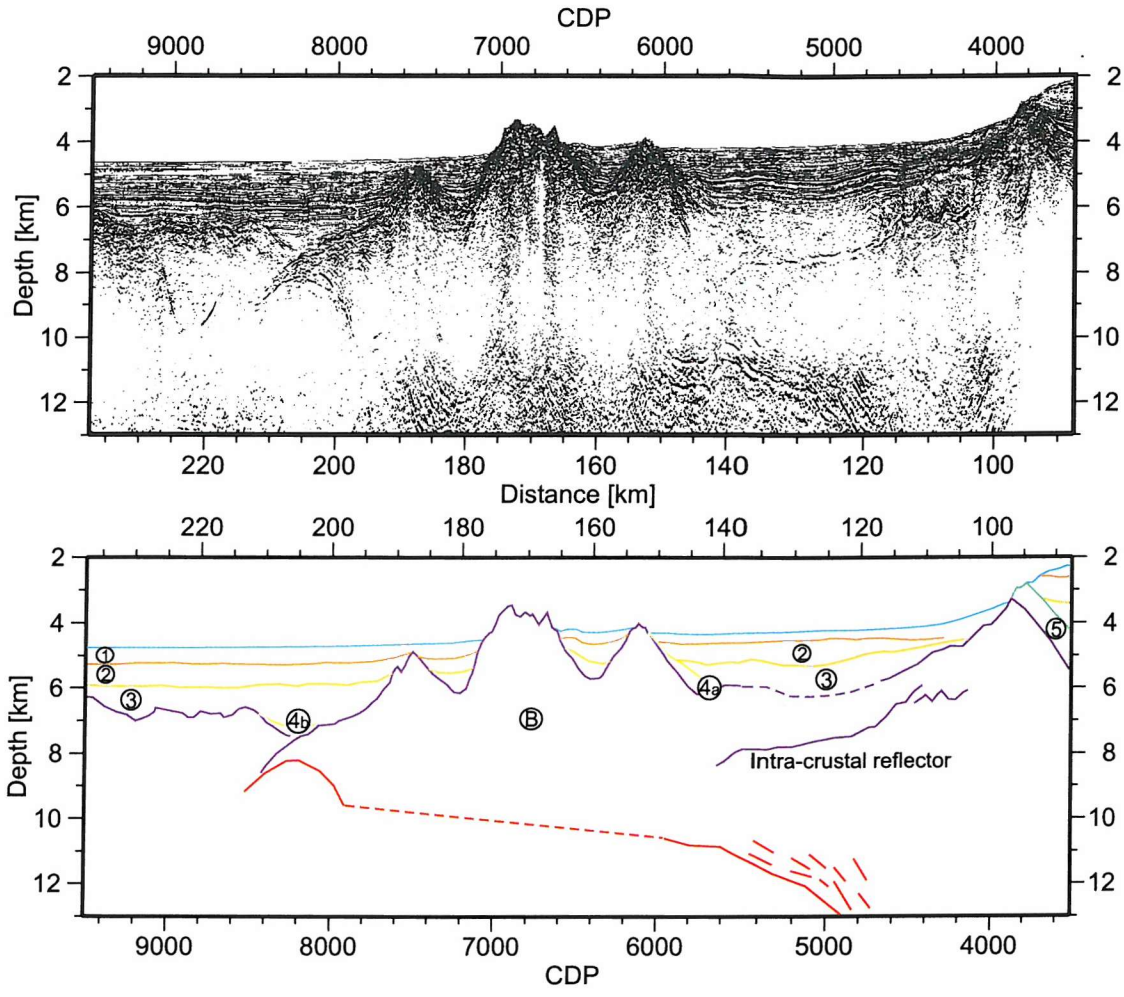

Figure 7.17: Line drawing and interpretation of CM-13. Layers are numbered following the notation of Montadert et al. (1979) (Section 1.4.4). 1=Miocene to present, 2=Eocene-Oligiocene, 3=Cretaceous, 4a=early Cretaceous syn-rift, 4b=syn-subsidence (late/end rifting), 5=pre-rift, B=basement. Dashed lines indicate where reflectors are absent or boundaries uncertain, and the events are interpolated.

increase in sedimentation during early rifting followed by a decrease towards late-stage rifting. A low sedimentation rate may be caused by a low influx of depositional material to the region, but this seems unlikely as syn-rift sediments have been widely identified elsewhere on the margin (e.g., Montadert et al., 1979). Strong ocean bottom currents may have dispersed sediments laterally along the margin. Alternatively, thermal buoyancy of the margin during rifting may have caused uplift to very shallow water depths and a decrease in sedimentation rate to near zero. The thermal anomaly required to produce this

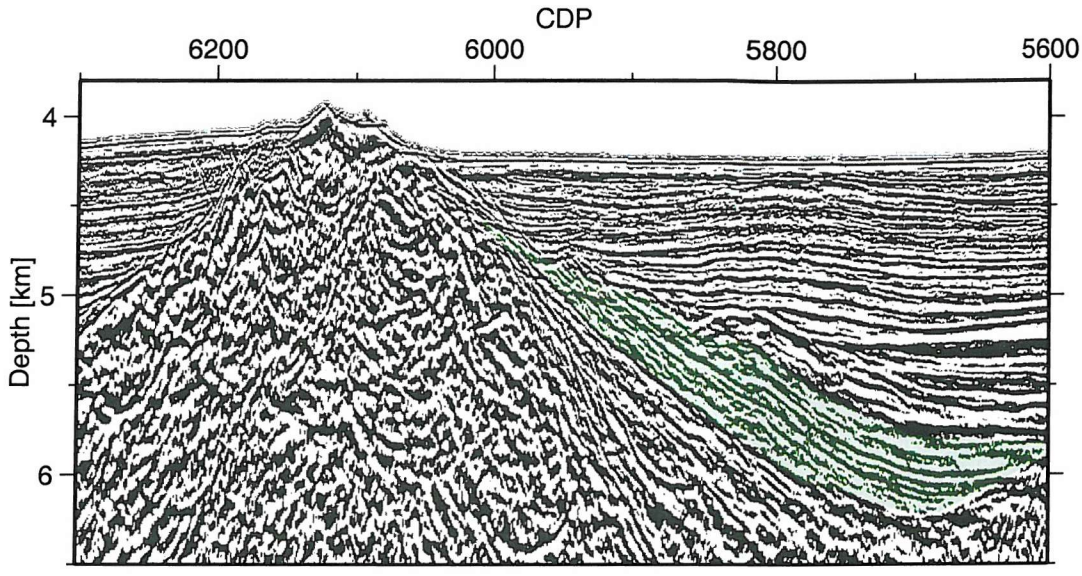

Figure 7.18: Syn-rift sediments (shaded region) on CM-13 show a typical divergent (fan-like) pattern away from the fault block crest. The small thickness of this package and its absence elsewhere on the line suggests the sedimentation rate during rifting was very low. Post-rift sediments onlap this sequence towards the south.

extreme uplift would likely encourage significant volumes of melt production, which are not observed on the seismic sections or in the magnetic anomaly pattern. Extreme uplift and subaerial exposure would also have flattened the fault block crests, however this is not observed on CM-13.

Post-rift sediment sequences are sub-horizontal across the entire margin, infilling space between tilted fault blocks to a maximum thickness of ~2 km. Sediments are generally considered turbiditic (de Graciansky et al., 1979), although the post-rift black shales have also been interpreted with a predominantly pelagic source (Mélières, 1979); sediment thickness increases southwards from ~1 to ~2 km, probably due to the increased deposition from settling towards the abyssal plain or, if pelagic, an increased supply from the thicker water column. The increase in sediment thickness is not limited to any particular seismic strata, but all strata show approximately equal thickening.

Between 0 and ~90 km, basement is largely transparent within the top 2-4 km; shallow water depths mean any deeper arrivals, if present, are masked by a strong water bottom multiple which has been muted in Figure 7.14.

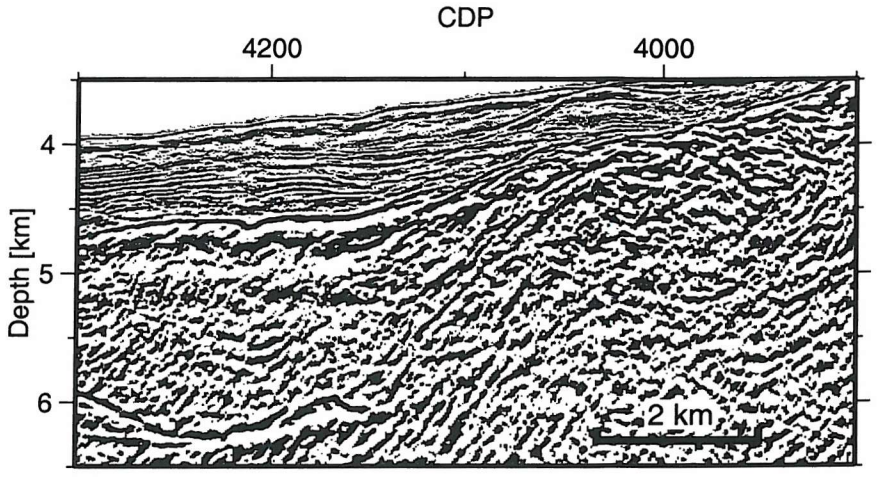

Figure 7.19: The break-away of the intra-crustal detachment on CM-13 is poorly imaged. This reflector emerges at top basement around CDP ~4000, on the seaward side of a tilted fault block, indicated here by the shallowing of basement.

Between 100 and 145 km is a region of anomalously flat basement situated between tilted fault blocks (Figure 7.17). This region divides large continental blocks of the continental slope in the north from smaller fault blocks at abyssal depths to the south. The transition from sediment to basement in this region is marked by an abrupt loss of seismic layering: top basement becomes largely unreflective and similar to the adjacent tilted fault blocks (Figure 7.20*a*). Approximately 1 to 1.5 km beneath top basement, located within the crust, is a strong reflection event continuous for ~30 km (Figures 7.14, 7.19, 7.20*a*). This reflection is of high amplitude and consists of a single wave cycle, suggesting it comes from an abrupt interface within the crust. Material beneath this event is seismically transparent to ~11 km depth and similar to material above this reflector. The breakaway of this event is not clearly imaged and it appears to merge with top basement towards the north at CDP 4000 (~100 km) (Figure 7.19), where it coincides with the southern edge of a continental fault block (Figure 7.14). This reflection is further considered in Section 7.5 by examination of its waveform and amplitude.

Beneath this region of flat basement, at 11-17 km depth, is a 2-3 km thick package of reflectors dipping northwards at ~20° and reaching a maximum depth of 16-17 km at ~105 km distance (CDP 4400) (Figure 7.20*b*). Individual reflection events are continuous over ~3 km laterally and the entire package can be identified for >35 km between 100 and

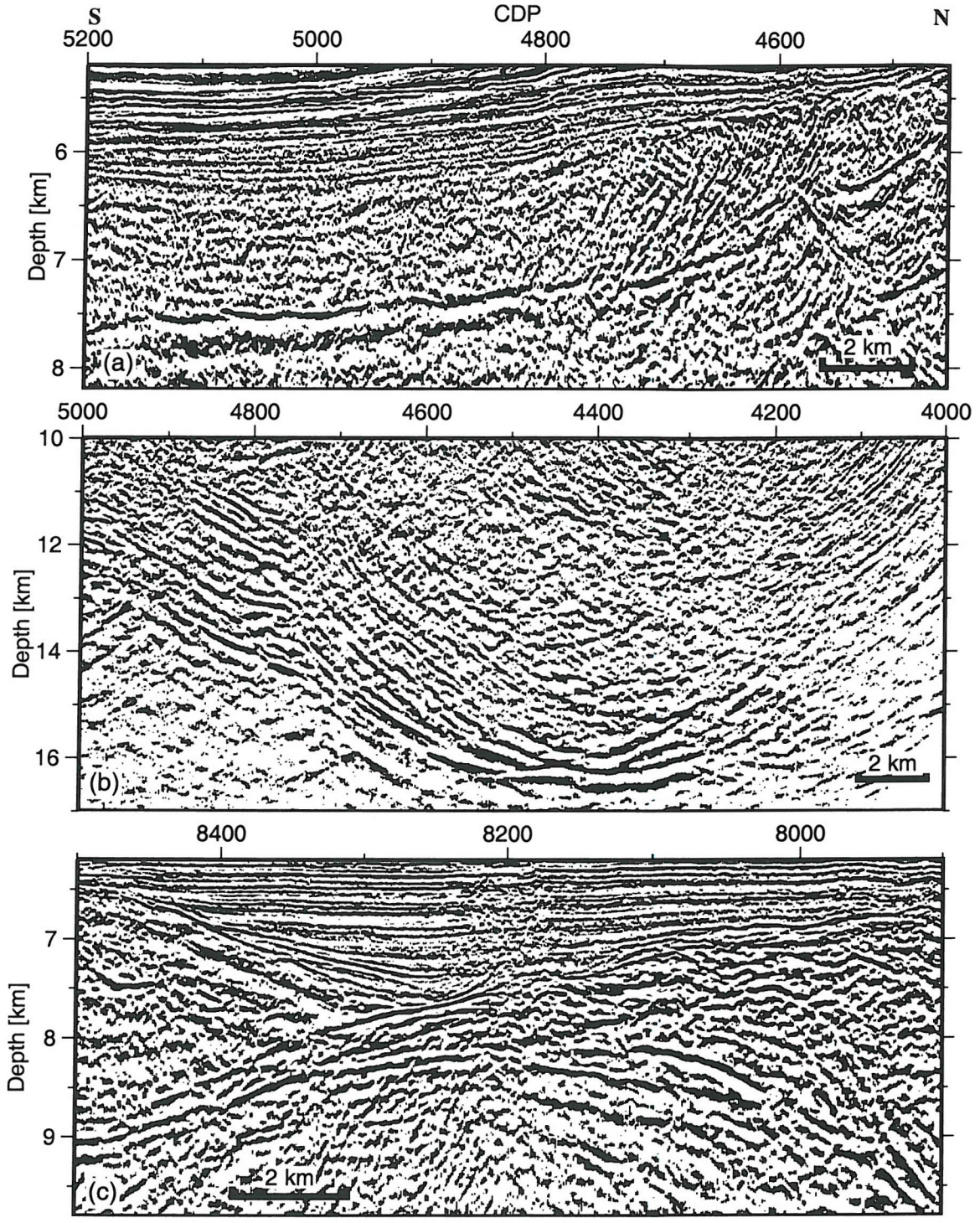

Figure 7.20: Enlarged panels from the CM-13 depth migration. (a) Zone of top basement with very low relief. A strong reflection event can be seen ~1 km into basement. (b) Deep reflections beneath the zone of smooth basement in (a) are continuous over short lateral distances (~3 km) and form a package 2-3 km thick. They dip northwards and appear to flatten at CDP 4400. (c) Towards the southern end of CM-13 a deep reflection rises towards top basement and continental crust is pinched out. This event is further considered in Section 7.5. The vertical exaggeration varies between panels.

145 km, dying out beneath the reappearance of tilted continental blocks and basement topography. The loss of imaging of these deep reflections may be explained by reduced energy penetration beneath continental blocks, caused by increased scattering and attenuation, and does not necessarily imply that the physical cause terminates. However the base of the crust inferred from gravity modelling fits well with these reflections (Figure 7.14) and supports the interpretation of these reflections as the base of lower continental crust, which pinches out at ~145 km.

A similar reflection package is imaged further seaward, between 195 and 205 km, with a comparable dip of ~20° and a smaller package thickness of ~1 km (Figure 7.14). This reflector rises to merge with top basement at 205 km (CDP 8200) and a depth of ~8 km; upper basement tends to zero thickness at this point (Figure 7.20*c*). Even with this rapid lateral change of structure there is little corresponding free-air gravity anomaly (Figure 7.7), implying local isostatic balance of any corresponding density contrasts. A ~1 km increase in depth to top basement at 205 km compared to the adjacent 2 km thick crust is observed and is evidence for such isostatic compensation. This basement depression is infilled with <0.3 km of divergent sedimentary layering which may represent syn-subsidence deposition (Unit 4b: Figure 7.17; CDP 8250-8400: Figure 7.20*c*). Due to the position of this sequence seaward of continental fault blocks, this layering is not considered to be syn-rift sedimentation. Draped over this region are horizontal sedimentary sequences which onlap top basement to the north and south. Comparison with the sediment column further north shows no layers are missing from the sequence, and the undeformed nature of the oldest layers immediately overlying basement further supports the interpretation that this reflecting feature was formed during the late stages of rifting and not by later tectonism. Neither top basement nor the overlying sediments show any evidence for post-rift deformation or faults cutting through pre-existing structures.

Northward extrapolation of these reflectors with a dip of ~20° projects them to the deep events further landward at 95-145 km and suggests they may relate to the same subsurface feature. Gravity modelling shows a density contrast at these depths (Figure 7.16*b*) with the base of continental crust predicted to coincide with these reflectors from 100 to 200 km distance (Figure 7.14).

Seaward of the basement pinch-out at 205 km, these sub-basement reflectors can be observed dipping southward at ~15° for 7.5 km where they appear to mark the lower boundary of a re-emerging upper basement. Basement has a different appearance here compared

to further north: top basement is unreflective and undulates over a much shorter length-scale (~5 km) and with smaller depth variations than over the continental blocks (e.g., ±0.3 km compared to ±1 km). This change coincides with the first marine magnetic anomaly at 200-230 km distance (Figure 7.7).

7.4 CM-15 analysis

Line CM-15 is situated towards the eastern end of the North Biscay margin and extends from the continental slope to the abyssal plain; the deep water portion of the margin was reprocessed here, in water depths >4 s TWT. Two large fault blocks can be seen at 0 km (CDP 3000) and 30 km (CDP 4000) with a width of ~25 km (Figure 7.21). There is an abrupt change in fault block size at ~40 km, marking the foot of the continental slope (Figure 7.11), where a zone of five tilted blocks each 10 to 15 km wide extends to 125 km distance (CDP 8000). The thin sedimentary cover on the continental slope is most likely due to decreased sedimentation in shallower water depths. Channels up to 30 km wide and 2.5 km deep e.g., at 10 km (CDP 3400) can be seen running for >50 km along margin strike (Figure 1.9). The absence of recent sedimentary infill suggests that the channels form part of the modern day deep water transport off the continental slope.

Pre-rift sediments can be seen at the top of some tilted continental fault blocks (e.g., CDP 5100: Figure 7.21), where reflections form a ~1 km thick layer dipping northward at ~30°, approximately orthogonal to the strong reflector bounding the southern side of the block. Pre-rift sediment reflectivity is visible within the top ~1.5 km of the block only and becomes less prominent with depth, possibly due to attenuation within the compacted sediments. The top of the underlying fault block cannot be clearly delineated beneath the pre-rift sediments and is taken to be indicated by the change from weak layering to a seismically unreflective structure (Figure 7.22). The lack of a clear reflection suggests a small or non-existent impedance contrast at this boundary. Where no pre-rift sediment can be identified, e.g., at CDP 5650, the top of continental crust is marked by a strong reflector that results from a high impedance contrast between sediment and basement. The crest of the fault block at CDP 5650 appears rounded, as if substantial erosion of the crest has occurred. This erosion is unlikely to be subaerial as, during the same phase as the proposed uplift, a thick syn-rift sediment package can be seen infilling the top of this fault block and overlying the eroded crest. Rounding of this fault block crest may have been caused by erosion due to deep water currents. Eroded material was likely re-deposited as part of the syn-rift sediments within the developing half grabens.

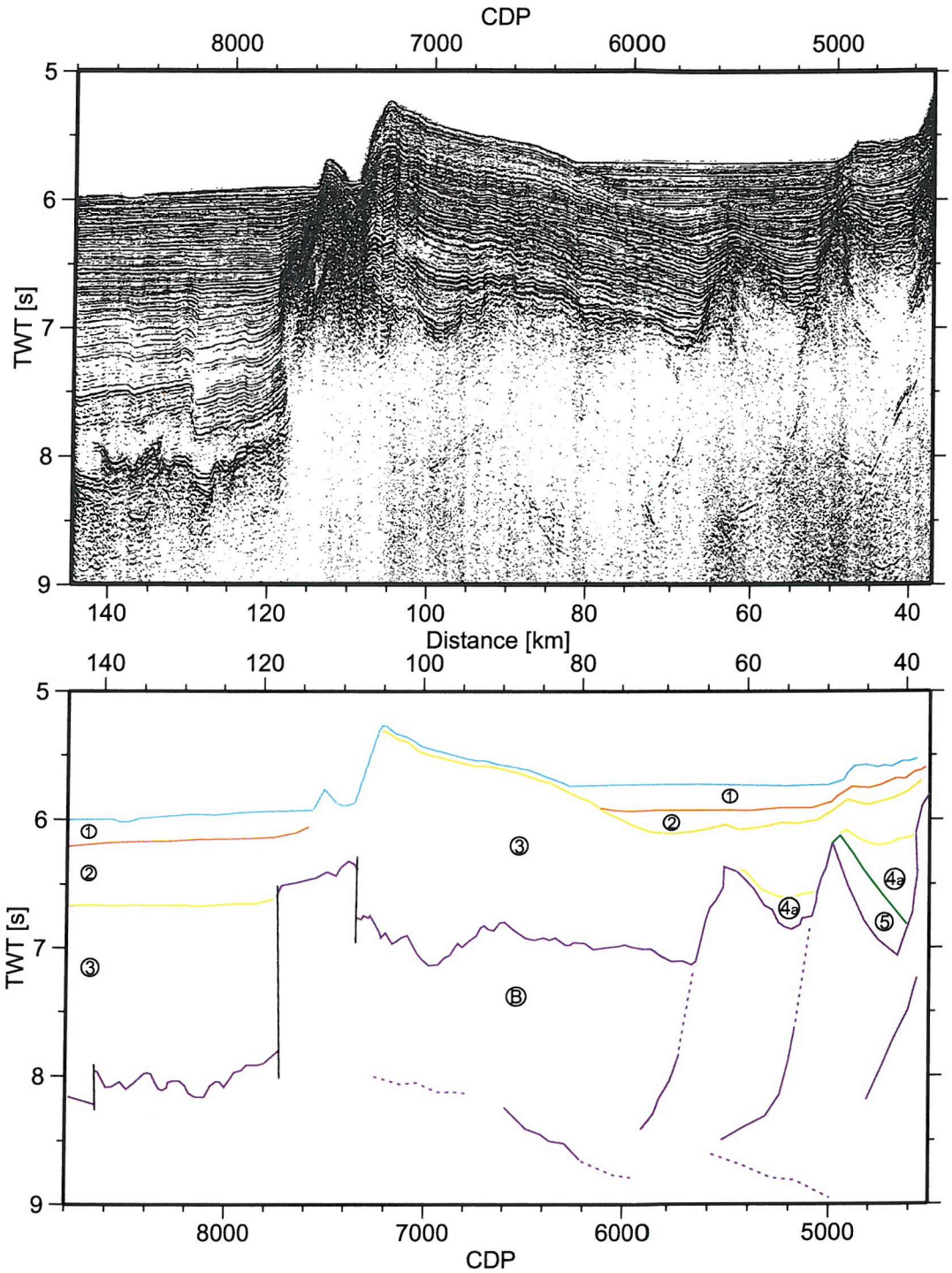

Figure 7.21: Line drawing and interpretation of part of CM-15. Layers are numbered following the notation of Montadert et al. (1979) (Section 1.4.4). 1=Miocene to present, 2=Eocene-Oligiocene, 3=Cretaceous, 4a=early Cretaceous syn-rift, 5=pre-rift, B=basement. Dashed lines indicate where reflections are not clearly identified, but interpolated between observation points. The time section is shown as it covers a wider region than the depth migrated section.

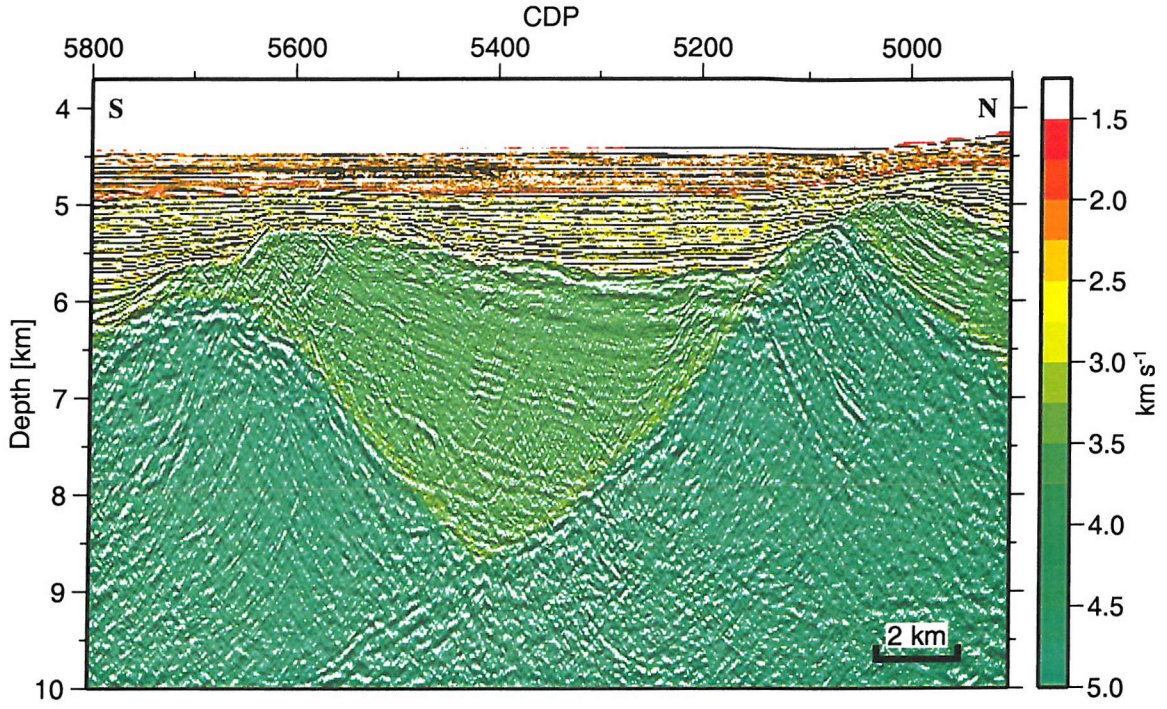

Figure 7.22: Depth migrated panel of CM-15 between CDP 4900-5800 with the depth migration velocity model overlain. Syn-rift sediments can be identified over the tilted fault blocks at CDP 5600 and 5000. Pre-rift sedimentary layering is observed to parallel the top of the continental block at CDP 5000, but not observed on the block further south. Pre-rift sediments are assigned basement velocities for this depth migration (Section 7.1.4).

Syn-rift sediments are identified based on their divergent layering away from the fault block crests, infilling the graben formed by the rotation and subsidence of the fault blocks and producing a sediment layer up to 3 km thick (Figure 7.22). South of 80 km (CDP 6200) syn-rift sediments are not clearly identifiable and there are no distinct reflection events between post-rift sediments above and basement below (Figure 7.11). These observations will be further considered later, but it appears likely that the disappearance of syn-rift sediments and a clear basement reflection are due to disruption of the layering during a later tectonic inversion.

The post-rift sediments, 1-2 km thick, are horizontally stratified and overlie the continental fault blocks, increasing in thickness southward to a maximum of ~2.7 km from CDPs 8200 to 9100 at the southern end of the line (Figure 7.8). Sediments here have not been depth migrated, but a layer extent of 2.4 s TWT and a velocity of 2.2 km s^{-1} are assumed.

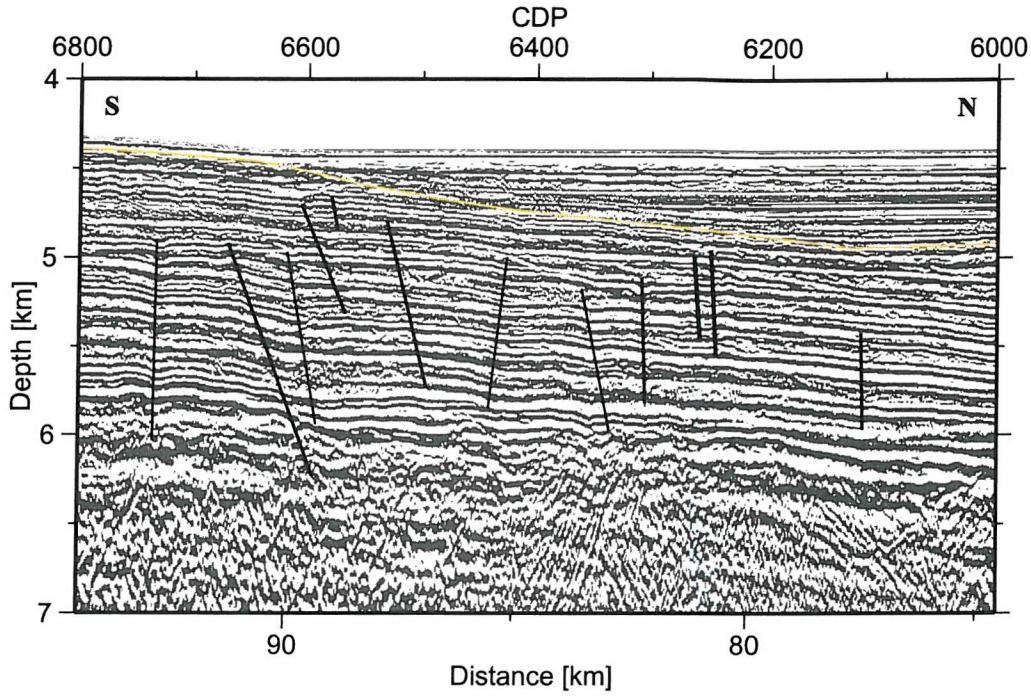

Figure 7.23: Eocene compression caused uplift and compressional faulting within the sediments on CM-15. Faults have generally small displacements and do not penetrate the Oligocene to recent sediments. The Eocene-Oligiocene boundary is marked in yellow; faults are shown by black lines.

Uplift of the sedimentary column has occurred south of CDP 5700, producing a ~400 m high ridge on the sea-bed (Figure 7.8). Between CDP 6000 and 6500 horizontal sedimentary layering onlaps the uplifted sequences, forming a post-uplift layer ~500 m thick (Figure 7.11), identified as post-Eocene from the sampling at DSDP Site 400 (Figure 1.21) (Montadert and Roberts, 1979). North and southward dipping faults are imaged through these uplifted sediments with very small displacement along each fault (<10 m) and form a series of reflectors stepping up to the south (Figure 7.23). These faults penetrate into upper basement between 100 and 125 km (CDP 7000-8000) only, at the seaward end of the line; uplift and deformation of basement further north likely occurred by reactivation of the normal faults formed during rifting. Above the uplifted fault blocks between 80 and 95 km no clear syn-rift sediment can be identified. It seems unlikely that spatial variation in syn-rift sedimentation was great enough to prevent deposition in this area so it is proposed that syn-rift sedimentary layering here was disrupted during the later inversion.

Basement between 40 and 120 km (CDP 4600-8000) consists of tilted continental fault blocks which are generally unreflective and delineated by bounding faults dipping at <20° and which appear listric in depth. These block-bounding reflections sole out with depth, merging to form the S-reflector described by Le Pichon and Barbier (1987). S comprises a single reflector on the more steeply dipping, block bounding, portions and a group of anastomosing reflections on the flatter portions (Figure 7.11). When it was active, S may have been a single event along its entire length, but, as previously suggested, the later inversion caused reactivation of the more steeply dipping fault sections cutting across and displacing the flatter regions. S rises from a depth of ~12 km at 55 km distance (CDP 5200) to ~9 km depth at 95 km distance (CDP 6800). If this depth change was caused by the Eocene uplift then this is strong evidence that S is an early feature: at least pre-Eocene and likely formed during rift related extension, and that there has been a maximum uplift of ~3 km at the seaward end of CM-15. Uplift calculated by this method may be incorrect if S was not horizontal prior to inversion. The original orientation of S is not clear as, to allow the seaward movement, under gravity, of fault blocks along the detachment, S must have been dipping south while it was active, however, Le Pichon and Barbier (1987) propose it was dipping landward, inconsistent with this type of motion. A similar low angle intra-crustal fault at the Galicia Bank margin has been observed to shallow seaward, producing a domal feature (e.g., GP-11: Reston et al., 1996a), although other lines show this event dipping seaward and its orientation may be dependent on more recent isostatic adjustment rather than reflecting its position at the end of extension.

7.5 S-reflector analysis

The S-reflector is described in Section 1.4.5 from existing studies of the North Biscay margin and the relationship of S between CM-13 and CM-15 is shown by tracing the reflector along margin strike (Figure 1.22). To constrain the lithologies above and below S, the waveform and amplitude of the S-reflector were considered at 65 km on CM-15 and at 200 km on CM-13 (Figure 7.20*c*), the along margin continuation of S. The intra-basement event at 120 km on CM-13 (Figure 7.20*a*) was also examined and compared to the S-reflector event. The deep events on CM-13 (Figure 7.20*b*) are not considered for amplitude analysis as they form a thick reflection package and not a single interface. To constrain the nature of S, and the lithologies above and below S, the waveform and amplitude of the reflections were considered.

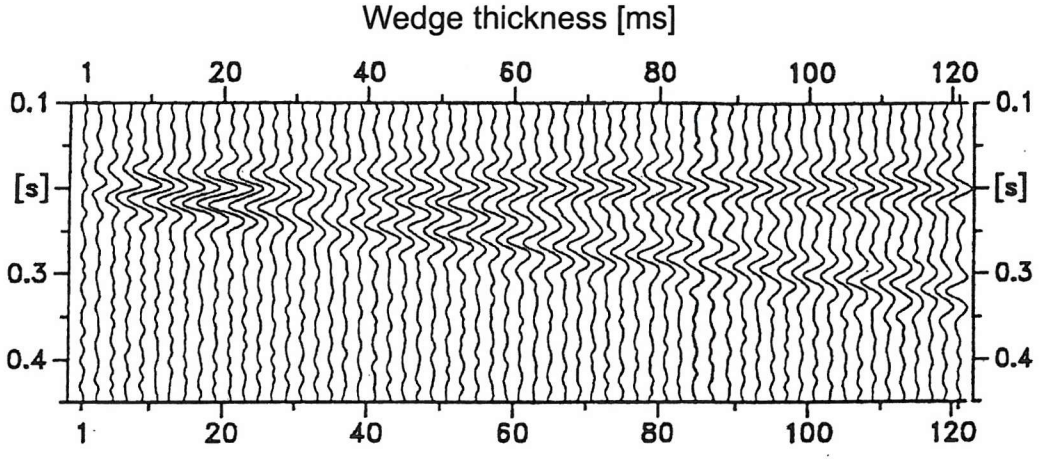

Figure 7.24: The synthetic waveform generated by a wedge of high velocity material. As the wedge thins, the waveform becomes complex as reflections from the top and bottom of the wedge interfere. From Reston (1996).

7.5.1 Waveform analysis

The various suggested interpretations for S (Section 1.4.5) can be distinguished by the reflecting interface that they imply. A fault zone dividing upper and lower continental crust implies a sharp tectonic boundary at S, while a brittle–ductile boundary produces a more diffuse interface at S and the observed reflection becomes less abrupt. Reston (1996) showed through synthetic modelling of a wedge shaped body that the reflection from the top of a thick body can be distinguished from the reflection caused by a thin intrusion because interference of reflected energy from the top and base will produce a complex waveform (Figure 7.24).

The method applied here follows that of Reston (1996) and compares the waveform of S to that of the sea bed reflection. Figure 7.25 shows that for each sample panel S closely resembles the seabed reflection, having a simple waveform that has not been modified greatly by interaction with S. The waveform of the inverted seabed multiple closely resembles that of the seabed reflection and shows that there are no time-dependent waveform changes and any variations in the waveform are caused by interaction with the subsurface. These results imply that S is a reflection from a single interface with a positive impedance contrast.

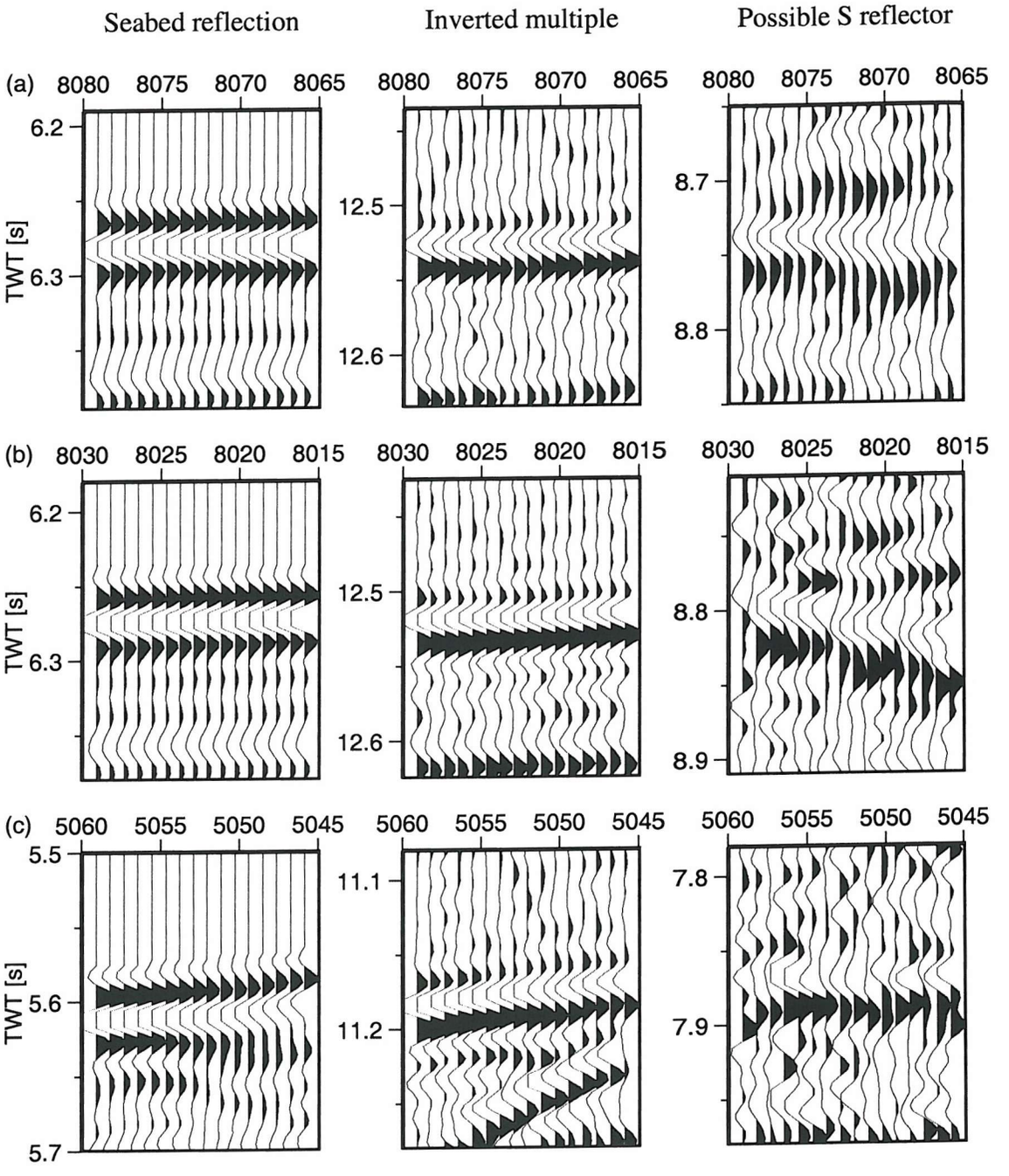

Figure 7.25: Comparison of the waveform of the seabed reflection, the inverted seabed multiple and possible S events on CM-13 at (a) CDP 8065 to 8080, (b) CDP 8015 to 8030 and (c) CDP 5045 to 5060. Amplitudes in each panel are individually scaled.

7.5.2 Amplitude analysis

The observed amplitude of a reflection event depends on the reflection coefficient at the reflecting interface which is given by Equation 7.5, where R is the reflection coefficient, v_1 and v_2 the velocities above and below the interface and ρ_1 and ρ_2 the densities above and below the boundary.

$$R = \frac{v_2\rho_2 - v_1\rho_1}{v_2\rho_2 + v_1\rho_1} \quad . \tag{7.5}$$

Absolute amplitudes depend on the scaling applied during the recording procedure, but the reflection coefficient at S can be determined by calibrating the system with the known seabed reflection coefficient. Corrections are applied for geometrical spreading and attenuation which effect the reflection amplitude.

Calibration with seabed reflection

The seabed reflection was calibrated by comparison of the amplitudes of the seabed reflection and the seabed multiple, following the method of Warner (1990). The seabed reflection coefficient is given by

$$R_{sb} = 2\frac{A_m}{A_p} \quad , \tag{7.6}$$

where A_p and A_m are the amplitudes of the seabed reflection and the multiple respectively. This calculation is carried out on data uncorrected for attenuation and geometrical spreading. This method assumes that the seabed reflection is smooth and horizontal and that the waveform is unaffected by subsurface reflections. A comparison of the waveform of the primary and multiple events, inverted to account for the reflection off the sea surface, show that this is a reasonable assumption (Figure 7.25).

Attenuation and geometrical spreading corrections were made by assuming that the path length of the multiple is double that of the primary reflection. The factors that act to reduce the amplitude have twice the effect and are incorporated as a multiplication factor in Equation 7.6. For this path length assumption to hold, energy must be reflected at normal incidence. Amplitude analysis was carried out on a nine-fold near-offset stack with a maximum angle of incidence of $\sim 7^\circ$ in abyssal water depths (maximum streamer offset of 1125 m).

The absolute seabed reflection coefficient is averaged over the 45 traces considered for

further analysis and gives us an estimate of $R_{sb} = 0.19 \pm 0.06$. This is consistent with the reflection coefficient of 0.22 calculated according to Equation 7.5, assuming a water velocity and density of 1.5 km s^{-1} and 1.03 $\times 10^3$ kg m^{-3} and a velocity and density of the shallowest sediments of 1.5 km s^{-1} and 1.6 $\times 10^3$ kg m^{-3} (Montadert and Roberts, 1979).

Reflection coefficient at S

The reflection coefficient at the potential S events, R_s, is calculated relative to the seabed reflection according to the equation

$$R_s = \frac{A_s}{A_{sb}} \times R_{sb} \quad , \tag{7.7}$$

where A_s and A_{sb} are the amplitudes of S and the seabed reflection respectively measured from the zero crossing point to the peak amplitude.

These data were corrected for geometrical spreading using the stacking velocity model (Section 7.1.2). This correction does not account for focusing and defocusing effects of the real earth that is not horizontally stratified, but the mean correction can be considered valid by averaging amplitudes over several traces (Reston, 1996). A comparison was made between the spectral content at the seabed and at S. Attenuation is frequency dependent (e.g., Sheriff and Geldart, 1995) and a 8-11-25-50 Hz bandpass filter was applied to the dataset to reduce the seabed reflection to the frequency content of S, approximating, and compensating for, the effect of attenuation at S.

Following the above corrections the reflection coefficient of S was averaged over 15 CDPs to give $R_s = 0.40$ between CDPs 8065 and 8080, $R_s = 0.37$ between 8015 and 8030 and $R_s = 0.19$ between 5045 and 5060. S has approximately double the seabed reflection coefficient at the southern end of the line, but the reflection event further north has a much lower reflection coefficient, equal to the seabed reflection. These reflection coefficients are considered in terms of velocity contrasts by re-arranging Equation 7.5 to give

$$v_2 = \frac{\rho_1 v_1 (R_s + 1)}{\rho_2 (1 - R_s)} \quad . \tag{7.8}$$

Densities above and below the reflection event are assumed from gravity modelling (Figure 7.16*b*) and velocities above S are taken from the Ginzburg et al. (1985) wide-angle velocity model.

Between CDP 8065 and 8080, S rises to ~0.5 km beneath top basement and coincides with the transition to a density of ~3.0 $\times 10^3$ kg m^{-3} (Figure 7.16); a velocity and density of 4.0 km s^{-1} and 2.4 $\times 10^3$ kg m^{-3} were assumed above S and a density of 3.0 $\times 10^3$ kg m^{-3} beneath. A reflection coefficient of 0.40 results in an estimated velocity beneath S of 7.5 km s^{-1}. Low velocities and densities are assumed above S because of its position beneath very thin crust (~0.5 km) that may be heavily fractured and therefore have a reduced velocity and density. The gravity modelling presented here (Section 7.2) developed the simplest model to fit the observed data and assumed a constant density for each layer, not accounting for any density gradients that may be present. It is likely that density increases with depth, so to account for this increase an upper density of 2.36 $\times 10^3$ kg m^{-3} was assumed (Ginzburg et al., 1985); a lower density of 2.9 $\times 10^3$ kg m^{-3} is also assumed to account for a density gradient within the high density body. The repeated calculations result in a velocity estimate beneath S of 8.5 km s^{-1}. These velocities are very high and illustrate the importance of constraining the velocity above S: a 0.1 km s^{-1} increase in v_1 correspondingly increases the calculated v_2 by ~0.2 km s^{-1}. Unfortunately, upper crustal velocities are poorly constrained in this highly thinned region.

Between CDP 8015 and 8030 S underlies thinned continental basement (Figure 7.20*a*) with a velocity and density of ~4.5 km s^{-1} and 2.60 $\times 10^3$ kg m^{-3} respectively. A density of 3.0 $\times 10^3$ kg m^{-3} is assumed beneath S, and with an average reflection coefficient of 0.37, the velocity beneath S is estimated at 8.5 km s^{-1}. As above, the calculation is repeated with density estimates adjusted to account for possible density gradients: 2.48 $\times 10^3$ kg m^{-3} is assumed for upper continental crust, as calculated by Ginzburg et al. (1985) along CM-14, and 2.9 $\times 10^3$ kg m^{-3} beneath S. These modified assumptions result in a velocity beneath S of 8.3 km s^{-1}.

Identical calculations were made for the reflection event between CDPs 5045 and 5060, assuming a velocity of 4.5 km s^{-1} within top basement and a density of 2.6 $\times 10^3$ kg m^{-3}. When no density change is assumed across the interface a velocity beneath the reflector of 5.88 km s^{-1} is predicted. Assuming a density contrast of 0.1 at this interface (2.5 to 2.6 $\times 10^3$ kg m^{-3}) reduces the implied velocity jump and predicts a velocity of 5.7 km s^{-1} beneath S. This situation likely better represents the real world, but the velocity contrast is changed by a small amount and not significant within the uncertainty of these calculations.

The S-reflector on CM-15 lies beneath tilted continental blocks and appears to form a con-

tinuous event with the block bounding faults (Figure 7.11). A panel is chosen for analysis where S can be clearly identified and is smooth and has a low angle of dip. Along-line amplitude variations in S may be related to focusing and defocusing effects of the overburden, so by only analysing regions where S is clear this approach may overestimate the amplitude at this boundary. Basement velocities and densities are not well known along CM-15 so identical properties to the intra-crustal event on CM-13 are assumed: a density step from 2.5 to 2.6 $\times 10^3$ kg m^{-3} at S and a velocity above S of 4.5 km s^{-1}. The seabed reflection coefficient is assumed to be 0.19, the same as along CM-13. Solving Equation 7.8 with R_s=0.16, predicts a velocity beneath S of 6.0 km s^{-1}.

This amplitude analysis predicts a velocity of >7.5 km s^{-1} beneath S on CM-13. This forms a large velocity range because of the uncertainty in density across the interface and in the velocities above the reflector, but the velocity is very distinct from upper continental or oceanic crustal velocities. These results support the MCS image and gravity modelling which suggest that this event is located at the base of continental crust. The velocity contrast at S varies along the margin and this analysis does not allow us to conclude whether the event between CDPs 5045 and 5060 was formed by the same or similar mechanisms to S.

7.6 Discussion: North Biscay

The structure of the North Biscay margin will be considered along each profile, CM-13 and CM-15, separately and the results will then considered together to examine margin development processes. A comparison with similar structures at the Amorican and Galicia Bank margins is also made.

7.6.1 CM-15 interpretation

The deep-water portion of CM-15 was reprocessed in this study. Along the line there is a change in continental block size from the broad (~25 km) blocks of the continental slope to smaller and more closely spaced blocks 10-15 km wide further seaward. These blocks are bounded by listric faults which sole out within the crust at the S-reflector; along margin changes in S are considered later in this discussion.

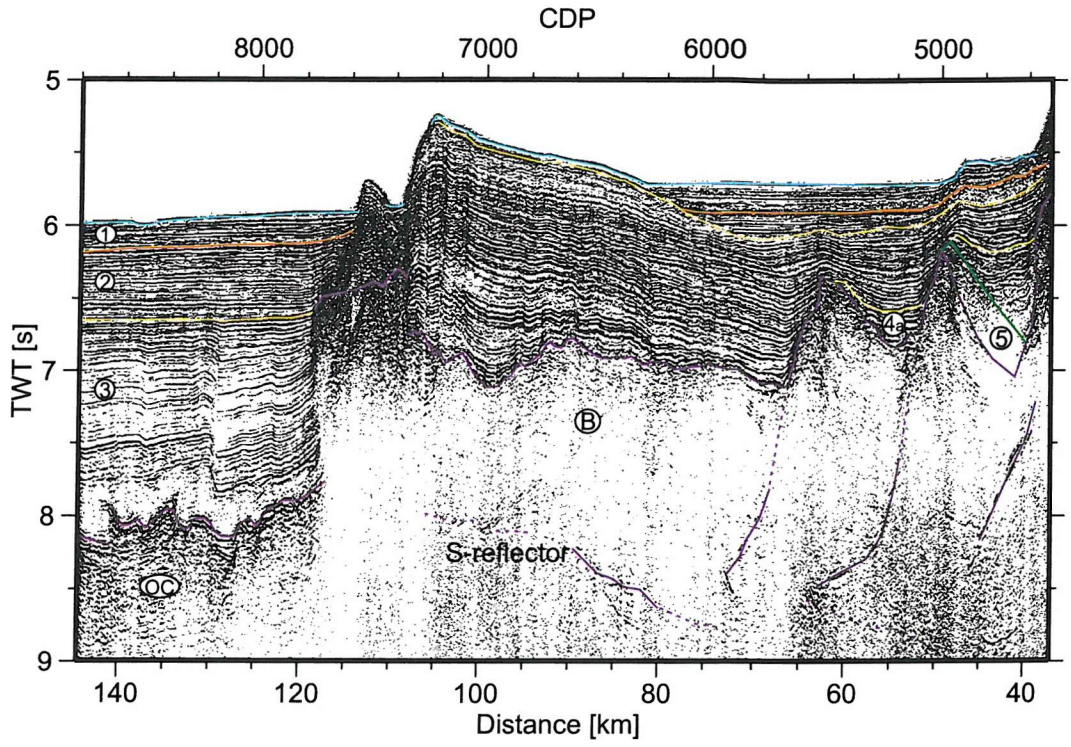

Figure 7.26: Geological interpretation along line CM-15 between CDP 4500 and 8800. Labelled sequences follow the notation of Montadert et al. (1979) (Section 1.4.4) and are as applied in Figure 7.21. Oceanic crust (OC) is defined seaward of 120 km on the basis of a change in basement appearance and newly observed magnetic anomalies.

A tectonic inversion over the southern 80 km of the line resulted in uplift of the sedimentary column. This inversion occurred during the Eocene and is associated with the Pyrenean orogeny (Masson and Parson, 1983). Uplift and deformation of basement likely occurred by reactivation of normal faults formed during rifting as no evidence for a second generation of faults can be seen. Small scale faulting within the sedimentary column has displacements <10 m, dipping both north and south and show a general trend to step up towards the south, suggesting that within this two-dimensional profile compression was acting from south to north.

The east-west orientation of Eocene compression within the Bay of Biscay means that most of the shortening occurred normal to line CM-15 and that out of the plane material was brought into the line by dextral strike-slip faulting at the ocean-continent boundary (Masson and Parson, 1983; Thinon et al., 2001). The extent of this motion is difficult to

quantify when considering single, or widely spaced, 2-D profiles, but the regional bathymetric map (Figure 1.9) adds some important constraints. Water depth decreases towards the eastern boundary of the North Biscay margin and abruptly increases at the boundary with the Amorican margin. Eastward compression may have been focused between 8° and 10° W by westward subduction of Bay of Biscay crust beneath the North Biscay margin (Olivet, 1996; Thinon et al., 2001); the amount of subduction must be small as there is no evidence for arc-type melt formation, long-wavelength raised basement features supported at depth or imaged subducted crust. The raised seabed, which can be at least partly attributed to eastward compression and thrust stacking, continues for 50-80 km along margin strike and is consistent with estimates of 100-150 km of closure between Iberia and Europe post rifting (Olivet, 1996) (Section 1.4.2).

7.6.2 CM-13 interpretation

The geological interpretation of CM-13 was based on the depth migrated multichannel seismic study (Section 7.3) and physical properties predicted by gravity modelling (Figure 7.27). Crustal thickness decreases from ~24 km to ~3 km over a distance of 200 km; full continental thickness of ~30 km is not sampled along this line. Average upper crustal densities of 2.6 $\times 10^3$ kg m^{-3} are consistent with gravity modelling further east, along CM-14, and higher than seen at Goban Spur (Section 5.2.2). Broad continental blocks of the continental slope are separated from smaller, more closely spaced continental blocks by a ~50 km wide zone of upper continental crust with smooth and unreflective top basement (Figure 7.20*a*) bounded at the base by a strong reflection 1-1.5 km into basement. This reflection event comes from a step increase in basement velocity of ~1.7 km s^{-1} (Section 7.5), but is disconnected from the S-reflector on this line. Reflectivity does not change noticeably over this reflection and it is located within the low density upper crust on the gravity modelling so is interpreted as an intra-crustal reflector.

Beneath this reflector is a zone of deep reflectivity 2-3 km thick that marks the base of lower continental crust, dipping northward at ~20° and disappearing at 140 km distance and 10 km depth into the base of upper continental crust. Between 145 and 205 km basement consists of upper continental crust only; the Moho is predicted to be at 8.5-10 km depth in this region from gravity modelling, but no reflection Moho can be seen, probably due to decreased energy penetration beneath the tilted fault blocks.

The region from 100 to 145 km appears to mark a zone of differential stretching where

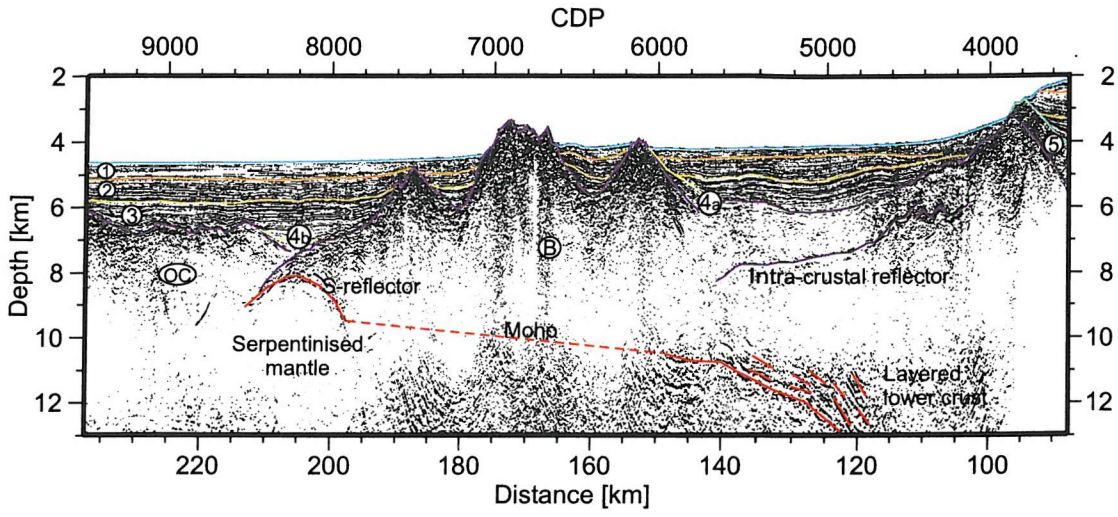

Figure 7.27: Geological interpretation of line CM-13 between CDP 3500 and 9500. Lower continental crust pinches out by CDP 6000; the S-reflector indicates the top of serpentinised upper mantle at the seaward end of continental crust and coincides with the Moho. Oceanic crust (OC) is interpreted on the basis of a change in basement reflectivity and the appearance of a magnetic anomaly. The layer numbering follows the notation of Montadert et al. (1979) (Section 1.4.4) and are as for Figure 7.17.

preferential thinning of the lower continental crust has occurred (Figure 7.27). This is similar to the zone of necking proposed by Thinon et al. (2001) at the Amorican margin. As extension occurred progressively seaward, strain was greatest in the lower crust which deformed by ductile flow. Stress may have accumulated within the upper crust during this period and allowed formation of a detachment fault, producing the observed reflection event. Upper continental crust was displaced ~50 km seaward along this fault and experienced continued thinning.

The material overlying this fault is unreflective and interpreted as disrupted continental material. Two hypotheses are presented for the development of this fault and the material immediately overlying it. A process resembling the formation of a metamorphic core complex (e.g., Wernicke, 1985; Chéry, 2001) may allow upper crustal fault blocks to experience large amounts of rotation, such that their final orientation was near-horizontal in this zone of extreme thinning. Seismic layering within the blocks was disrupted or poorly imaged due to its near-vertical orientation. This mechanism is not favoured because thinning did not occur at the point of maximum stress, at the rift axis, but within the crust of a developing passive margin. A seaward jump in the position of maximum stress could explain

these observations, but rotation of the continental blocks now located between 150 and 200 km would initially have occurred in the opposite direction and would be evidenced in the imaged sedimentary sequences; no such evidence is observed and this proposal is discounted.

Alternatively, this region may consist of brecciated continental crust produced within the fault zone and deposited on top of the footwall as the hanging wall was displaced southwards. Sediment infilling of fault gouge material may negate the impedance contrast at this interface and explain the observed loss of layering from sediment to crust. This explanation is favoured for formation of this region, but in order to provide the 50-75 km^2 of material forming the layer on this profile, fault gouge material may be supplemented by fractured continental material from the footwall where it intersects with top basement and combined with disrupted pre- and syn-rift sediments. The sudden, and large scale, detachment likely occurred due to an increase in stress within the upper crust as the lower crust was pinched out. This spatially abrupt change did not allow for stress to be dispersed over many developing faults, but encouraged large scale failure within the upper crust.

Volumetric constraints from gravity modelling tell us that not all crustal material observed between 150 and 200 km can have originally been located above this detachment, but must have existed seaward of this position prior to faulting; reconstructing the margin and restoring all of this crust to above the detachment would result in a significant southward thickening of the upper crust prior to this faulting and a deep Moho in this region (Figure 7.16, 7.27). A crustal thickness of 4-5 km is estimated at 170 km to represent the maximum thickness of continental crust seaward of the lower continental crust pinch-out prior to continued thinning.

S is present at the seaward end of CM-13 where it marks, or coincides with, the Moho and a transition from upper continental crust to low density mantle. Waveform and amplitude analysis of S suggest this is a sharp boundary stepping from velocities of 4.5 to $\sim$7.5 km s^{-1} and to a body with an average density of 3 $\times 10^3$ kg m^{-3}. These velocities and densities are consistent with serpentinised upper mantle; 7.5 km s^{-1} equates to $\sim$3.2 $\times 10^3$ kg m^{-3} , significantly greater than seen here, but within the uncertainty of the amplitude analysis calculation. Serpentinisation of upper mantle beneath the rift axis was encouraged by pervasive fluid flow along faults bounding the tilted fault blocks. A crustal thickness <4 km allows fault penetration to the upper mantle and therefore provides a pathway for water input.

Due to the sparsity of syn-rift sedimentation, or the later uplift and deformation along the North Biscay margin it is not possible to determine the detailed timing of activity on S, or the dip at which it was active. Evidence presented here suggests a seaward dip, possibly at a low angle, and southward gravitational sliding of continental blocks, but opposes a previous interpretation of S as a landward dipping feature (Le Pichon and Barbier, 1987).

7.6.3 Along margin changes

Both CM-13 and CM-15 show a change in fault block size at the foot of the continental slope from ~30 km to 10-15 km width. The width of this region decreases from CM-13 to CM-15, but a greater number of fault blocks are present and not as widely spaced. As the Bay of Biscay opened by rotation about a pole to the east of the ocean basin it is possible that a greater strain rate in the west caused these variations in deformation and appearance. The relationship of S to the thinning continental crust may also have had a strong influence. At CM-15, faults bounding the tilted blocks sole out onto S and extension along this detachment and brittle faulting within the upper crust are linked. At CM-13, S is located at the base of the crust and may act as a zone of weakness and allow decoupling from the mantle beneath.

The area effected by Eocene compression has in previous studies been considerably underestimated in extent normal to the margin (Masson and Parson, 1983); the results presented here show 85 km of CM-15 has experienced this deformation, including the seawardmost 55 km of thinned continental crust (Figure 7.8). Eocene deformation can be observed on line CM-14 however it is much less widespread and of a lower magnitude than seen on CM-15. Masson and Parson (1983) suggest this deformation is limited in lateral extent and dies out to the west along the margin strike (Figure 7.28). The absence of Eocene uplift and deformation on CM-13 supports this conclusion, however the exact nature of these changes can not be documented due to the large spacing between seismic lines.

7.6.4 Comparison with the Amorican margin

The Amorican margin has been less heavily studied than the North Biscay margin over the last few decades. Wide angle seismic data shows thinning of continental crust from ~30 km to ~5 km over a distance of ~80 km and an abrupt transition to oceanic crust

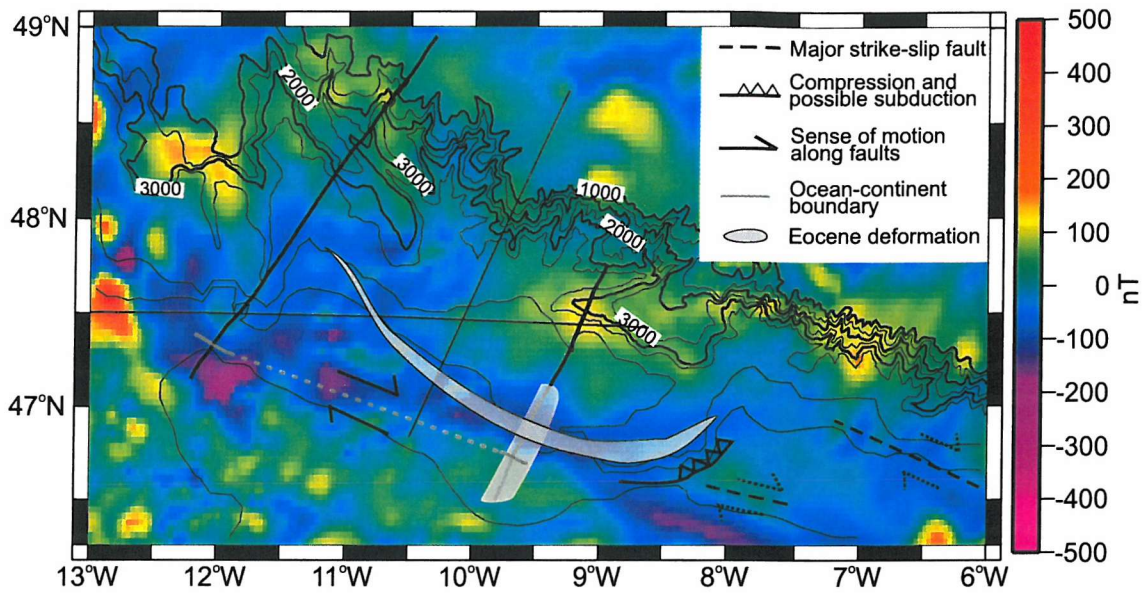

Figure 7.28: The North Biscay bathymetric map overlain on the regional magnetic anomaly. Contour interval is 0.25 km between 4 and 5 km water depth and 0.5 km elsewhere. Multichannel seismic profiles from the CM survey are shown as black lines and in bold if included in this thesis. The continent-ocean boundary at each of these lines is marked by a grey line and interpolated between these positions (dashed grey line); the region effected by Eocene compression as mapped by Masson and Parson (1983) is marked by the transparent grey area and extended along CM-15 from this study. A weak linear magnetic anomaly can be identified at the seawardmost boundary of continental crust, along the ocean-continent boundary.

(Bott and Watts, 1971) which Le Pichon and Sibuet (1981) use to show that pure shear extension provides a good first order fit to the observed margin profile. Le Pichon and Barbier (1987) identify the S-reflector beneath the Amorican margin on a detailed MCS survey and show it to be situated at the base of the tilted fault blocks within continental crust and dipping down towards the continent. The *NORGASIS* survey (Avedik et al., 1996) provided detailed coverage over the Amorican margin and was interpreted by Thinon et al. (2003), using additional constraints from wide-angle velocity modelling, to detail thinning of continental crust and the crustal composition seaward of the continental slope (Figure 7.29). Crustal thinning was concentrated beneath the continental slope, in a region 15-40 km wide; lower crustal thinning is constrained by thinning of the layered lower crust and its uplift to higher structural levels. A 30 km wide 'neck area' exhibits smaller tilted blocks and some deep layering, but is interpreted as a glide zone unrelated to crustal thinning, in which the tilted blocks have slid under gravity to their present position (Thinon et al., 2003). A 3-4 km thick, and up to 120 km wide, high velocity

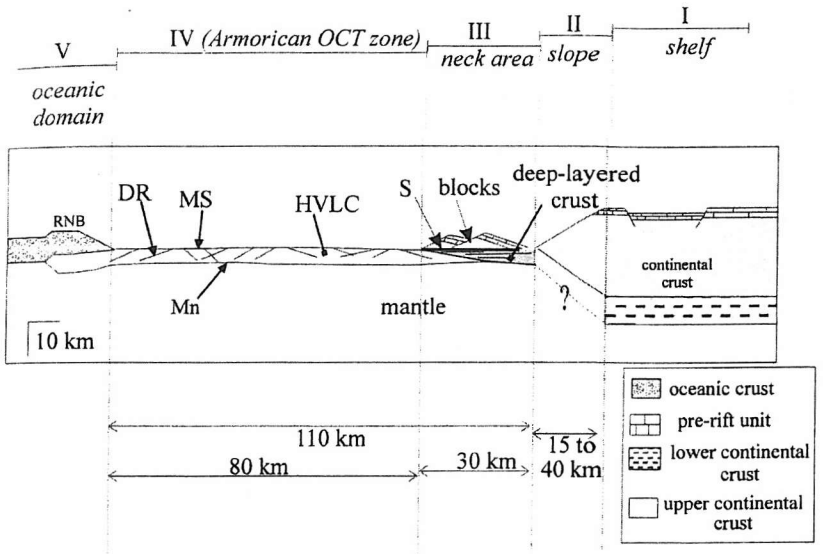

Figure 7.29: Schematic illustration of the Amorican margin. MS=basement in the ocean-continent transition zone; M=Moho; DR=dipping reflectors; S=S-reflector; Mn=top of normal mantle; HVLC=high velocity lower crustal layer; RNB=North Biscay ridge. From Thinon et al. (2003).

(7.4-7.5 km s^{-1}) lower crust is identified seaward of the tilted fault blocks. This region exhibits low magnitude magnetic anomalies and is interpreted as a ocean-continent transition zone dissimilar to the adjacent continental and oceanic crust (Thinon et al., 2003). Normal incidence Moho reflections are identified beneath this region.

Many features of the Amorican margin are also observed at the North Biscay margin. Crustal thinning occurs primarily at the continental slope; lower crust pinches out here on CM-13, but continues seaward of the continental slope on the Amorican margin. It is not clear whether this change occurs between the two margin segments or is a gradual change from CM-13 eastward. No layered lower crust is identified on CM-13, but amplitude analysis of S and wide-angle velocity modelling along CM-14 do not preclude the presence of lower crust beneath S. Above S, in the 'neck area' south of the continental slope, are smaller tilted blocks, ~15 km in width. These are observed along the full width of both margins, but have different interpretations. The data along CM-15 do not support an interpretation of S as a gravity slide structure; S is an intra-crustal event, possibly at the boundary between thinned upper and lower continental crust. Eocene uplift has masked the exact crustal thickness, but estimates from wide-angle modelling suggest that crust continues to thin within this area to a minimum of ~4 km (Ginzburg et al., 1985).

The abrupt bathymetric differences between the North Biscay and Amorican margins are not repeated in lateral changes of crustal structure. The bathymetric boundary delineates the region effected by Eocene uplift and is not related to along-margin changes in crustal deformation.

Thinon et al. (2003) suggest that high velocity lower crust is identified directly beneath high velocity sediments at the seaward tip of continental crust on *NORGASIS* line 14, in the west of the Amorican margin. This feature is comparable to the low density upper mantle raised to top basement as upper continental crust pinches out. Oceanic crust is formed south of continental crust on CM-13, interpreted on the basis of a change in basement reflectivity and the first oceanic magnetic anomaly, but the comparable region is interpreted as transitional basement, with a different structure to oceanic crust, at the Amorican margin (Thinon et al., 2003).

7.6.5 The conjugate margin of northern Iberia

Although there is considerable uncertainty in the reconstruction of the Bay of Biscay to its pre-rift position (Section 1.4.2) the North Biscay margin is conjugate with northern Iberia and the closest published seismic line is IAM-12 (Figure 1.18). Southward subduction of 35-40 km of Bay of Biscay crust beneath the North Iberia margin (Srivastava et al., 1990b; Alvarez-Marron et al., 1997) has removed the transition from continental thinning to oceanic crustal accretion from the original position. Present day models show crustal thickening under the continental slope and a rapid transition to oceanic velocities and densities seaward of the slope (Alvarez-Marron et al., 1997; Fernández-Viejo et al., 1998). Velocity and density models along IAM-12 show proportional thinning of all continental layers, but with increased lower continental crust thinning beneath the continental slope, similar to that identified at North Biscay and implying symmetrical depth dependent thinning during extension. No strong conclusions can be drawn from these observations due to subduction of the highly thinned crust and uncertainties introduced to the identified deep structure by the presence of subducted crust.

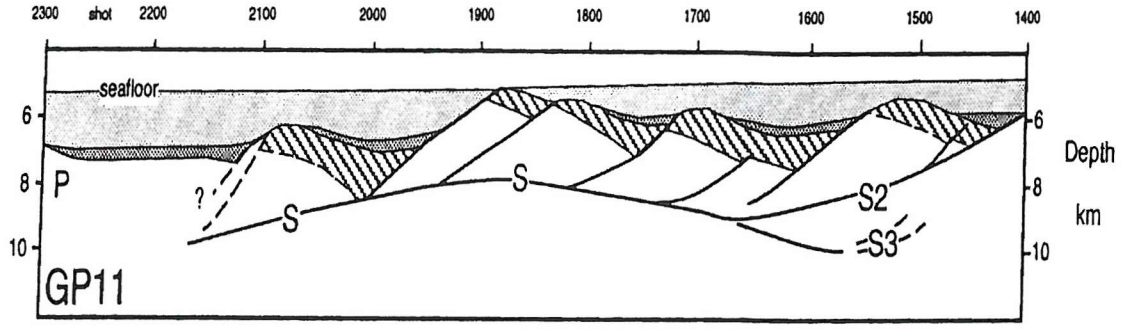

Figure 7.30: Example depth model along line GP11 over Galicia Bank, showing the relationship of S to the tilted fault blocks. Post-rift sediments are shaded light grey, syn-rift sediments in dark grey and pre-rift are shown by dipping lines. P marks the peridotite ridge. From Reston et al. (1996a).

7.6.6 Comparison with Galicia Bank

The Galicia Bank margin formed during the separation of Iberia from the Grand Banks at ~114 Ma (Boillot and Winterer, 1988) during the formation of the Atlantic ocean basin. Galicia Bank is a region of elevated continental crust rising to ~3 km above the surrounding abyssal plain and separated from Iberia by the Galicia Interior basin. Several experiments have been carried out over Galicia Bank, resulting in detailed seismic reflection and refraction studies (e.g., Mauffret and Montadert, 1987; Whitmarsh et al., 1996a). These seismic results show a region of thinned continental crust with tilted fault block structures (Whitmarsh et al., 1996a), extending seaward into a region interpreted as both thinned continental crust (Whitmarsh et al., 1996a) or transitional between continental and oceanic crust (Mauffret and Montadert, 1987), possibly similar to the exhumed mantle observed further south off West Iberia (Dean et al., 2000; Whitmarsh et al., 2001a) which is bounded on its seaward side by a peridotite ridge (Boillot et al., 1980; Sibuet, 1992). Initial oceanic crust is thin, only 2.5-3.5 km thick, and increases rapidly to 6-7 km, normal for Atlantic oceanic crust (White, 1992). Continental fault blocks at Galicia Bank are underlain by the S-reflector, which consists of a series of undulating reflections (e.g., Mauffret and Montadert, 1987; Boillot et al., 1988; Pérez-Gussinyé et al., 2003) at 8-10 s TWT (e.g., Figure 7.30).

Various models for S at Galicia Bank have been proposed since its initial identification (e.g., de Charpal et al., 1978; Hoffmann and Reston, 1992); waveform, phase and ampli-

tude analysis of S was considered by Reston (1996) who interpret it as a step increase in impedance caused by a westward dipping detachment fault separating upper continental crust from serpentinised mantle beneath. Reston et al. (1996a) go further and describe S as a low angle detachment accommodating top to the west shear and active at <20°, 1-3 km beneath top basement (Figure 7.30). This interpretation is similar to that presented for S at CM-13 on the North Biscay margin; differences with CM-15 exist due to along margin changes in S so that it is an intra-crustal event in the eastern part of the North Biscay margin. S at CM-13 marks the boundary between upper continental crust and serpentinised mantle, close to the seaward edge of thinned crust as observed at Galicia Bank, but there must have been differences in final break-up processes as initial oceanic crust appears immediately seaward of S on CM-13 and seaward of a transition zone at Galicia Bank.

Although there are many similarities in S between the two margins they are not part of the same tectonic feature. If we accept the M0 identification, break-up occurred slightly earlier at the North Biscay margin than at Galicia Bank so they are not directly related, but may result from similar processes and/or conditions towards the end of rifting, e.g., extension rates, crustal thickness or heat flow. It is possible that, because Iberia and Europe were once connected, similar pre-existing weaknesses existed within continental crust, encouraging the formation of detachments at similar structural levels.

7.7 North Biscay conclusions

Reprocessing and migration of multichannel seismic profiles from the North Biscay margin combined with gravity modelling and sampling results from DSDP Leg 48 leads to the following conclusions.

1. Continental thinning occurred from >24 km to ~3 km over a distance of ~200 km. Crustal thinning occurred at the expense of both upper and lower crust, but gravity modelling shows the preferential thinning of lower crust which pinches out, corresponding with the disappearance of layered reflectivity.

2. Seaward of the lower crust pinch-out, 60 km of upper continental crust, 3-6 km thick, directly overlies a body of serpentinised mantle <3 km thick and with an

average density of 3 $\times 10^3$ kg m^{-3}. The upper crust - serpentinised mantle boundary coincides with S on CM-13 and a step increase in velocity of 1.8-3 km s^{-1}.

3. Along CM-15, towards the east of the margin, the S-reflector is continuous beneath tilted blocks whose bounding faults sole out onto it. Amplitude analysis and gravity modelling shows S to be an intra-basement event with crustal velocities and densities beneath.

4. S changes significantly along the margin, shallowing westward from a maximum of 12 km depth on CM-15 to CM-13 where it rises to just beneath top basement. The reflection coefficient of S, R_s, is 0.37-0.43 on CM-13 which equates to a velocity step consistent with a transition from upper continental crust to serpentinite and can therefore be considered to mark the Moho. S becomes an intra-crustal event on CM-15 with R_s=0.16 and is continuous along the margin.

5. A 25 km long intra-crustal reflection on CM-13, ~80 km north of the seawardmost extent of continental crust is present <1 km beneath top basement and is interpreted as a detachment fault. Overlying material appears seismically disrupted and may consist of broken upper continental crust and fault gouge material. This event is isolated from S and overlies the region of preferential thinning of the lower crust; development of this fault may be influenced by the sudden release of stress accumulated within the upper crust during the period of maximum lower crustal strain.

6. Eocene compression resulted in uplift and deformation along the North Biscay margin from a maximum of ~3 km on CM-15, decreasing westward to CM-15 where it is largely absent. Maximum deformation is closest to the continent-ocean boundary, but effects a width of 55 km of thinned continental crust on CM-15.

Chapter 8

Discussion, conclusions and further work

The preceding chapters have considered various aspects of the crustal structure and development of the UK rifted margins of Goban Spur and North Biscay, in the North Atlantic and Bay of Biscay respectively. The results are brought together in this chapter and the regional implications considered; the global context is also discussed, some final conclusions reached and some suggestions for future work made. I refer the reader to Section 6.3 and Section 7.7 for summaries of the Goban Spur and North Biscay results.

8.1 Discussion

8.1.1 Cretaceous rifting in the eastern Atlantic

The Goban Spur and North Biscay margins were formed by continental rifting at approximately the same time and the same latitude; the two margins, however, appear to have developed in very different ways. Goban Spur was part of the much larger northward progression of North Atlantic stretching and opening, and displays an abrupt termination of thinned continental crust, with a small volume of melt emplaced towards the end of rifting. North Biscay formed as part of an eastward trending arm off the North Atlantic Ridge and displays a broad zone of continental thinning, possibly broadened by the presence of detachment faults within the brittle layer, allowing relatively large seaward displacements of upper crust.

Both margins show evidence for depth dependent stretching, but experienced in a differ-

ent way. At Goban Spur, lower continental crust was thinned 4-10 times as much as the upper crust (Davis and Kusznir, 2004), but is present on seismic and gravity models at the seawardmost point of continental crust; along CM-13 at North Biscay, the lower crust was also thinned by a greater amount, but was pinched out ~60 km before the last continental crust. It is not clear from the data presented here how crustal thinning occurred further east, along CM-15, but a wide-angle seismic velocity model along CM-14 shows the presence of lower crustal velocities, 6.6-7.4 km s^{-1}, at the continent-ocean transition and are well constrained by the synthetic seismogram modelling of Whitmarsh et al. (1986), so it seems likely that there is some element of along-margin variation in the thinning processes.

A 70 km wide zone of exhumed mantle is present seaward of the continental slope at Goban Spur, but no such feature is observed at the seaward end of CM-13 or CM-15, where magnetic data and seismic reflection characteristics suggest the presence of basaltic ocean crust. Beneath the most heavily thinned crust on CM-13 is a ~3 km thick serpentinised upper mantle body; serpentinisation was likely encouraged by the influx of water along bounding faults within the upper crust. I propose that strain was concentrated along the S-reflector and that serpentinisation of the upper mantle occurred during the late stages of rifting. A gradual transfer of strain seaward resulted in melt production at break-up time and the formation of initially thin oceanic crust (Figure 8.1*a*). By contrast, at Goban Spur I propose that strain was rapidly transferred to the mantle lithosphere at break-up, possibly due to the emplacement of melt products acting as a boundary for a large strain gradient or intrusive strengthening of the crust, and upper mantle was exhumed with little or no melting, due to the ultra-slow extension rate (Figure 8.1*b*). This model is consistent with both the symmetric and asymmetric rifting models presented in Section 6.2.4.

8.1.2 Continental rifting within the North Atlantic

This study firmly places the Goban Spur rifted margin within the amagmatic class of rifted margin rather than intermediate between amagmatic to the south and volcanic to the north. The North Atlantic margins of the Southern Iberia Abyssal Plain, Galicia Bank, Porcupine Bank and now Goban Spur are all documented members of this class and, within the eastern North Atlantic, amagmatic margins may extend from the Azores-Gibraltar plate boundary in the south to the Charlie-Gibbs fracture zone in the north at ~54° N (Figure 8.2). North of the Charlie-Gibbs fracture zone, there is a change in margin strike to 045°-225° and considerable syn-rift volcanism is observed; these changes are due to younger rifting, under the influence of the Iceland mantle plume.

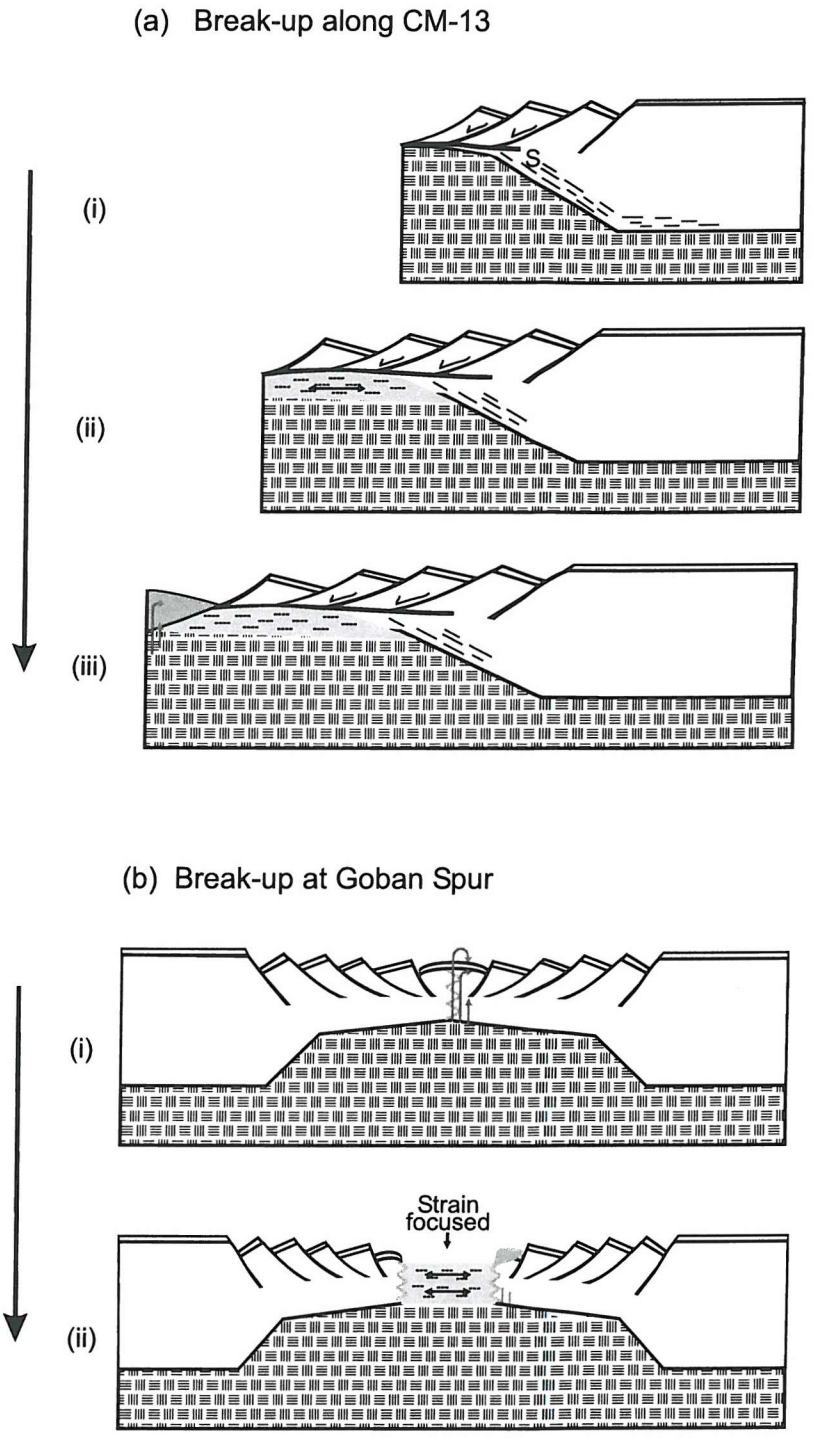

Figure 8.1: Time series development of models of final break-up for North Biscay and Goban Spur. (a) Rifting along CM-13 at the North Biscay margin preferentially thins the lower crust, allows the development of S and continued extension of the upper crust (i). Serpentinisation of upper mantle beneath is encouraged by water flow along block bounding faults (ii) and final break-up forms initially thin oceanic crust (iii). (b) Towards the end of rifting at Goban Spur, basalt was emplaced at the foot of the continental slope and possibly intruded into the base of the crust (i); this strengthened the continent at the seaward end and assisted the rapid transfer of strain to the exhuming mantle at the rift axis (ii).

Detachment faults have been identified at the Southern Iberia Abyssal Plain, Galicia Bank, Amorican margin and the North Biscay margin. The H reflector, west of Iberia, is a low-angle detachment formed within thinned continental crust beneath tilted fault blocks, and assisted in the extreme thinning to 3-6 km (Chian et al., 1999; Whitmarsh et al., 2000), but it was not directly involved in mantle exhumation. A further generation of detachment faulting, with a top-to-the-west sense of shear, was proposed to control final break-up and mantle exhumation (Whitmarsh et al., 2001a). In contrast to the models for West Iberia, the S-reflector at Galicia Bank has been identified beneath tilted fault blocks and was a low angle detachment fault that controlled the final break-up of the continent (Reston et al., 1996a). As it extends westwards, S coincides with the top of a serpentinite body (Whitmarsh et al., 1996a), although a broad zone of mantle is not exhumed. Towards the west of the Bay of Biscay, S is present at the Amorican margin beneath tilted fault blocks. It is present only in the narrow region of maximum crustal thinning, and interpreted as a decollement, allowing rotation and seaward movement of the upper crust, but had a minor influence in crustal thinning (Thinon et al., 2003).

Evidence presented from the North Biscay margin shows the important role of S in crustal thinning, to a minimum of 3-4 km thickness, and in final break-up processes. Along-margin changes show S to be intra-crustal on CM-15, beneath block-bounding faults and potentially acting as a decollement, while on CM-13 it is observed to coincide with the crust-mantle boundary, the the top of a serpentinite body and the transition to oceanic crust. The results from widely separated seismic lines presented here illustrates the three-dimensional nature of continental margins and the importance of considering closely spaced profiles to understand rifting and break-up processes.

8.1.3 The role of serpentinised mantle in continental break-up

Serpentinised mantle appears to play an important role in the late stages of continental break-up at some rifted margins. Broad regions of exhumed mantle have now been identified at the Goban Spur and Amorican margins and the Southern Iberia Abyssal Plain within the eastern North Atlantic and serpentinite bodies underlying thinned continental or oceanic crust at the Galicia Bank, Amorican and North Biscay margins (Figure 8.2); serpentinite may be present as far north as the Porcupine Basin, as a diapiric structure emplaced during extension (Reston et al., 2001). The conjugate margins of southwest Greenland (Chian and Louden, 1994) and Labrador Sea (Chian et al., 1995b) have also

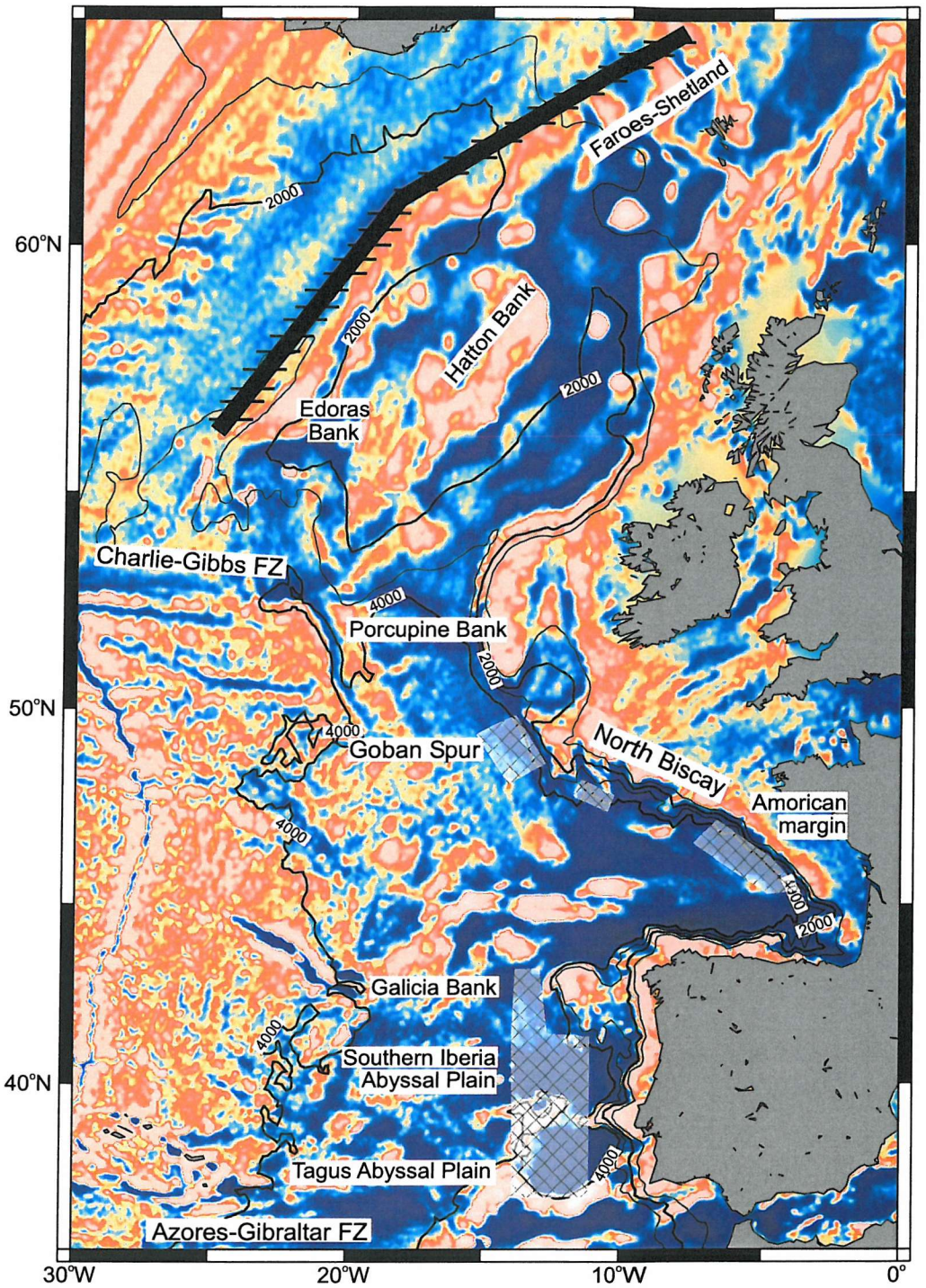

Figure 8.2: Distribution of exhumed mantle within the eastern North Atlantic overlain on the free-air gravity anomaly for the region. Amagmatic extension and mantle exhumation is indicated by cross-hatching and has been identified at the southern Iberia Abyssal Plain (e.g., Dean et al., 2000), Galicia Bank (Sibuet, 1992) and the Amorican margin (Thinon et al., 2003) in addition to the North Biscay and Goban Spur margins presented here. Volcanic margins are shown by a bold black line and cross-bars. Amagmatic margins are situated between the Azores-Gibraltar fracture zone in the south and the Charlie-Gibbs fracture zone to the north. Bathymetric contours are plotted every 1 km.

been interpreted as having abundant serpentinisation beneath the transition to sea-floor spreading (Chian et al., 1995a).

The presence of serpentinite at rifted margins appears highly dependent on the way in which crust is deformed and the extension rate at the time of break-up which acts to inhibit melt formation as mantle material is exhumed or raised to higher structural levels. Mantle has been exhumed at ultra-slow extension rates e.g., 10 mm yr^{-1} at Goban Spur, ~20 mm yr^{-1} at west Iberia (Sawyer, 1994; Whitmarsh and Sawyer, 1996; Minshull et al., 2001) and the Amorican margin at ~10 mm yr^{-1} (Thinon et al., 2003). Changes in mantle exhumation along the margin may be explained by variations in the style of rift development within continental crust, a boundary now indicated by the presence of oceanic fracture zones which formed along the pre-existing continental weakness. For example, the Amorican and North Biscay margins were separated by a fracture zone at the eastern boundary of Meriadzek Terrace (Garcia-Mondéjar, 1996) and appear to have thinned in different ways. A narrow neck of crustal thinning followed by mantle exhumation at the Amorican margin compares to a broad region of crustal thinning at North Biscay and a rapid transition to oceanic crust. The along margin decrease of mantle exhumation may also be explained by the presence of large tectonic features, such as the Galicia Bank, which acts as a northern boundary to mantle exhumation west of Iberia; serpentinite is present at Galicia Bank beneath highly thinned continental crust and as a peridotite ridge.

8.2 Conclusions

This thesis examined wide-angle seismic data from the Goban Spur margin and normal incidence seismic data from the North Biscay margin, integrated with gravity and magnetic modelling and existing seismic studies, to reveal the crustal structure and rifting processes that operated during Cretaceous extension and continental break-up of the UK continental margins. The principal results are as follows.

1. At Goban Spur a 70 km wide zone of exhumed mantle is identified between thinned continental and oceanic crust. This zone exhibits very low basement relief, P-wave velocities of 4.5-7.6 km s^{-1} and high Poisson's ratio (0.34-0.36) within the top 1 km of basement. The observed velocities correspond to an extent of serpentinisation of 100-50% up to 5 km beneath top basement and <25% from 5-8 km into basement.

Strong magnetisation, 2-3 A m^{-1}, within the top 1-1.5 km of this exhumed mantle is attributed to intense serpentinisation during a prolonged contact with seawater.

2. Initial oceanic crust is anomalously thin, ~5 km, and defined by small (~5 km wide, ~500 m high) ridges bounded by westward dipping faults, an absence of clear normal-incidence Moho reflections and velocities >7 km s^{-1} at depth. Normal oceanic crust is indicated by marine magnetic anomaly 34r, 120 km west of the continental slope, and the appearance of a seismic reflection Moho.

3. Continental break-up between Goban Spur and northern Flemish Cap may have occurred in a symmetric or asymmetric manner and potential rifting models were presented, but insufficient evidence is available to reach a definitive conclusion here. The observed melt can be explained by decompression melting with a crustal stretching factor of 8 to 10. It seems likely there was a rapid transfer of strain to the rift axis after final break-up.

4. North Biscay crust thinned from >24 km to ~3 km over a distance of ~200 km at the expense of both upper and lower crust, with preferential thinning of lower crust occurring beneath a large detachment within the upper crust. Towards the continent-ocean boundary, 60 km of 3-6 km thick upper continental crust directly overlies a <3 km thick serpentinite body.

5. The S-reflector changes significantly along the margin, shallowing westward from a maximum of 12 km depth on CM-15, where it lies beneath tilted fault blocks, to CM-13 where it rises to just beneath top basement and coincides with the Moho and the upper crust–serpentinite body boundary.

6. Eocene compression resulted in uplift and deformation along the North Biscay margin from a maximum of ~3 km on CM-15, decreasing westward to CM-13 where it is largely absent. Maximum deformation occurred close to the continent-ocean boundary, but along CM-15 a width of 55 km of thinned continental crust is uplifted. This compressional event is not observed at Goban Spur, except for the formation of Pastouret Ridge by reactivation of an oceanic fracture zone.

7. Goban Spur and North Biscay are non-volcanic rifted margins within the North Atlantic and Bay of Biscay. Amagmatic margins are now mapped from the Azores-Gibraltar plate boundary in the south to the Charlie-Gibbs fracture zone in the north.

8. Depth dependent stretching and low angle detachments may be inter-related and appear to play an important role in the late stages of rifted margin development. These processes may be especially important at low extension rates, where decompression melting is limited and mantle may be exhumed and brought into the brittle deformation regime.

8.3 Suggested further work

This thesis has developed a new model for crustal structure at the Goban Spur and North Biscay margins, but significant questions remain. Specifically, at the Goban Spur margin, some uncertainty exists about the relative timing of melt emplacement at the continental slope and the onset of sea-floor spreading. Ar/Ar dating of the basalts recovered at DSDP Sites 550 and 551 and the dredge sample from above anomaly 34 will answer some of these questions and allow a period of mantle exhumation to be considered in the context of the timing of magmatic events. In order to develop an accurate model for continental rifting and break-up, results from Goban Spur must be combined with a model of its conjugate, Flemish Cap. A wide-angle seismic experiment has been completed and it is hoped that results will soon be available to consider the conjugate pair.

Along-margin variations must also be further considered. Structural changes across Pastouret Ridge at Goban Spur can be considered by examination of existing multichannel seismic data, but ideally wide-angle velocity constraints would be acquired as well. Along-margin changes in the S-reflector at North Biscay may be revealed along seismic line CM-16 and this should be re-examined. DSDP Leg 48 holes did not penetrate the syn-rift horizons; accurate dating of the complete sedimentary column and subsidence analysis would allow reconstruction of the crustal structure along CM-15 prior to the Pyrenean orogeny, but may require a dedicated ocean drilling leg to complete.

Appendix A

CD-124 instrument deployment list

This appendix lists all ocean bottom instruments and sensors deployed as part of the seismic survey during CD-124. Instruments 15, 13, 11, 10, 9, 8 and 6 recorded useful data and were used as part of this work; the remaining instruments recorded no useful data due to shooting being cut short or were not recovered because of the poor weather.

Table A.1: Ocean bottom instruments deployed during CD-124. Unless indicated, water depth are uncorrected for variations in sound velocity. All instruments have a sampling interval of 10 ms.

Inst. No.	Hyd. channel	Geo. channel	Depth [m]	Deployment location Latitude N	Longitude E	Internal clock start/end/drift day/time	day/time	[ms]
1	Hyd	Owen	1138	49°15.11′	-12°24.84′	269/0811	278/0819	-7
2	Hyd	–	1179	49°11.64′	-12°35.55′	269/0854	300/1618[t]	-67
3	Hyd	–	1488	49°08.36′	-12°47.33′	269/0932	–[l]	–
4	DPG	–	2162	49°05.26′	-12°58.59′	269/0946	276/1300	-2
5	DPG	–	3533	49°01.97′	-13°10.00′	269/1003	276/1058	+14
6	Hyd	–	3679[c]	48°58.37′	-13°21.38′	269/1119	276/0919	-10
7	Hyd	–	4493	48°54.20′	-13°34.08′	269/1324	–[f]	–
8	DPG	Webb	4512[c]	48°52.08′	-13°44.35′	269/1448	319/1312[t]	+115
9	Hyd	–	4535[c]	48°48.76′	-13°55.74′	269/1552	–[f]	–
10	Hyd	Webb	4527[c]	48°45.55′	-14°06.93′	269/1706	300/1529[t]	+20
11	DPG	–	4538[c]	48°42.54′	-14°18.49′	269/1900	333/1148[b]	-91
12	Hyd	–	4638	48°39.19′	-14°29.62′	269/1959	–[f]	–
13	Hyd	Owen	4747[c]	48°36.22′	-14°41.24′	269/2047	300/0940[t r]	–
14	Hyd	–	4754	48°33.02′	-14°52.28′	269/2118	274/1225[e]	-4
15	DPG	–	4840[c]	48°29.71′	-15°03.76′	269/2136	–[f b r]	–
16	Hyd	Owen	4809	48°26.43′	-15°15.10′	269/2320	274/1007[e]	-4
17	Hyd	–	4463	48°38.29′	-14°01.00′	270/1517	–[f]	–
18	Hyd	–	4487	48°30.80′	-13°54.83′	270/1622	–[f]	–
19	DPG	Webb	4497	48°23.74′	-13°48.66′	270/1802	300/1526[t]	+45
20	Hyd	–	4450	48°27.30′	-13°37.50′	270/1831	–[f]	–
21	Hyd	–	4392	48°30.99′	-13°26.84′	270/1850	300/1609[t]	-14
22	Hyd	–	4146	48°34.32′	-13°15.59′	270/2020	–[f]	–
23	Hyd	–	4208	48°37.83′	-13°32.12′	270/2154	–[f]	–
24	DPG	–	4460	48°44.80′	-13°38.16′	270/2251	300/1405[t]	-23

[t]= Recovered by trawler cruise
[l]= Instrument lost on seafloor
[c]= Water depth corrected using Carter's Tables (Carter, 1980)
[f]= On timed release and lost at sea
[b]= On timed release and drifted onto coast
[r]= Recovery time given, no power left for clock drift calculations
[e]= Recovered before shooting started

Appendix B

CD-124 XBT profiles

This appendix details the XBT temperature-depth profiles taken during cruise CD-124 in the Goban Spur region. A full list of deployment sites is given in Table 4.1.

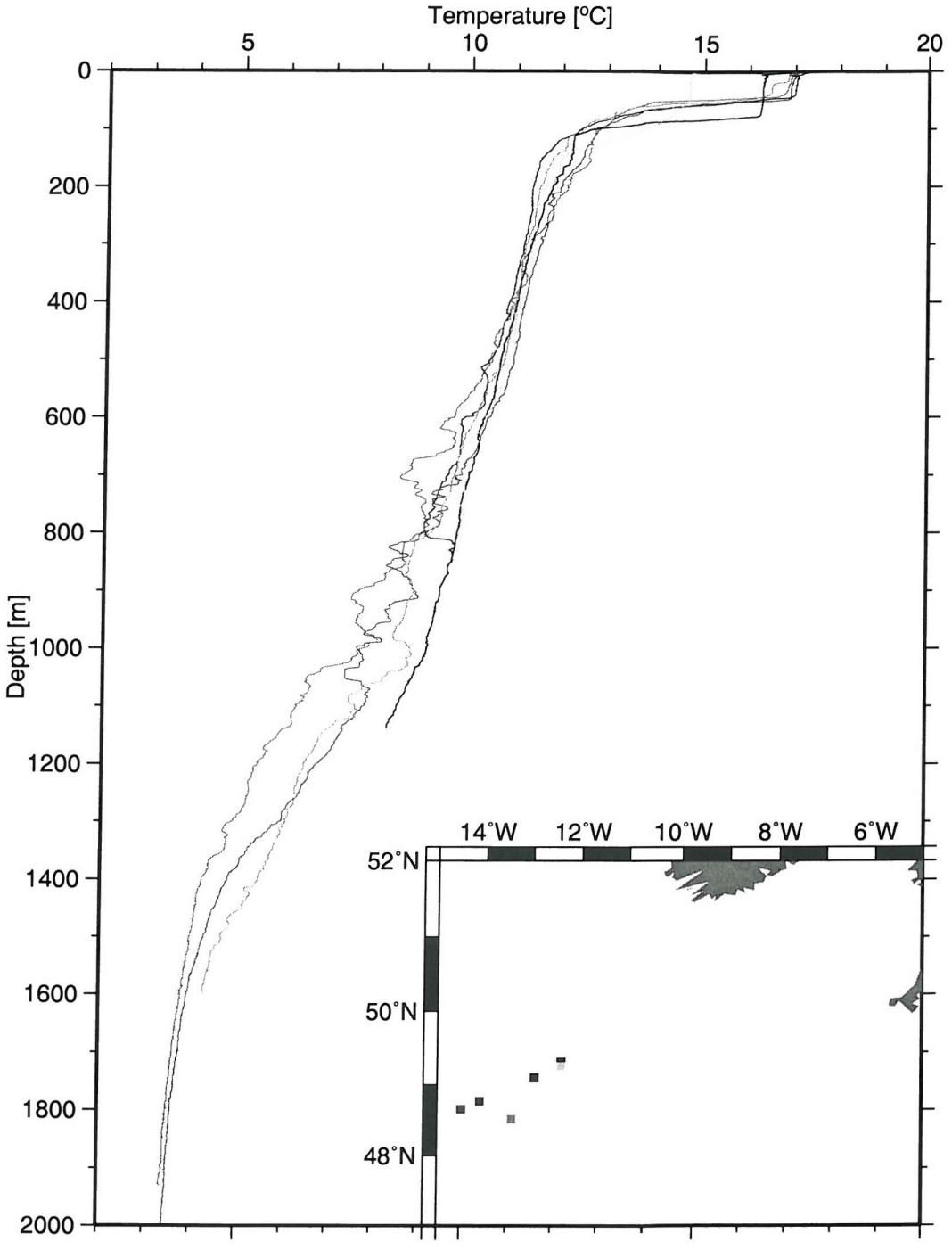

Figure B.1: XBT temperature-depth profiles collected during CD-124 in the Goban Spur region. The individual profiles are colour-coded from black (XBT 1) to light grey (XBT 6) and their location shown in the inset and given in Table 4.1.

References

Abers, G. A. (1991), 'Possible seismogenic shallow-dipping normal faults in the Woodlark-D'Entrecasteaux extensional province, Papa New Guinea', *Geology* **19**, 1205–1208.

Abers, G. A., Ferris, A., Craig, M., Davies, H., Lerner-Lam, A. L., Mutter, J. C. and Taylor, B. (2002), 'Mantle compensation of active metamorphic core complexes at Woodlark rift in Papa New Guinea', *Nature* **418**, 862–865.

Abers, G. A., Mutter, C. Z. and Fang, J. (1997), 'Shallow dips of normal faults during rapid extension: earthquakes in the Woodlark-D'Entrecasteaux rift system, Papa New Guinea', *J. Geophys. Res.* **102**, 15,301–15,317.

Aki, K. and Richards, P. G. (1980), *Quantitative seismology. Theory and methods*, W.H. Freeman and Company, San Francisco.

Alt, J., Kinoshita, H. and Stocking, L., eds (1993), *Proc. of the Ocean Drilling Program, Init. Reports*, Vol. 148, U.S. Government Printing Office, College Station, TX.

Alvarez-Marron, J., Rubio, E. and Torne, M. (1997), 'Subduction-related structures in the North Iberian Margin', *J. Geophys. Res.* **102**(B10), 22497–22511.

Anderson, E. M. (1942), *The dynamics of faulting*, Oliver and Boyd, London.

Arkani-Hamed, J. (1988), 'Remanent magnetization of the oceanic upper mantle', *Geophys. Res. Letters* **15**(1), 48–51.

Auffret, G., Pastouret, L., Cassat, G., de Charpal, O., Cravatte, J. and Guennoc, P. (1979), Dredged rocks from the Amorican and Celtic margins, *in* L. Montadert and D. Roberts, eds, 'Initial Reports of the Deep Sea Drilling Project', Vol. 48, U.S. Government Printing Office, Washington, pp. 995–1008.

Auzende, J.-M., Cousin, M., Coutelle, A., Dobson, M., Geoghegan, M., Masson, D., Rolet, J. and Vaillant, P. (1989), 'Stratigraphie des escarpements encadrant la baie

de Porcupine: résultats préliminaires de la campagne Cyaporc (juillet-août 1986)', *Oceanologica Acta* **12**(3), 117–131.

Avedik, F., Camus, A., Ginsburg, A., Montadert, L., Roberts, D. and Whitmarsh, R. (1982), 'A seismic refraction and reflexion study of the continent-ocean transition beneath the North Biscay margin', *Philosophical Transactions of the Royal Society of London, A* **305**, 5–25.

Avedik, F., Hirn, A., Renard, V., Nicolich, R., Olivet, J. and Sachpazi, M. (1996), '"Single-bubble" marine source offers new perspectives for lithospheric exploration', *Tectonophysics* **267**, 57–71.

Avedik, F. and Howard, D. (1979), Preliminary results of a seismic refraction study in the Meriadzek-Trevelyan area, Bay of Biscay, *in* L. Montadert and D. Roberts, eds, 'Initial Reports of the Deep Sea Drilling Project', Vol. 48, U.S. Government Printing Office, Washington, pp. 1015–1023.

Axen, G. (2004), Mechanics of low-angle normal faults, *in* G. D. Karner, B. Taylor, N. W. Driscoll and D. L. Kohlstedt, eds, 'Rheology and deformation of the lithosphere at continental margins', Columbia University Press, New York, pp. 46–91.

Barton, A. and White, R. (1997), 'Crustal structure of the Edoras Bank continental margin and mantle thermal anomalies beneath the North Atlantic', *J. Geophys. Res.* **102**, 3109–3129.

Bassi, G. (1995), 'Relative importance of strain rate and rheology for the mode of continental extension', *Geophys. J. Int.* **122**, 195–210.

Beard, J. S. (2000), Occurrence and composition of tochilinite and related minerals in site 1068 serpentinites, *in* M.-O. Beslier, R. Whitmarsh, P. Wallace and J. Girardeau, eds, 'Proc. of the Ocean Drilling Program, Sci. Results', Vol. 173, Ocean Drilling Program, College Station TX, pp. 1–9 [CDROM].

Berndt, C., Planke, S., Alvestad, E., Tsikalas, F. and Rasmussen, T. (2001), 'Seismic volcanostratigraphy of the Norweigan Margin: constraints on tectonomagmatic break-up processes', *J. Geol. Soc., London* **158**, 413–426.

Bialas, J. and Flueh, E. R. (1999), 'Ocean bottom seismometers', *Sea Technology* **40**(4), 41–46.

Birch, F. (1961), 'The velocity of compressional waves in rocks to 10 kilobars, part 2', *J. Geophys. Res.* **66**(7), 2199–2224.

Bitri, A., Brun, J.-P., Chantraine, J., Guennoc, P., Marquis, G., Marthelot, J.-M., Perrin, J., Pivot, F. and Truffert, C. (1997), 'Structure crustale du bloc cadomien de Bretagne Nord (France): sismique réflexion verticale et sondage magnétotellurique (projet géofrance 3d - armor', *C. R. Acad. Sci. Paris, Sciences de la terre et des planètes* **325**, 171–177.

Boillot, G. and Capdevila, R. (1977), 'The Pyrenees: subduction and collision', *Earth Planet. Sci. Letters* **35**, 151–160.

Boillot, G., Girardeau, J. and Kornprobst, J. (1988), Rifting of the Galicia margin: crustal thinning and emplacement of mantle rocks on the seafloor, *in* G. Boillot and E. Winterer, eds, 'Proc. of the Ocean Drilling Program, Sci. Results', Vol. 103, Ocean Drilling Program, College Station, TX, pp. 741–756.

Boillot, G., Grimaud, S., Mauffret, A., Mougenot, D., Kornprost, J., Mergoil-Daniel, J. and Torrent, G. (1980), 'Ocean-continent boundary off the Iberian margin: a serpentinite diapir west of the Galicia Bank', *Earth Planet. Sci. Letters* **48**, 23–34.

Boillot, G., M.O.Beslier, Krawczyk, C., Rappin, D. and Reston, T. (1995), The formation of passive margins: Constraints from the crustal structure and segmentation of the deep Galicia margin, Spain, *in* R. Scrutton, ed., 'The tectonics, sedimentation and palaeoceanography of the North Atlantic region', Vol. 90 of *Geological Society Special Publication*, Geol. Soc. of London, London, pp. 71–91.

Boillot, G. and Winterer, E. (1988), Drilling on the Galicia margin: retrospect and prospect, *in* G. Boillot and E. Winterer, eds, 'Proc. of the Ocean Drilling Program, Sci. Results', Vol. 103, Ocean Drilling Program, College Station, TX, pp. 809–828.

Bois, C., Lefort, J.-P., Le Gall, B., Sibuet, J.-C., Gariel, O., Pinet, B. and Cazes, M. (1990), 'Superimposed Variscan, Caledonian and Proterozoic features inferred from deep seismic profiles recorded between southern Irelan, southwestern Britain and western France', *Tectonophysics* **177**, 15–37.

Bonatti, E. (1985), 'Punctiform initiation of seafloor spreading in the Red Sea during transition from a continental to an oceanic rift', *Nature* **316**, 33–37.

Bott, M. and Watts, A. (1971), Deep structure of the continental margin adjacent to the British Isles, *in* 'The geology of the east Atlantic continental margin', Vol. Rep. 70/14, Inst. of Geol. Sci., London, pp. 89–109.

Bown, J. W. and White, R. S. (1994), 'Variation with spreading rate of oceanic crustal thickness and geochemistry', *Earth Planet. Sci. Letters* **121**, 435–449.

Bown, J. W. and White, R. S. (1995), 'Effect of finite extension rate on melt generation at rifted continental margins', *J. Geophys. Res.* **100**(B9), 18,011–18,029.

Braile, L., Keller, G., Wendlandt, R., Morgan, P. and Khan, M. (1995), The East African rift system, *in* K. Olsen, ed., 'Continental rifts: evolution, structure, tectonics', Vol. 25 of *Developments in geotectonics*, Elsevier Science, Amsterdam, The Netherlands, pp. 213–231.

Braile, L. W. (1977), Interpretation of crustal velocity gradients and Q structure using amplitude-corrected seismic refraction profiles, *in* J. G. Heacock, ed., 'The Earth's crust: It's nature and physical properties', Vol. 20 of *Geophysical monograph*, American Geophysical Union, Washington, D.C., pp. 427–439.

Bruguier, N. (1997), Inversion of first-arrival travel-times from the Chicxulub impact crater, *in* 'Journal of Conference Proceedings', Vol. 1, CCSS Workshop June 4th-6th, Cambridge Publications, Cambridge, UK, pp. 47–52.

Brun, J. and Beslier, M. (1996), 'Mantle exhumation at passive margins', *Earth Planet. Sci. Letters* **142**, 161–173.

Brun, J.-P. and Choukroune, P. (1983), 'Normal faulting, block tilting and décollement in a stretched crust', *Tectonics* **2**(4), 345–356.

Buck, W. R. (1986), 'Small-scale convection induced by passive rifting: the cause for uplift of rift shoulders', *Earth Planet. Sci. Letters* **77**, 362–372.

Buck, W. R. (1988), 'Flexural rotation of of normal faults', *Tectonics* **7**, 959–973.

Buck, W. R. (1991), 'Modes of continental lithospheric extension', *J. Geophys. Res.* **96**, 20,161–20,178.

Bull, J. M. and Masson, D. G. (1996), 'The southern margin of the Rockall Plateau: stratigraphy, Tertiary volcanism and plate tectonic evolution', *J. Geol. Soc., London* **153**, 601–612.

Bull, J. M. and Scrutton, R. (1992), 'Seismic reflection images of intraplate deformation, central Indian Ocean, and their tectonic significance', *J. Geol. Soc., London* **149**(6), 955–966.

Bullard, E. and Mason, R. (1961), 'The magnetic field astern of a ship', *Deep Sea Research* **8**, 20–27.

Byerlee, J. (1978), 'Friction of rocks', *Pure and Applied Geophysics* **116**, 615–626.

Byerlee, J. D. (1968), 'Brittle-ductile transition in rocks', *J. Geophys. Res.* **73**(14), 4741–4750.

Cande, S. C. and Kent, D. V. (1992), 'A new geomagnetic polarity time scale for the late Cretaceous and Cenozoic', *J. Geophys. Res.* **97**(B10), 13,917–13,951.

Cande, S. C. and Kristoffersen, Y. (1977), 'Late Cretaceous magnetic anomalies in the North Atlantic', *Earth Planet. Sci. Letters* **35**, 215–224.

Cann, J., Blackman, D., Smith, D., McAllister, E., Janssen, B., Mello, S., Avgerinos, E., Pascoe, A. and Escartin, J. (1997), 'Corrugated slip surfaces formed at ridge-transform intersections on the Mid-Atlantic Ridge', *Nature* **385**, 329–332.

Cann, J., Langset, M., Honnorez, J., Herzen, R. V. and White, S., eds (1983), *Initial Reports of the Deep Sea Drilling Project*, Vol. 69, U.S. Government Printing Office, Washington.

Cannat, M. (1993), 'Emplacement of mantle rocks in the seafloor at mid-ocean ridges', *J. Geophys. Res.* **98**(B3), 4163–4172.

Cannat, M. (1996), 'How thick is the magmatic crust at slow spreading oceanic ridges?', *J. Geophys. Res.* **101**(B2), 2847–2857.

Cannat, M., Carson, J. and Miller, D., eds (1995), *Proc. of the Ocean Drilling Program, Init. Reports*, Vol. 153, Ocean Drilling Program, College Station, TX.

Cannat, M., Rommevaux-Jestin, C., Sauter, D., Deplus, C. and Mendel, V. (1999), 'Formation of the axial relief at the very slow spreading Southwest Indian Ridge (49° to 69°E)', *J. Geophys. Res.* **104**(B10), 22,825–22,843.

Carlson, R. (2001), 'The abundance of ultramafic rocks in the Atlantic Ocean crust', *Geophys. J. Int.* **144**, 37–48.

Carter, D. (1980), *Echo-sounding correction tables (formerly Matthew's tables)*, 3rd edn, The Hydrographic department, Taunton.

Červený, V., Molotkov, I. and Pšenčík, I. (1977), *Ray Method in Seismology*, University of Karlova, Prague, Czechoslovakia.

Chalmers, J. (1997), 'The continental margin off southern Greenland: along-strike transition from an amagmatic to a volcanic margin', *J. Geol. Soc., London* **154**, 571–576.

Chalmers, J. A. and Laursen, K. H. (1995), 'Labrador sea: the extent of continental and oceanic crust and the timing of the onset of seafloor spreading', *Marine and Petroleum Geology* **12**(2), 205–217.

Cheadle, M., Matthews, D., McGeary, S., Warner, M., Armstrong, E., Blundell, D., Chadwick, A., Day, G., Edwards, J., Mascle, A., Gariel, O., Montadert, L., Lefort, J., Gall, B. L., Sibuet, J.-C., Cazes, M. and Schroeder, I. (1986), 'Deep seismic reflection profiling between England, France and Ireland', *J. Geol. Soc., London* **143**, 45–52.

Chen, W.-P. and Molnar, P. (1983), 'Focal depth of intracontinental and intraplate earthquakes and their implications for the thermal and mechanical properties of the lithosphere', *J. Geophys. Res.* **88**(B5), 4183–4214.

Chéry, J. (2001), 'Core complex mechanics: From the Gulf of Corinth to the Snake Range', *Geology* **29**(5), 439–442.

Chian, D., Keen, C., Reid, I. and Louden, K. E. (1995a), 'Evolution of nonvolcanic rifted margins: New results from the conjugate margins of the Labrador Sea', *Geology* **23**(7), 589–592.

Chian, D. and Louden, K. E. (1994), 'The continent-ocean crustal transition across the southwest Greenland margin', *J. Geophys. Res.* **99**(B5), 9117–9135.

Chian, D., Louden, K. E., Minshull, T. A. and Whitmarsh, R. B. (1999), 'Deep structure of the ocean-continent transition in the southern Iberia Abyssal Plain from seismic refraction profiles: Ocean Drilling Program (legs 149 and 173) transect', *J. Geophys. Res.* **104**(B4), 7443–7462.

Chian, D., Louden, K. E. and Reid, I. (1995b), 'Crustal structure of the Labrador Sea conjugate margin and implications for the formation of nonvolcanic continental margins', *J. Geophys. Res.* **100**(B12), 24,239–24,253.

Choukroune, P. (1992), 'Tectonic evolution of the Pyrenees', *Annual Review of Earth and Planetary Science* **20**, 143–158.

Choukroune, P. and the ECORS team (1989), 'The ECORS Pyrenean deep seismic profile reflection data and the overall structure of an orogenic belt', *Tectonics* **8**(1), 23–39.

Christensen, N. I. (1966), 'Elasticity of ultrabasic rocks', *J. Geophys. Res.* **71**(24), 5921–5931.

Christensen, N. I. (1972), 'The abundance of serpentinites in the oceanic crust', *Journal of Geology* **80**(6), 709–719.

Christensen, N. I. (1978), 'Ophiolites, seismic velocities and oceanic crustal structure', *Tectonophysics* **47**, 131–157.

Christensen, N. I. (1996), 'Poisson's ratio and crustal seismology', *J. Geophys. Res.* **101**(B2), 3139–3156.

Christensen, N. I. and Mooney, W. D. (1995), 'Seismic velocity structure and composition of the continental crust: A global view', *J. Geophys. Res.* **100**(B7), 9761–9788.

Christensen, N. I. and Salisbury, M. (1972), 'Sea floor spreading, progressive alteration of layer 2 basalts, and associated changes in seismic velocities', *Earth Planet. Sci. Letters* **15**, 367–375.

Christensen, N. I. and Shaw, G. H. (1970), 'Elasticity of mafic rocks from the Mid-Atlantic Ridge', *Geophys. J. R. Astr. Soc.* **20**, 271–284.

Christensen, N. I. and Smewing, J. D. (1981), 'Geology and seismic structure of the northern section of the Oman ophiolite', *J. Geophys. Res.* **86**(B4), 2545–2555.

Christeson, G., Kent, G., Purdy, G. and Detrick, R. (1996), 'Extrusive thickness variability at the East Pacific Rise, 9°-10° N: constraints from seismic techniques.', *J. Geophys. Res.* **101**(B2), 2859–2873.

Claerbout, J. (1976), *Fundamentals of geophysical data processing: with applications to petroleum prospecting*, McGraw-Hill, New York.

Coffin, M., Gahagan, L., Lawver, L., Lee, T.-Y. and Rosencrantz, E. (1992), 'Atlas of Mesozoic/Cenozoic reconstructions (200 Ma to present day)', *PLATES progress report* **1-0192**(Tech. report no. 122), 49 pp.

Cole, P. B. (2003), Anisotropy of the zone of exhumed continental mantle and the structure of the earliest-formed oceanic crust west of Iberia, Phd thesis, University of Southampton.

Colin, J.-P., Ioannides, N. S. and Vining, B. (1992), 'Mesozoic stratigraphy of the Goban Spur, offshore south-west Ireland', *Marine and Petroleum Geology* **9**, 527–541.

Collier, J. and Singh, S. (1998), 'Poisson's ratio structure of young oceanic crust', *J. Geophys. Res.* **103**(B9), 20,981–20,996.

Constable, S., Parker, R. and Constable, C. (1987), 'Occam's inversion: a practical algorithm for generating smooth models from electromagnetic sounding data', *Geophysics* **52**, 289–300.

Davis, M. and Kusznir, N. (2004), Depth-dependent lithospheric stretching at rifted continental margins, *in* G. D. Karner, B. Taylor, N. W. Driscoll and D. L. Kohlstedt, eds, 'Rheology and deformation of the lithosphere at continental margins', Columbia University Press, New York, pp. 92–137.

Davy, P. and Cobbold, P. R. (1991), 'Experiments on shortening of a 4-layer continental lithosphere', *Tectonophysics* **188**, 1–25.

de Charpal, O., Montadert, L., Guennoc, P. and Roberts, D. (1978), 'Rifting, crustal attenuation and subsidence in the Bay of Biscay', *Nature* **275**, 706–711.

de Voogd, B. and Keen, C. E. (1987), 'Lithoprobe east: results from reflection profiling of the continental margin: Grand Banks Region', *Geophys. J. R. Astr. Soc.* **89**, 195–200.

Dean, S. M. (1999), Structure of the ocean-continent transition in the Southern Iberia Abyssal Plain, Phd thesis, University of Cambridge.

Dean, S., Minshull, T., Whitmarsh, R. and Louden, K. (2000), 'Deep structure of the ocean-continent transition in the southern Iberia Abyssal Plain from seismic refraction profiles: The IAM-9 transect at 40°20′ N', *J. Geophys. Res.* **105**, 5859–5885.

Detrick, R., , Collins, J., Stephen, R. and Swift, S. (1994), 'In situ evidence for the nature of the seismic layer 2/3 boundary in oceanic crust', *Nature* **370**, 288–290.

Dick, H. (1989), Abyssal peridotites, very slow spreading ridges and ocean ridge magmatism, *in* A. Saunders and N. M.J., eds, 'Magmatism in the ocean basins', Vol. 42 of *Geological Society Special Publication*, pp. 71–105.

Dick, H. J., Lin, J. and Schouten, H. (2003), 'An ultraslow-spreading class of ocean ridge', *Nature* **426**, 405–412.

Dick, H. J., Natland, J. H. and others, . (2000), 'A long in situ section of the lower ocean crust: results of ODP Leg 176 drilling at the Southwest Indian Ridge', *Earth Planet. Sci. Letters* **179**, 31–51.

Didier, J., Guennoc, P. and Pautot, G. (1977), 'Granodiorites, granulites et charnokites de l'éperon de Goban (marge amoricaine), au contact du domaine océanique', *C. R. Acad. Sci. Paris* **284**, 369–373.

Dix, C. H. (1955), 'Seismic velocities from surface measurements', *Geophysics* **20**, 65–86.

Driscoll, N. W. and Karner, G. D. (1998), 'Lower crustal extension across the Northern Carnarvon basin, Australia: Evidence for an eastward dipping detachment', *J. Geophys. Res.* **103**(B3), 4975–4991.

Dunbar, J. A. and Sawyer, D. S. (1989a), 'How pre-existing weaknesses control the style of continental breakup', *J. Geophys. Res.* **94**, 7278–7292.

Dunbar, J. A. and Sawyer, D. S. (1989b), 'Patterns of continental extension along the conjugate margins of the Central and North Atlantic oceans and the Labrador Sea', *Tectonics* **8**(5), 1059–1077.

Durand, C., Ballu, V., Gente, P. and Dubois, J. (1996), 'Horst and graben structures on the flanks of the Mid-Atlantic Ridge in the MARK area (23°22'N): Submersible observations', *Tectonophysics* **265**, 275–297.

Edwards, M., Kurras, G., Tolstoy, M., Bohnenstiehl, D., Coakley, B. and Cochran, J. (2001), 'Evidence of recent volcanic activity on the ultraslow-spreading Gakkel ridge', *Nature* **409**, 808–812.

Erickson, A., Avera, W. and Byrne, R. (1979), Heat-flow results, DSDP Leg 48, *in* L. Montadert and D. Roberts, eds, 'Initial Reports of the Deep Sea Drilling Project', Vol. 48, U.S. Government Printing Office, Washington, pp. 277–288.

Escartín, J., Hirth, G. and Evans, B. (1997a), 'Nondilatant brittle deformation of serpentinites: Implications for Mohr-Coulomb theory and the strength of faults', *J. Geophys. Res.* **102**(B2), 2897–2913.

Escartín, J., Hirth, G. and Evans, B. (1997b), 'Effects of serpentinization on the lithospheric strength and the style of normal faulting at slow-spreading ridges', *Earth Planet. Sci. Letters* **151**, 181–189.

Escartín, J., Hirth, G. and Evans, B. (2001), 'Strength of slightly serpentinized peridotites: implications for the tectonics of oceanic lithosphere', *Geology* **29**(11), 1023–1026.

Fernández-Viejo, G., Gallart, J., Pulgar, J., Gallastegui, J. and Dañobeitia, J. (1998), 'Crustal transition between continental and oceanic domains along the North Iberian margin from wide angle seismic and gravity data', *Geophysical Research Letters* **25**(23), 4249–4252.

Fisher, R. (1997), *GEBCO digital atlas*, British Oceanographic Data Centre, Birkenhead, UK.

Floyd, J., Mutter, J., Goodliffe, A. and Taylor, B. (2001), 'Evidence for fault weakness and fluid flow within an active low-angle normal fault', *Nature* **411**, 779–783.

Fornari, D. J., Haymon, R. M., Perfit, M. R., Gregg, T. K. and Edwards, M. H. (1998), 'Axial summit trough of the East Pacific Rise 9°-10° N: geological characteristics and evolution of the axial zone on fast spreading mid-ocean ridges', *J. Geophys. Res.* **103**(B5), 9827–9855.

Foucher, J., Chenet, P., Montadert, L. and Roux, J. (1985), Geothermal measurements during Deep Sea Drilling Project Leg 80, *in* P. de Graciansky and C. Poag, eds, 'Initial Reports of the Deep Sea Drilling Project', Vol. 80, U.S. Government Printing Office, Washington, pp. 423–436.

Foucher, J.-P. and Sibuet, J. (1980), 'Thermal régime of the northern Bay of Biscay continental margin in the vicinity of the D.S.D.P. Sites 400-402', *Philosophical Transactions of the Royal Society of London, A* **294**, 157–167.

Fowler, C. (1990), *The Solid Earth: An introduction to global geophysics*, Cambridge University Press, Cambridge, UK.

Fowler, S., White, R., Spence, G. and Westbrook, G. (1989), 'The Hatton Bank continental margin - II. Deep structure from two–ship expanding spread seismic profiles', *Geophys. Jour.* **96**, 295–309.

Garcia-Mondéjar, J. (1996), 'Plate reconstruction of the Bay of Biscay', *Geology* **24**(7), 635–638.

Ginzburg, A., Whitmarsh, R., Roberts, D., Montadert, L., Camus, A. and Avedik, F. (1985), 'The deep seismic structure of the northern continental margin of the Bay of Biscay', *Annales Geophysicae* **3**(4), 499–510.

Goetze, C. (1978), 'The mechanisms of creep in olivine', *Philosophical Transactions of the Royal Society of London, A* **288**, 99–119.

Goff, J. A. (1991), 'A global and regional stochastic analysis of near-ridge abyssal hill morphology', *J. Geophys. Res.* **96**(B13), 21,713–21,737.

Goff, J. A. (1992), 'Quantitative charecterisation of abyssal hill morphology along flow lines in the Atlantic Ocean', *J. Geophys. Res.* **97**, 9183–9202.

de Graciansky, P., Auffret, G., Dupeuble, P., Montadert, L. and Müller, C. (1979), Interpretation of depositional environments of the Aptian/Albian black shales of the north margin of the Bay of Biscay DSDP Sites 400 and 402, *in* L. Montadert and D. Roberts, eds, 'Initial Reports of the Deep Sea Drilling Project', Vol. 48, U.S. Government Printing Office, Washington, pp. 877–907.

de Graciansky, P. C., Poag, C., Cunningham, Jr, R., Loubere, P., Masson, D. G., Mazzullo, J. M., Montadert, L., Müller, C., Otsuka, K., Reynolds, L. A., Sigal, J., Snyder, S. W., Vaos, S. P. and Waples, D. (1985), 'The Goban Spur transect: Geologic evolution of a sediment-starved passive continental margin', *Gelogical Society of America Bulletin* **96**, 58–76.

de Graciansky, P. and Poag, C., eds (1985), *Initial Reports of the Deep Sea Drilling Project*, Vol. 80, U.S. Government Printing Office, Washington.

Gradstein, F. M., Agterberg, F. P., Ogg, J. G., Hardenbol, J., van Veen, P., Thierry, J. and Huang, Z. (1994), 'A Mesozoic time scale', *J. Geophys. Res.* **99**(B12), 24,051–24,074.

Grandjean, G., Guennoc, P., Recq, M. and Andréo, P. (2001), 'Refraction/wide-angle reflection investigation of the Cadomian crust between northern Brittany and the Channel Islands', *Tectonophysics* **331**, 45–64.

Grimaud, S., Boillot, G., Collete, B., Mauffret, A., Miles, P. and Roberts, D. (1982), 'Western extension of the Iberian-Eropean plate boundary during Early Cenozoic (Pyrenean) convergence: a new model', *Marine Geology* **45**, 63–77.

Hamilton, E. (1978), 'Sound velocity-density relations in seafloor sediments and rocks', *Jour. Acoust. Soc. America* **63**, 366–377.

Hardage, B., ed. (1985), *Vertical seismic profiling, part A: Principles*, 2nd edn, Geophysical Press, London.

Harding, A., Orcutt, J., Kappus, M., Vera, E., Mutter, J., Buhl, P., Detrick, R. and Brocher, T. (1989), 'Structure of young oceanic crust at 13° N on the East Pacific Rise from expanding spread profiles', *J. Geophys. Res.* **B9**, 12,163–12,196.

Hardy, N. (1991), A marine geophysical study of the Pacific margins of Columbia and southeast Panama, Phd thesis, University of Birmingham.

Harland, W., Armstrong, R., Cox, A., Craig, L., Smith, A. and Smith, D. (1990), *A geologic time scale 1989*, Cambridge University Press, Cambridge.

Harry, D. and Bowling, J. (1999), 'Inhibiting magmatism on nonvolcanic rifted margins', *Geology* pp. 895–898.

Heezen, B. C. (1960), 'The rift in the ocean floor', *Scientific American* **203**(3), 98–110.

Hess, H. (1962), History of ocean basins, *in* A. Engel, H. James and B. Leonard, eds, 'Petrologic Studies: a volume in honour of A.F. Burlington Volume', Geological Society of America, Boulder, Colorado, pp. 599–620.

Hill, M. (1957), 'Recent geophysical exploration of the ocean floor', *Phys. Chem. Earth* **2**, 129–163.

Hobbs, R. (1990), 'Effective Q determination using frequency methods on BIRPS data', *Tectonophysics* **173**, 25–30.

Hobro, J. W. D. (1999), Three-dimensional tomographic inversion of combined reflection and refraction seismic travel-time data, Phd thesis, University of Cambridge.

Hoffmann, H. and Reston, T. (1992), 'The nature of the S reflector beneath the Galicia Bank rifted margin: Preliminary results from pre-stack depth migration', *Geology* **20**, 1091–1094.

Hofmann, A. (1997), 'Mantle geochemistry: the message from oceanic volcanism', *Nature* **385**, 219–229.

Holbrook, W., Purdy, G., Collins, J., Sheridan, R., Musser, D., III, L. G., Talwani, M., Ewing, J., Hawman, R. and Smithson, S. (1992), 'Deep velocity structure of rifted continental crust, U.S. Mid-Atlantic margin, from wide-angle reflection/refraction data', *Geophys. Res. Letters* **19**(16), 1699–1702.

Holbrook, W. S., Larsen, H., Korenaga, J., Dahl-Jensen, T., Reid, I., Kelemen, P., Hopper, J., Kent, G., Lizarralde, D., Bernstein, S. and Detrick, R. (2001), 'Mantle thermal structure and active upwelling during continental breakup in the North Atlantic', *Earth Planet. Sci. Letters* **190**, 251–266.

Hölker, A. B., Manatschal, G., Holliger, K. and Bernoulli, D. (2003), 'Tectonic nature and seismic response of top-basement detachment faults in magma-poor rifted margins', *Tectonics* **22**(4).

Hooft, E. and Detrick, R. (1993), 'The role of density in the accumulation of basaltic metals at mid-ocean ridges', *Geophys. Res. Letters* **20**(6), 423–426.

Hopper, J. R. and Buck, W. R. (1996), 'The effect of lower crustal flow on continental extension and passive margin formation', *J. Geophys. Res.* **101**, 20,175–20,194.

Hopper, J. R. and Buck, W. R. (1998), 'Styles of extensional decoupling', *Geology* **26**(8), 699–702.

Horsefield, S. J., Whitmarsh, R. B., White, R. S. and Sibuet, J.-C. (1994), 'Crustal structure of the Goban Spur rifted continental margin, NE Atlantic', *Geophys. J. Int.* **119**, 1–19.

Huang, P. Y. and Solomon, S. C. (1988), 'Centroid depths of mid-ocean ridge earthquakes: dependence on spreading rate', *J. Geophys. Res.* **93**(B11), 13,445–13,477.

Huismans, R. and Beaumont, C. (2003), 'Symmetric and asymmetric lithospheric extension: relative effects of frictional-plastic and viscous strain softening', *J. Geophys. Res.* **108**(B10).

Jackson, J. A. (1987), Active normal faulting and crustal extension, *in* M. P. Howard, J. F. Dewey and P. Hancock, eds, 'Continental extensional tectonics', Vol. 28 of *Geological Society special publication*, The Geological Society, London, pp. 3–17.

Jacobson, R. and Lewis, B. (1990), 'The first direct measurements of upper oceanic crustal compressional wave attenuation', *J. Geophys. Res.* **95**(B11), 17,417–17,429.

Johnston, J. E. and Christensen, N. I. (1997), 'Seismic properties of layer 2 basalts', *Geophys. J. Int.* **128**, 285–300.

Joron, J., Bougault, H., Maury, R., Bohn, M. and Desprairies, A. (1984), Strongly depleted tholeiites from the Rockall Plateau margin, North Atlantic: Geochemistry and min-

eralogy, *in* D. Roberts and D. Schnitker, eds, 'Initial Reports of the Deep Sea Drilling Project', Vol. 81, U.S. Government Printing Office, Washington, pp. 783–794.

Juárez, M., Lowrie, W., Osete, M. and Meléndez, G. (1998), 'Evidence of widespread Cretaceous remagnetisation in the Iberian Range and its relation with the rotation of Iberia', *Earth Planet. Sci. Letters* **160**, 729–743.

Judson, D., Lin, J., Schultz, P. and Sherwood, J. (1980), 'Depth migration after stack', *Geophysics* **45**, 361–375.

Karson, J. A. and Lawrence, R. M. (1997), Tectonic setting of serpentinite exposures on the western median valley wall of the MARK area in the vicinity of Site 920, *in* J. Karson, M. Canat, D. Miller and D. Elthon, eds, 'Proc. of the Ocean Drilling Program, Sci. Results', Vol. 153, Ocean Drilling Program, College Station TX, pp. 5–21.

Karson, J., Collins, J. and Casey, J. (1984), 'Geologic and seismic velocity structure of the crust/mantle transition in the Bay of Islands ophiolite complex', *J. Geophys. Res.* **89**(B7), 6126–6138.

Kearey, P. and Vine, F. (1990), *Global Tectonics*, 1st edn, Blackwell Scientific Publications, Oxford.

Keen, C. and Barrett, D. (1981), 'Thinned and subsided continental crust on the rifted margin of Eastern Canada: crustal structure, thermal evolution and subsidence history', *Geophys. J. R. Astr. Soc.* **65**, 443–465.

Keen, C. and de Voogd, B. (1988), 'The continent-ocean boundary at the rifted margin off eastern Canada: New results from deep seismic reflection studies', *Tectonics* **7**(1), 107–124.

Keen, C., Peddy, C., de Voogd, B. and Matthews, D. (1989), 'Conjugate margins of Canada and Europe: Results from deep reflection profiling', *Geology* **17**, 173–176.

Kern, H., Liu, B. and Popp, T. (1997), 'Relationship between anisotropy of P and S wave velocities and anisotropy in serpentinite and amphibolite', *J. Geophys. Res.* **102**(B2), 3051–3065.

Klemperer, S. and Hobbs, R. (1991), *The BIRPS atlas: deep seismic reflection profiles around the British Isles*, Cambridge University Press, Cambridge.

Klemperer, S. L. (1989), Processing BIRPS deep seismic reflection data: a tutorial review, *in* R. Cassinis, G. Nolet and G. F. Panza, eds, 'Digital seismology and fine modelling of the lithosphere', Vol. 42 of *Ettore Majorana International Science Series. Physical Sciences*, pp. 229–257.

Kohlstedt, D., Evans, B. and Mackwell, S. (1995), 'Strength of the lithosphere: constraints imposed by laboratory experiments', *J. Geophys. Res.* **100**(B9), 17,587–17,602.

Kristoffersen, Y. (1978), 'Sea-floor spreading and the early opening of the North Atlantic', *Earth Planet. Sci. Letters* **38**, 273–290.

Kroenke, L., Manghnani, M., Rai, C., Fryer, P. and Ramananantoandro, R. (1976), Elastic properties of selected ophiolitic rocks from Papa New Guinea: nature and composition of oceanic lower crust and upper mantle, *in* G. Sutton, M. Manghnani and R. Moberly, eds, 'The geophysics of the Pacific ocean basin and it's margins', Vol. 19, American Geophysical Union, pp. 407–421.

Kusznir, N. J. and Park, R. G. (1987), The extensional strength of the continental lithosphere: its dependence on geothermal gradient, and crustal composition and thickness, *in* M. P. Coward, J. F. Dewey and P. L. Hancock, eds, 'Continental extensional tectonics', Vol. 28 of *Geological Society Special Publication*, Geol. Soc. of London, London, pp. 35–52.

Larner, K., Hatton, L., Gibson, B. and Hsu, I.-C. (1981), 'Depth migration of imaged time sections', *Geophysics* **46**, 734–750.

Larsen, H., Duncan, R. A., Allan, J. and Brooks, K., eds (1999), *Proc. of the Ocean Drilling Program, Sci. Results*, Vol. 163, Ocean Drilling Program, College Station, TX.

Larsen, H. and Saunders, A. (1997), Tectonism and volcanism at the Southeast Greenland rifted margin: a record of plume impact and later continental rupture, *in* A. Saunders, H. Larsen and S. Wise, Jr, eds, 'Proc. of the Ocean Drilling Program, Sci. Results', Vol. 152, Ocean Drilling Program, College Station TX, pp. 503–533.

Lase Study Group (1986), 'Deep structure of the US East Coast passive margin from large aperture seismic experiments (LASE)', *Marine and Petroleum Geology* **3**(4), 234–242.

Latin, D. and White, N. (1990), 'Generating melt during lithospheric extension: Pure shear vs. simple shear', *Geology* **18**, 327–331.

Lavier, L. L., Buck, W. R. and Poliakov, A. N. . B. (1999), 'Self-consistent rolling-hinge model for the evolution of large-offset low-angle normal faults', *Geology* **27**(12), 1127–1130.

Lawrence, R. M., Gee, J. S. and Karson, J. A. (2002), 'Magnetic anisotropy of serpentinized peridotites from the MARK area: Implications for the orientation of mesoscopic structures and major fault zones', *J. Geophys. Res.* **107**(B4).

Lay, T. and Wallace, T. C. (1995), *Modern global seismology*, Academic Press, London.

Le Pichon, X. (1969), 'Comments on a paper by D.H. Matthews and C.A. Williams "Linear magnetic anomalies in the Bay of Biscay: a qualitative interpretation"', *Earth Planet. Sci. Letters* **5**, 251–252.

Le Pichon, X. and Barbier, F. (1987), 'Passive margin formation by low-angle faulting within the upper crust: The northern Bay of Biscay margin', *Tectonics* **6**(2), 133–150.

Le Pichon, X. and Sibuet, J. (1971), 'Western extension of the boundary between European and Iberian plates during the Pyrenean orogeny', *Earth Planet. Sci. Letters* **12**, 83–88.

Le Pichon, X. and Sibuet, J.-C. (1981), 'Passive margins: A model of formation', *J. Geophys. Res.* **86**(B5), 3708–3720.

Limond, W., Gray, F., Grau, G. and Patriat, P. (1972), 'Mantle reflections in the Bay of Biscay', *Earth Planet. Sci. Letters* **15**, 361–366.

Lister, G. and Davis, G. A. (1989), 'The origin of metamorphic core complexes and detachment faults formed during Tertiary continental extension in the northern Colorado River region, U.S.A.', *Journal of Structural Geology* **11**, 65–94.

Lister, G., Etheridge, M. and Symonds, P. (1986), 'Detachment faulting and the evolution of passive continental margins', *Geology* **14**, 246–250.

Louden, K. and Chian, D. (1999), 'The deep structure of non-volcanic rifted continental margins', *Philosophical Transactions of the Royal Society of London, A* **357**, 767–804.

Louden, K., Sibuet, J.-C. and Foucher, J.-P. (1991), 'Variations in heat flow across the Goban Spur and Galicia Bank continental margins', *J. Geophys. Res.* **96**(B10), 16131–16150.

Louvel, V., Dyment, J. and Sibuet, J.-C. (1997), 'Thinning of the Goban Spur continental margin and formation of early oceanic crust: constraints from forward modelling and inversion of marine magnetic anomalies', *Geophys. J. Int.* **128**, 188–196.

Louvel, V., Sibuet, J.-C., Whitmarsh, R. B., Horsefield, S. J. and White, R. S. (1992), 'Modélisation gravimétrique de la marge de l'éperon de Goban (SW Irlande): Conséquences sur les modéles de formation des marges continentales stables', *C. R. Acad. Sci. Paris* **315**(II), 1333–1340.

Ludwig, W. J., Nafe, J. E. and Drake, C. L. (1970), Seismic refraction, *in* A. E. Maxwell, ed., 'The Sea', Vol. 4, part 1, Wiley-Interscience, pp. 53–84.

MacDonald, K. C. (1982), 'Mid-ocean ridges: fine scale tectonic, volcanic and hydrothermal processes within a plate boundary zone', *Annual Review of Earth and Planetary Science* **10**, 155–190.

MacLeod, C., Escartin, J., Banerji, D., Banks, G., Gleeson, M., Irving, D., Lilly, R., McCaig, A., Niu, Y. and Smith, D. (2002), 'Direct geological evidence for oceanic detachment faulting at the Mid-Atlantic Ridge, 15°45'n', *Geology* **30**(10), 879–882.

Maggi, A., Jackson, J., McKenzie, D. and Priestley, K. (2000), 'Earthquake focal depths, effective elastic thickness, and the strength of the continental lithosphere', *Geology* **28**(6), 495–498.

Malinverno, A. (1991), 'Inverse square-root dependence of mid-ocean-ridge flank roughness on spreading rate', *Nature* **352**, 58–60.

Malod, J. and Mauffret, A. (1990), 'Iberian plate motion during the Mesozoic', *Tectonophysics* **184**, 261–278.

Masson, D. and Miles, P. (1984), 'Mesozoic seafloor spreading between Iberia, Europe and North America', *Marine Geology* **56**, 279–287.

Masson, D., Montadert, L. and Scrutton, R. (1985), Regional geology of the Goban Spur continental margin, *in* P. de Graciansky and C. Poag, eds, 'Initial Reports of the Deep Sea Drilling Project', Vol. 80, U.S. Government Printing Office, Washington, pp. 1115–1139.

Masson, D. and Parson, L. (1983), 'Eocene deformation on the continental margin SW of the British Isles', *J. Geol. Soc., London* **140**, 913–920.

Matthews, D. and Williams, C. (1968), 'Linear magnetic anomalies in the Bay of Biscay: a qualitative interpretation', *Earth Planet. Sci. Letters* **4**, 315–320.

Mauffret, A. and Montadert, L. (1987), 'Rift tectonics on the passive continental margin off Galicia (Spain)', *Mar. Petrol. Geol.* **4**, 49–70.

Maury, R., Bellon, H., Bougault, H., Joron, J., Bohn, M. and de Graciansky, P. (1985), Oceanic tholeiites from Leg 80 sites (Celtic Sea passive margin, northeastern Atlantic): Geochemistry and mineralogy, *in* P. de Graciansky and C. Poag, eds, 'Initial Reports of the Deep Sea Drilling Project', Vol. 80, U.S. Government Printing Office, Washington, pp. 939–946.

McKenzie, D. (1978), 'Some remarks on the development of sedimentary basins', *Earth Planet. Sci. Letters* **40**, 25–32.

McKenzie, D. and Bickle, M. (1988), 'The volume and composition of melt generated by extension of the lithosphere', *Journal of Petrology* **29**, 625–679.

Mélières, F. (1979), Mineralogy and geochemistry of selected Albian sediments from the Bay of Biscay, Deep Sea Drilling Project Leg 48, *in* L. Montadert and D. Roberts, eds, 'Initial Reports of the Deep Sea Drilling Project', Vol. 48, U.S. Government Printing Office, Washington, pp. 855–875.

Mercuriev, S., Patriat, P. and Sochevanova, N. (1996), 'Évolution de la dorsale de Carlsberg: évidence pour une phase d'expansion trés lente entre 40 et 25 ma (A18 á A7)', *Oceanologica Acta* **19**(1), 1–13.

Michon, L. and Merle, O. (2003), 'Mode of lithospheric extension: Conceptual models from analogue modelling', *Tectonics* **22**(4).

Miller, D. J. and Christensen, N. I. (1997), Seismic velocities of lower crustal and upper mantle rocks from the slow-spreading Mid-Atlantic Ridge, south of the Kane transform zone (MARK), *in* J. Karson, M. Cannat, D. Miller and D. Elthon, eds, 'Proc. of the Ocean Drilling Program, Sci. Results', Vol. 153, Ocean Drilling Program, College Station TX, pp. 437–454.

Minshull, T. (1993), 'Poisson's ratio of a seaward-dipping reflector series, Hatton Bank', *Geophys. J. Int.* **115**, 332–335.

Minshull, T. (1999), 'On the roughness of Mesozoic oceanic crust in the western North Atlantic', *Geophys. J. Int.* **136**, 286–290.

Minshull, T. (2000), A geophysical and geochemical study of the ocean-continent transition at the Western Approaches margin, CD-124 cruise report, University of Southampton.

Minshull, T. A. (2002a), Oceanic crust, *in* 'Encyclopedia of Physical Science and Technology, Third edition', Vol. 11, Academic Press, pp. 91–98.

Minshull, T. A. (2002b), Seismic structure of the oceanic crust and passive continental margins, *in* 'International handbook of earthquake and engineering seismology', Vol. 81A, pp. 911–924.

Minshull, T., Dean, S., White, R. and Whitmarsh, R. (2001), Anomalous melt production after continental break-up in the southern Iberia Abyssal Plain, *in* R. Wilson, R. Whitmarsh, B. Taylor and N. Froitzheim, eds, 'Non-Volcanic Rifting of Continental Margins: A Comparison of Evidence from Land and Sea.', Vol. 187 of *Geological Society, London, Special Publications*, Geol. Soc. of London, pp. 537–550.

Minshull, T., Muller, M., Robinson, C., White, R. and Bickle, M. (1998), Is the oceanic Moho a serpentization front?, *in* R. Mills and K. Harrison, eds, 'Modern Ocean Floor Processes and the Geological Record', Vol. 148 of *Geological Society, London, Special Publications*, pp. 71–80.

Mittermayer, E. (1969), 'Numerical formulas for the geodetic reference system 1967', *Bolletino di Geofisca Teorica ed Applicata* **11**, 96–107.

Molnar, P. (1988), 'Continental tectonics in the aftermath of plate tectonics', *Nature* **335**, 131–137.

Montadert, L. and Roberts, D., eds (1979), *Initial Reports of the Deep Sea Drilling Project*, Vol. 48, U.S. Government Printing Office, Washington.

Montadert, L., Roberts, D. G., Charpal, O. D. and Guennoc, P. (1979), Rifting and subsidence of the northern continental margin of the Bay of Biscay, *in* L. Montadert and D. Roberts, eds, 'Initial Reports of the Deep Sea Drilling Project', Vol. 48, U.S. Government Printing Office, Washington, pp. 1025–1060.

Mooney, W. D., Prodehl, C. and Pavlenkova, N. I. (2002), Seismic velocity structure of the continental lithosphere from controlled source data, *in* 'International handbook of earthquake and engineering seismology', Vol. 81A, pp. 887–910.

Morgan, J. and Barton, P. (1990), 'A geophysical study of the Hatton Bank volcanic margin: a summary of the results from a combined seismic, gravity and magnetic experiment', *Tectonophysics* **173**, 517–526.

Morgan, J., Barton, P. and White, R. (1989), 'The Hatton Bank continental margin–III. Structure from wide-angle OBS and multichannel seismic refraction profiles', *Geophys. J. Int.* **98**, 367–384.

Muller, M. R., Minshull, T. A. and White, R. S. (1999), 'Segmentation and melt supply at the Southwest Indian Ridge', *Geology* **27**(10), 867–870.

Mutter, C. Z. and Mutter, J. C. (1993), 'Variations in thickness of layer 3 dominate oceanic crustal structure', *Earth Planet. Sci. Letters* **117**, 295–317.

Mutter, J., Buck, W. and Zehnder, C. (1988), 'Convective partial melting 1. A model for the formation of thick basaltic sequences during the initiation of spreading', *J. Geophys. Res.* **93**(B2), 1031–1048.

Mutter, J. C. (1993), 'Margins declassified', *Nature* **364**, 393–394.

Mutter, J. C., Talwani, M. and Stoffa, P. L. (1982), 'Origin of seaward-dipping reflectors in oceanic crust off the Norwegian margin by 'subaerial sea-floor spreading", *Geology* **10**, 353–357.

Newman, P. (1973), 'Divergence effects in a layered earth', *Geophysics* **38**, 481–488.

Nielsen, T. K., Larsen, H. C. and Hopper, J. R. (2002), 'Contrasting rifted margin styles south of Greenland: implications for mantle plume dynamics', *Earth Planet. Sci. Letters* **200**, 271–286.

Officer, C. B. (1974), *Introduction to theoretical geophysics*, Springer-Verlag, New York.

O'Hanley, D. S. (1996), *Serpentinites. Records of tectonic and petrological history*, Vol. 34 of *Oxford Monographs on geology and geophysics*, Oxford University Press, New York.

Olivet, J. L. (1996), 'La cinématique de la plaque Ibérique', *Bull. Centres Rech. Explor. - Prod. Elf Aquitaine* **20**(1), 131–195.

Olsen, K. and Morgan, P. (1995), Introduction: Progress in understanding continental rifts, *in* K. Olsen, ed., 'Continental rifts: evolution, structure, tectonics', Vol. 25 of *Developments in geotectonics*, Elsevier Science, Amsterdam, The Netherlands, pp. 3–26.

Oufi, O., Cannat, M. and Horen, H. (2002), 'Magnetic properties of variably serpentinized abyssal peridotites', *J. Geophys. Res.* **107**(B5).

Peddie, N. (1983), 'International geomagnetic reference field – its evolution and the difference in total field intensity between new and old models for 1965–1980.', *Geophysics* **48**, 1691–1696.

Peddy, C. and Hobbs, R. (1987), 'Lower crustal reflectivity of the continental margin southwest of Britain', *Annales Geophysicae* **5B**(4), 331–338.

Peddy, C., Pinet, B., Masson, D., R. Scrutton, J.-C. S., Warner, M., Lefort, J., Shroeder, I., BIRPS and ECORS (1989), 'Crustal structure of the Goban Spur continental margin, northeast Atlantic, from deep seismic reflection profiling', *J. Geol. Soc., London* **146**, 427–437.

Pedersen, T. and Ro, H. (1992), 'Finite duration extension and decompression melting', *Earth Planet. Sci. Letters* **113**, 15–22.

Pérez-Gussinyé, M., Ranero, C., Reston, T. and Sawyer, D. (2003), 'Mechanisms of extension at nonvolcanic margins: Evidence from the Galicia interior basin, west of Iberia', *J. Geophys. Res.* **208**(B5).

Pérez-Gussinyé, M. and Reston, T. J. (2001a), 'Rheological evolution during extension at nonvolcanic rifted margins: Onset of serpentinization and development of detachments leading to continental breakup', *J. Geophys. Res.* **106**(B3), 3961–3975.

Pérez-Gussinyé, M., Reston, T. J. and Phipps Morgan, J. (2001b), Serpentinisation and magmatism during extension at non-volcanic margins - the effect of initial lithospheric structure, *in* R. Wilson, R. Whitmarsh, B. Taylor and N. Froitzheim, eds, 'Non-volcanic rifting of continental margins: a comparison from land and sea', Vol. 187 of *Geological Society special publication*, The Geological Society, London, pp. 551–576.

Phipps Morgan, J. and Chen, Y. J. (1993), 'Dependence of ridge-axis morphology on magma supply and spreading rate', *Nature* **364**, 706–708.

Pickup, S., Whitmarsh, R., Fowler, C. and Reston, T. (1996), 'Insight into the nature of the ocean-continent transition off West Iberia from a deep multichannel seismic reflection profile', *Geology* **24**(12), 1079–1082.

Pinet, B., Sibuet, J.-C., Lefort, J.-P., Schroeder, I. and Montadert, L. (1991), 'Structure profonde de la marge des entrées de la Manche et du plateau continental celtique: le profil WAM', *Mém. Soc. géol. Fr.* **159**, 167–183.

Planke, S., Cerney, B., Bücker, C. J. and Nilsen, O. (1999), Alteration effects on petrophysical properties of subaerial flood basalts: Site 990, southeast Greenland margin, *in* H. Larsen, R. Duncan, J. Allan and B. K., eds, 'Proc. of the Ocean Drilling Program, Sci. Results', Vol. 163, Ocean Drilling Program, College Station TX, pp. 17–28.

Planke, S., Symonds, P., Alvestad, E. and Skogseid, J. (2000), 'Seismic volcanostratigraphy of large-volume basaltic extrusive complexes on rifted margins', *J. Geophys. Res.* **105**(B8), 19,335–19,351.

Press, W. H., Teukolsky, S. A., Vetterling, W. T. and Flannery, B. P. (1992), *Numerical recipies in FORTRAN*, 2nd edn, Cambridge University Press, New York.

Rabinowitz, P. and Labrecque, J. (1977), 'The isostatic gravity anomaly: key to the evolution of the ocean-continent boundary at passive continental margins', *Earth Planet. Sci. Letters* **35**, 145–150.

Raitt, R. (1963), The crustal rocks, *in* M. Hill, ed., 'The Sea', Vol. 3, Interscience, New York, pp. 85–102.

Raynaud, B. (1988), 'A 2-D, ray based, depth migration method for deep seismic reflections', *Geophysical Journal* **93**, 163–171.

Reid, I. and Keen, C. (1990), 'High seismic velocities associated with reflections from within the lower oceanic crust near the continental margin of eastern Canada', *Earth Planet. Sci. Letters* **99**, 118–126.

Reitbrock, A. C., Tiberi, C., Scherbaum, F. and Lyon-Caen, H. (1996), 'Seismic slip on a low angle normal fault in the Gulf of Corinth: evidence from high-resolution cluster analysis of microearthquakes', *Geophys. Res. Letters* **23**, 1817–1820.

Reston, T. (1987), 'Spatial interference, reflection character and the structure of the lower crust under extension. Results from 2-D seismic modelling', *Annales Geophysicae* **5B**(4), 339–348.

Reston, T. (1990), 'Shear in the lower crust during extension: not so pure and simple', *Tectonophysics* **173**, 175–183.

Reston, T. (1996), 'The S reflector west of Galicia: the seismic signature of a detachment fault', *Geophys. J. Int.* **127**, 230–244.

Reston, T., Krawczyk, C. and Klaeschen, D. (1996a), 'The S reflector west of Galicia (Spain): Evidence from prestack depth migration for detachment faulting during continental breakup', *J. Geophys. Res.* **101**(B4), 8075–8091.

Reston, T., Pennell, J., Stubenrauch, A., Walker, I. and Perez-Gussinye, M. (2001), 'Detachment faulting, mantle serpentinization, and serpentinite-mud volcanism beneath the Porcupine Basin, southwest of Ireland', *Geology* **29**(7), 587–590.

Reston, T., Perez-Gussinye, M., Gaw, V. and Phipps Morgan, J. (2003), 'The formation of non-volcanic rifted margins by the progressive extension of the continental lithosphere', *EOS, Trans. AGU* **84**(46), Fall Meet Suppl., Abstract T11E–07.

Reston, T. and Phipps Morgan, J. (2004), 'Continental geotherm and the evolution of rifted margins', *Geology* **32**(2), 133–136.

Reston, T., Ruoff, O., McBride, J., Ranero, C. and White, R. (1996b), 'Detachment and steep normal faulting in Atlantic oceanic crust west of Africa', *Geology* **24**(9), 811–814.

Rey, P. F., Fountain, D. M. and Clement, W. P. (1994), 'P wave velocity across a noncoaxial ductile shear zone and its associated strain gradient: Consequences for upper crustal reflectivity', *J. Geophys. Res.* **99**(B3), 4533–4548.

Ries, A. (1978), 'The opening of the Bay of Biscay - A review', *Earth-Science Reviews* **14**, 35–63.

Roberts, D., Masson, D., Montadert, L. and de Charpal, O. (1981), Continental margin from the Porcupine Seabight to the Amorican marginal basin, *in* L. Illing and G. Hobson, eds, 'Petroleum Geology of the continental shelf of North-West Europe', Institute of Petroleum, London, pp. 455–473.

Roberts, D. and Schnitker, D., eds (1984), *Initial Reports of the Deep Sea Drilling Project*, Vol. 81, U.S. Government Printing Office, Washington.

Roest, W. and Srivastava, S. (1991), 'Kinematics of the plate boundaries between Eurasia, Iberia and Africa in the North Atlantic from the Late Cretaceous to the present', *Geology* **19**, 613–616.

Röhm, A., Snieder, R., Goes, S. and Trampert, J. (2000), 'Thermal structure of continental upper mantle inferred from S-wave velocity and surface heat flow', *Earth Planet. Sci. Letters* **181**, 395–407.

Rohr, K. M. (1994), 'Increase of seismic velocities in upper oceanic crust and hydrothermal circulation in the Juan de Fuca plate', *Geophys. Res. Letters* **21**(19), 2163–2166.

Roure, F., Choukroune, P., Berastegui, X., Munoz, J., Villien, A., Matheron, P., Bareyt, M., Seguret, M., Camara, P. and Deramond, J. (1989), 'ECORS deep seismic data and balanced cross sections: geometric constraints on the evolution of the Pyrenees', *Tectonics* **8**(1), 41–50.

Rudnick, R. L. and Fountain, D. M. (1995), 'Nature and composition of the continental crust: a lower crustal perspective', *Reviews of Geophysics* **33**, 267–309.

Ruppel, C. (1995), 'Extensional processes in continental lithosphere', *J. Geophys. Res.* **100**(B12), 24,187–24,215.

Russell, S. and Whitmarsh, R. (2003), 'Magmatism at the west Iberia non-volcanic rifted continental margin: evidence from analyses of magnetic anomalies', *Geophys. J. Int.* **154**, 706–730.

Salisbury, M. H. and Christensen, N. I. (1978), 'The seismic velocity structure of a traverse through the Bay of Islands ophiolite complex, Newfoundland, an exposure of oceanic crust and upper mantle', *J. Geophys. Res.* **83**(B2), 805–817.

Sandwell, D. T. and Smith, W. H. (1997), 'Marine gravity anomaly from Geosat and ERS-1 satellite altimetry', *J. Geophys. Res.* **102**(B5), 10,039–10,054.

Sauter, D., Carton, H., Mendel, V., Munschy, M., Rommevaux-Jestin, C., Schott, J.-J. and Whitechurch, H. (2004), 'Ridge segmentation and the magnetic structure of the Southwest Indian Ridge (at 50°30′ E, 55°30′ E and 66°20′ E): Implications for magmatic processes at ultraslow-spreading centers', *Geochemistry, Geophysics, Geosystems* **5**(5).

Sawyer, D. (1994), 'The case for slow-spreading oceanic crust landward of the peridotite ridge in the Iberia Abyssal Plain', *EOS, Trans. AGU* **75**(44), Fall Meet Suppl., 616.

Sclater, J. G., Parsons, B. and Jaupart, C. (1981), 'Oceans and continents: similarities and differences in the mechanisms of heat loss', *J. Geophys. Res.* **86**(B12), 11,535–11,552.

Scrutton, R. (1979), 'Structure of the crust and upper mantle at Goban Spur, southwest of the British Isles - some implications for margin studies', *Tectonophysics* **59**, 201–215.

Scrutton, R. A. (1985), Modeling of magnetic and gravity anomalies at Goban Spur, northeastern Atlantic, *in* P. de Graciansky and C. Poag, eds, 'Initial Reports of the Deep Sea Drilling Project', Vol. 80, U.S. Government Printing Office, Washington, pp. 1141–1151.

Sengör, A. and Burke, K. (1978), 'Relative timing of rifting and volcanism on Earth and its tectonic implications', *Geophys. Res. Letters* **5**(6), 419–421.

Shaw, P. R. (1994), 'Age variations of oceanic crust Poisson's ratio: Inversion and a porosity evolution model', *J. Geophys. Res.* **99**(B2), 3057–3066.

Shaw, P. R. and Orcutt, J. A. (1985), 'Waveform inversion of seismic refraction data and applications to young Pacific crust', *Geophys. J. R. Astr. Soc.* **82**, 375–414.

Shearer, P. M. (1999), *Introduction to seismology*, Cambridge University Press, New York.

Sheriff, R. E. and Geldart, L. P. (1995), *Exploration seismology*, 2nd edn, Cambridge University Press, Cambridge.

Shipboard Scientific Party (1985a), Site 550, *in* P. de Graciansky and C. Poag, eds, 'Initial Reports of the Deep Sea Drilling Project', Vol. 80, U.S. Government Printing Office, Washington, pp. 251–355.

Shipboard Scientific Party (1985b), Site 551, *in* P. de Graciansky and C. Poag, eds, 'Initial Reports of the Deep Sea Drilling Project', Vol. 80, U.S. Government Printing Office, Washington, pp. 357–385.

Sibuet, J.-C. (1987), Contribution a l'etude mećanismes de formation des marges continentales passives, Thèse de doctorat, Universitè de Bretagne.

Sibuet, J.-C. (1989), 'Paleoconstraints during rifting of the Northeast Atlantic passive margins', *J. Geophys. Res.* **94**, 7265–7277.

Sibuet, J.-C. (1992), 'New constraints on the formation of the non-volcanic continental Galicia-Flemish Cap conjugate margins', *J. Geol. Soc., London* **149**, 829–840.

Sibuet, J.-C. and Collette, B. J. (1991), 'Triple junctions of Bay of Biscay and North Atlantic: new constraints on the kinematic evolution', *Geology* **19**, 522–525.

Sibuet, J.-C., Dyment, J., Bois, C., Pinet, B. and Ondreas, H. (1990), 'Crustal structure of the Celtic Sea and Western Approaches from gravity data and deep seismic profiles: Constraints on the formation of continental basins', *J. Geophys. Res.* **95**(B7), 10,999–11,020.

Sibuet, J.-C., Louvel, V., Whitmarsh, R. B., White, R. S., Horsefield, S. J., Sichler, B., Léon, P. and Recq, M. (1995), Constraints on rifting processes from refraction and deep-tow magnetic data: The example of the Galicia continental margin (west Iberia), *in* E. Banda, M. Torne and M. Talwani, eds, 'Rifted Ocean-Continent Boundaries', Kluwer Academic Publishers, The Netherlands, pp. 197–217.

Sibuet, J.-C., Mathis, B., Pastouret, L., Auzende, J.-M., Foucher, J.-P., Hunter, P. M., Guennoc, P., de Graciansky, P.-C., Montadert, L. and Masson, D. G. (1985), Morphology and basement structures of the Goban Spur continental margin (northeastern Atlantic) and the role of the Pyrenean orogeny, *in* P. de Graciansky and C. Poag, eds, 'Initial Reports of the Deep Sea Drilling Project', Vol. 80, U.S. Government Printing Office, Washington, pp. 1153–1165.

Sibuet, J.-C., Srivastava, S. and Spakman, W. (2002), 'Pyrenean orogeny and plate kinematics', *EOS, Trans. AGU* **83**(47), Fall Meet Suppl., Abstract T51A–1127.

Sinton, C. and Duncan, R. (1997), ^{40}Ar-^{39}Ar ages of lavas from the southeast Greenland margin, ODP Leg 152, and the Rockall Plateau, DSDP Leg 81, *in* A. Saunders, H. Larsen and S. Wise, Jr, eds, 'Proc. of the Ocean Drilling Program, Sci. Results', Vol. 152, Ocean Drilling Program, College Station TX, pp. 387–401.

Small, C. (1994), 'A global analysis of mid-ocean ridge axial topography', *Geophys. J. Int.* **116**, 64–84.

Small, C. (1998), Global systematics of mid-ocean ridge morphology, *in* W. Buck, P. Delaney, J. Karson and Y. Lagabrielle, eds, 'Faulting and magmatism at mid-ocean ridges', American Geophysical Union, Washington DC, pp. 1–26.

Smith, W. and Wessel, P. (1990), 'Gridding with continuous curvature splines in tension', *Geophysics* **55**(3), 293–305.

Smithson, S. B., Johnson, R. A. and Wong, Y. K. (1981), 'Mean crustal velocity: a critical parameter for interpreting crustal structure and crustal growth', *Earth Planet. Sci. Letters* **53**, 323–332.

Spohn, T. and Schubert, G. (1982), 'Convective thinning of the lithosphere: a mechanism for the initiation of continental rifting', *J. Geophys. Res.* **87**(B6), 4669–4681.

Spudich, P. and Orcutt, J. (1980), 'Petrology and porosity of an oceanic crustal site: Results from wave form modeling of seismic refraction data', *J. Geophys. Res.* **85**(B3), 1409–1433.

Srivastava, S., Roest, W., Kovacs, L., Oakey, G., Levesque, S., Verhoef, J. and Macnab, R. (1990b), 'Motion of Iberia since the Late Jurassic: results from detailed aeromagnetic measurements in the Newfoundlan Basin', *Tectonophysics* **184**, 229–260.

Srivastava, S., Schouten, H., Roest, W., Klitgord, K., Kovacs, L., Verhoef, J. and Macnab, R. (1990a), 'Iberian plate kinematics: a jumping plate boundary between Eurasia and Africa', *Nature* **344**, 756–759.

Srivastava, S., Sibuet, J.-C., Cande, S., Roest, W. and Reid, I. (2000), 'Magnetic evidence for slow seafloor spreading during the formation of the Newfoundland and Iberian margins', *Earth Planet. Sci. Letters* **182**, 61–76.

Srivastava, S. and Verhoef, J. (1992), Evolution of Mesozoic sedimentary basins around the North Central Atlantic: a preliminary plate kinematic solution, *in* J. Parnell, ed., 'Basins on the Atlantic seaboard: petroleum geology, sedimentology and basin evolution', Vol. 62 of *Geological Society Special Publication*, Geol. Soc. of London, London, pp. 397–420.

Srivastava, S., Verhoef, J. and Macnab, R. (1988a), 'Results from a detailed aeromagnetic survey across the northeast Newfoundland margin, part I: spreading anomalies and the relationship between magnetic anomalies and the ocean-continent boundary', *Marine and Petroleum Geology* **5**, 306–323.

Srivastava, S., Verhoef, J. and Macnab, R. (1988b), 'Results from a detailed aeromagnetic survey across the northeast Newfoundland margin, part II: Early opening of the North Atlantic between the British Isles and Newfoundland', *Marine and Petroleum Geology* **5**, 324–337.

Staples, R. K. (1997), Cruatal structure above the Iceland mantle plume, Phd thesis, University of Cambridge.

Talwani, M. (1965), 'Computation with the help of a digital computer of magnetic anomalies caused by bodies of arbitrary shape', *Geophysics* **30**(5), 797–817.

Talwani, M., Windisch, C. C. and Marcus G. Langseth, J. (1971), 'Reykjanes ridge crest: a detailed geophysical study', *J. Geophys. Res.* **76**(2), 473–517.

Talwani, M., Worzel, J. L. and Landisman, M. (1959), 'Rapid gravity computations for two-dimensional bodies with application to the Mendocino submarine fracture zone', *J. Geophys. Res.* **64**(1), 49–59.

Tankard, A. and Welsink, H. (1987), 'Extensional tectonics and stratigraphy of Hibernia oil field, Grand Banks, Newfoundland', *Am. Assoc. Petr. Geol. Bulletin* **71**(10), 1210–1232.

Tate, M. and Dobson, M. (1988), Syn- and post-rift igneous activity in the Porcupine Seabight Basin and adjacent continental margin W of Ireland, *in* A. Morton and L. Parson, eds, 'Early Tertiary Volcanism and the Opening of the NE Atlantic', Vol. 39 of *Geological Society Special Publication*, pp. 309–334.

Taylor, B., Goodliffe, A. and Martinez, F. (1999), 'How continents break up: Insights from Papua New Guinea', *J. Geophys. Res.* **104**(B4), 7947–7512.

Teixell, A. (1998), 'Crustal structure and orogenic material budget in the west central Pyrenees', *Tectonics* **17**(3), 395–406.

Thinon, I. (1999), Structure profonde de la Marge Nord Gascogne et du Bassin Armoricain, Thèse de doctorat, Université de Bretagne Occidentale.

Thinon, I., Fidalgo-González, L., Réhault, J.-P. and Olivet, J.-L. (2001), 'Déformations pyrénéennes dans le golfe de Gascogne', *C. R. Acad. Sci. Paris, Sciences de la Terre et des planètes* **332**, 561–568.

Thinon, I., Matias, L., Réhault, J., Hirn, A., Fidalgo-González, L. and Avedik, F. (2003), 'Deep structure of the Amorican Basin (Bay of Biscay): a review of Norgasis seismic reflection and refraction data', *J. Geol. Soc., London* **160**, 99–116.

Thinon, I., Réhault, J.-P. and Fidalgo-González, L. (2002), 'La couverture sédimentaire syn-rift de la marge Nord-Gascogne et du Bassin armoricain (golfe de Gascogne): à partir de nouvelles données de sismique réflexion', *Bulletin Soc. géol. Fr.* **173**(6), 515–522.

Tittmann, B. (1977), Internal friction measurements and their implications in seismic Q structure models of the crust, *in* J. G. Heacock, ed., 'The Earth's crust: Its nature and physical properties', Vol. 20 of *Geophysical monograph*, American Geophysical Union, Washington, D.C., pp. 197–213.

Tucholke, B. E., Lin, J. and Kleinrock, M. C. (1998), 'Megamullions and mullion structure defining oceanic metamorphic core complexes on the Mid-Atlantic Ridge', *J. Geophys. Res.* **103**(B5), 9857–9866.

Twiss, R. and Moores, E. (1992), *Structural Geology*, Freeman, New York.

Van der Voo, R. (1967), 'The rotation of Spain: paleomagnetic evidence from the Spanish Meseta', *Paleogeography, Paleoclimatology, Paleoecology* **3**(4), 393–416.

Van der Voo, R. (1969), 'Paleomagnetic evidence for the rotation of the Iberian peninsula', *Tectonophysics* **7**, 5–56.

Van der Voo, R. (1990), 'Phanerozoic paleomagnetic poles from Europe and North America and comparisons with continental reconstructions', *Rev. of Geophys.* **28**(2), 167–206.

Verhoef, J., Collette, B., Miles, P., Searle, R., Sibuet, J.-C. and Williams, C. (1986), 'Magnetic anomalies in the northeast Atlantic Ocean (35°-50° N)', *Marine Geophysical Researches* **8**, 1–25.

Verhoef, J., Roest, W., MacNab, R., Arkani Hamed, J. and Members of the Working Group (1996), 'Magnetic anomalies of the Arctic and North Atlantic Oceans and adjacent land areas', *Geological Survey of Canada* **Open File 3125a**.

Viereck, L., Taylor, P., Parson, L., Morton, A., Hertogen, J., Gibson, I. and the ODP Leg 104 Scientific Party (1988), Origin of the Palaeogene Vøring Plateau volcanic sequence, *in* A. Morton and L. Parson, eds, 'Early Tertiary Volcanism and the Opening of the NE Atlantic', Vol. 39 of *Geological Society Special Publication*, Geol. Soc. of London, London, pp. 69–83.

Vogt, P., Taylor, P., Kovacs, L. and Johnson, G. (1989), 'Detailed aeromagnetic investigation of the Arctic Basin', *J. Geophys. Res.* **84**, 1071–1089.

Warner, M. (1990), 'Absolute reflection coefficients from deep seismic reflections', *Tectonophysics* **173**, 15–23.

Watts, A. (2001a), *Isostasy and flexure of the lithosphere*, 1st edn, Cambridge University Press, Cambridge, UK.

Watts, A., Bodine, J. and Steckler, M. (1980), 'Observations of flexure and the state of stress in the oceanic lithosphere', *J. Geophys. Res.* **85**, 6369–6376.

Watts, A. and Marr, C. (1995), Gravity anomalies and the thermal and mechanical structure of rifted continental margins, *in* E. Banda, M. Torne and M. Talwani, eds, 'Rifted Ocean-Continent Boundaries', Kluwer Academic Publishers, The Netherlands, pp. 65–94.

Webb, S. C. (2002), Seismic noise on land and on the sea floor, *in* 'International handbook of earthquake and engineering seismology', Vol. 81A, pp. 305–318.

Wegener, A. (1929), *The origin of continents and oceans*, english translation of the 4th edn, Methuen and Co. Ltd., London.

Wernicke, B. (1981), 'Low-angle normal faults in the Basin and Range Province: nappe tectonics in an extending orogen', *Nature* **291**, 645–647.

Wernicke, B. (1985), 'Uniform-sense normal simple shear of the continental lithosphere', *Canadian Journal of Earth Science* **22**, 108–125.

Wessel, P. and Smith, W. (1991), 'Free software helps map and display data', *EOS Trans., AGU* **72441**, 445–446.

Wever, T. and Meissner, R. (1987), 'About the nature of reflections from the lower continental crust', *Annales Geophysicae* **5B**(4), 349–352.

White, N. (1989), 'The nature of lithospheric extension in the North Sea', *Geology* **17**, 111–114.

White, R. (1992), 'Crustal structure and magmatism of North Atlantic continental margins', *J. Geol. Soc., London* **149**, 841–854.

White, R. and McKenzie, D. (1989), 'Magmatism at rift zones: The generation of volcanic continental margins and flood basalts', *J. Geophys. Res.* **94**(B6), 7685–7729.

White, R., McKenzie, D. and O'Nions, R. (1992), 'Oceanic crustal thickness from seismic measurements and rare earth element inversions', *J. Geophys. Res.* **97**, 19,683–19,715.

White, R., Minshull, T., Bickle, M. and Robinson, C. (2001), 'Melt generation at very slow-spreading oceanic ridges: constraints from geochemical and geophysical data', *Journal of Petrology* **42**(6), 1171–1196.

White, R. and Peddy, C. (1990), 'Discussion on crustal structure of the Goban Spur continental margin, Northeast Atlantic, from deep seismic reflection profiling', *J. Geol. Soc., London* **147**, 892–894.

White, R. S., Spence, G. D., Fowler, S. R., McKenzie, D. P., Westbrook, G. K. and Bowen, A. N. (1987a), 'Magmatism at rifted continental margins', *Nature* **330**(6147), 439–444.

White, R. S., Westbrook, G., Fowler, S., Spence, G., Barton, P., Joppen, M., Morgan, J., Bowen, A., Prescott, C. and Bott, M. (1987b), 'Hatton Bank (northwest U.K.) continental margin structure', *Geophys. J. R. astr. Soc.* **89**, 265–272.

Whitmarsh, R., Avedik, F. and Saunders, M. (1986), 'The seismic structure of thinned continental crust in the northern Bay of Biscay', *Geophys. J. R. Astr. Soc.* **86**, 589–602.

Whitmarsh, R. B., White, R. S., Horsefield, S. J., Sibuet, J.-C., Recq, M. and Louvel, V. (1996a), 'The ocean-continent boundary off the western continental margin of Iberia: Crustal structure west of Galicia Bank', *J. Geophys. Res.* **101**(B12), 28,291–28,314.

Whitmarsh, R., Dean, S., Minshull, T. and Tompkins, M. (2000), 'Tectonic implications of exposure of lower continental crust beneath the Iberia Abyssal Plain, Northeast Atlantic Ocean: Geophysical evidence', *Tectonics* **19**(5), 919–942.

Whitmarsh, R., Manatschal, G. and Minshull, T. (2001a), 'Evolution of magma-poor continental margins from rifting to seafloor spreading', *Nature* **413**, 150–154.

Whitmarsh, R., Minshull, T., Russell, S., Dean, S., Louden, K. and Chian, D. (2001b), The role of syn-rift magmatism in the rift-to-drift evolution of the West Iberia continental margin: geophysical observations, *in* R. Wilson, R. Whitmarsh, B. Taylor and N. Froitzheim, eds, 'Non-volcanic rifting of continental margins: a comparison from land and sea', Vol. 187 of *Geological Society special publication*, The Geological Society, London, pp. 107–124.

Whitmarsh, R., Sawyer, D., Klaus, A. and Masson, D., eds (1996b), *Proc. of the Ocean Drilling Program, Sci. Results*, Vol. 149, Ocean Drilling Program, College Station, TX.

Whitmarsh, R. and Sawyer, D. S. (1996), The ocean/continent transition beneath the Iberia Abyssal Plain and continental-rifting to seafloor-spreading processes, *in* R. Whitmarsh, D. Sawyer, A. Klaus and D. Masson, eds, 'Proc. of the Ocean Drilling Program, Sci. Results', Vol. 149, Ocean Drilling Program, College Station TX, pp. 713–733.

Whitmarsh, R. and Wallace, P. (2001), The rift-to-drift development of the west Iberia nonvolcanic continental margin: a summary and review of the contribution of Ocean Drilling Program leg 173, *in* M.-O. Beslier, R. Whitmarsh, P. Wallace and J. Girardeau, eds, 'Proc. of the Ocean Drilling Program, Sci. Results', Vol. 173, Ocean Drilling Program, College Station TX, pp. 1–36.

Wiens, D. and Stein, S. (1984), 'Intraplate seismicity and stresses in young oceanic lithosphere', *J. Geophys. Res.* **89**, 11,442–11,464.

Williams, C. (1973), 'A fossil triple junction in the NE Atlantic west of Biscay', *Nature* **244**, 86–88.

Williams, C. (1975), 'Sea-floor spreading in the Bay of Biscay and its relationship to the North Atlantic', *Earth Planet. Sci. Letters* **24**, 440–456.

Williamson, P. (1988), 'Origin, structural and tectonic history of the Macquarie Island region', *Papers and Proceedings of the Royal Society of Tasmania* **122**(1), 27–43.

Winterer, E., Gee, J. and Van Waasbergen, R. (1988), The source area for lower Cretaceous clastic sediment of the Galicia margin: geology and tectonic and erosional history, *in* G. Boillot and E. Winterer, eds, 'Proc. of the Ocean Drilling Program, Sci. Results', Vol. 103, Ocean Drilling Program, College Station, TX, pp. 697–732.

Yilmaz, O. (1987), *Seismic data processing*, Vol. 2, Society of Exploration Geophysics, USA.

Zelt, C. A. (1999), 'Modelling strategies and model assessment for wide-angle seismic traveltime data', *Geophys. J. Int.* **139**, 183–204.

Zelt, C. and Ellis, R. (1988), 'Practical and efficient ray tracing in two-dimensional media for rapid traveltime and amplitude forward modelling', *Canadian Journal of Exploration Geophysics* **24**, 16–31.

Zelt, C. and Forsyth, D. (1994), 'Modelling wide-angle seismic data for crustal structure; southeastern Grenville Province', *J. Geophys. Res.* **99**(6), 11,687–11,704.

Zelt, C. and Smith, R. (1992), 'Seismic traveltime inversion for 2-D crustal velocity structure.', *Geophys. J. Int.* **108**, 16–34.

Zhao, X. (1996), Magnetic signatures of peridotite rocks from Sites 897 and 899 and their implicitions, *in* R. Whitmarsh, D. Sawyer, A. Klaus and D. Masson, eds, 'Proc. of the Ocean Drilling Program, Sci. Results', Vol. 149, Ocean Drilling Program, College Station TX, pp. 431–446.

Zhao, X., Turrin, B. D., Jackson, M. and Solheid, P. (2001), Data report: Paleomagnetic and rock magnetic characterization of rocks recovered from Leg 173 Sites, *in* M.-O. Beslier, R. Whitmarsh, P. Wallace and J. Girardeau, eds, 'Proc. of the Ocean Drilling Program, Sci. Results', Vol. 173, Ocean Drilling Program, College Station TX, pp. 1–34 [CDROM].